

**SYNTHESIS AND CHARACTERIZATION OF MONO- AND
DIRUTHENIUM COMPOUNDS**

by

Lyndsy A. Miller-Clark

A Dissertation

Submitted to the Faculty of Purdue University

In Partial Fulfillment of the Requirements for the degree of

Doctor of Philosophy



Department of Chemistry

West Lafayette, Indiana

December 2022

THE PURDUE UNIVERSITY GRADUATE SCHOOL
STATEMENT OF COMMITTEE APPROVAL

Dr. Tong Ren, Chair

Department of Chemistry

Dr. Suzanne Bart

Department of Chemistry

Dr. Libai Huang

Department of Chemistry

Dr. Christina Li

Department of Chemistry

Approved by:

Dr. Christine Hrycyna

Dedicated to my family: my parents for their encouragement in all that I do, my brothers for always being there, and my husband for his unwavering love and support.

ACKNOWLEDGMENTS

I was able to make it to where I am today in large part because of the community I had around me. I was able to weather all the challenges graduate school and life threw at me because of their support.

To my parents, who never hesitated to come and help me move, who celebrated my successes, and commiserated with me on my failures. They have always been in my corner, and it has helped me grow up and flourish here at Purdue. To my brothers, who never failed to help make me laugh, gave great books and board game recommendations, and who helped remind me to just enjoy being present. Thank you, family.

I would also like to express my sincere gratitude to my advisor, Prof. Tong Ren. He let me continue to work with ruthenium, and his continuous support of my PhD studies and research was greatly appreciated. His patience and motivation helped me find my 'bench hands' in the lab, and his expertise was invaluable during my whole PhD. Thank you for these years in your lab.

I want to thank Drs. Bart, Li, and McMillin for their advice throughout my years at Purdue. Their perspectives helped me grow as a writer, researcher, and group leader in the Ren Lab.

I want to also thank my fellow Ren lab mates, past and present, for the fun times and for their support when things went awry. I know I wouldn't have become the scientist I am today without Drs. Susie Banziger, Adharsh Raghavan, and Ashley Schuman. They listened to my research problems, mentored me through confusing or encouraging results, and overall provided me with many happy times in and out of lab. Thank you for helping show me what it is to be a researcher. For the current members: I want to thank Reese for the board game nights and Leo for being an amazing desk partner, taco buddy, and for encouraging my crossword habit.

I also want to thank all my friends from Hope College and Purdue. They helped me get through classes, my OP, and just writing papers. They were always able to lend a hand when something happened in the lab or when new things arrived, and old ones had to be moved out. You all made my time in graduate school happier, and I thank you for that.

And finally, Dan, I can't thank you enough for coming to Purdue to be with me. I made it through the hard times and good times because of you and your love and support. Thank you for all the smiles and laughter, all your chemistry advice. I don't think I would have made it to this point without you. So, thank you.

TABLE OF CONTENTS

LIST OF TABLES	9
LIST OF FIGURES	10
LIST OF SCHEMES	14
LIST OF ABBREVIATIONS	15
ABSTRACT	17
CHAPTER 1. DIRTUHENIUM ARYL COMPOUNDS – TUNING OF ELECTROCHEMICAL RESPONSES AND SOLUBILITY	18
1.1 Abstract	18
1.2 Introduction	18
1.3 Results and Discussion	20
1.3.1 Synthesis	20
1.3.2 Molecular Structures	22
1.3.3 Electronic Absorption Spectra	28
1.3.4 Electrochemical Studies	30
1.4 Conclusions	34
1.5 Experimental Section	34
1.5.1 Synthesis Details	35
1.5.2 X-ray Crystallographic Details	40
CHAPTER 2. PHENYLENE AS AN EFFICIENT MEDIATOR FOR INTERMETALLIC ELECTRONIC COUPLING	42
2.1 Abstract	42
2.2 Introduction	42
2.3 Results and Discussion	43
2.3.1 Synthesis	43
2.3.2 Molecular Structures	45
2.3.3 Electrochemical Studies	47
2.3.4 Vis-NIR and IR Spectroelectrochemistry Experiments	49
2.3.5 Density Functional Theory Analysis	55
2.4 Conclusions	59

2.5	Experimental Section	59
2.5.1	Synthesis Details.....	60
2.5.2	X-ray Crystallographic Details	62
2.5.3	Computational Details	63
CHAPTER 3. BIS-ARYL AND BIS-ALKYNYL DIRUTHENIUM (III,III) COMPOUNDS BASED ON AN ELECTRON-DEFICIENT BUILDING BLOCK		65
3.1	Abstract	65
3.2	Introduction.....	65
3.3	Results and Discussion	68
3.3.1	Synthesis	68
3.3.2	Molecular Structures.....	72
3.3.3	Electronic Absorption Spectra	76
3.3.4	Electrochemical Studies.....	77
3.3.5	Density Functional Theory Analysis	81
3.4	Conclusions	84
3.5	Experimental Section	84
3.5.1	Synthesis Details.....	85
3.5.2	X-ray Crystallographic Details	88
3.5.3	Computational Methods.....	88
3.5.4	Synthesis of Ru ₂ (amtfmp) ₄ Cl ₂ following literature procedure	89
3.5.5	Synthesis of Ru ₂ (amtfmp) ₄ (Ph) ₂ using material from 3.5.4	89
3.5.6	Synthesis of Ru ₂ (amtfmp) ₄ (C ₂ TIPS) ₂	89
CHAPTER 4. SYNTHESSES AND MATERIAL APPLICATIONS OF RU(II)(BISPHOSPHINE) ₂ ALKYNYLS		91
4.1	Abstract	91
4.2	Introduction.....	91
4.3	Synthetic methods for Ru bis-alkynyl complexes	92
4.3.1	Synthesis from trimethylstannyl alkynyl	92
4.3.2	Synthesis through vinylidene formation	96
	Starting with cis-RuCl ₂ (L-L) ₂ (L-L = dppm/dppe)	96
	Use of lithiated poly-ynyls	99

Starting with $[\text{RuCl}(\text{dppe})_2]^+$	100
Use of mixed ligand complexes $[\text{Ru}(\text{C}_2\text{R})(\text{X})(\text{dppe})_2]^+$ ($\text{X} = \text{NH}_3, \text{H}, \text{CN}, \text{N}\equiv\text{C-R}$)	102
4.3.3 Single bond metathesis synthesis of mono- and bis- Ru alkynyls	105
4.4 Electronic and opto-electronic materials	107
4.4.1 Non-linear optical materials	107
4.4.2 Molecular switches and wires	108
Molecular switches	108
Wire-like molecules and molecular wires	110
4.4.3 Dye-sensitized solar cells	112
4.5 Conclusions and future outlooks	115
CHAPTER 5. SYNTHESIS, STRUCTURAL & SPECTROSCOPIC ANALYSIS OF MONO- AND UNSYMMETRIC BIS-ALKYNYL COMPOUNDS BASED ON $\text{Ru}(\text{II})(\text{C}_2\text{NAP}^{\text{R}})$	116
5.1 Abstract	116
5.2 Introduction	116
5.3 Results and Discussion	118
5.3.1 Synthesis	118
5.3.2 Molecular Structures	121
5.3.3 UV/Vis Absorption and Emission Spectra	124
5.3.4 Electrochemical Studies	128
5.3.5 Density Functional Theory Analysis	131
5.4 Conclusions	134
5.5 Experimental Section	135
5.5.1 Synthesis details	136
5.5.2 X-ray Crystallographic Details	138
5.5.3 Computational Methods	139
APPENDIX A: ADDITIONAL MATERIALS FOR DIRUTHENIUM ARYL COMPOUNDS – TUNING OF ELECTROCHEMICAL RESPONSES AND SOLUBILITY	140
APPENDIX B: ADDITIONAL MATERIALS FOR PHENYLENE AS AN EFFICIENT MEDIATOR FOR INTERMETALLIC COUPLING	143
APPENDIX C: ADDITIONAL MATERIALS FOR BIS-ARYL AND BIS-ALKYNYL (III,III) COMPOUNDS BASED ON AN ELECTRON-DEFICIENT BUILDING BLOCK	160

APPENDIX D: ADDITIONAL MATERIALS FOR SYNTHESIS, STRUCTURAL & SPECTROSCOPIC ANALYSIS OF MONO- AND UNSYMMETRIC BIS-ALKYNYL COMPOUNDS BASED ON RU(II)(C ₂ NAP ^R)	173
REFERENCES	179
VITA.....	202
LIST OF PUBLICATIONS	203

LIST OF TABLES

Table 1.1. Solubility comparisons between 2a/2b and Ru ₂ (ap) ₄ (C ₆ H ₄ - ^t Bu).....	21
Table 1.2. Selected Bond Lengths (Å) and angles (deg) for compounds 1a, 2a/2b, 3a/3b, 4a/4b and 5a.....	27
Table 1.3. Electrochemical data (in V vs Fc ⁺⁰) from DPV for 1a–6a and 1b–5b in THF.....	30
Table 2.1. Selected bond lengths (Å) and angles (deg) for 8 and 9.....	46
Table 2.2. Room temperature magnetism data reported as per compound (Evans method ⁴⁵). Solvent: CDCl ₃ , Reference: Ferrocene	56
Table 2.3. Frontier MOs for 8 with respective orbital compositions (minor contributions < 5% not included)*†	57
Table 3.1. Selected bond lengths (Å) and angles (deg) for 10–12.....	75
Table 3.2. Electrode Potentials (in V vs Fc ⁺⁰) for Ru ₂ (amtftp) ₄ (Y) ₂ in THF.....	79
Table 3.3. Electrochemical data from CV (V vs Ag/AgCl).....	80
Table 3.4. Molecular orbital diagram of 10' and 11' with corresponding energies (eV)	82
Table 5.1. Selected bond lengths (Å) and angles (deg.) for compounds 13–17	124
Table 5.2. Absorption and emission data for 13–17	125
Table 5.3. Electrode Potentials (in V vs Fc ⁺⁰) for 13–17 in THF	128
Table 5.4. Selected MO diagram of 14', 15' and 17' with corresponding energies (eV)	133

LIST OF FIGURES

Figure 1.1. Diruthenium alkynyl and aryl compounds	19
Figure 1.2. ORTEP plot of 1a at 30% probability level. H atoms and solvent molecules removed for clarity	23
Figure 1.3. ORTEP plot of 2a at 30% probability level. H atoms and $-^t\text{Bu}$ moiety disorder removed for clarity	23
Figure 1.4. ORTEP plot of 2b at 30% probability level. Solvent molecules, ligand disorder, and H atoms removed for clarity	24
Figure 1.5. ORTEP plot of 3a at 30% probability level. H atoms removed for clarity	24
Figure 1.6. ORTEP plot of 3b at 30% probability level. H atoms removed for clarity	25
Figure 1.7. ORTEP plot of 4a at 30% probability level. H atoms removed for clarity	25
Figure 1.8 ORTEP plot of 4b at 30% probability level. H atoms and solvent molecules omitted for clarity	26
Figure 1.9. ORTEP plot of 5a at 30% probability level. H atoms and $-\text{CF}_3$ moiety disorder omitted for clarity	26
Figure 1.10. Qualitative MO diagram of $\text{Ru}_2(\text{ap}')_4$ core upon attachment of aryl ligand (energy levels not drawn to scale).....	28
Figure 1.11. Vis-NIR absorption spectra of compounds 1a–6a in THF	29
Figure 1.12. Vis-NIR absorption spectra of 1b–5b in THF	29
Figure 1.13. Cyclic (black) and differential pulse (red) voltammograms of compounds 1a–6a (1.0 mM) recorded in 0.10 M THF solutions of $[\text{Bu}_4\text{N}][\text{PF}_6]$ at a scan rate of 0.1 V/s.....	31
Figure 1.14. Cyclic (black) and differential pulse (red) voltammograms of compounds 1b–5b (1.0 mM) recorded in 0.10 M THF solutions of $[\text{Bu}_4\text{N}][\text{PF}_6]$ at a scan rate of 0.1 V/s.....	32
Figure 1.15. Hammett plot of 1a–6a oxidation potentials ($E(\text{Ru}_2^{6+/5+})$) versus σ_Y . The squares are measured oxidation potentials and the solid line is the linear best-fit line	33
Figure 1.16. Hammett plot of 1b–5b oxidation potentials ($E(\text{Ru}_2^{6+/5+})$) versus σ_Y . The squares are measured oxidation potentials and the solid line is the linear best-fit line	33
Figure 2.1. Polymetallaynes (I) and polymetallaarylene (II) structural motifs.....	43
Figure 2.2. ESI-MS of the crude reaction mixture of Scheme 2.2 at low fragmentation voltages, courtesy of Dr. Adarsh Raghavan. Isotopic distribution characteristic of $(\text{Ru}_2)_2$ corresponding to $[\mathbf{7}]^{2+}$ ($m/z = 1834.0 / 2 = 917$, left). Side product $\text{Ru}_2(\text{ap})_4\text{Ph}$ (right).....	44
Figure 2.3. ORTEP plot of 8 at 30% probability level. H atoms and solvent molecules omitted for clarity	47

Figure 2.4. ORTEP plot of 9 at 30% probability level. H atoms and solvent molecules omitted for clarity	47
Figure 2.5. Cyclic (black) and differential pulse (red) voltammograms of compounds 8 and 9 (1.0 mM) recorded in 0.1 M [Bu ₄ N][PF ₆] in THF at a scan rate of 0.1 V/s.....	48
Figure 2.6. Cyclic (black) and differential pulse (red) voltammograms of 7 (< 1.0 mM) recorded in 0.1 M [Bu ₄ N][PF ₆] in THF at a scan rate of 0.1 V/s, courtesy of Dr. A. Raghavan.....	49
Figure 2.7. Vis-NIR absorption spectra of 7–9 in THF	50
Figure 2.8. (a) Spectroelectrochemistry Vis-NIR of 9 at –1.15 V in THF vs Ag wire. Instrument artifacts/solvent overtones noted as *. (b) FT-IR spectroelectrochemistry of 9 at –1.15 V vs Ag wire. 2 mM analyte with 0.1 M [Bu ₄ N][PF ₆] in THF for both (a) and (b) with grey lines denoting intermediate scans for each SEC experiment.....	50
Figure 2.9. Full spectroelectrochemical UV-Vis-NIR changes of 8 at –1.1 V (a) and –1.2 V (b) vs Ag wire. 2 mM analyte with 0.1 M [Bu ₄ N][PF ₆] in THF in all cases. Instrument artifacts/solvent overtones noted as * with grey lines denoting intermediate scans for each SEC experiment. Isosbestic point located at 1000 nm (20000 cm ⁻¹)	51
Figure 2.10. FT-IR spectroelectrochemistry of 8 at –1.1 V (a) and –1.35 V (b) vs Ag wire. 2 mM analyte with 0.1 M [Bu ₄ N][PF ₆] in THF in all cases, with grey lines denoting intermediate scans for each SEC experiment	52
Figure 2.11. Vis-NIR and IR spectroelectrochemistry of 8 with Gaussian fit of the IVCT band (black dash) at 0.4 V (a) and 0.65 V (b) vs Ag wire, 2 mM analyte with 0.1 M [Bu ₄ N][PF ₆] in THF in all cases. Instrument artifacts / solvent overtones noted as * with grey lines denoting intermediate scans for each SEC experiment.....	53
Figure 2.12. (a) Vis-NIR spectroelectrochemistry of 9 at 0.3 V (a) in THF vs Ag wire. Instrument artifacts/solvent overtones noted as *. (b) FT-IR spectroelectrochemistry of 9 at 0.4 V (b) vs Ag wire. 2 mM analyte with 0.1 M [Bu ₄ N][PF ₆] in THF in all cases. Grey lines denoting intermediate scans for each SEC experiment.....	54
Figure 2.13. FT-IR spectroelectrochemistry of 8 at 0.1 V (a) and 0.3-0.4 V (b) vs Ag wire. 2 mM analyte with 0.1 M [Bu ₄ N][PF ₆] in THF in all cases with grey lines denoting intermediate scans for each SEC experiment	55
Figure 2.14. HOMO (top) and LUMO (bottom) of the DFT-optimized structure of 8. Isovalue = 0.020, courtesy of Dr. A. Raghavan.....	57
Figure 2.15. Natural transition donor (left) and acceptor (right) orbitals corresponding to the IVCT band, extracted from excited state #5 of [8] ⁺ . Experimental (Figure 2.11) ca. 4000 cm ⁻¹ , Calculated (Figure 2.16) 4647.1 cm ⁻¹ . Isovalue = 0.025, courtesy of Dr. A. Raghavan	58
Figure 2.16. TD-DFT calculated electronic absorption spectrum of [8] ⁺ , courtesy of Dr. A. Raghavan.....	58
Figure 3.1. a) symmetric and asymmetric <i>N,N'</i> bridging ligands and b) possible configurations of Ru ₂ compounds (Y = -Cl, -C≡C and -Ar).....	67

Figure 3.2. TLC plates of the Soxhlet product (left lane in all plates, abbreviated as ‘Sox’), a co-spot of the Soxhlet and literature products (center lane, abbreviated as ‘Co’), and the literature product (right lane in all plates, abbreviated as ‘Lit’).....	69
Figure 3.3. Normalized vis-NIR absorption spectra in MeOH of [Ru ₂ (amtfmp) ₄ Cl ₂] [−] (red line) and the baseline material from arylations (black line).....	71
Figure 3.4. FTIR spectra of 10.....	72
Figure 3.5. ORTEP plot of 10 at 30% probability level. Most H atoms omitted for clarity.....	73
Figure 3.6. ORTEP plot of 11 at 30% probability level. Most H atoms omitted for clarity.....	73
Figure 3.7. ORTEP plot of 12 at 30% probability level. Most H atoms omitted for clarity.....	74
Figure 3.8. Vis-NIR absorption spectra of 10–12 and Ru ₂ (amtfmp) ₄ Cl ₂ in THF.....	76
Figure 3.9. Cyclic (black) and differential pulse (red) voltammograms of a mixture of <i>cis</i> (2:2) and (3:1) Ru ₂ (amtfmp) ₄ Cl ₂ (top) and <i>cis</i> (2:2) Ru ₂ (amtfmp) ₄ Cl ₂ (bottom) (1.0 mM) recorded in 0.10 M THF solutions of [Bu ₄ N][PF ₆] at a scan rate of 0.1 V/s.....	77
Figure 3.10. Cyclic (black) and differential pulse (red) voltammograms of compounds 10–12 (1.0 mM) recorded in 0.10 M THF solutions of [Bu ₄ N][PF ₆] at a scan rate of 0.10 V/s.....	78
Figure 3.11. Cyclic (black) and differential pulse (red) voltammograms of 10 recorded in 0.10 M THF solutions of [Bu ₄ N][PF ₆] at a scan rate of 0.10 V/s. Possible degradation product peak denoted as * in the scan	79
Figure 3.12. Molecular orbital diagrams of 10' (left) and 11' (right) obtained from DFT calculations, represented at isovalue = 0.03. The HOMO-1 for 10' was omitted as it consists of the dπ - π interactions akin to the HOMO of 10' but in the orthogonal orientation (plotted in Table 3.4)...	81
Figure 4.1. Representative structures of <i>trans</i> mono- and bis-alkynyl compounds based on dppm (left) and dppe (right).....	92
Figure 4.2. Molecular structure of [<i>cis</i> -Ru(C≡C-Fc) ₂ (dppm) ₂]CuI generated from CCDC 1238773	95
Figure 4.3. Molecular structure of [Ru(η ³ -{HC(C ₆ H ₄ -4-Me)=C-C≡C-C ₆ H ₄ -4-Me})-(dppm) ₂] ⁺ generated from CCDC 1426051	97
Figure 4.4. Molecular structure of [RuCl(dppe) ₂]OTf, generated from CCDC 719111.....	101
Figure 4.5. Molecular structure of <i>trans</i> -[Ru(C ₂ Ph)(NH ₃)(dppe) ₂] ⁺ generated from CCDC 1234388	103
Figure 4.6. Molecular structure of [(dppe) ₂ (Ph-C≡C)Ru(N≡CC ₆ H ₄ C≡N)Ru(C≡C-Ph)(dppe) ₂][PF ₆] ₂ generated from CCDC 211235	104
Figure 4.7. Molecular structure of <i>trans</i> -Ru(dmpe) ₂ Me ₂ generated from CCDC 665447	105
Figure 4.8. Molecular structure of <i>trans</i> -Ru(dmpe) ₂ Me(C≡C-Ph) generated from CCDC 665448	106

Figure 4.9. Schematics of the functionalized nanogap devices based on -Ru-(C ₂ -DTE-C ₂)-Ru-complex. Inset: SEM image of a device fabricated by OWL-generated nanowire. Taken from Ref. ⁶⁸	109
Figure 4.10. Molecular conductance of -(C _{2n})Ru(dppe) ₂ (C _{2n})- measured with the STM-break junction technique; n = 2 (1 ²), 3 (1 ³) and 4 (1 ⁴). Taken from Ref. ⁶⁷	112
Figure 4.11. Representative ‘D-B-A’ molecules with varying anchors and ‘acceptor’ ligands for DSSCs from Ref. ²¹² , colored as they appear as CH ₂ Cl ₂ solutions.....	113
Figure 4.12. (top) Incident photon-to-current conversion efficiency (IPCE) and (bottom) current density–voltage profiles of a DSSC with a representative Ru dye (insert), under 100 mW cm ⁻² illumination (solid line) and in the dark (dashed line). Modified from Ref. ¹⁸⁴	114
Figure 5.1. (top) <i>trans</i> -RuCl(C ₂ NAP ^R) compounds (<i>B-A</i>) based on dppe (13 and 14) or dppm (16 and 17) units; (bottom) <i>trans</i> -Ru(C ₂ NAP ^{mes})(C ₂ Ph)(dppe) ₂ (15) (<i>D-B-A</i>) compound	118
Figure 5.2. FTIR spectra of 13–17	120
Figure 5.3. ORTEP plot of 13 at 30% probability level. H atoms, disorder and solvent molecules removed for clarity.....	121
Figure 5.4. ORTEP plot of 14 at 30% probability level. H atoms, disorder and solvent molecules removed for clarity.....	122
Figure 5.5. ORTEP plot of 15 at 30% probability level. H atoms and disorder removed for clarity	122
Figure 5.6. ORTEP plot of 16 at 30% probability level. H atoms, disorder and solvent molecules removed for clarity.....	122
Figure 5.7. ORTEP plot of 17 at 30% probability level. H atoms and disorder removed for clarity	123
Figure 5.8. UV-vis absorption spectra of compounds 13–15 and HC ₂ NAP ^{mes} in THF.....	126
Figure 5.9. UV-vis absorption spectra of compounds 16 and 17 in THF.....	126
Figure 5.10. Normalized absorption (dashed lines) and emission spectra (solid lines) of 13, 14, and 17 in THF as N ₂ -degassed solutions	127
Figure 5.11. Normalized absorption (dashed lines) and emission spectra (solid lines) of 15 in hexanes (red lines) or THF (blue lines) as N ₂ -degassed solutions.....	128
Figure 5.12. Cyclic (black) and differential pulse (red) voltammograms of compounds 13–15 (1.0 mM) recorded in 0.10 M THF solutions of [Bu ₄ N][PF ₆] at a scan rate of 0.10 V/s.....	129
Figure 5.13. Cyclic (black) and differential pulse (red) voltammograms of compounds 16 and 17 (1.0 mM) recorded in 0.10 M THF solutions of [Bu ₄ N][PF ₆] at a scan rate of 0.10 V/s.....	130
Figure 5.14. Frontier molecular orbitals of 14' (left), 15' (center), and 17' (right) derived from DFT calculations. MOs are plotted at isovalue = 0.025	132
Figure 5.15. TD-DFT calculated UV-Vis spectrum of 15' in THF (first 20 transitions).....	134

LIST OF SCHEMES

Scheme 1.1. Synthesis of modified 2-anilinopyridine ligands	20
Scheme 1.2. Synthesis of $\text{Ru}_2(\text{ap}')_4\text{Cl}$	20
Scheme 1.3. Synthesis of modified Ru_2 aryl compounds. Conditions: 6 – 10 equiv LiAr, THF, room temperature, N_2 , 1 – 3 hours	21
Scheme 2.1. Compounds discussed in this chapter.....	43
Scheme 2.2. Synthesis of 7 from $\text{Ru}_2(\text{ap})_4\text{Cl}$ and a slight excess of 1,4-dilithiobenzene	44
Scheme 2.3. Synthesis of 8 from the reaction between 7, CN^- and O_2	45
Scheme 2.4. Synthesis of 9 from the reaction of $\text{Ru}_2(\text{ap})_4\text{Ph}$, ³⁵ CN^- and O_2	45
Scheme 3.1. Synthesis of $\text{Ru}_2(\text{amtftp})_4\text{Cl}_2$ following literature procedures ¹²⁴	68
Scheme 3.2. Synthesis of $\text{Ru}_2(\text{amtftp})_4\text{Cl}_2$ used in this work	68
Scheme 3.3. Synthetic approach to produce $\text{Ru}_2(\text{amtftp})_4(\text{Y})_2$ ($\text{Y} = \text{C}_2\text{Ph}$, Ph) compounds	10–12
.....	70
Scheme 4.1. Synthesis based on trimethylstannyl alkynyls; X = bridge groups	93
Scheme 4.2. Synthesis of Ru bis-alkynyls utilizing trimethylstannyl reagents	94
Scheme 4.3. Unsymmetric Ru alkynyl synthesis through formation of vinylidene intermediate	96
Scheme 4.4. Synthesis of mono-alkynyl compounds using lithiated poly-ynyl	99
Scheme 4.5. Pathway to generate unsymmetric Ru bis-alkynyls from $[\text{RuCl}(\text{dppe})_2]\text{OTf}$	101
Scheme 4.6. Alternative pathway to unsymmetric Ru bis-alkynyls from $[\text{RuCl}(\text{dppe})_2]\text{OTf}$	102
Scheme 4.7. Unsymmetric <i>trans</i> - bis-alkynyl Ru compounds via $[\text{trans-Ru}(\text{C}\equiv\text{C-R})(\text{NH}_3)(\text{dppe})_2]^+$	103
Scheme 4.8. Ru(II) bis-alkynyl synthesis from single-bond metathesis.....	105
Scheme 5.1. Synthesis of 13 and 14 using <i>cis</i> - $\text{RuCl}_2(\text{dppe})_2$, $\text{HC}_2\text{NAP}^{\text{R}}$ ($\text{R} = \text{iPr}$, mesityl) and weak base conditions.....	118
Scheme 5.2. Synthesis of 16 and 17 using <i>cis</i> - $\text{RuCl}_2(\text{dppm})_2$, $\text{HC}_2\text{NAP}^{\text{R}}$ ($\text{R} = \text{iPr}$, mesityl) and weak base conditions	119
Scheme 5.3. Synthesis of 15 (and by-product 14) using $[(\text{dppe})_2\text{Ru}(\text{NH}_3)(\text{C}_2\text{Ph})]\text{PF}_6$, $\text{HC}_2\text{NAP}^{\text{mes}}$ and weak base conditions.....	119

LIST OF ABBREVIATIONS

amtcmp	2-amino-3-(trifluoromethyl)pyridinate
<i>ap</i>	2-anilinopyridinate
<i>ap'</i>	Substituted derivatives of <i>ap</i>
Ar	Aryl
<i>B-A</i>	Bridge-Acceptor
CDCl ₃	Chloroform- <i>d</i> ₆
CHCl ₃	Chloroform
CH ₂ Cl ₂	Dichloromethane
CSS	Charge separated state
CV	Cyclic voltammogram/voltammetry
<i>D-B-A</i>	Donor-Bridge-Acceptor
DFT	Density Functional Theory
DMBA	<i>N,N'</i> -dimethylbenzamidinate
dmpe	1,2-bis(dimethylphosphino)ethane
dppe	1,2-bis(diphenylphosphino)ethane
dppm	1,2-bis(diphenylphosphino)methane
DPV	Differential pulse voltammogram/voltammetry
DSSC	Dye-sensitized solar cell
ESI-MS	Electrospray ionization mass spectrometry

EtOAc	Ethyl acetate
Fc ⁺⁰	Ferrocenium/Ferrocene
HOMO	Highest occupied MO
IR	Infrared
IVCT	Intervalence charge transfer
LUMO	Lowest unoccupied MO
LMCT	Ligand to metal charge transfer
MLCT	Metal to ligand charge transfer
MO	Molecular orbital
NAP ^R	<i>N</i> -R-1,8-naphthalimide; R = isopropyl (iPr), mesityl (mes)
ⁿ BuLi	<i>n</i> -butyl lithium
NMR	Nuclear magnetic resonance
PET	Photo induced electron transfer
SEC	Spectroelectrochemistry experiment
SOMO	Singly occupied MO
TD-DFT	Time-dependent DFT
THF	Tetrahydrofuran
TIPS	Triisopropylsilyl
TMS	Trimethylsilyl
UV-vis/NIR	Ultraviolet-visible/Near infrared
XRD	X-ray diffraction

ABSTRACT

This thesis will focus on two broad topics: the synthesis and characterization of various diruthenium aryl compounds and of mono- and bis-alkynyl unsymmetric compounds based on Ru(II)(dppm)₂ and Ru(II)(dppe)₂ bridges (dppm = 1,2-bis(diphenylphosphino)methane; dppe = 1,2-bis(diphenylphosphino)ethane).

Chapters 1–3 focus on multiply bonded metal–metal compounds, utilizing four different ‘paddlewheel’ motifs (dinuclear ruthenium units that are supported by four bidentate ligands). These highly stable mono- and bis-aryl diruthenium compounds are readily prepared using lithium-halogen exchange reactions. Two different oxidation states have been accessed, Ru₂(II,III) and Ru₂(III,III), through modification of the paddlewheel ligands or coordination of a small, π -accepting ligand at the vacant ruthenium site in Ru₂(*ap*)₄(Ar) compounds (*ap* = 2-anilinyridinate; Ar = aryl). Chapter 1 discusses the modification of the bidentate ligand to yield two unique Ru₂(*ap'*)₄(Ar) series, which both exhibit improved solubility over the previously reported unmodified Ru₂(*ap*)₄(Ar) series, and the structural, electronic, and optical characterizations of the compounds within these two new Ru₂(II,III) series. Chapter 2 builds upon our lab’s previous studies on electron transfer between the two ruthenium centers in [Ru₂(*ap*)₄](μ -C \equiv C)_x compounds and applies this towards synthesizing and characterizing mixed-valency within a Ru₂(III,III) phenylene bridged compound [(NC)Ru₂(*ap*)₄]₂(μ -1,4-C₆H₄). Chapter 3 highlights the synthesis and characterization of bis-aryl and bis-alkynyl Ru₂(III,III) compounds, Ru₂(amtfmp)₄(Y)₂ (Y = -C \equiv CPh, -Ph), supported with the electron-withdrawing paddlewheel ligand amtfmp (amtfmp = 2-amino-3-(trifluoromethyl)pyridinate).

Chapters 4 and 5 are focused on the synthesis and characterization of both mono- and bis-alkynyl unsymmetric compounds to study photo-induced electron transfer (PET) processes. Chapter 4 features as an introduction to the synthesis of these Ru(II)(dppm)₂ and Ru(II)(dppe)₂ alkynyl compounds along with some material applications. Chapter 5 discusses the mono- and bis-alkynyl compounds based on Ru(II)(dppm)₂ and Ru(II)(dppe)₂ bridges that utilized a highly electron-withdrawing chromophore ‘acceptor’ ligand, NAP^R (R = isopropyl, mesityl), to generate the *B-A* (mono-alkynyl) and *D-B-A* (unsymmetric bis-alkynyl) compounds.

CHAPTER 1. DIRUTHENIUM ARYL COMPOUNDS – TUNING OF ELECTROCHEMICAL RESPONSES AND SOLUBILITY

Reproduced (adapted) from L. A. Miller-Clark, P. E. Christ and T. Ren, *Dalton Trans.*, 2022, **51**, 580-586 with permission from the Royal Society of Chemistry. DOI: 10.1039/D1DT03957A

1.1 Abstract

Reported herein are the two new series of diruthenium aryl compounds: $\text{Ru}_2(\text{DiMeOap})_4(\text{Ar})$ (**1a–6a**) (DiMeOap = 2-(3,5-dimethoxyanilino)pyridinate) and $\text{Ru}_2(m\text{-}^i\text{PrOap})_4(\text{Ar})$ (**1b–5b**) ($m\text{-}^i\text{PrOap}$ = 2-(3-*iso*-propoxyanilino)pyridinate), prepared through the lithium-halogen exchange reaction with a variety of aryl halides (Ar = $\text{C}_6\text{H}_4\text{-4-NMe}_2$ (**1**), $\text{C}_6\text{H}_4\text{-4-}^t\text{Bu}$ (**2**), $\text{C}_6\text{H}_4\text{-4-OMe}$ (**3**), $\text{C}_6\text{H}_3\text{-3,5-(OMe)}_2$ (**4**), $\text{C}_6\text{H}_4\text{-4-CF}_3$ (**5**), C_6H_5 (**6**)). The molecular structures of these compounds were established with X-ray diffraction studies. Additionally, these compounds were characterized using electronic absorption and voltammetric techniques. Compounds **1a–6a** and **1b–5b** are all in the Ru_2^{5+} oxidation state, with a ground state configuration of $\sigma^2\pi^4\delta^2(\pi^*\delta^*)^3$ ($S = 3/2$). Use of the modified *ap* ligands (*ap'*) resulted in moderate increases of product yield when compared to the unsubstituted $\text{Ru}_2(\text{ap})_4(\text{Ar})$ (*ap* = 2-anilinopyridinate) series. Comparisons of the electrochemical properties of **1a–6a** and **1b–5b** against the $\text{Ru}_2(\text{ap}')\text{Cl}$ starting material reveals the addition of the aryl ligand cathodically shifted the $\text{Ru}_2^{6+/5+}$ oxidation and $\text{Ru}_2^{5+/4+}$ reduction potentials. These oxidation and reductions potentials are also strongly dependent on the *p*-substituent of the axial aryl ligands.

1.2 Introduction

Chemistry of diruthenium paddlewheel compounds has prospered since the discovery and structural characterization of diruthenium(II,III) tetracarboxylates by the groups of Wilkinson¹ and Cotton,² respectively. Besides carboxylates, a variety of *N,O*- and *N,N'*-bridging bidentate ligands have been employed to support diruthenium paddlewheel motifs.^{3,4} Among the distinctive features of diruthenium compounds are the rich redox characteristics and a remarkable range of accessible oxidation states from $\text{Ru}_2(\text{I,II})$ to $\text{Ru}_2(\text{III,IV})$, which have been detailed in a comprehensive review by Kadish and co-workers.⁵ The closeness of the π^* and δ^* orbital energies in these compounds has resulted in interesting magnetic properties, and potential molecular magnets based on 1D, 2D

and 3D extended structures have been explored by the groups of Handa^{6,7} and Miller.^{8,9} Diruthenium compounds supported by carboxylates, carbonates, and amidates are also capable of catalyzing homogeneous oxidation reactions.^{10–15}

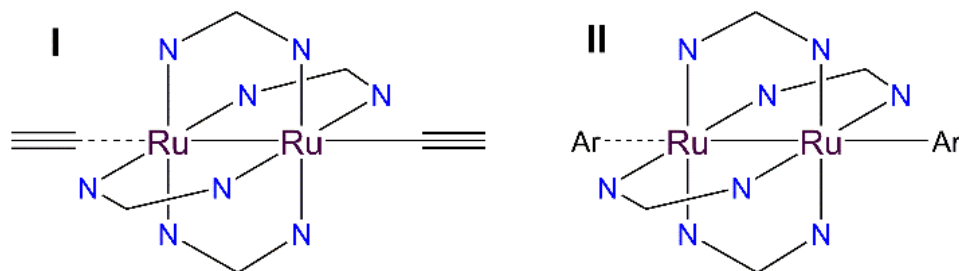


Figure 1.1. Diruthenium alkynyl and aryl compounds

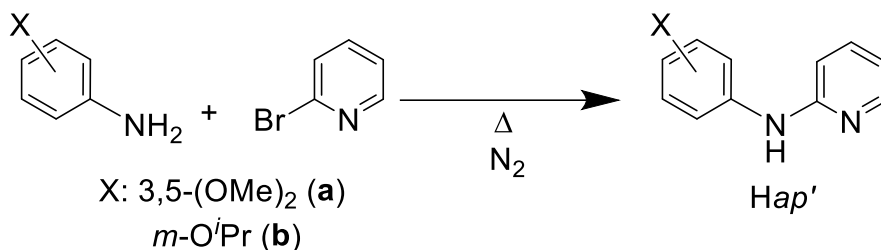
In the realm of diruthenium organometallic compounds, alkynylation reactions were first explored by the groups of Cotton,¹⁶ and Bear and Kadish,^{17–19} based on the $\text{Ru}_2(\text{ap})_4$ building block (ap = 2-anilinopyridinate). Inspired by these pioneering efforts, our laboratory has extensively explored both mono- and bis-alkynyl diruthenium compounds (type **I** in Figure 1.1) with three classes of bridging ligands, DArF (N,N' -diarylformamidinate), ap and DMBA (N,N' -dimethylbenzamidinate).^{20,21} The aforementioned rich and robust redox chemistry has rendered these Ru_2 alkynyl compounds, primarily ap based, ideal candidates for the investigation of electron delocalization across oligoyn-diyls,^{22–25} and fabrication of molecular wires and devices.^{26–29} Groups of Lehn,³⁰ Kuhn,³¹ Peng,³² and Zuo³³ also explored the chemistry of Ru_2 alkynyl compounds with outcomes complementary to ours. Most recently, Akita and co-workers demonstrated the enhancement of molecular conductance through proper alignment between the HOMO energy of $\text{trans-Ru}_2(\text{DArF})_4(\text{C}_2\text{Ar})_2$ species and the Fermi level of metal electrode.³⁴ In parallel to alkynylation, our laboratory recently demonstrated that both $\text{Ru}_2(\text{ap})_4\text{Cl}$ and $\text{Ru}_2(\text{DMBA})_4\text{Cl}_2$ undergo arylation reactions when treated with LiAr to afford $\text{Ru}_2(\text{ap})_4(\text{Ar})$ ³⁵ and $\text{Ru}_2(\text{DMBA})_4(\text{Ar})_2$,³⁶ respectively (type **II** in Figure 1.1). $\text{Ru}_2(\text{ap})_4(\text{Ar})$ undergoes further reactions with small molecules (Z), namely CN^- , C_2H^- and CO , at the vacant axial site to afford $[\text{Z-Ru}_2(\text{ap})_4(\text{Ar})]$ products that are diverse in electronic and magnetic properties.³⁷ The only other known aryl/alkyl species based on the bimetallic paddlewheel motif are bis(phenyl)dirhodium(III) species reported by Doyle and co-workers,^{38–41} and $\text{Rh}_2(\text{ap})_4(\text{Ph})$ and $\text{Rh}_2(\text{ap})_4(\text{Me})$ by Bear and Kadish.⁴² Both the paucity of bimetallic aryl compounds and interesting physical properties

unveiled for $\text{Ru}_2(\text{ap})_4(\text{Ar})$ and $\text{Ru}_2(\text{DMBA})_4(\text{Ar})_2$ warrant further investigation of Ru_2 -aryl chemistry. Aiming at the improvement of organic solubility, we have explored the arylation reactions of $\text{Ru}_2(\text{ap}')_4\text{Cl}$ ($\text{ap}' = 2$ -(3-*iso*-propoxyanilino)pyridinate (*m*-*i*PrOap) and 2-(3,5-dimethoxyanilino)pyridinate (DiMeOap)), and the details are reported here.

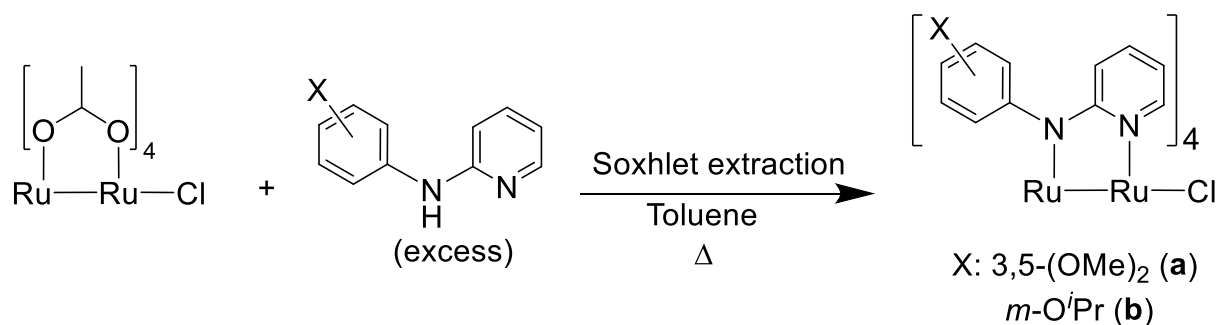
1.3 Results and Discussion

1.3.1 Synthesis

The precursor for the deprotonated ligand, Hap' , was prepared from the reaction between 2-bromopyridine and modified aniline compounds, as outlined in Scheme 1.1, and the $\text{Ru}_2(\text{II,III})$ starting materials, $\text{Ru}_2(\text{DiMeOap})_4\text{Cl}$ (**a** series)⁴³ and $\text{Ru}_2(\text{m-}i\text{PrOap})_4\text{Cl}$ (**b** series),⁴⁴ from the reaction between $\text{Ru}_2(\text{OAc})_4\text{Cl}$ and Hap' , per Scheme 1.2.



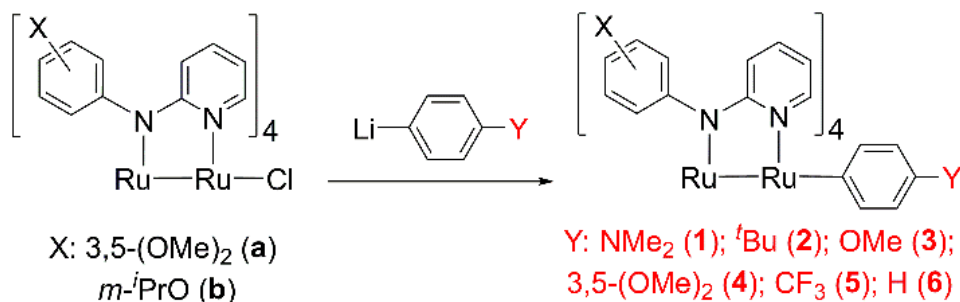
Scheme 1.1. Synthesis of modified 2-anilino pyridine ligands



Scheme 1.2. Synthesis of $\text{Ru}_2(\text{ap}')_4\text{Cl}$

As shown in Scheme 1.3, the reaction between $\text{Ru}_2(\text{ap}')_4\text{Cl}$ and LiAr resulted in the generation of $\text{Ru}_2(\text{ap}')_4(\text{Ar})$ and LiCl . These reactions were usually complete within 2 h and the completion is accompanied with easily identifiable color changes. The $\text{Ru}_2(\text{DiMeOap})_4(\text{Ar})$ series

was isolated with either purification over deactivated silica or simple recrystallization with yields ranging from 28-91%.



Scheme 1.3. Synthesis of modified Ru₂ aryl compounds. Conditions: 6 – 10 equiv LiAr, THF, room temperature, N₂, 1 – 3 hours

Meanwhile, purification of the Ru₂(*m*-*i*PrOap)₄(Ar) compounds was only successful using Et₃N deactivated silica, in yields ranging between 21–68%. While both *ap'* series exhibited improved solubility in non-polar organic solvents compared to the *ap* series (see Table 1.1 for solubility comparisons), the higher yields and easier purification for compounds **1a–6a** points to the advantage of the DiMeOap ligand over the *m*-*i*PrOap ligand.⁴⁴

Table 1.1. Solubility comparisons between **2a/2b** and Ru₂(*ap*)₄(C₆H₄-*t*Bu)

Solvent	2a	2b	Ru ₂ (<i>ap</i>) ₄ (C ₆ H ₄ - <i>t</i> Bu)
Pentane	Sparingly soluble	Sparingly soluble	Insoluble
Hexanes	Soluble	Soluble	Insoluble
Diethyl Ether	Very soluble	Very soluble	Sparingly soluble
CH ₂ Cl ₂	Very soluble	Very soluble	Soluble
THF	Very soluble	Very soluble	Soluble

*Sparingly soluble = < 1.0 mg / 1.50 mL solvent; soluble = 1.00 – 4.00 mg / 1.00 mL solvent; very soluble = > 8.0 mg / 1.00 mL solvent

While **3a/b** undergo partial degradation over the course of a week resulting in low yields (**3a**: 28% and **3b**: 21%), all other reported aryl compounds are stable in ambient conditions as both

solutions and solids over a month. The effective magnetic moments (Evans method⁴⁵) for both Ru₂(DiMeOap)₄(Ar) and Ru₂(*m*-^{*i*}PrOap)₄(Ar) series range from 3.4 to 4.3 μ_B , all in agreement with an $S = 3/2$ ground state (Table A.4 in Appendix A below). Compounds **1a–6a** and **1b–5b** were further characterized using mass spectrometry (ESI-MS), electronic absorption spectra, cyclic and differential pulse voltammetry, and single crystal X-ray diffraction studies.

1.3.2 Molecular Structures

The structures of compounds **1a**, **2a/b**, **3a/b**, **4a/b** and **5a** were determined with single crystal X-ray diffraction and are shown in Figures 1.2–1.9 with selected bond lengths and angles provided in Table 1.2. The structures for **2b**, **3b** and **4b** represent the first crystal structures with the modified *m*-^{*i*}PrOap ligand. The bridging *ap'* ligands adopt the (4,0) arrangement, where all pyridine *N*-centers coordinate to the Ru center bonded to Ar, and all anilino *N*-centers coordinate to the other Ru.²⁰

The Ru–Ru bond lengths for the compounds range from 2.3277(4) (**2a**) to 2.3467(8) (**4b**) Å and are significantly lengthened compared to Ru₂(DiMeOap)₄Cl (2.2797(7) Å),⁴³ highlighting the stronger electron-donating nature of the aryl ligand compared to that of the chloro ligand. These Ru–Ru bond lengths have a wider range than those observed in the Ru₂(*ap*)₄(Ar) series (2.3370(5) to 2.3423(5) Å),³⁵ demonstrating that modification of the bridging *ap'* ligands does mildly impact the electronic structure of the Ru₂ core. The Ru–Ru bond lengths in these Ru₂(*ap'*)₄(Ar) compounds are also increased when compared to σ -alkynyl compounds Ru₂(DiMeOap)₄(C_{2n}R) ($n = 1,2$), which have Ru–Ru bond lengths of *ca.* 2.322–2.328 Å.⁴³

The Ru–C_{sp2} bond lengths for all structures are greater than 2.16 Å, an increase of 0.05–0.10 Å over Ru–C_{sp} bond lengths in the Ru₂(DiMeOap)₄(C_{2n}R) type compounds (2.05–2.1 Å).^{22,24,43} While there is a large range in the donicity of aryl substituents, there is no discernible trend in the Ru–C_{sp2} bond lengths in both series. Additionally, an intriguing feature of **1a** is the planarity of the -NMe₂ substituent, which was not observed in Ru₂(*ap*)₄-C₆H₄-4-NMe₂.³⁵ The bond lengths and angles (**1a**: C4-N9-C7 = 119.8(2)°; C4-N9 = 1.390(3) Å; Ru₂(*ap*)₄-C₆H₄-4-NMe₂: C4-N9-C7 = 116.3(10)°; C4-N9 = 1.408(8) Å) suggest conjugation of the -NMe₂ moiety with the Ru₂ core through the phenylene.

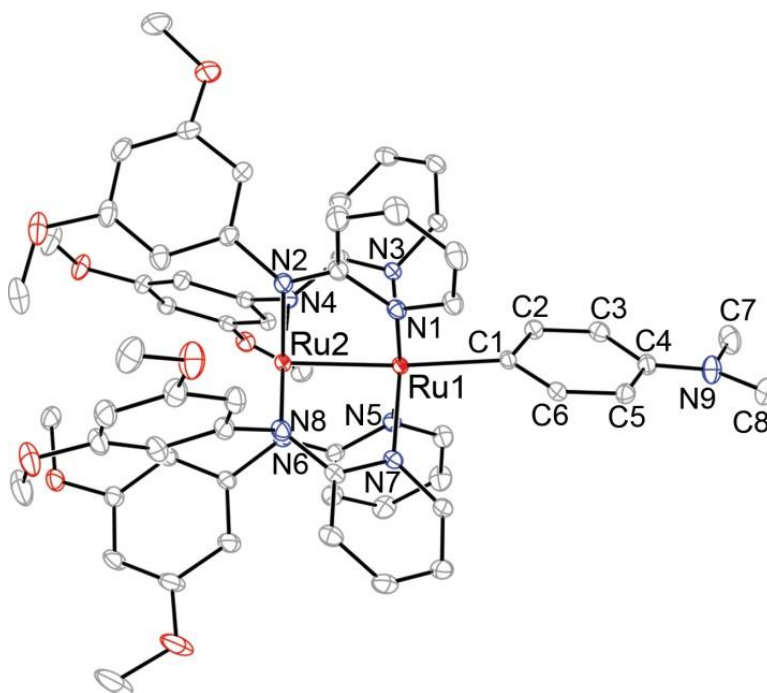


Figure 1.2. ORTEP plot of **1a** at 30% probability level. H atoms and solvent molecules removed for clarity

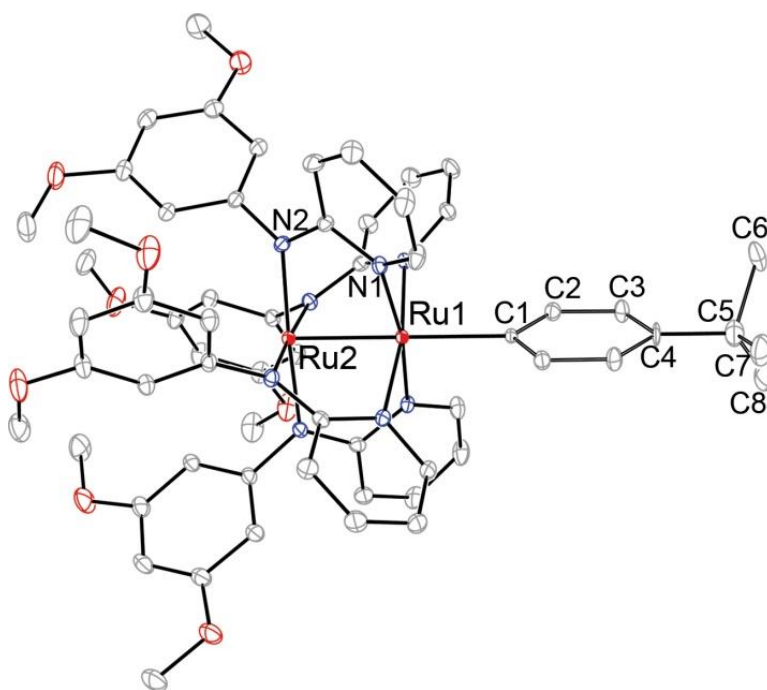


Figure 1.3. ORTEP plot of **2a** at 30% probability level. H atoms and -^tBu moiety disorder removed for clarity

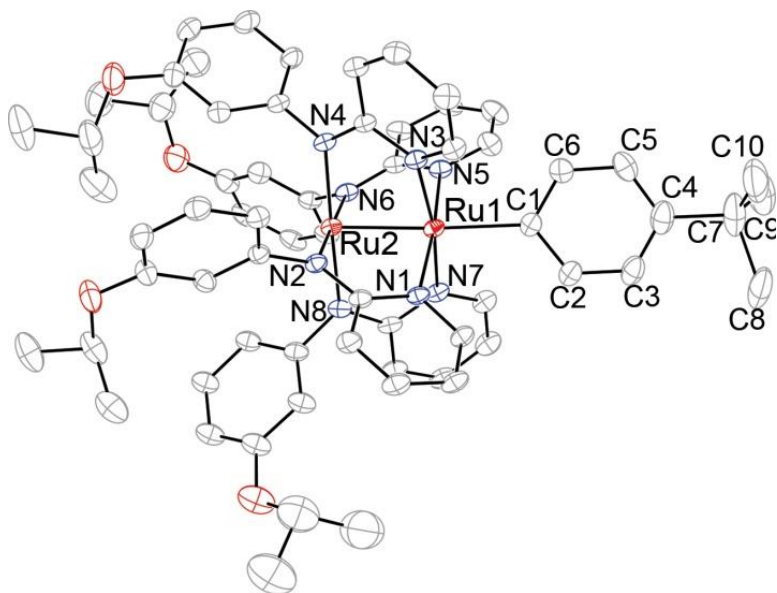


Figure 1.4. ORTEP plot of **2b** at 30% probability level. Solvent molecules, ligand disorder, and H atoms removed for clarity

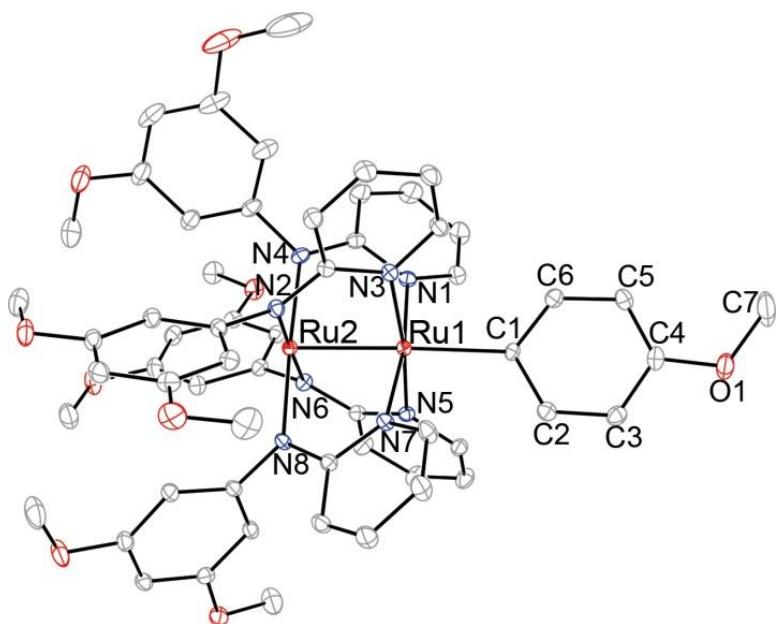


Figure 1.5. ORTEP plot of **3a** at 30% probability level. H atoms removed for clarity

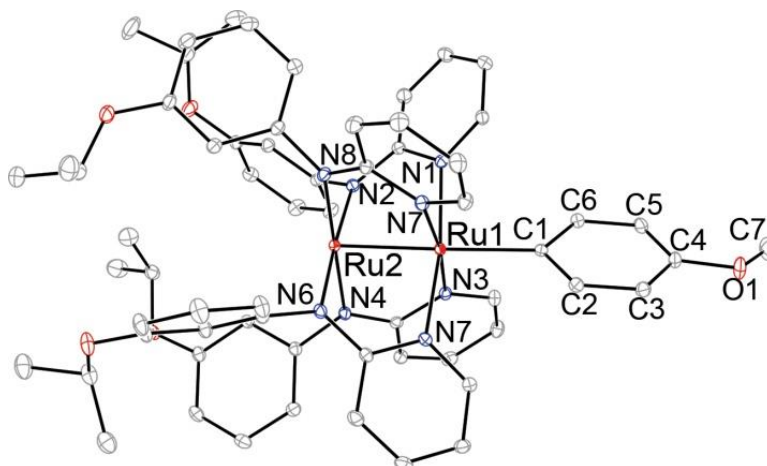


Figure 1.6. ORTEP plot of **3b** at 30% probability level. H atoms removed for clarity

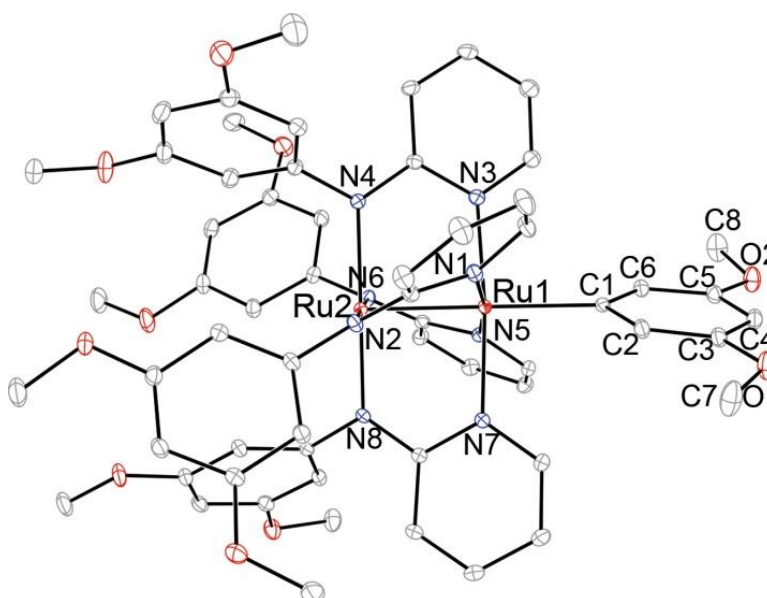


Figure 1.7. ORTEP plot of **4a** at 30% probability level. H atoms removed for clarity

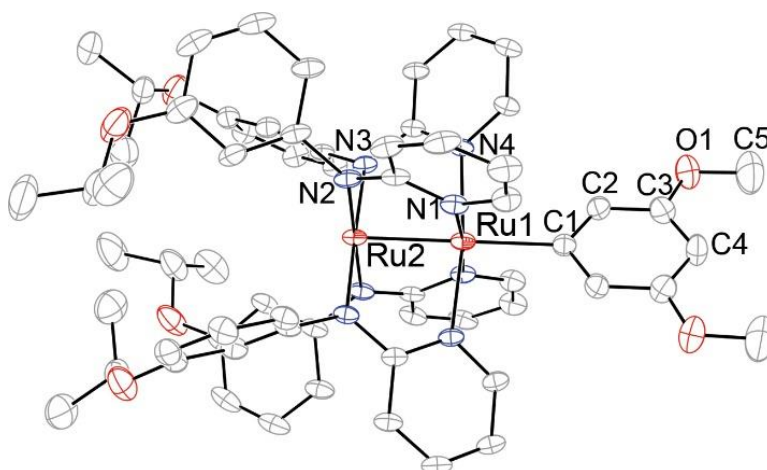


Figure 1.8 ORTEP plot of **4b** at 30% probability level. H atoms and solvent molecules omitted for clarity

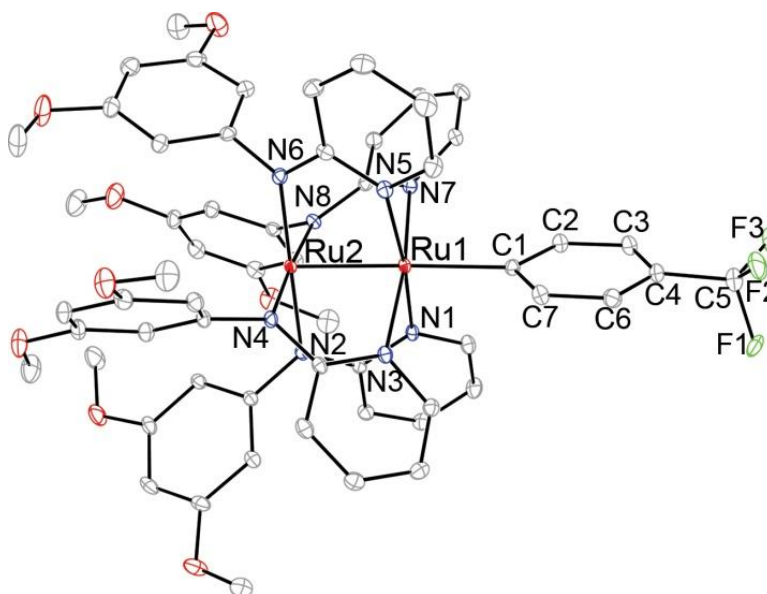


Figure 1.9. ORTEP plot of **5a** at 30% probability level. H atoms and -CF₃ moiety disorder omitted for clarity

Table 1.2. Selected Bond Lengths (Å) and angles (deg) for compounds **1a**, **2a/2b**, **3a/3b**, **4a/4b** and **5a**

	1a	2a	2b	3a	3b	4a	4b	5a
Ru1–Ru2	2.3414(2)	2.3277(4)	2.3399(4)	2.3365(2)	2.3326(2)	2.3407(2)	2.3467(8)	2.3341(3)
Ru1–C1	2.179(2)	2.207(4)	2.184(4)	2.193(2)	2.187(2)	2.207(4)	2.174(6)	2.179(2)
Ru2–Ru1–C1	172.41(6)	180.0	176.3(1)	178.03(6)	177.82	177.07(5)	180.0	177.38(6)
Ru1–N1	2.106(2)	2.112(2)	2.114(3)	2.133(2)	2.102(1)	2.134(2)	2.118(3)	2.125(2)
Ru1–N3	2.117(2)	–	2.136(3)	2.116(2)	2.144(1)	2.121(2)	2.119(3)	2.115(2)
Ru1–N5	2.156(2)	–	2.124(3)	2.076(2)	2.096(1)	2.104(2)	–	2.136(2)
Ru1–N7	2.098(2)	–	2.092(3)	2.111(2)	2.113(1)	2.146(2)	–	2.0961(1)
Ru2–N2	2.035(2)	2.034(2)	2.049(3)	2.036(2)	2.049(1)	2.046(2)	2.033(3)	2.003(2)
Ru2–N4	2.047(2)	–	2.032(3)	2.026(2)	2.025(1)	2.036(2)	2.038(3)	2.041(2)
Ru2–N6	2.020(2)	–	2.033(3)	2.049(2)	2.049(1)	2.041(2)	–	2.022(2)
Ru2–N8	2.044(2)	–	2.045(3)	2.038(2)	2.027(2)	2.023(2)	–	2.041(2)

1.3.3 Electronic Absorption Spectra

The vis-NIR absorption spectra of compounds **1a–6a** and **1b–5b** are shown in Figure 1.11 and Figure 1.12, respectively. These compounds are intensely colored, akin to other diruthenium paddlewheel compounds. Like the $\text{Ru}_2(\text{ap})_4(\text{Ar})$ compounds,³⁵ the $\text{Ru}_2(\text{ap}')_4(\text{Ar})$ compounds all display two major electronic transitions (*ca.* 470 and 800 nm) in the visible region that are characteristic of Ru_2^{5+} compounds. In $\text{Ru}_2(\text{ap})_4\text{Cl}$, the transition at ~ 470 nm has previously been assigned as $\delta \rightarrow \delta^*$ and the peak at ~ 800 nm as $\delta \rightarrow \pi^*$.⁴⁶ However, as noted for the $\text{Ru}_2(\text{ap})_4(\text{Ar})$ compounds, spectra for **1a–6a** (Figure 1.11) and **1b–5b** (Figure 1.12) exhibit two distinct $\delta \rightarrow \pi^*$ transitions between 600 – 800 nm. The presence of two transitions was attributed to the removal of the degeneracy of π^* orbitals upon introduction of the aryl ligand based on the DFT study of $\text{Ru}_2(\text{ap})_4(\text{Ar})$.³⁵ This reduces the rotation symmetry about the $\text{Ru}_2(\text{ap}')_4$ core from four-fold (with chloro or mono-alkynyl ligands) to two-fold as demonstrated in Figure 1.10 below.

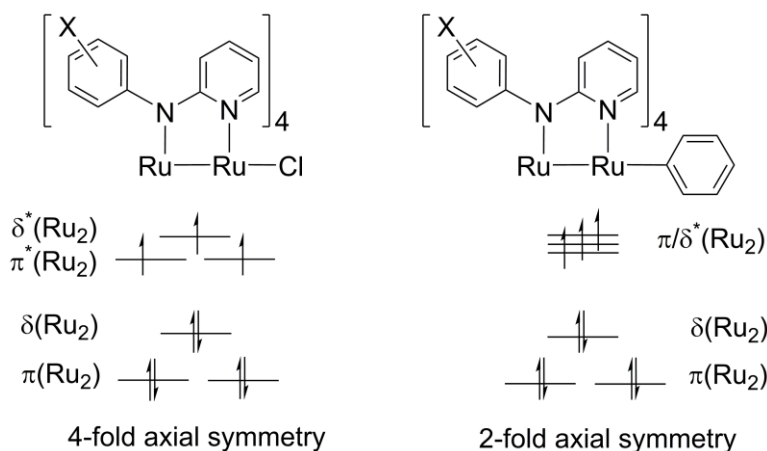


Figure 1.10. Qualitative MO diagram of $\text{Ru}_2(\text{ap}')_4$ core upon attachment of aryl ligand (energy levels not drawn to scale)

For **1b–5b** these transitions are reminiscent of $\text{Ru}_2(\text{ap})_4(\text{Ar})$, with a small, higher energy shoulder visible. However, this spectroscopic feature is more pronounced in the $\text{Ru}_2(\text{DiMeOap})_4(\text{Ar})$ series (as shown in Figure 1.11) where the shoulder present at *ca.* 650 nm in the $\text{Ru}_2(m\text{-}i\text{PrOap})_4(\text{Ar})$ (Figure 1.12) and $\text{Ru}_2(\text{ap})_4(\text{Ar})$ ³⁵ series is blue-shifted to approximately 610 nm and has become a distinct transition.

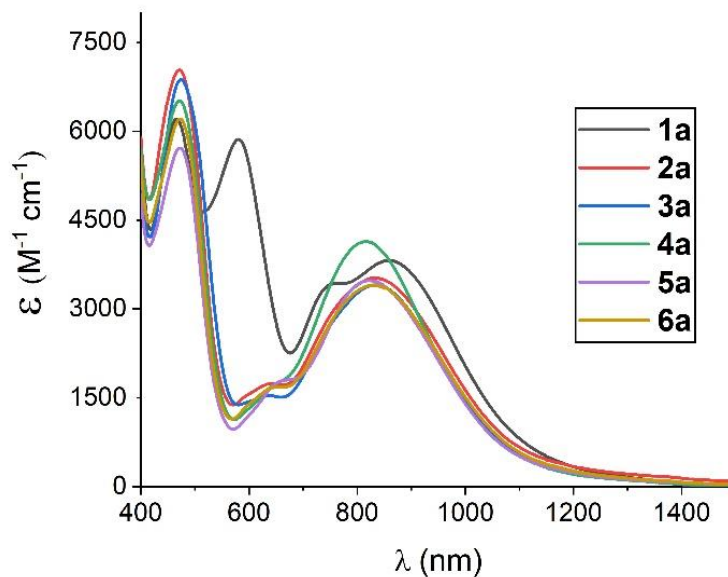


Figure 1.11. Vis-NIR absorption spectra of compounds **1a–6a** in THF

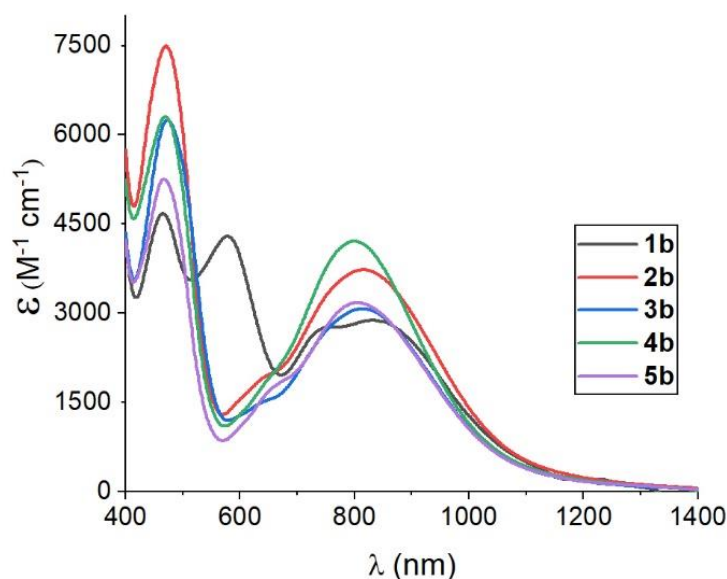


Figure 1.12. Vis-NIR absorption spectra of **1b–5b** in THF

Compounds **1a/b** ($Y = 4\text{-NMe}_2$) display a unique peak centered at 580 nm, which gives these compounds their unique color (black) compared to the rest of the compounds (green). This unique peak has been assigned with DFT as a high-lying $\pi(\text{Ar/Ru}_2) \rightarrow \pi^*(\text{Ar/Ru}_2)$ transition.³⁵ The lack of a corresponding peak in compounds **2a/b** ($Y = 4\text{-}^t\text{Bu}$) and **3a/b** ($Y = 4\text{-OMe}$) highlights the necessity of a strong electron-donating lone pair on the *para*-substituent to enable this unique transition.

1.3.4 Electrochemical Studies

The redox properties of **1a–6a** and **1b–5b** were examined using cyclic (CV) and differential pulse voltammetry (DPV). The voltammograms for **1a–6a** are displayed in Figure 1.13 and those for **1b–5b** are in Figure 1.14; electrode potentials for all compounds are given in Table 1.3. All the $\text{Ru}_2(\text{ap}')(\text{Ar})$ species exhibit one reversible oxidation **B** ($\text{Ru}_2^{6+/5+}$) and one reversible reduction **A** ($\text{Ru}_2^{5+/4+}$). Compounds **1a** and **1b** exhibit the second reversible one electron oxidation (**C**), which is attributed to the 4- NMe_2 substituent. Additionally, compound **1b** also displayed the third oxidation at 0.50 V (*versus* Fc, see Figure 1.14), that is likely Ru_2 based ($\text{Ru}_2^{7+/6+}$), analogous to those observed in the $\text{Ru}_2(\text{ap})_4(\text{Ar})$ series.³⁵ Such a wave was not detected in **1a–6a** and **2b–5b** because they are shifted outside the potential window allowed by THF solvent.

Table 1.3. Electrochemical data (in V vs $\text{Fc}^{+/0}$) from DPV for **1a–6a** and **1b–5b** in THF

	1a	2a	3a	6a	4a	5a	1b	2b	3b	4b	5b
C	0.09	–	–	–	–	–	0.00	–	–	–	–
B	–0.26	–0.20	–0.20	–0.18	–0.18	–0.12	–0.37	–0.21	–0.20	–0.19	–0.13
A	–1.63	–1.60	–1.59	–1.56	–1.56	–1.45	–1.70	–1.61	–1.61	–1.58	–1.48

The modification to the bridging ligands resulted in slight shifts in electrode potentials between two $\text{Ru}_2(\text{ap}')_4(\text{Ar})$ series, as evidenced in the data for the DMAP ($\text{C}_6\text{H}_4\text{-4-NMe}_2$) derivatives (Table 1.3). Due to the mild electron withdrawing nature of *meta*-alkoxy group (Hammett constant $\sigma \sim 0.10$), compound **1a** (eight methoxy substituents) is slightly more electron deficient than **1b** (four isopropoxy substituents), and hence its electrode potentials are anodically shifted (70 – 100 mV) from those of **1b**. Direct comparison between the current $\text{Ru}_2(\text{ap}')_4(\text{Ar})$ series and the original $\text{Ru}_2(\text{ap})_4(\text{Ar})$ series is complicated by the fact that the voltammograms of the latter were recorded in a different solvent (CH_2Cl_2). Further comparison of the $\text{Ru}_2(\text{DiMeOap})_4(\text{Ar})$ series to $\text{Ru}_2(\text{DiMeOap})_4\text{Cl}^{43}$ reveals that the averaged (of compounds **1a–6a**) $E_{1/2}(\text{Ru}_2^{6+/5+})$ and $E_{1/2}(\text{Ru}_2^{5+/4+})$ potentials are cathodically shifted by ca. 270 mV and 340 mV, respectively (Table A.3 in Appendix A below), a testament to the strong donicity of aryl ligands.

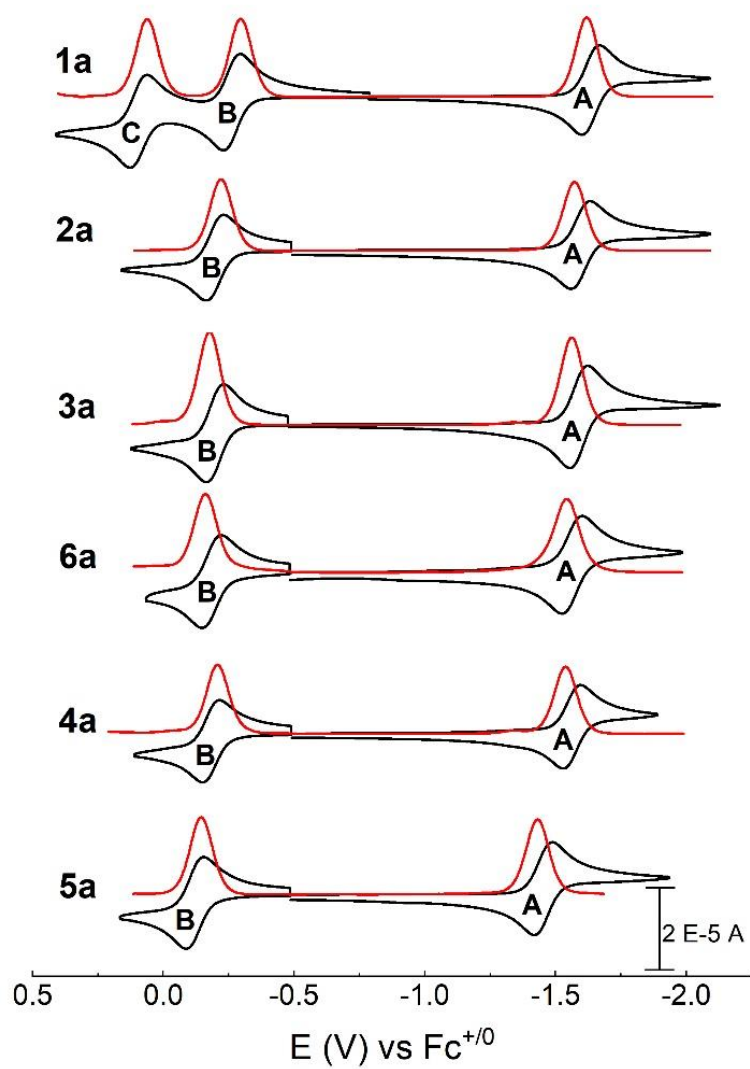


Figure 1.13. Cyclic (black) and differential pulse (red) voltammograms of compounds **1a–6a** (1.0 mM) recorded in 0.10 M THF solutions of $[\text{Bu}_4\text{N}][\text{PF}_6]$ at a scan rate of 0.1 V/s

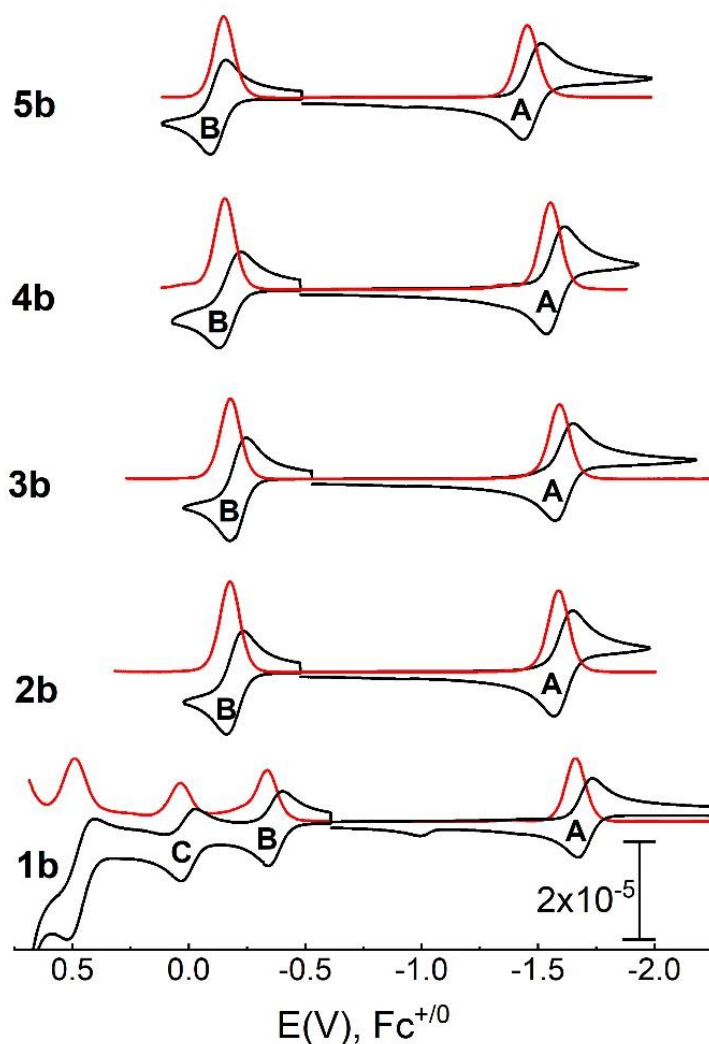


Figure 1.14. Cyclic (black) and differential pulse (red) voltammograms of compounds **1b–5b** (1.0 mM) recorded in 0.10 M THF solutions of $[\text{Bu}_4\text{N}][\text{PF}_6]$ at a scan rate of 0.1 V/s

As shown in Table 1.3, both the reversible reduction (**A**) and oxidation (**B**) potentials for the $\text{Ru}_2(\text{ap}')_4(\text{Ar})$ series vary significantly across each series. These variations depend on the electron donating / withdrawing nature of the aryl *p*-substituent as measured by its Hammett constant (σ_Y). Linear fit plots of the $\text{Ru}_2^{5+/6+}$ oxidation potentials of $\text{Ru}_2(\text{DiMeOap})_4(\text{Ar})$ (Figure 1.15) and $\text{Ru}_2(m\text{-}^i\text{PrOap})_4(\text{Ar})$ (Figure 1.16) against the σ_Y of the aryl substituent support this correlation.^{47–49} For $\text{Ru}_2(\text{DiMeOap})_4(\text{Ar})$, a reactivity constant (ρ , the slope of the fit) of *ca.* 93 mV (Eqn. 1) was obtained, which matches the ρ obtained from the $\text{Ru}_2(\text{ap})_4(\text{Ar})$ series (*ca.* 98 mV) but is lower than that of $\text{Ru}_2(m\text{-}^i\text{PrOap})_4(\text{Ar})$ ($\rho = 167$ mV).

$$E_{1/2}(X) = \rho\sigma_Y + E_{1/2}(H) \quad (1)$$

The reactivity constants of the reduction couple (**A**) for Ru₂(DiMeOap)₄(Ar) (134 mV) and Ru₂(*m*-^{*i*}PrOap)₄(Ar) (154 mV) agree with each other, but are significantly higher than that of Ru₂(ap)₄(Ar) (107 mV).³⁵

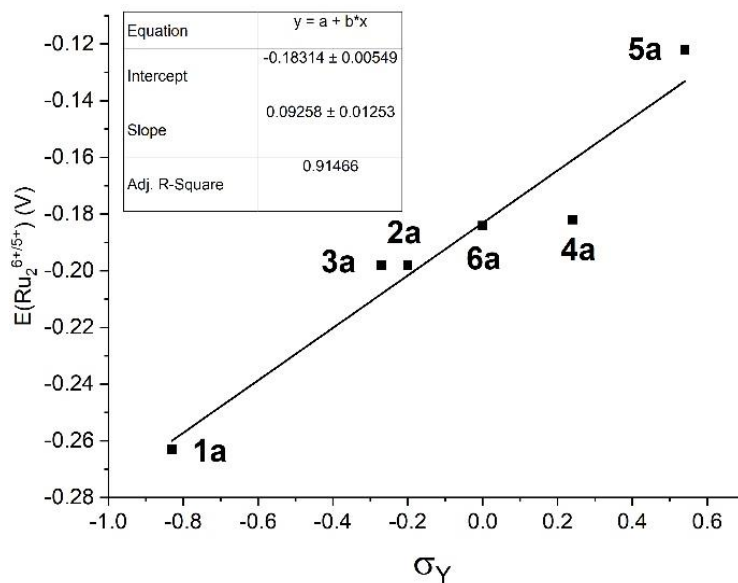


Figure 1.15. Hammett plot of **1a–6a** oxidation potentials ($E(\text{Ru}_2^{6+/5+})$) versus σ_Y . The squares are measured oxidation potentials and the solid line is the linear best-fit line

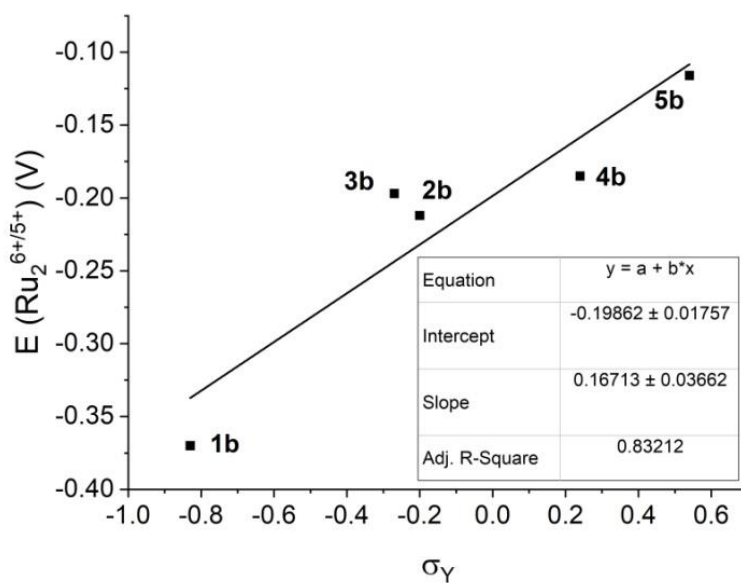


Figure 1.16. Hammett plot of **1b–5b** oxidation potentials ($E(\text{Ru}_2^{6+/5+})$) versus σ_Y . The squares are measured oxidation potentials and the solid line is the linear best-fit line

1.4 Conclusions

Reported in this contribution are two new series of $\text{Ru}_2(\text{ap}')_4(\text{Ar})$ compounds with significantly improved solubility in organic solvents (**1a–6a**). All $\text{Ru}_2(\text{ap}')_4(\text{Ar})$ type compounds are of the Ru_2^{5+} oxidation state, and a ground state configuration of $\sigma^2\pi^4\delta^2(\pi^*\delta^*)^3$ ($S = 3/2$). All compounds display at least one reversible oxidation and one reversible reduction, both Ru_2 centered, while those containing an amine functionality (**1a/b**) support a second reversible oxidation. Both the oxidation and reduction electrochemical potentials were tunable through varying the aryl substituent. The much enhanced solubility will enable further exploration of Ru_2 -aryls as both molecular wires and active species in devices similar to the efforts based on Ru_2 -alkynyls,²⁰ which is currently under investigation.

1.5 Experimental Section

General methods. $\text{Ru}_2(\text{DiMeOap})_4\text{Cl}^{43}$ and $\text{Ru}_2(m\text{-}^i\text{PrOap})_4\text{Cl}^{44}$ were prepared using literature methods. $n\text{-BuLi}$ (2.5 M in hexanes) was purchased from Sigma-Aldrich. All other halogenated ligands were purchased from commercial vendors and used without further purification. Tetrahydrofuran (THF) was freshly distilled over sodium/benzophenone. All reactions were performed under a dry nitrogen atmosphere implementing standard Schlenk procedures unless otherwise noted, with workups occurring in ambient conditions. The syntheses of **1a–6a** and **1b–5b** were performed using modified literature procedures.³⁵

Physical methods. UV-vis-NIR spectra were obtained with a JASCO V-670 spectrophotometer in THF solutions. ESI-MS were analyzed on an Advion Mass Spectrometer. ^1H NMR spectra were recorded on a Varian Inova 300 spectrometer operating at 300 MHz. Effective magnetic moments (at 20–22°C) were obtained using the Evans method⁴⁵ with ferrocene as the standard. Cyclic and differential pulse voltammograms were recorded in 0.1 M $[\text{Bu}_4\text{N}][\text{PF}_6]$ solution (4 mL THF, Ar-degassed) on a CHI620A voltammetric analyzer with a glassy-carbon working electrode (diameter 2 mm), a Pt-wire auxiliary electrode, and a Ag/AgCl reference electrode. The concentration of Ru_2 species was always *ca.* 1.0 mM. Elemental analyses were performed by Atlantic Microlab, Inc. Single crystal X-ray diffraction data were collected on Nonius Kappa CCD and Bruker Quest Instruments as detailed in section 1.5.2.

1.5.1 Synthesis Details

Ru₂(DiMeOap)₄(C₆H₄-4-NMe₂) (1a). 4-Bromo-N,N-dimethylaniline (217 mg, 1.1 mmol) was dissolved in 5 mL THF and treated with 0.58 mL ⁿBuLi (1.5 mmol) at 0°C. The aryllithium solution was then cannula-transferred to a 30 mL solution of Ru₂(DiMeOap)₄Cl in THF (125 mg, 0.11 mmol). An immediate color change from green to black was observed. The reaction was stirred for 1 hour at room temperature. Upon exposure to atmosphere, the color of the solution remained black. After filtering over Celite and the removal of solvents, the crude product mixture was run through a deactivated (with triethylamine) silica pad. The filtrate was collected, solvents removed, and recrystallized using a 1/15 (v/v) acetone/pentane recrystallization at -20°C. The black solid was collected with a frit and purified by column chromatography. The black band was collected with 1:1 THF/hexanes (v/v), and a deep black solid was isolated. Single crystals suitable for X-ray diffraction were grown by slow evaporation of **1a** in acetone. Yield: 57 mg (43% based on Ru). Elem. Anal. Found (Calcd) for C₆₀H₆₆N₉O₁₀Ru₂ (**1a**·2H₂O·0.5THF): C, 56.36 (56.78); H, 5.29 (5.38); N, 9.44 (9.61). ESI-MS (*m/z*, based on ¹⁰¹Ru): [M+H]⁺ = 1241.1. UV-Vis (in THF) λ / nm (ε / M⁻¹ cm⁻¹): 465 (6200), 581 (5900), 760 (3400), 858 (3800). μ_{eff} (21°C) = 3.9 μ_B. Electrochemistry (THF, vs Fc⁺⁰) E_{1/2} / V, ΔE_p / mV, *i*_{backward}/*i*_{forward}: 0.09, 68, 0.92; -0.26, 66, 0.91; -1.63, 70, 0.99.

Ru₂(DiMeOap)₄(C₆H₄-4-^tBu) (2a). 1-Bromo-4-(*tert*-butyl)-benzene (0.20 mL, 1.2 mmol) was dissolved in 5 mL THF and was treated with 0.60 mL ⁿBuLi (1.5 mmol) at 0 °C. The aryllithium solution was then cannula-transferred to a 30 mL solution of Ru₂(DiMeOap)₄Cl in THF (125 mg, 0.11 mmol). A color change from green to red-brown was observed. The reaction stirred for 1 h and upon exposure to air the color of the solution changed back to dark green. After filtering over Celite and removal of the solvent, the crude product mixture was purified by column chromatography on deactivated (with triethylamine) silica. The dark green band was eluted with 1:1 THF/hexanes (v/v), and a dark green solid was isolated from the filtrate. Single crystals suitable for X-ray diffraction were grown by layering hexanes over a concentrated solution of **2a** in EtOAc. Yield: 102 mg (75% based on Ru). Elem. Anal. Found (Calcd) for C₇₆H₉₅N₈O₁₀Ru₂ (**2a**·1.5THF·1C₆H₁₄): C, 61.95 (61.44); H, 6.14 (6.34); N, 7.58 (7.75). ESI-MS (*m/z*, based on ¹⁰¹Ru): [M+H]⁺ = 1253.9. UV-Vis (in THF) λ / nm (ε / M⁻¹ cm⁻¹): 472 (7000), 642 (1700), 834 (3500). μ_{eff} (21°C) = 3.9 μ_B. Electrochemistry (THF, vs Fc⁺⁰) E_{1/2} / V, ΔE_p / mV, *i*_{backward}/*i*_{forward}: -0.20, 65, 0.96; -1.60, 71, 0.96.

Ru₂(DiMeOap)₄(C₆H₄-4-OMe) (3a). 4-Bromoanisole (0.14 mL, 1.1 mmol) was dissolved in 5 mL THF and then treated with 0.57 mL ⁿBuLi (1.5 mmol) at 0°C. The aryllithium solution was then cannula-transferred to a 30 mL solution of Ru₂(DiMeOap)₄Cl in THF (126 mg, 0.11 mmol). A color change from dark green to dark red was observed. The reaction mixture stirred for 1 hour at room temperature. Upon exposure to atmosphere, the color changed to a brown. After filtering over Celite and the solvent was removed, the crude product mixture was first recrystallized using 1:20 THF/hexanes (v/v) recrystallization at -20°C. The solid was collected and final purification was achieved via column chromatography on deactivated (with triethylamine) silica. The light brown band was collected with 1:1 THF/hexanes (v/v), and a dark brown solid was isolated. Single crystals suitable for X-ray diffraction were grown by layering pentane over a concentrated solution of **3a** in THF. Yield: 38 mg (28% based on Ru). Elem. Anal. Found (calcd) for C₆₃H₇₁N₈O₁₂Ru₂ (**3a**·2H₂O·1THF): C, 56.65 (56.71); H, 5.27 (5.36); N, 8.12 (8.40). ESI-MS (*m/z*, based on ¹⁰¹Ru): [M⁺] = 1225.9. UV-Vis (in THF) λ / nm (ε / M⁻¹ cm⁻¹): 473 (6900), 634 (1500), 833 (3400). μ_{eff} (21°C) = 4.0 μ_B. Electrochemistry (THF, vs Fc^{+/0}) E_{1/2} / V, ΔE_p / mV, *i*_{backward}/*i*_{forward}: -0.20, 67, 0.92; -1.59, 67, 0.99.

Ru₂(DiMeOap)₄(C₆H₃-3,5-(OMe)₂) (4a). 1-Bromo-3,5-dimethoxybenzene (165 mg, 0.76 mmol) was dissolved in 5 mL THF and treated with 0.4 mL ⁿBuLi (1 mmol) at -78°C. The aryllithium solution was then cannula-transferred to a 30 mL solution of Ru₂(DiMeOap)₄Cl in THF (125 mg, 0.11 mmol). A color change from green to red brown was observed. The reaction mixture stirred for 1 hour at room temperature. Upon exposure to atmosphere, the color changed to a green-black. After filtering over Celite and removal of the solvent, the crude mixture was purified by column chromatography on deactivated (w/ triethylamine) silica. The green band was eluted with 1:1 EtOAc/hexanes (v/v), and a dark green solid was isolated. Single crystals suitable for X-ray diffraction were grown by layering hexanes over a concentrated solution of **4a** in ethyl acetate (EtOAc). Yield: 81.2 mg (59% based on Ru). Elem. Anal. Found (Calcd) for C₇₆H₁₀₅N₈O₂₄Ru₂ (**4a**·4.5EtOAc·5.5H₂O): C, 53.13 (53.48); H, 6.09 (6.21); N, 6.18 (6.40). ESI-MS (*m/z*, based on ¹⁰¹Ru): [M⁺] = 1257.5. UV-Vis (in THF) λ / nm (ε / M⁻¹ cm⁻¹): 471 (6500), 650 (1700), 815 (4100). μ_{eff} (21°C) = 3.5 μ_B. Electrochemistry (THF, vs Fc^{+/0}) E_{1/2} / V, ΔE_p / mV, *i*_{backward}/*i*_{forward}: -0.18, 60, 0.89; -1.56, 69, 0.98.

Ru₂(DiMeOap)₄(C₆H₄-4-CF₃) (5a). 4-Bromobenzotrifluoride (0.1 mL, 0.71 mmol) was dissolved in 5 mL THF and then treated with 0.4 mL ⁿBuLi (1 mmol) at -78°C. The aryllithium

solution was then cannula transferred to a 30 mL solution of $\text{Ru}_2(\text{DiMeOap})_4\text{Cl}$ in THF (126 mg, 0.11 mmol). No immediate color change was observed, with the solution remaining a dark green. The reaction stirred for 1 h at room temperature. Upon exposure to atmosphere, the color of the solution remained dark green. After filtering over Celite and solvent removal, the crude product mixture was purified by column chromatography on deactivated (w/ triethylamine) silica. The dark green band was eluted with 1:1 EtOAc/hexanes (v/v), and a dark green solid collected after removal of solvents. Single crystals suitable for X-ray diffraction were grown by layering hexanes over a concentrated solution of **5a** in ethyl acetate. Yield: 116 mg (84% based on Ru). Elem. Anal. Found (Calcd) for $\text{C}_{77}\text{H}_{97}\text{N}_8\text{O}_9\text{F}_3\text{Ru}_2$ (**5a**·0.5EtOAc·2.5C₆H₁₄): C, 60.42 (59.91); H, 5.92 (6.28); N, 6.99 (7.35). ESI-MS (m/z , based on ^{101}Ru): $[\text{M}+\text{H}]^+ = 1265.6$. UV-Vis (in THF) λ / nm ($\epsilon / \text{M}^{-1} \text{cm}^{-1}$): 472 (5700), 675 (1800), 820 (3500). μ_{eff} (21°C) = 3.8 μ_{B} . Electrochemistry (THF, vs $\text{Fc}^{+/0}$) $E_{1/2} / \text{V}$, $\Delta E_{\text{p}} / \text{mV}$, $i_{\text{backward}}/i_{\text{forward}}$: -0.12, 65, 0.99; -1.45, 67, 0.98.

$\text{Ru}_2(\text{DiMeOap})_4(\text{Ph})$ (6a). Bromobenzene (0.09 mL, 0.86 mmol) was dissolved in 5 mL THF and treated with 0.5 mL $n\text{BuLi}$ (1.25 mmol) at 0°C. The aryllithium solution was then cannula-transferred to a 30 mL solution of $\text{Ru}_2(\text{DiMeOap})_4\text{Cl}$ in THF (102 mg, 0.088 mmol). A color change from green to red-brown was observed. The reaction mixture stirred for 1.5 hours at room temperature, and after exposure to air changed back to dark green. After filtering over Celite and removing the solvent, the crude product mixture was purified by column chromatography on deactivated (w/ triethylamine) silica. The green band was eluted with 1:1 THF/hexanes (v/v), and a dark green solid was collected from the filtrate. Yield: 95 mg (91% based on Ru). Elem. Anal. Found (Calcd) for $\text{C}_{68}\text{H}_{71}\text{N}_8\text{O}_{11.5}\text{Ru}_2$ (**6a**·2.5THF·1H₂O): C, 58.84 (58.57); H, 5.55 (5.71); N, 8.04 (8.04). ESI-MS (m/z , based on ^{101}Ru): $[\text{M}^+] = 1196.4$. UV-Vis (in THF) λ / nm ($\epsilon / \text{M}^{-1} \text{cm}^{-1}$): 472 (6200), 649 (1700), 829 (3400). μ_{eff} (21°C) = 4.3 μ_{B} . Electrochemistry (THF, vs $\text{Fc}^{+/0}$) $E_{1/2} / \text{V}$, $\Delta E_{\text{p}} / \text{mV}$, $i_{\text{backward}}/i_{\text{forward}}$: -0.18, 76, 0.97; -1.56, 77, 0.97.

$\text{Ru}_2(m\text{-}^i\text{PrOap})_4(\text{C}_6\text{H}_4\text{-4-NMe}_2)$ (1b). 4-Bromo-*N,N*-dimethylaniline (178 mg, 0.87 mmol) was dissolved in 10 mL THF and treated with 0.4 mL $n\text{BuLi}$ (1 mmol) at 0°C. The aryllithium solution was cannula-transferred to a 70 mL THF solution of $\text{Ru}_2(m\text{-}^i\text{PrOap})_4\text{Cl}$ (103 mg, 0.087 mmol). Upon addition an immediate color change from dark green to black was observed. The reaction mixture stirred for 1 hour at room temperature. Upon exposure to air, the solution stayed black. After filtering over Celite and removal of solvent, the crude mixture was purified by column chromatography on deactivated (with triethylamine) silica. The black band was eluted with 1:5

EtOAc/hexanes (v/v), and a black microcrystalline solid, **1b**, was obtained after condensing. Yield: 50 mg (45% based on Ru). Elem. Anal. Found (Calcd) for $C_{84}H_{144}N_9O_{31}Ru_2$ (**1b**·17H₂O·5EtOAc): C 50.89 (51.0); H 6.91 (7.34); N 5.98 (6.37). ESI-MS (m/z , based on ^{101}Ru): $[M^+] = 1232.1$. UV-Vis (in THF) λ / nm ($\epsilon / M^{-1} cm^{-1}$): 465 (4700), 580 (4300), 760 (2800), 830 (2900). μ_{eff} (21°C) = 3.5 μ_B . Electrochemistry (THF, vs Fc⁺⁰), $E_{1/2} / V$, $\Delta E_p / mV$, $i_{backward}/i_{forward}$: 0.00, 60, 0.37; -0.38, 70, 0.85; -1.70, 80, 0.30.

$Ru_2(m^iPrOap)_4(C_6H_4-4^tBu)$ (2b). 1-Bromo-4-(*tert*-butyl)-benzene (0.10 mL, 0.87 mmol) was dissolved in 5 mL THF and treated with 0.50 mL *n*BuLi (1.3 mmol) at 0°C. The aryllithium solution was cannula-transferred to a 70 mL THF solution of $Ru_2(m^iPrOap)_4Cl$ (100 mg, 0.087 mmol). An immediate color change from dark green to red-brown was observed. The reaction mixture stirred for 3 h at room temperature. Upon exposure to air, the solution changed from red-brown to dark green. After filtration over Celite and removal of solvent, the crude reaction mixture was purified via recrystallization from *n*-pentane at -20°C. The microcrystalline green precipitate was collected on a frit and rinsed with cold pentane, then dried under vacuum. Compound was later purified for EA using column chromatography on deactivated (w/ triethylamine) silica. The dark green band was eluted with 1:5 EtOAc/hexanes (v/v) from which a dark green solid was isolated. Single crystals suitable for X-ray diffraction were grown from slow evaporation of **2b** in hexanes. Yield: 84 mg (78% based on Ru). Elem. Anal. Found (Calcd) for $C_{80}H_{103}N_8O_8Ru_2$ (**2b**·1C₆H₁₄·2EtOAc): C 64.14 (63.77); H 6.93 (6.89); N 7.16 (7.44). ESI-MS (m/z , based on ^{101}Ru): $[M^+] = 1244.2$. UV-Vis (in THF) λ / nm ($\epsilon / M^{-1} cm^{-1}$): 470 (7500), 650 (2000), 817 (3700). μ_{eff} (20°C) = 4.1 μ_B . Electrochemistry (THF, vs Fc⁺⁰), $E_{1/2} / V$, $\Delta E_p / mV$, $i_{backward}/i_{forward}$: -0.21, 69, 0.91; -1.61, 76, 0.90.

$Ru_2(m^iPrOap)_4(C_6H_4-4-OMe)$ (3b). 4-Bromoanisole (0.1 mL, 1.1 mmol) was dissolved in 5 mL THF and then treated with 0.4 mL *n*BuLi (1.5 mmol) at 0°C. The aryllithium solution was then cannula-transferred to a 70 mL solution of $Ru_2(m^iPrOap)_4Cl$ in THF (90.4 mg, 0.08 mmol). A color change from dark green to brown was observed. The reaction mixture stirred for 3 hours at room temperature. Upon exposure to atmosphere, no color change was observed. After filtering over Celite and solvent removed, the crude product mixture was purified by column chromatography on deactivated (with triethylamine) silica. The light brown band was collected with 1:5 THF/hexanes (v/v), and a dark brown solid was isolated. This solid was noted to be relatively unstable in ambient conditions, degrading to $Ru_2(m^iPrOap)_4Cl$ and an unknown yellow

impurity. Single crystals suitable for X-ray diffraction were grown by slow evaporation of a concentrated solution of **3b** in diethyl ether. Yield: 20 mg (21% based on Ru). Elem. Anal. Found (Calcd) for $C_{83}H_{113}N_8O_{13}Ru_2$ (**3b**·3H₂O·5THF): C 61.14 (61.05); H 7.02 (6.97); N 6.59 (6.86). ESI-MS (m/z , based on ^{101}Ru): $[M^+] = 1218.5$. UV-Vis (in THF) λ / nm ($\epsilon / M^{-1} cm^{-1}$): 473 (6200), 649 (1500), 813 (3000). μ_{eff} (21°C) = 3.6 μ_B . Electrochemistry (THF, vs Fc^{+/0}), $E_{1/2} / V$, $\Delta E_p / mV$, $i_{backward}/i_{forward}$: -0.20, 74, 0.88; -1.61, 80, 0.97.

Ru₂(*m*-^{*i*}PrOap)₄(C₆H₄-3,5-(OMe)₂) (4b). 1-Bromo-3,5-(dimethoxy)-benzene (200 mg, 0.91 mmol) was dissolved in 10 mL THF and was treated with 0.4 mL ^{*n*}BuLi (1 mmol) at -78°C. The ligand solution was warmed slightly and was cannula-transferred to a 30 mL THF solution of Ru₂(*m*-^{*i*}PrOap)₄Cl (149 mg, 0.131 mmol). An immediate color change to red-brown from dark green was observed upon addition. The reaction mixture was stirred for 1.5 hours at room temperature. Upon exposure to air, the solution changed back to dark green. After filtering over Celite and removal of the solvent, the crude mixture was first purified using a 1/20 (v/v) THF/hexanes recrystallization at -20°C. The dark green solid that was collected was then run through a Celite plug with 1:5 THF/hexanes (v/v). The filtrate was collected, and solvents were removed to give a dark green solid. Single crystals suitable for X-ray diffraction were grown by layering hexane over a concentrated solution of **4b** in THF. Yield: 86 mg (53% based on Ru). Elem. Anal. Found (Calcd) for $C_{79}H_{104}N_8O_6Ru_2$ (**4b**·2.5C₆H₁₄·1THF): C 64.83 (64.36); H 6.80 (7.09); N 7.29 (7.51). ESI-MS (m/z , based on ^{101}Ru): $[M^+] = 1249.0$. UV-Vis (in THF) λ / nm ($\epsilon / M^{-1} cm^{-1}$): 469 (6300), 648 (1900), 800 (4200). μ_{eff} (21°C) = 3.4 μ_B . Electrochemistry (THF, vs Fc^{+/0}), $E_{1/2} / V$, $\Delta E_p / mV$, $i_{backward}/i_{forward}$: -0.19, 79, 0.84; -1.58, 85, 0.98.

Ru₂(*m*-^{*i*}PrOap)₄(C₆H₄-4-CF₃) (5b). 4-Bromobenzotrifluoride (0.1 mL, 0.71 mmol) was dissolved in 5 mL THF and then treated with 0.4 mL ^{*n*}BuLi (1 mmol) at -78°C. The aryllithium solution was then warmed to room temperature and 4.5 mL of the solution was transferred via syringe to a 60 mL THF solution of Ru₂(*m*-^{*i*}PrOap)₄Cl (106 mg, 0.092 mmol). An immediate color change from dark green to red-brown was observed upon addition. The reaction mixture was stirred for 2 hours at room temperature. Upon exposure to air, the solution changed back to dark green. After filtering over Celite and removal of the solvent, the crude mixture was purified first with a hexanes recrystallization at -20°C followed by final purification by column chromatography on deactivated (w/ triethylamine) silica. The green band was collected with 1:5 EtOAc/hexanes (v/v), and a dark green solid was isolated. Yield: 79 mg (68% based on Ru). Elem. Anal. Found

(Calcd) for $C_{83}H_{116}N_8O_{20}F_3Ru_2$ (**5b**·6H₂O·5EtOAc): C 55.08 (55.23); H 6.45 (6.48); N 5.96 (6.21). ESI-MS (m/z , based on ^{101}Ru): $[M^+] = 1257.0$. UV-Vis (in THF) λ / nm ($\epsilon / M^{-1} cm^{-1}$): 466 (5300), 668 (1800), 810 (3200). μ_{eff} (20°C) = 3.9 μ_B . Electrochemistry (THF, vs Fc^{+/0}), $E_{1/2} / V$, $\Delta E_p / mV$, $i_{backward}/i_{forward}$: -0.13, 64, 0.86; -1.48, 80, 0.96.

1.5.2 X-ray Crystallographic Details

Crystals suitable for X-ray diffraction analysis were grown by layering hexanes over a concentrated solution of either **2a**, **4a**, or **5a** in ethyl acetate or of **3a** or **4b** in THF. Crystals suitable for X-ray diffraction analysis were grown by slow evaporation of either **1a** in acetone, **2b** in hexanes or of **3b** in Et₂O. Single crystals of **2a**, **3a**, **4a**, **5a**, **3b**, and **4b** were coated with paraffin oil and quickly transferred to the goniometer head of a Bruker Quest diffractometer with a fixed chi angle, a sealed tube fine focus X-ray tube, single crystal curved graphite incident beam monochromator, a Photon II area detector and an Oxford Cryosystems low temperature device. Examination and data collection were performed with Mo K α radiation ($\lambda = 0.71073 \text{ \AA}$) at 150 K. Single crystals of **1a** and **2b** were coated with paraffin oil and quickly transferred to the goniometer head of a Bruker Quest diffractometer with kappa geometry, an I- μ -S microsource X-ray tube, laterally graded multilayer (Goebel) mirror single crystal for monochromatization, a Photon-III C14 area detector and an Oxford Cryosystems low temperature device. Examination and data collection were performed with Cu K α radiation ($\lambda = 1.54178 \text{ \AA}$) at 150 K. Full details of the crystals can be found in Tables A.1 and A.2 in Appendix A below. In some of the structures, **2b** and **4b**, only part of the solvent molecules were sufficiently resolved to model, and were included as partially occupied. Based on the XRD data it was not possible to determine whether the remaining volume remained unoccupied, or if additional highly disordered solvate molecules are present. A complete removal of the partially occupied solvent molecules via the Squeeze procedure did not substantially improve the overall quality of the structure, and we thus decided to include the resolved fraction of the void content as partially occupied solvate molecules.

Data were collected, reflections were indexed and processed, and the files scaled and corrected for absorption using APEX3⁵⁰ and SADABS.⁵¹ The space groups were assigned using XPREP within the SHELXTL suite of programs⁵² and solved by direct methods using ShelXS⁵³ or dual methods using ShelXT⁵⁴ and refined by full matrix least squares against F^2 with all reflections using Shelxl2018^{55,56} using the graphical interface Shelxle.⁵⁷ Complete crystallographic

data, in CIF format, have been deposited with the Cambridge Crystallographic Data Centre. CCDC 2123249-2123256 contains the supplementary crystallographic data for this paper. These data can be obtained free of charge from The Cambridge Crystallographic Data Centre via www.ccdc.cam.ac.uk/data_request/cif

CHAPTER 2. PHENYLENE AS AN EFFICIENT MEDIATOR FOR INTERMETALLIC ELECTRONIC COUPLING

Reproduced (adapted) from L. A. Miller-Clark, A. Raghavan, R. A. Clendening, and T. Ren, *Chem. Commun.*, 2022, **58**, 5478–5481 with permission from Royal Society of Chemistry. DOI: 10.1039/D2CC00949H

2.1 Abstract

The new compound $[(\text{NC})\text{Ru}_2(\text{ap})_4]_2(\mu\text{-1,4-C}_6\text{H}_4)$ (ap = 2-anilinopyridinate) was prepared to address the open question of whether a 1,4-phenylene bridge can mediate intermetallic electronic coupling. As a manifestation of strong coupling, hole delocalization between the Ru_2 centers on the IR time scale (10^{-14} s) was established using spectroelectrochemistry. An orbital mechanism for coupling was elaborated with DFT analysis.

2.2 Introduction

Conjugated organometallic compounds are promising building blocks for soft functional materials,^{58–60} where the extensive $d\pi\text{-}\pi$ interactions render rich redox and optical properties unattainable in pure organic systems. Polymers based on metal-alkynyl units, polymetallaynes (**I** in Figure 2.1), are particularly attractive as electronic materials due to their structural rigidity, reduced band gaps and excellent charge mobility.^{60–62} Correspondingly, the charge transfer processes across metal-acetylide backbones in mono- and bimetallic compounds have been extensively probed based on mixed-valency therein, and the structure-property relationships derived provide useful insight for material design.^{63–65} Metal-acetylide motifs with proven proficiency in mediating charge transfer have been incorporated into nano-junctions with substantial conductance,^{66,67} and have been shown to function as switches⁶⁸ and flash-like memory devices.²⁸ While the scope of metal-aryl chemistry is immense due to its relevance to cross coupling reactions,⁶⁹ polymetallaarylenes (**II** in Figure 2.1) have yet to be used for material applications. Furthermore, intermetallic coupling across a simple metal-($\mu\text{-1,4-phenylene}$)-metal backbone has never been experimentally demonstrated.

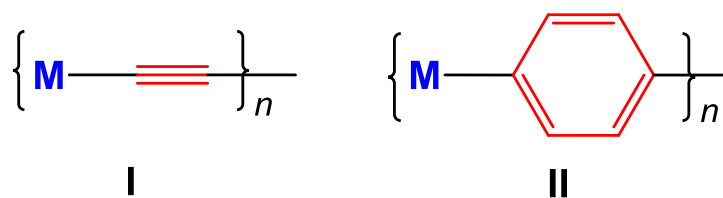
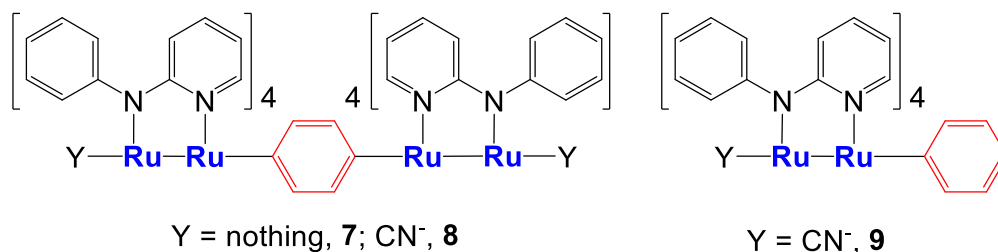


Figure 2.1. Polymetallaynes (**I**) and polymetallaarylene (**II**) structural motifs

Diruthenium paddlewheel type compounds are well known for their robust redox responses.^{4,5} Facile charge delocalization across the bridging oligoyn-diyl (C_{2n}) has been demonstrated in $[\text{Ru}_2(\text{ap})_4]_2(\mu\text{-C}_{2n})$ type compounds (ap = 2-anilinopyridinate) through Vis-NIR spectroelectrochemical (SEC) experiments in bulk solutions.^{22,25} The rich redox characteristics of Ru_2 compounds further enable a broad range of applications as wires in nano-junctions,^{26,34} spin-chains,⁷⁰ and catalytic activation of small molecules.^{15,71,72} More recently, $\text{Ru}_2(\text{ap})_4(\text{Ar})$ type compounds (Ar = aryl) were prepared,³⁵ and their capacity in binding small linear ligands such as CO , CN^- and C_2H^- at the axial site *trans*- to Ar was demonstrated.³⁷ Interested in expanding this chemistry to investigate bridging arylenes, we report herein the formation and characterization of $[\text{Ru}_2(\text{ap})_4]_2(\mu\text{-1,4-C}_6\text{H}_4)$ (**7**, Scheme 2.1) and its derivative $[(\text{NC})\text{Ru}_2(\text{ap})_4]_2(\mu\text{-1,4-C}_6\text{H}_4)$ (**8**, Scheme 2.1), the unambiguous evidence of strong intermetallic coupling across the phenylene bridge through the SEC study of $[\textbf{8}]^+$, and companion DFT and TD-DFT analyses.



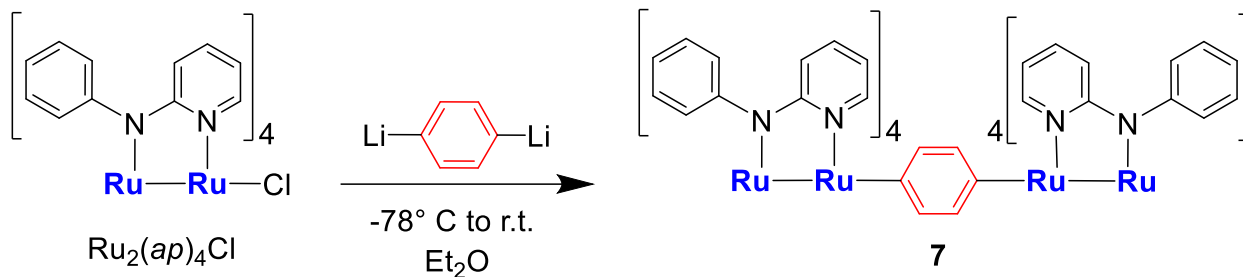
Scheme 2.1. Compounds discussed in this chapter

2.3 Results and Discussion

2.3.1 Synthesis

As shown in Scheme 2.2 below, the reaction of $\text{Ru}_2(\text{ap})_4\text{Cl}$ with a slight excess of 1,4-dithiobenzene yielded the phenylene bridged compound **7** (62%), and its ‘dimeric’ nature was verified by the isotopic distribution of Ru in the ESI-MS of **7** (Figure 2.2). Efforts to probe **7**

spectroscopically were thwarted by its high sensitivity to air / moisture (see comments in sections 2.3.3 and 2.3.5) and low solubility in organic solvents.



Scheme 2.2. Synthesis of **7** from $\text{Ru}_2(\text{ap})_4\text{Cl}$ and a slight excess of 1,4-dilithiobenzene

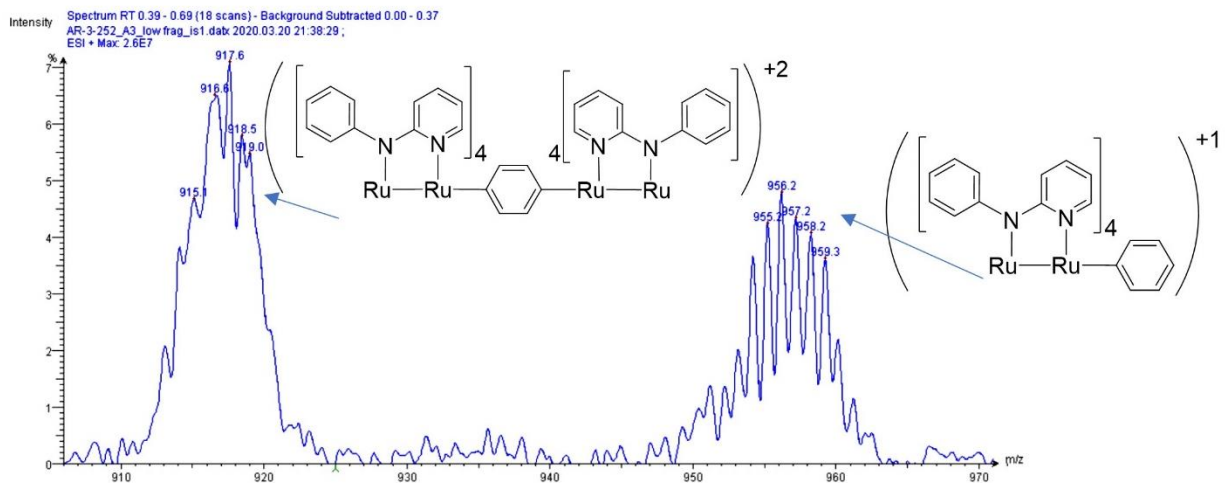
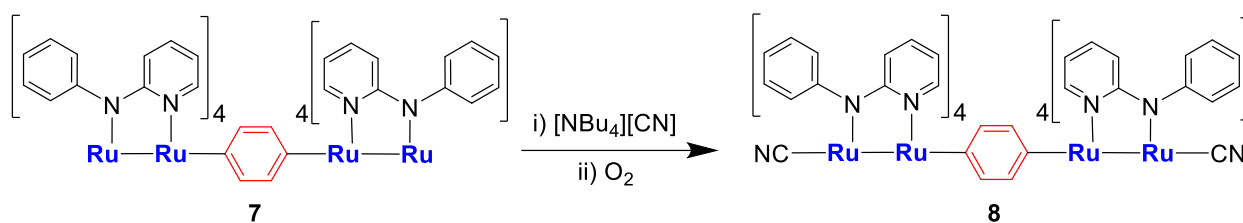
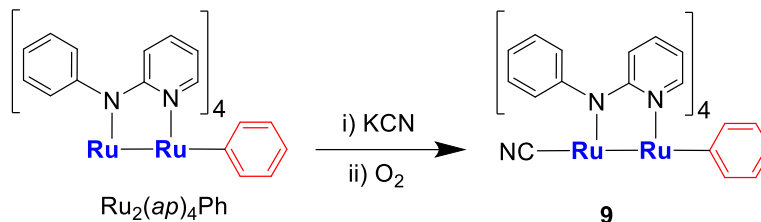


Figure 2.2. ESI-MS of the crude reaction mixture of Scheme 2.2 at low fragmentation voltages, courtesy of Dr. Adarsh Raghavan. Isotopic distribution characteristic of $(\text{Ru}_2)_2$ corresponding to $[\mathbf{7}]^{2+}$ ($m/z = 1834.0 / 2 = 917$, left). Side product $\text{Ru}_2(\text{ap})_4\text{Ph}$ (right)

Seeking a more stable form of the dimer, **7** was treated with $[\text{Bu}_4\text{N}][\text{CN}]$ under N_2 , which was followed by exposure to O_2 to yield **8** (59%) as shown in Scheme 2.3. Purification of **8** was achieved by multiple CH_2Cl_2 / hexanes recrystallization at room temperature to produce a purple microcrystalline solid. Compound **8**, a dimer of $\text{Ru}_2(\text{III,III})$ units, is air-stable and significantly more soluble than **7**. In order to benchmark electronic properties of **8**, the corresponding ‘monomer’ $(\text{NC})\text{Ru}_2(\text{ap})_4(\text{C}_6\text{H}_5)$ (**9**), was prepared from $\text{Ru}_2(\text{ap})_4(\text{C}_6\text{H}_5)^{35}$ using the same procedure and purification that was used for **8** (Scheme 2.4).



Scheme 2.3. Synthesis of **8** from the reaction between **7**, CN[−] and O₂



Scheme 2.4. Synthesis of **9** from the reaction of Ru₂(ap)₄Ph,³⁵ CN[−] and O₂

2.3.2 Molecular Structures

Both the dimeric nature of **8** and the phenylene bridging are unambiguously established with the single crystal X-ray structure of **8** shown in Figure 2.3, with key metric parameters also provided in Table 2.1. The Ru₂ units in **8** display significant distortions from an idealized uniaxial paddlewheel structure as exemplified by the large deviation of Ru–Ru–C_{ph} from linearity, which is likely caused by a second order Jahn-Teller effect.³⁷ Both the Ru–Ru (*ca.* 2.49 Å) and Ru–C_{aryl} (*ca.* 2.05 Å) bond lengths closely match those found for the monomer **9** (Ru–Ru, 2.50 Å; Ru–C_{aryl}, 2.05 Å), shown in Figure 2.4 and values given in Table 2.1, indicating similar electronic structures around the Ru₂ core between **8** and **9**.

Table 2.1. Selected bond lengths (Å) and angles (deg) for **8** and **9**

	8 (Ru1-Ru2)	8 (Ru3-Ru4)	9
Ru1–Ru2	2.4892(3)	2.4829(3)	2.5011(2)
Ru1–C _{aryl}	2.052(3)	2.051(3)	2.0523(16)
Ru2–C _{CN}	2.019(3)	2.013(3)	2.0081(15)
Ru2–Ru1–C _{aryl}	152.21(9)	147.14(9)	156.27(5)
Ru1–Ru2–C _{CN}	168.02(10)	170.60(9)	170.88(4)
Ru1–N1	2.153(3)	2.165(3)	2.0423(13)
Ru1–N3	2.031(3)	2.024(3)	2.1589(13)
Ru1–N5	2.036(3)	2.042(3)	2.1331(13)
Ru1–N7	2.155(3)	2.119(3)	2.0293(13)
Ru2–N2	1.985(3)	1.969(3)	2.0399(12)
Ru2–N4	2.200(3)	2.073(3)	1.9775(13)
Ru2–N6	2.045(3)	2.169(3)	1.9963(12)
Ru2–N8	1.973(3)	1.982(3)	2.1462(12)
C–N (CN [−])	1.140(4)	1.143(4)	1.156(2)

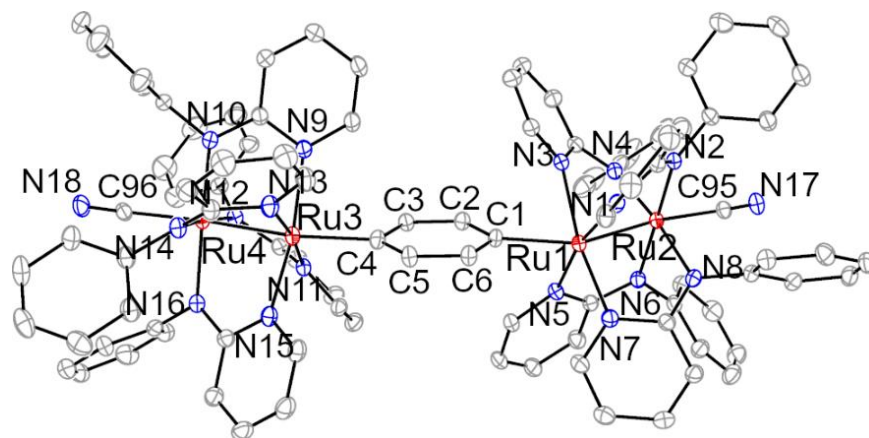


Figure 2.3. ORTEP plot of **8** at 30% probability level. H atoms and solvent molecules omitted for clarity

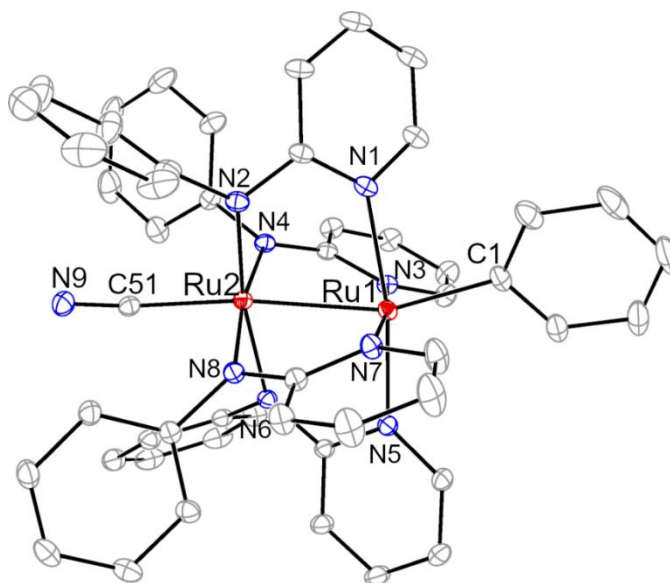


Figure 2.4. ORTEP plot of **9** at 30% probability level. H atoms and solvent molecules omitted for clarity

2.3.3 Electrochemical Studies

Electronic coupling mediated by phenylene in **8** was first probed with voltammetric analysis. As shown in Figure 2.5, compound **9** exhibits two reversible $1e^-$ Ru_2 -based couples: an oxidation **A** at 0.21 V (*versus* $Fe^{+/0}$) and a reduction **B** at -0.92 V, which is a characteristic common to $Ru_2(III,III)$ species supported by the *ap* scaffold.^{20,37}

Compound **8** exhibits two $1e^-$ oxidations at potentials close to that of **A** in **9**: 0.29 (**A2**) and 0.01 V (**A1**), and two $1e^-$ reductions at potentials close to that of **B** in **9**: -0.91 (**B1**) and -1.09 V

(**B2**). A reduction event (**C**) beyond **B2** is attributed to a species derived from the degradation of [**8**]²⁻. The stepwise appearance for the redox couples in **8** is a hallmark of significant intermetallic coupling through the bridging ligand.⁷³ Furthermore, the $\Delta E_{1/2(+1)}$ (calculated as: $E_{1/2}(\mathbf{A2}) - E_{1/2}(\mathbf{A1})$) of **8**, 291 mV, is slightly higher than that reported for $[\text{Ru}_2(\text{ap})_4]_2(\mu\text{-C}_2)$ (280 mV),²² suggesting that the coupling in [**8**]⁺ may be substantial. On the other hand, the $\Delta E_{1/2(-1)}$ ($E_{1/2}(\mathbf{B1}) - E_{1/2}(\mathbf{B2})$; 174 mV) of **8** is much smaller than that of $[\text{Ru}_2(\text{ap})_4]_2(\mu\text{-C}_2)$ (660 mV) (further comparisons in Table B.4, see Appendix B below), hinting that the phenylene is less efficient in mediating coupling in [**8**]⁻. It is worth mentioning that voltammograms of compound **7** (Figure 2.6), though less-than-ideal due to low solubility, also display the pattern of pairwise oxidations and reductions similar to that of **8**.

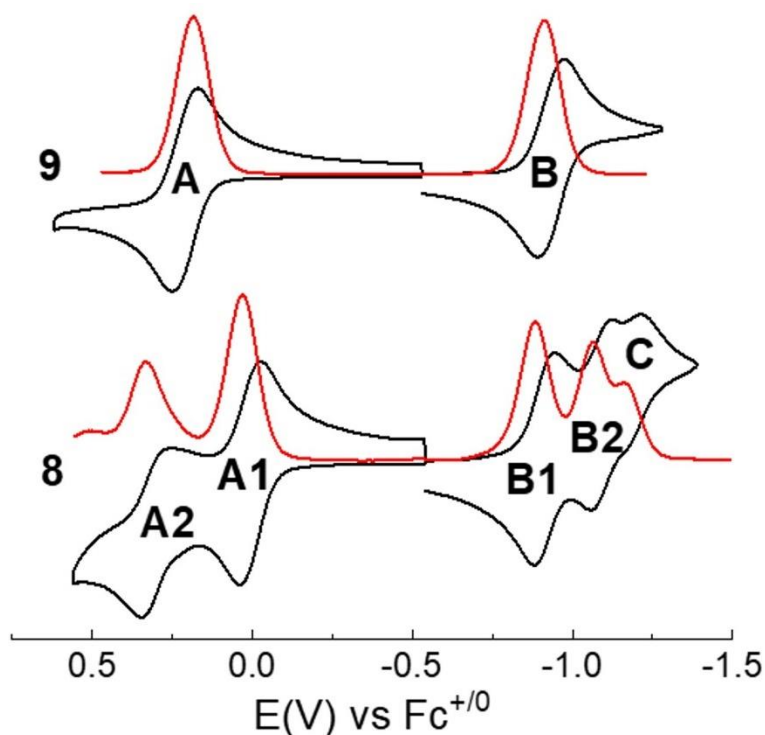


Figure 2.5. Cyclic (black) and differential pulse (red) voltammograms of compounds **8** and **9** (1.0 mM) recorded in 0.1 M $[\text{Bu}_4\text{N}][\text{PF}_6]$ in THF at a scan rate of 0.1 V/s

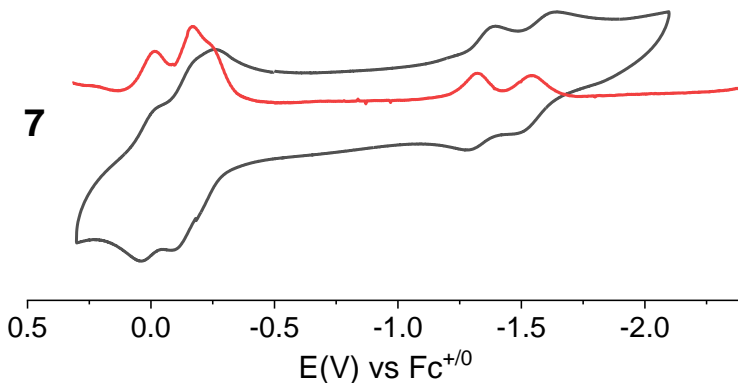


Figure 2.6. Cyclic (black) and differential pulse (red) voltammograms of **7** (< 1.0 mM) recorded in 0.1 M [Bu₄N][PF₆] in THF at a scan rate of 0.1 V/s, courtesy of Dr. A. Raghavan

2.3.4 Vis-NIR and IR Spectroelectrochemistry Experiments

To quantify the degree of electronic coupling in **8**, mixed valency in both [**8**]⁺ and [**8**]⁻ were probed with Vis-NIR and IR SEC experiments and compared with that of the monomer molecule, **9**. As shown in Figure 2.7, both compounds **8** and **9** display an intense peak around 550 nm (18,350 cm⁻¹, band I), which is assigned to $\pi(\text{Ru}_2) \rightarrow \pi^*(\text{N})/\delta^*(\text{Ru}_2)$.⁴⁶ Compound **9** also absorbs strongly around 950 nm (10,500 cm⁻¹, band II), and the analogous peak in **8** is shifted to 1025 nm (9,900 cm⁻¹), which are likely the transitions between HOMO and LUMO ($\pi^*(\text{Ru}_2) \rightarrow \delta^*(\text{Ru}_2)$), see the DFT discussion in section 2.3.5).

Upon the 1e⁻ reduction of **9**, both bands I and II are blue shifted with reduced intensities (Figure 2.8(a)). Significantly, there is no discernible peak emerging in the red-NIR region. Furthermore, a red-shifted $\nu(\text{C}\equiv\text{N})$ (2070 cm⁻¹) was located in the IR SEC of [**9**]⁻ (Figure 2.8(b)), which confirms increased π -backdonation upon the addition of an electron to **9**.

Upon the first 1e⁻ reduction of **8**, both bands I and II are blue shifted with reduced intensities (Figure 2.9(a)). On the second 1e⁻ reduction, both bands are further blue shifted with the former intensifying and the latter weakening (Figure 2.9(b)). Significantly, there is no discernible peak emerging in the red-NIR region, hinting at the localized nature of [**8**]⁻ despite a sizable $\Delta E_{1/2}(-1)$. Furthermore, two distinctive $\nu(\text{C}\equiv\text{N})$ (2092 and 2069 cm⁻¹) were located in the IR SEC of [**8**]⁻ (Figure 2.10) which clearly confirms localization of the added electron on the IR time scale.⁷³

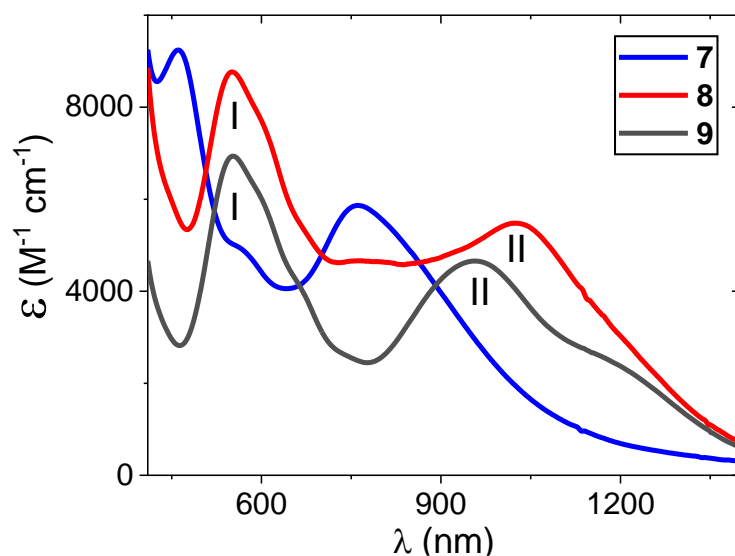


Figure 2.7. Vis-NIR absorption spectra of **7–9** in THF

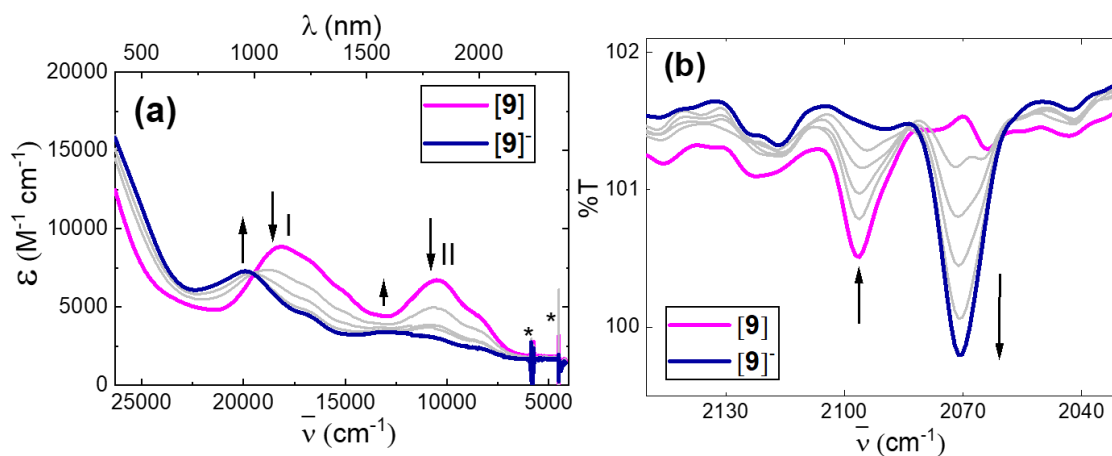


Figure 2.8. (a) Spectroelectrochemistry Vis-NIR of **9** at -1.15 V in THF vs Ag wire. Instrument artifacts/solvent overtones noted as *. (b) FT-IR spectroelectrochemistry of **9** at -1.15 V vs Ag wire. 2 mM analyte with 0.1 M $[\text{Bu}_4\text{N}][\text{PF}_6]$ in THF for both (a) and (b) with grey lines denoting intermediate scans for each SEC experiment

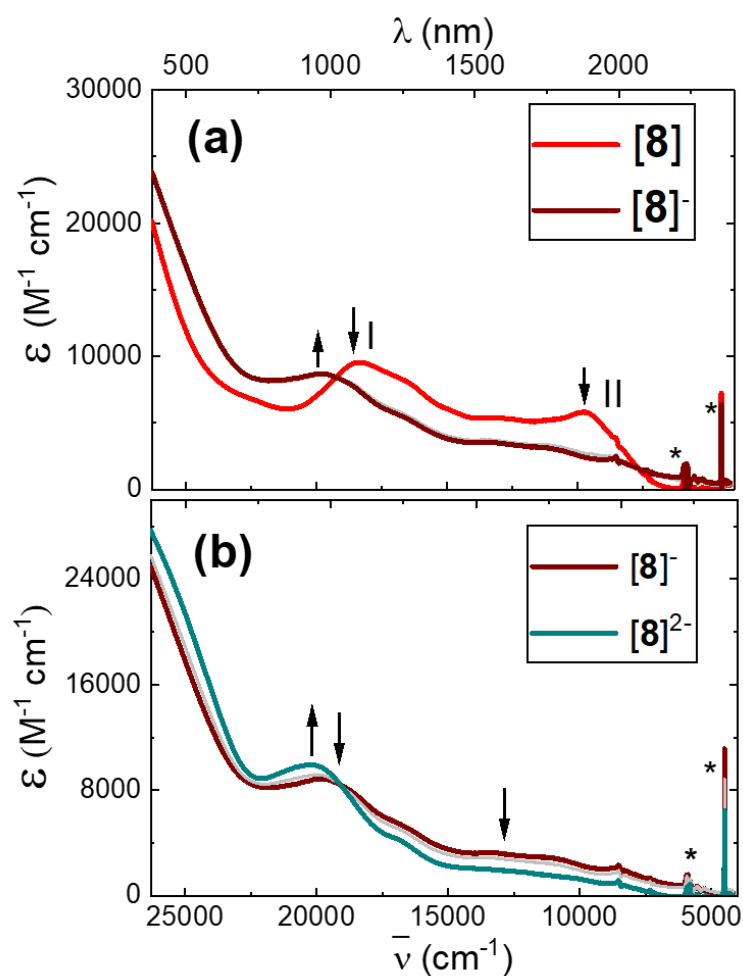


Figure 2.9. Full spectroelectrochemical UV-Vis-NIR changes of **8** at -1.1 V (a) and -1.2 V (b) vs Ag wire. 2 mM analyte with 0.1 M $[\text{Bu}_4\text{N}][\text{PF}_6]$ in THF in all cases. Instrument artifacts/solvent overtones noted as * with grey lines denoting intermediate scans for each SEC experiment. Isosbestic point located at 1000 nm (20000 cm^{-1})

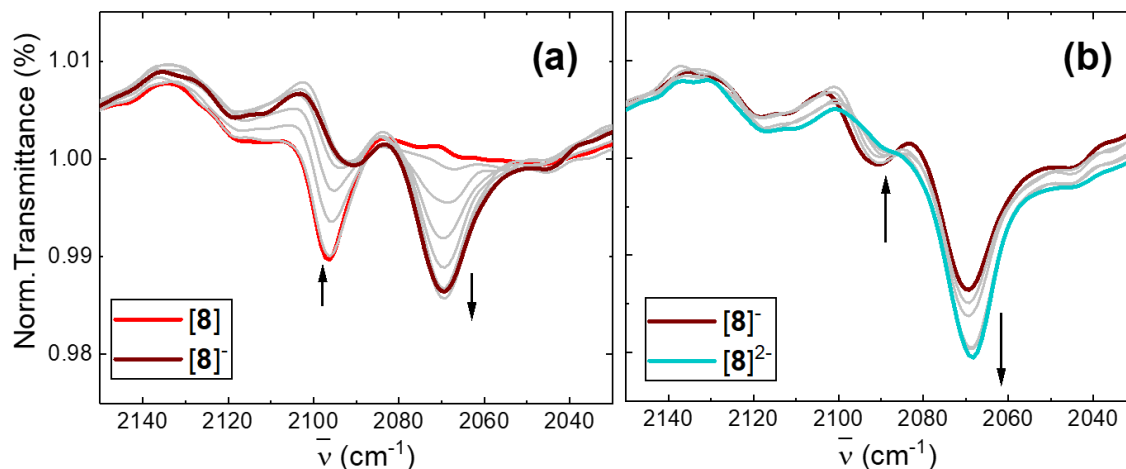


Figure 2.10. FT-IR spectroelectrochemistry of **8** at -1.1 V (a) and -1.35 V (b) vs Ag wire. 2 mM analyte with 0.1 M $[\text{Bu}_4\text{N}][\text{PF}_6]$ in THF in all cases, with grey lines denoting intermediate scans for each SEC experiment

Upon the first $1e^-$ oxidation of **8**, both bands I and II are red shifted, with II intensified. Very intriguingly, an intense new band (III) grows in with an onset around $5,800\text{ cm}^{-1}$ as shown in Figure 2.11. Because of the cutoff of the NIR spectrometer (2400 nm , 4167 cm^{-1}), only half of band III is recorded in the NIR SEC. Fortunately, much of the remaining half of band III is located in the IR SEC of $[\text{8}]^+$ (Figure B.7 in Appendix B below) from which a nearly complete peak is constructed for band III. On the second $1e^-$ oxidation, band III is completely bleached (Figure 2.11(b)), while bands I and II are further intensified.

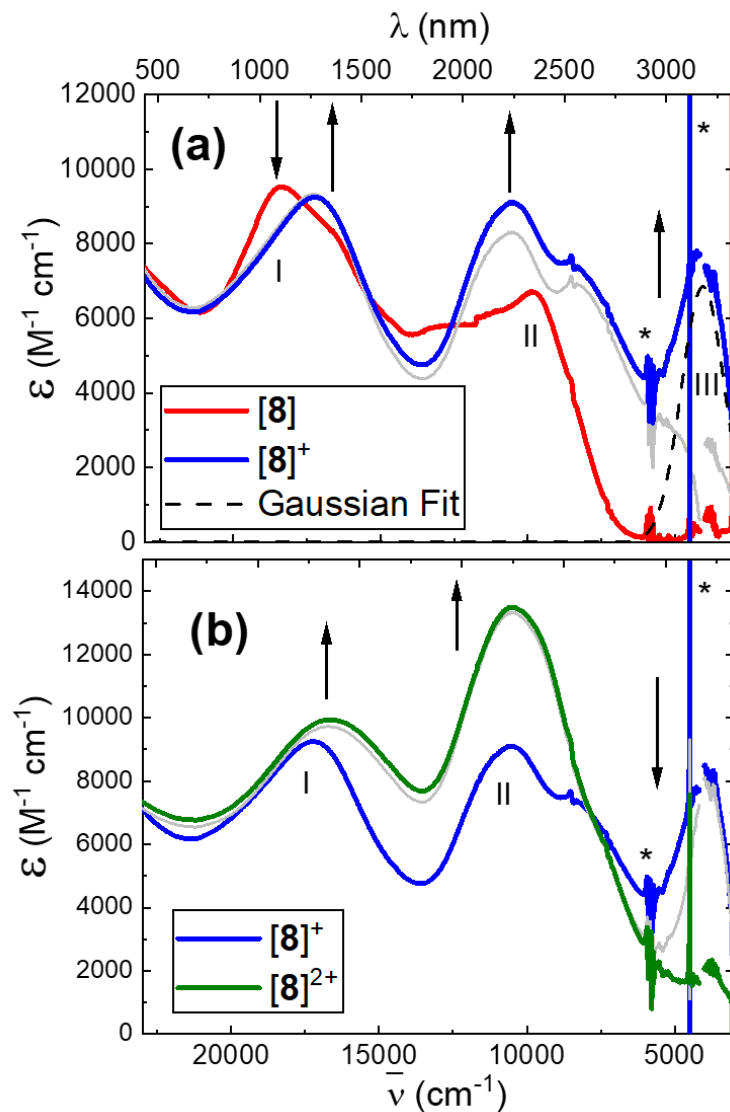


Figure 2.11. Vis-NIR and IR spectroelectrochemistry of **8** with Gaussian fit of the IVCT band (black dash) at 0.4 V (a) and 0.65 V (b) vs Ag wire, 2 mM analyte with 0.1 M [Bu₄N][PF₆] in THF in all cases. Instrument artifacts / solvent overtones noted as * with grey lines denoting intermediate scans for each SEC experiment

As a baseline study, the SEC of the first 1e⁻ oxidation of **9** was recorded (Figure 2.12(a)), where both bands I and II are red shifted with the latter slightly intensified, similar to those of [8]⁺. Nonetheless, there is no new significant peak emerging for [9]⁺ in the NIR-IR region. Hence, the absence of band III in both [8]⁺² and [9]⁺ establishes it as an intervalence charge-transfer transition (IVCT).^{63,73,74}

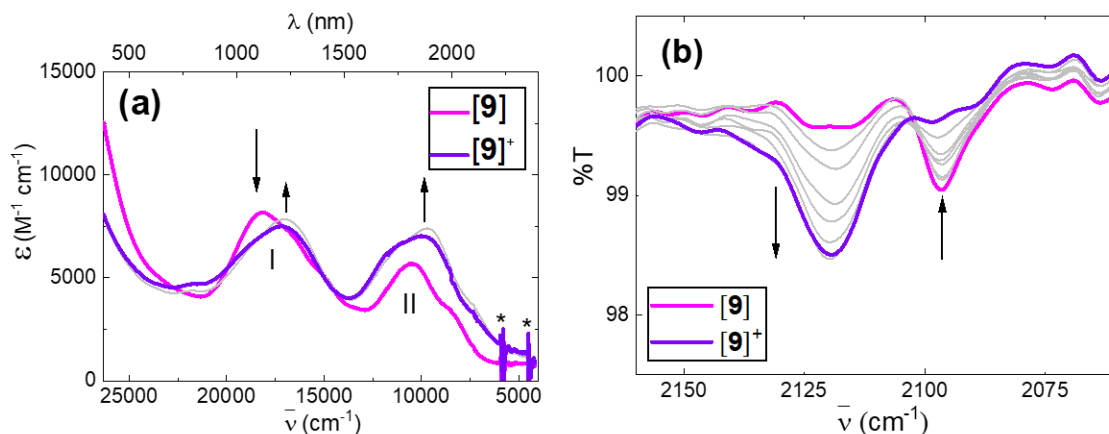


Figure 2.12. (a) Vis-NIR spectroelectrochemistry of **9** at 0.3 V (a) in THF vs Ag wire. Instrument artifacts/solvent overtones noted as *. (b) FT-IR spectroelectrochemistry of **9** at 0.4 V (b) vs Ag wire. 2 mM analyte with 0.1 M [Bu₄N][PF₆] in THF in all cases. Grey lines denoting intermediate scans for each SEC experiment

Further analysis of the IVCT band is enabled with Gaussian deconvolution of the Vis-NIR and IR SEC of [**8**]⁺, which yields the following parameters for the fit (black dash in Figure 2.11): $\bar{\nu}_{\text{IVCT}} = 4,050 \text{ cm}^{-1}$, $\epsilon = 6,860 \text{ M}^{-1} \text{ cm}^{-1}$, $\Delta\bar{\nu}_{1/2} = 1,716 \text{ cm}^{-1}$ (Figures B.3–5 in Appendix B below). Importantly, the $\Delta\bar{\nu}_{1/2}$ is significantly smaller than the predicted value by the Hush model ($\Delta\bar{\nu}_{1/2}(\text{Hush}) = (2310 \nu_{\text{IVCT}})^{1/2} = 3,060 \text{ cm}^{-1}$),⁷⁴ which, along with the large ϵ , suggests that [**8**]⁺ is a highly delocalized (Robin-Day class III) mixed valence species. Further evidence cementing this assessment is the IR SEC of [**8**]⁺ (Figure 2.13(a)) that consists of a single and narrow C≡N stretch peak ($\Delta\bar{\nu}_{1/2} \sim 8 \text{ cm}^{-1}$; in comparison, $\Delta\bar{\nu}_{1/2}(\text{C}\equiv\text{N})$ in [**9**]⁺ $\sim 15 \text{ cm}^{-1}$ (Figure 2.12(b)), indicating that two Ru₂ cores are equivalent on the IR time scale (10^{-14} s).⁷³ The lower threshold of the electronic coupling element H_{AB} can be calculated based on the above mentioned IVCT band parameters and a Ru3---Ru1 distance (r) of 6.95 Å with the Mulliken-Hush equation (1):^{63,74}

$$H_{\text{AB}} = (0.0206/r)(\bar{\nu}_{\text{IVCT}} \Delta\bar{\nu}_{1/2} \epsilon)^{1/2} = 647 \text{ cm}^{-1} \quad (1)$$

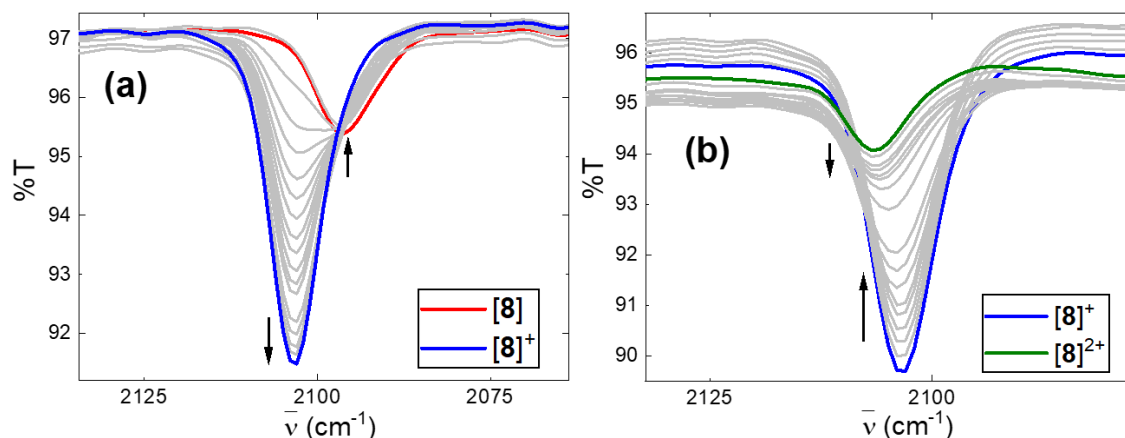


Figure 2.13. FT-IR spectroelectrochemistry of **8** at 0.1 V (a) and 0.3-0.4 V (b) vs Ag wire. 2 mM analyte with 0.1 M [Bu₄N][PF₆] in THF in all cases with grey lines denoting intermediate scans for each SEC experiment

2.3.5 Density Functional Theory Analysis

To understand the underlying orbital mechanism for the observed Ru₂—Ru₂ coupling in [8]⁺, DFT calculations were performed for **8**, [8]⁺ and **9**. Our previous work³⁷ with (Y)Ru₂(ap)₄(C₆H₄-4-NMe₂) indicated that the addition of axial ligands alters the ground state electron configuration from $\sigma^2\pi^4\delta^2(\pi^*\delta^*)^3$ in Ru₂(ap)₄(Ar) to either “ $\pi^4\delta^2(\pi^*)^4$ ” (Y = CN) or “ $\pi^4\delta^2(\pi^*)^4\delta^*$ ” (Y = CO). Note that for simplicity, the electronic configuration of (Y)Ru₂(ap)₄(C₆H₄-4-NMe₂) (Y = CN, CO) is denoted as “ $\pi^4\delta^2(\pi^*)^4$ ” (CN) or “ $\pi^4\delta^2(\pi^*)^4\delta^*$ ” (CO). This does not reflect the true energetic ordering of the MOs. It is easy to see that the π/π^* (Ru-Ru) orbitals are not identical. One set is perpendicular to the plane of the axial aryl, thereby interacting with its π/π^* set. The other set of π/π^* (Ru-Ru) orbitals, being parallel to the plane of the aryl ligand, does not interact in this fashion. When all the orbital contributions are summed up, we can indeed condense the representation of the valence d-manifold of the Ru-Ru motif in this way for convenience and d-electron counting purposes. Unfortunately, assignments of individual MOs are further complicated by the large structural deviations from idealized mono-axial/bis-axial paddlewheel structures observed in **8** and **9**, which result in extensive mixing among the fragment orbitals (see Table B.8 in Appendix B below).

Magnetic susceptibility measurements using the Evans method⁴⁵ yielded effective magnetic moments at 293 K of 5.81, 2.18 and 2.26 μ_B for **7**, **8** and **9**, respectively (Table 2.2). Compound **7** was predicted to contain 6 unpaired electrons (two Ru₂(II,III) centers). The

experimentally determined μ_{eff} is slightly lower than expected and is attributed to some degradation of **7** back to either $\text{Ru}_2(\text{ap})_4\text{Cl}$ or $\text{Ru}_2(\text{ap})_4(\text{C}_6\text{H}_5)$ in the presence of CDCl_3 during prep and running of the spectra. Both $\text{Ru}_2(\text{ap})_4\text{Cl}$ and $\text{Ru}_2(\text{ap})_4(\text{C}_6\text{H}_5)$ have a μ_{eff} *ca.* 3.8 (3 unpaired electrons).^{35,75}

Table 2.2. Room temperature magnetism data reported as per compound (Evans method⁴⁵). Solvent: CDCl_3 , Reference: Ferrocene

Compound	$\Delta\delta$ (Hz)	$[\text{Ru}_2]$ (mM)	χ_m (emu/mol)	μ_{eff} (B.M.)
7	36.6	2.18×10^{-3}	0.01336	5.81
8	2.04	1.59×10^{-3}	0.00105	2.18
9	9	4.25×10^{-3}	0.00218	2.26

Both **8** and **9** contain $[\text{Ru}_2(\text{ap})_4]^{2+}$ cores in the $\text{Ru}_2(\text{III,III})$ oxidation state, which is expected to be diamagnetic ($S = 0$ ground state). Population of a higher spin state ($S = 1$) is unusual for this class of compounds, but not unprecedented.^{37,76} A possible explanation for this is an extensive mixing between a $[\pi_{xz}^2\pi_{yz}^2\delta^2(\pi_{xz}^*)^2(\pi_{yz}^*)^2]_2$ singlet and a $[\pi_{xz}^2\pi_{yz}^2\delta^2(\pi_{xz}^*)^2]_2(\pi_{yz,1}^*)^2\pi_{yz,2}^*\delta^*$ triplet (phenylene moiety is parallel to the xz plane). DFT calculations on **8** and **9** predicted a singlet-triplet energy gap of 0.87 kcal/mol and 2.0 kcal/mol, respectively. Such small barriers indicate that a large population of the triplet state may be feasible, or that the ground state has some multireference character.

Mulliken orbital composition analysis of the frontier orbitals of **8** (Figure 2.14) reveals that its HOMO is primarily composed of the antibonding combination of $\pi^*(\text{Ru-Ru})$ (62%) and $\pi(\text{Ph})$ orbitals (25%). On the other hand, the LUMO mainly consists of the $\delta^*(\text{Ru-Ru})$ on the Ru_2 cores (49% Ru contribution), with $< 0.5\%$ contribution from the bridging phenylene unit (Table 2.3). DFT calculations on the $1e^-$ oxidized $[\mathbf{8}]^+$ predict an electronic configuration of “ $[\pi_{xz}^2\pi_{yz}^2\delta^2(\pi_{xz}^*)^2]_2(\pi_{yz}^*)^3$ ” with the HOMO in **8** becoming the SOMO (singly occupied molecular orbital). The electronic configuration of $[\mathbf{8}]^-$ is computed as $[\pi_{xz}^4\pi_{yz}^2\delta^2(\pi_{xz}^*)^2(\pi_{yz}^*)^2]_2\delta^*$ with the LUMO in **8** becoming the SOMO; the absence of phenylene contribution explains the lack of coupling in $[\mathbf{8}]^-$. This accounts for the SEC observations: i.e., $[\mathbf{8}]^+$ exhibits an IVCT band in the NIR region, whereas $[\mathbf{8}]^-$ does not.

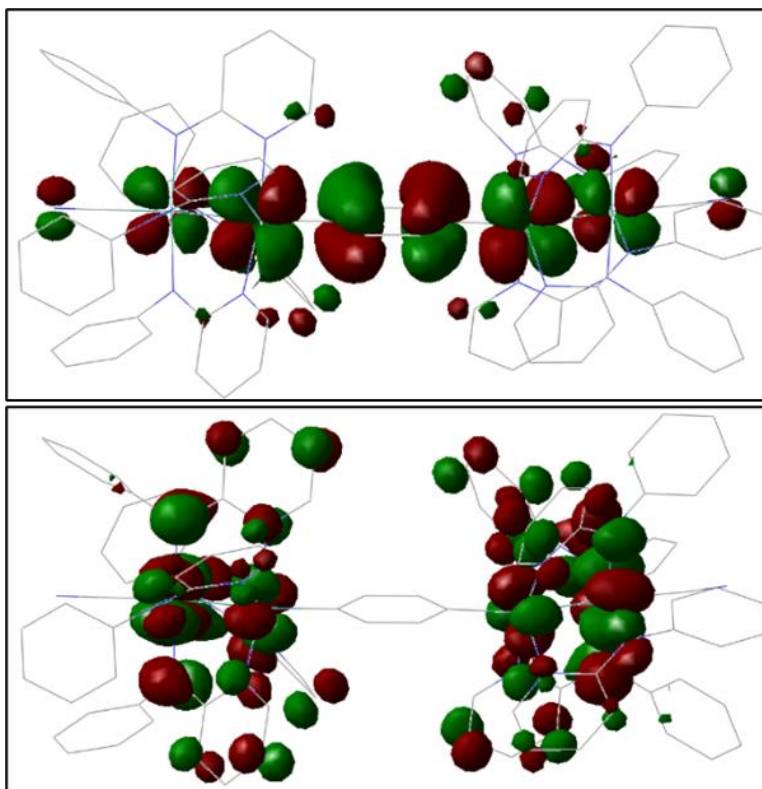


Figure 2.14. HOMO (top) and LUMO (bottom) of the DFT-optimized structure of **8**. |Isovalue| = 0.020, courtesy of Dr. A. Raghavan

Table 2.3. Frontier MOs for **8** with respective orbital compositions (minor contributions < 5% not included)*†

Molecular orbital	Assignment	% Contribution	
HOMO	$\pi^*(\text{Ru}_2) + \pi(\text{C}_6\text{H}_4)$	$d_{yz}(\text{Ru1} + \text{Ru3})$	44.3
	or	$p_\pi(\text{C}_6\text{H}_4)$	25.3
	$\pi^*(\text{Ru-C}_{\text{aryl}})$	$d_{yz}(\text{Ru2} + \text{Ru4})$	11.2
LUMO		$d_{xy}(\text{Ru2} + \text{Ru4})$	27.9
	$\delta^*(\text{Ru}_2)$	p_N	13.1
		Minor (Ru1 + Ru3)	6.8

*Atom labels are according to Figure 2.3. † The phenylene moiety lies on the xz plane. z axis and Ru-Ru bond are collinear

Time-dependent DFT calculations (TD-DFT) on $[\mathbf{8}]^+$ indicate that the observed IVCT band corresponds to a transition (calculated at $4,647\text{ cm}^{-1}$) from an orbital that is primarily a *bonding* combination of $\pi^*(\text{Ru-Ru})$ (43.2% Ru *d*) and $\pi(\text{Ph})$ (7.2% C *p_y*) to the above-mentioned SOMO of $[\mathbf{8}]^+$ (Figures 2.15-2.16). In comparison, the previously studied $[\text{Ru}_2(\text{ap})_4]_2(\mu\text{-C}_{2n})$ series ($[\text{Ru}_2(\text{II,III})]_2$) have the localized δ^* orbitals as SOMO/SOMO-1, while the antibonding combination of $\pi^*(\text{Ru-Ru})$ and $\pi(\text{C}\equiv\text{C})$ are of lower energies.^{22,25} Clearly, the phenylene ($\text{C}_6\text{H}_4^{2-}$) is a much stronger π -base ligand than oligoyn-diyl (C_{2n}^{2-}), and pushes $\pi^*(\text{Ru-Ru})$ up to HOMO / SOMO, enabling intermetallic coupling by a mechanism different from those of $\text{M-C}_{2n}\text{-M}$.

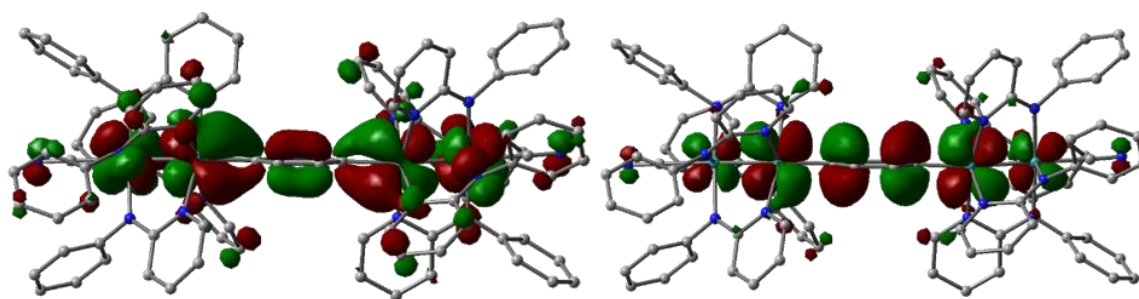


Figure 2.15. Natural transition donor (left) and acceptor (right) orbitals corresponding to the IVCT band, extracted from excited state #5 of $[\mathbf{8}]^+$. Experimental (Figure 2.11) ca. 4000 cm^{-1} , Calculated (Figure 2.16) 4647.1 cm^{-1} . |Isovalue| = 0.025, courtesy of Dr. A. Raghavan

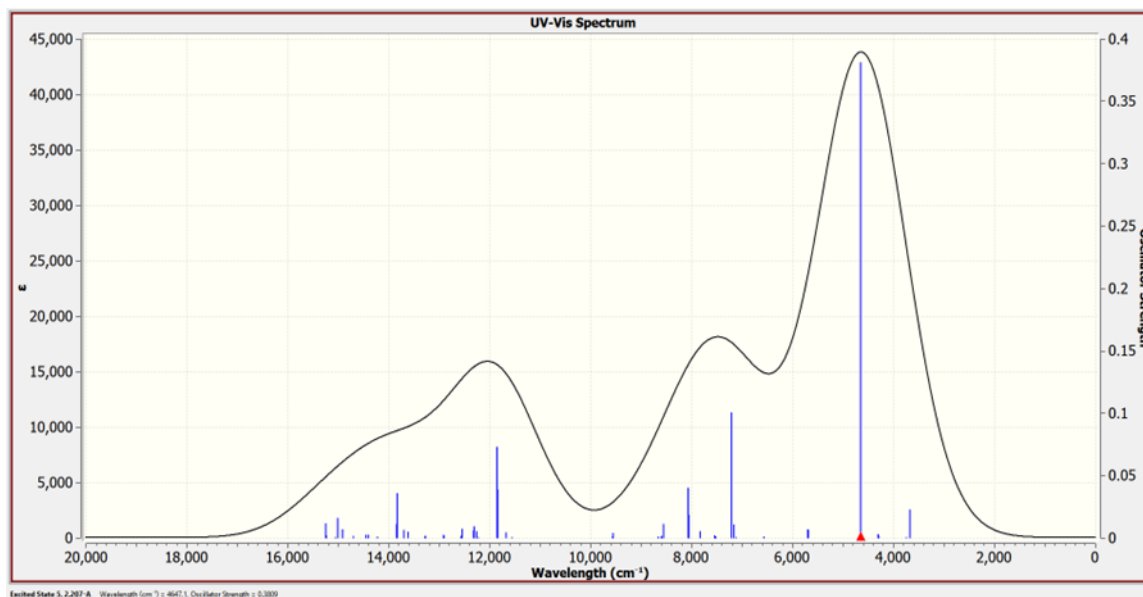


Figure 2.16. TD-DFT calculated electronic absorption spectrum of $[\mathbf{8}]^+$, courtesy of Dr. A. Raghavan

2.4 Conclusions

In conclusion, two new phenylene-bridged compounds, $[(Y)Ru_2(ap)_4]_2(\mu-1,4-C_6H_4)$ ($Y =$ nothing or CN^-), were prepared and characterized. Both Vis-NIR and IR SEC studies of $[8]^+$ reveal its nature as a class III Robin-Day mixed valent ion with the hole being delocalized on the IR time scale (10^{-14} s). DFT analysis provides a rationale for the efficacy of the phenylene bridge in mediating hole transfer over electron transfer, while TD-DFT calculations reveal the origin of the IVCT band. While the intermetallic coupling mediated by arylene in a cyclo-metallated *N,C,N*-tridentate ligand was demonstrated in the pioneering studies of Sauvage and Launay,^{77,78} this study provides the first unambiguous demonstration of strong coupling between metal units via a plain phenylene bridge. In-depth understanding of magnetism, distance dependence, variation of *ap* backbone, and further DFT analysis are in the scope of future work.

2.5 Experimental Section

General Methods. $Ru_2(ap)_4Cl$,⁷⁵ $Ru_2(ap)_4(C_6H_5)^{35}$ and $(NC)(Ru_2(ap)_4(C_6H_5))$ (**9**)³⁷ were prepared according to literature methods. Tetrahydrofuran (THF) was distilled over Na/benzophenone under a N_2 atmosphere. Et_2O was dried and deoxygenated using literature procedures with a Seca solvent purification system.⁷⁹ $[Bu_4N][CN]$, $[Bu_4N][PF_6]$ and $nBuLi$ were purchased from Sigma Aldrich and 1,4-diiodobenzene was purchased from Acros Organics. All reactions were performed under dry N_2 atmosphere using standard Schlenk techniques where noted.

Physical Methods. UV-Vis-NIR spectra were obtained with a JASCO V-670 spectrophotometer in THF solutions. Infrared spectra were obtained on a JASCO FT-IR 6300 spectrometer equipped with an attenuated total reflectance (ATR) accessory on a diamond crystal. ESI-MS were analyzed on an Advion Mass Spectrometer. 1H NMR spectra were recorded on a Varian Inova 300 spectrometer operating at 300 MHz. Magnetic susceptibility measurements of **9** were taken using a Johnson Matthey Mark-I magnetic susceptibility balance. The room temperature magnetic moments for **7**, **8** and **9** were determined using the Evans method⁴⁵ with chemical shifts of ferrocene as the reference. Elemental analyses were performed by Atlantic Microlab, Inc. Cyclic voltammograms were recorded in 0.1 M $[Bu_4N][PF_6]$ and 1.0 mM analyte solution (THF, Ar degassed) using a CHI620A voltammetric analyzer with a glassy carbon

working electrode (diameter = 2 mm), Pt-wire counter electrode, and an Ag/AgCl reference electrode with ferrocene used as an external reference. Spectroelectrochemical absorption data was taken with a JASCO V-670 spectrophotometer, and IR data was taken on a JASCO FT-IR 6300 spectrometer. Spectroelectrochemical analysis was performed using an optically transparent thin-layer electrochemistry (OTTLE) liquid-sample cell⁸⁰ with a 0.2 mm optical path length, 0.3 mL sample volume, and a CaF₂ window. The cell was equipped with a mesh Pt working electrode, mesh Pt auxiliary electrode, and Ag reference electrode; the analyte concentration was 2.0 mM in 4 mL dry THF at a 0.1 M [Bu₄N][PF₆] electrolyte concentration. X-ray diffraction (XRD) data (Table B.1 in Appendix B) for **8** was obtained on a Bruker Quest diffractometer with Cu K α radiation (λ = 1.54178 Å) at 150 K. XRD data (Table B.1 in Appendix B) for **9** was obtained on a Bruker Quest diffractometer with Mo K α radiation (λ = 0.71073 Å) at 150 K.

2.5.1 Synthesis Details

[Ru₂(ap)₄]₂(μ -1,4-C₆H₄) (7). 1,4-Diiodobenzene (0.157 g, 0.475 mmol) was dissolved in 10.0 mL Et₂O and was treated with 0.6 mL ⁿBuLi (1.5 mmol) at -78°C for 1 hour. Three half-equivalents (0.6 mL) of the aryllithium solution were added to a 15.0 mL solution of Ru₂(ap)₄Cl in THF (100 mg, 0.109 mmol) every hour. This reaction stirred overnight. The Et₂O was then removed and the green-brown solid resuspended in hexanes. The suspension was filtered and the dark solid washed with copious amounts of hexanes and pentane until the wash became colorless (ca. 75 mL total). The solid was then washed with 2 x 10 mL cold MeOH and the final wash with 2 x 10 mL 1:1 Et₂O/pentane. The brown solid was dried and either used immediately to make **8** or for characterization. Yield: 62.3 mg, 62%. Data for **7** are as follows. ESI-MS (m/z , based on ¹⁰¹Ru): [M]²⁺ = 917.6. UV-Vis (in THF) λ / nm (ϵ / M⁻¹ cm⁻¹): 461 (9200), (sh)567 (4900), 761 (5900). μ_{eff} (22°C) (Evans method) = 5.82 μ_B . Electrochemistry (THF, vs Fc^{+/0}), $E_{1/2}$ / V, ΔE_p / mV, $i_{\text{backward}}/i_{\text{forward}}$: -0.131, 79, 0.49; -0.010, 79, 0.72; -1.337, 115, 0.67; -1.566, 136, 0.87.

[(NC)Ru₂(ap)₄]₂(μ -1,4-C₆H₄) (8). A stock solution of **7** was made from 29.8 mg in 90 mL THF (2.42 x 10⁻⁴ M **7**). To 30.0 mL of the stock solution, [Bu₄N][CN] (15 mg, 0.06 mmol) in 5.0 mL THF was added. An immediate color change from dark brown-green to deep red was observed. O₂ was bubbled through this solution for 2 hours, resulting in a color change from red to a red-purple. The solvent was removed, and the product extracted from CH₂Cl₂/H₂O. The organic layers were combined and dried with Na₂SO₄. Removal of solvent gave a deep purple solid, and

purification was achieved through a 1:20 (v:v) CH₂Cl₂/hexanes recrystallization at room temperature. Single crystals suitable for X-ray diffraction were grown by layering diethyl ether over a concentrated solution of **8** in THF. Yield: 7 mg, 59%. Elem. Anal. Found (Calcd) for C_{101.5}H₈₇N₁₈Cl₃O₁Ru₄ (**8**·1.5CH₂Cl₂·THF): C, 58.46 (58.15); H, 4.20 (4.29); N, 12.09 (11.88). ESI-MS (m/z , based on ¹⁰¹Ru): [M – 2 CN]²⁺ = 917.0. UV-Vis (in THF) λ / nm (ϵ / M⁻¹ cm⁻¹): 346 (29400), 552 (8800), (sh)599 (7800), 756 (4700), 1025 (5500). IR $\bar{\nu}$ / cm⁻¹: 2099 $\bar{\nu}$ (C≡N). μ_{eff} (21°C) (Evans method) = 2.18 μ_B . Electrochemistry (THF, vs Fc^{+/0}), $E_{1/2}$ / V, ΔE_p / mV, $i_{\text{backward}}/i_{\text{forward}}$: 0.299, 92, 0.63; 0.008, 66, 0.83; -0.913, 62, 0.94; -1.09, 62, 0.61. ¹H NMR (300 MHz, CDCl₃) δ = 8.20 (d, J = 6.4 Hz, 8H, H(a)), 7.22 – 6.99 (m, 32H, H(b,c,f,h)), 6.40 (d, J = 9.0 Hz, 8H, H(d)), 6.24 (t, J = 6.3 Hz, 12H, H(g,j)), 6.12 (s, 8H, H(i)), 5.62 (s, 8H, H(e)). Isosbestic points for **8** → [**8**]⁺: ca. 15000 cm⁻¹ and ca. 23000 cm⁻¹; isosbestic points for [**8**]⁺ → [**8**]²⁺: 7500 cm⁻¹ and ca. 23000 cm⁻¹.

(NC)Ru₂(ap)₄(C₆H₅) (**9**). Ru₂(ap)₄(C₆H₅) (48.9 mg (0.05 mmol)) was dissolved in 20 mL THF, to which 23 mg KCN in 6 mL THF/MeOH (1:1 v/v) was added. An immediate color change from dark green to red was observed. Upon bubbling O₂ for ~10 minutes, the solution darkened to a deep purple. After removing the solvent, the product was extracted with three CH₂Cl₂/H₂O washes and the organic layer dried with Na₂SO₄. Removal of the solvent gave a deep purple solid, and purification achieved with a room temperature 1:20 CH₂Cl₂/hexanes (v/v) recrystallization. Single crystals suitable for X-ray diffraction were grown by layering pentane over a concentrated solution of **9** in ethyl acetate. Yield: 44 mg, 88%. Elem. Anal. Found (Calcd) for C₅₂H₄₄N₉Cl₂ORu₂ (**9**·CH₂Cl₂·H₂O): C, 57.57 (57.62); H, 3.99 (4.09); N, 11.25 (11.63). ESI-MS (m/z , based on ¹⁰¹Ru): [M]⁺ = 982.3. UV-Vis (in THF) λ / nm (ϵ / M⁻¹ cm⁻¹): 341 (17500), 553 (6900), (sh)597 (6100), (sh)611 (4200), 958 (4700), (sh)1166 (2600). IR $\bar{\nu}$ / cm⁻¹: 2089 $\bar{\nu}$ (C≡N). μ_{eff} (21°C) (Evans method) = 2.26 μ_B . Electrochemistry (THF, vs Fc^{+/0}), $E_{1/2}$ / V, ΔE_p / mV, $i_{\text{backward}}/i_{\text{forward}}$: 0.21, 82, 0.99; -0.916, 82, 0.95. ¹H NMR (300 MHz, CDCl₃) δ = 7.97 (d, J = 1.7 Hz, 4H, H(a)), 7.19 – 6.98 (m, 18H, H(b,c,f,h,k)), 6.92 (t, J = 7.0 Hz, 1H, H(m)), 6.63 (d, J = 7.8 Hz, 2H, H(j)), 6.40 (d, J = 8.8 Hz, 4H, H(d)), 6.20 (t, J = 6.5 Hz, 4H, H(g)), 6.09 (s, 4H, H(i)), 5.58 (s, 4H, H(e)). Isosbestic points for **9** → [**9**]⁺: ca. 15000 cm⁻¹.

2.5.2 X-ray Crystallographic Details

Crystals suitable for X-ray diffraction analysis were grown by either layering diethyl ether over a concentrated solution of **8** in THF or layering pentane over a concentrated solution of **9** in ethyl acetate. Single crystals of **8** were coated with paraffin oil and quickly transferred to the goniometer head of a Bruker Quest diffractometer with kappa geometry, an I- μ -S microsource X-ray tube, laterally graded multilayer (Goebel) mirror single crystal for monochromatization, a Photon-III C14 area detector and an Oxford Cryosystems low temperature device. Examination and data collection were performed with Cu K α radiation ($\lambda = 1.54178 \text{ \AA}$) at 150 K. Single crystals of **9** were coated with paraffin oil and quickly transferred to the goniometer head of a Bruker Quest diffractometer with a fixed chi angle, a sealed tube fine focus X-ray tube, single crystal curved graphite incident beam monochromator, a Photon II area detector, and an Oxford Cryosystems low temperature device. Examination and data collection were performed with Mo K α radiation ($\lambda = 0.71073 \text{ \AA}$) at 150 K. In one of the structures (**8**), only part of the solvent molecules were sufficiently resolved to model, and were included as partially occupied. Based on the XRD data it was not possible to determine whether the remaining volume remained unoccupied, or if additional highly disordered solvate molecules are present. A complete removal of the partially occupied solvent molecules via the Squeeze procedure did not substantially improve the overall quality of the structure, and we thus decided to include the resolved fraction of the void content as partially occupied solvate molecules.

Data were collected, reflections were indexed and processed, and the files scaled and corrected for absorption using APEX3⁸¹ and SADABS.⁸² The space groups were assigned using XPREP within the SHELXTL suite of programs^{52,53} and solved by direct methods using ShelXS⁵³ or dual methods using ShelXT⁵⁴ and refined by full matrix least squares against F^2 with all reflections using Shelxl2018^{56,83} using the graphical interface Shelxle.⁵⁷ Complete crystallographic data, in CIF format, have been deposited with the Cambridge Crystallographic Data Centre. CCDC 2149734-2149735 contains the supplementary crystallographic data for this paper. These data can be obtained free of charge from The Cambridge Crystallographic Data Centre via www.ccdc.cam.ac.uk/data_request/cif

2.5.3 Computational Details

Ground state DFT calculations were performed using Gaussian 16 version A.03.⁸⁴ The B97D3^{85,86} and B3LYP^{87–90} functionals were found suitable for geometry optimizations, single point energy calculations and frequency analyses. While B97D3 accurately reproduced the crystal structure metrical parameters and vibrational frequencies, B3LYP was found to be better for energies. The xyz coordinates for the initial geometries were obtained from the respective crystal structures of the compounds. Minima at the optimized geometries were confirmed through vibrational frequency analyses. For **9**, The def2tzvp basis set was employed for Ru (with ECP), N, C_{phenylene} and C_{CN} atoms and the def2svp for all others.^{91,92} For **8**, de2tzvp was employed for Ru (with ECP) and N and def2svp for all other atoms. Grimme's D3 dispersion correction was used with the B3LYP functional. In both cases, geometry optimizations were carried out for both the $S = 0$ and $S = 1$ states. Wavefunction stability analysis was carried out for the closed-shell and open shell singlet calculations, by mixing the HOMO and LUMO orbitals, and using the stable=opt keyword as implemented in Gaussian16 rev A.03. A broken symmetry singlet was not encountered. For **9**, both B97D3 and B3LYP predict the singlet to be lower in energy than the triplet by 4.9 kcal/mol and 2.0 kcal/mol respectively. For **8**, the singlet was found to be more stable by 2.5 kcal/mol and 0.87 kcal/mol using the B97D3 and B3LYP functional, respectively. These low energy barriers are scaled easily at room temperature, which could be the reason for non-zero magnetic moments. DFT methods are known to carry intrinsic errors for energies, so we acknowledge that for these molecules whose energy differences appear to be $< 3 - 5$ kcal/mol, the ground state may have multireference character. However, such calculations are outside the scope of this communication. Looking forward, variable temperature NMR can be utilized to experimentally determine this value, providing a reference point for future studies.

For the oxidized species **[8]⁺**, we hypothesize that it may not matter whether we start from a singlet or triplet state of **8**, for we end up with a doublet for **[8]⁺** in either case. DFT calculations carried out (see below) with a spin of $S = \frac{1}{2}$ for **[8]⁺** agree well with spectroelectrochemical observations. For **[8]⁺**, the optimized geometry of **8_{S=0}** was taken as the input geometry, and a geometry optimization and frequency analysis was carried out at the B97D3 level in the doublet state. TDDFT^{93–97} calculations were done using the B3LYP functional, CPCM solvation model⁹⁸ (THF) and Grimme's D3 dispersion correction. 50 excited states were calculated, but an intense low-energy transition was observed as the 5th excited state. So, 'functional screening' was done

with 7 excited states in the interest of saving computational cost and time. Other functionals like CAM-B3LYP,⁹⁹ M06,¹⁰⁰ and M06L¹⁰¹ gave comparable or much worse accuracy compared to B3LYP. Natural transition orbital analysis was done using the method of Martin.¹⁰²

CHAPTER 3. BIS-ARYL AND BIS-ALKYNYL DIRUTHENIUM (III,III) COMPOUNDS BASED ON AN ELECTRON-DEFICIENT BUILDING BLOCK

Reproduced (adapted) with permission from L. A. Miller-Clark, P. E. Christ, B. T. Barbarini, and T. Ren, *Inorg. Chem.*, 2022, **61**, 14871–14879. Copyright 2022, American Chemical Society. DOI: 10.1021/acs.inorgchem.2c02498

3.1 Abstract

Reported herein are a new series of diruthenium(III,III) bis-alkynyl and bis-aryl diruthenium(III,III) compounds supported with 2-amino-3-(trifluoromethyl)pyridinate (amtfmp). Using $\text{Ru}_2(\text{amtfmp})_4\text{Cl}_2$ from a modified preparation, *cis* (2:2) $\text{Ru}_2(\text{amtfmp})_4(\text{C}\equiv\text{CPh})_2$ (**10**), *cis* (2:2) $\text{Ru}_2(\text{amtfmp})_4(\text{Ph})_2$ (**11**) and (3:1) $\text{Ru}_2(\text{amtfmp})_4(\text{Ph})_2$ (**12**) were synthesized via a lithium-halogen exchange reaction using LiC_2Ph and LiPh , respectively. Compounds **10–12** are all $\text{Ru}_2(\text{III,III})$ species with a ground state configuration of $\pi^4\delta^2(\pi^*)^4$ ($S = 0$), and were characterized via mass spectrometry, electron absorption and ^1H / ^{19}F NMR spectroscopies, and voltammetry. The molecular structures of **10–12** were established using single-crystal X-ray diffraction analysis and preliminary DFT analysis was performed to elaborate the electronic structures of **10** and **11**. Comparisons of the electrochemical properties of **10–12** against the $\text{Ru}_2(\text{amtfmp})_4\text{Cl}_2$ starting material reveals cathodic shifts of the $\text{Ru}_2^{7+/6+}$ oxidation and the $\text{Ru}_2^{6+/5+}$ and $\text{Ru}_2^{5+/4+}$ reduction potentials. In comparison to related $\text{Ru}_2(\text{III,III})$ bis-alkynyl and bis-aryl compounds, the electrode potentials for **10–12** are anodically shifted up to *ca.* 0.95 V, highlighting the strong electron-withdrawing nature of the amtfmp ligand.

3.2 Introduction

Since the discovery of diruthenium(II,III) tetracarboxylates by Wilkinson and coworkers,¹ the chemistry of diruthenium paddlewheel compounds of the form $[\text{Ru}_2(\text{L})_4\text{X}_n]$ (L = bridging ligands, X = axial ligands; $n = 0, 1, 2$) has flourished.^{4,103} A common characteristic of diruthenium compounds is the rich redox properties and a large range of accessible oxidation states from $\text{Ru}_2(\text{I,II})$ to $\text{Ru}_2(\text{III,IV})$, which has recently been detailed in a review by Kadish and co-workers.⁵ Diruthenium(II,III) species are often of a $S = 3/2$ ground state, and these compounds have been

used as the building blocks for magnetic materials with pioneering contributions from the laboratories of Handa,^{6,104} Miller,^{8,105} Dunbar,¹⁰⁶ and Jiménez-Aparicio.^{107,108} Aerobic and peroxy oxidation catalysis by diruthenium species is another interesting development in recent years.^{10,11,15,109}

Many examples of Ru₂ organometallic compounds have been disclosed since the seminal report of Ru₂(*ap*)₄(C₂Ph) (*ap* = 2-anilinopyridinate) by Cotton and Chakravarty¹⁶ and subsequent studies by Bear and Kadish.^{17,18} Ru₂(*ap*)₄-based compounds are highly robust both under ambient conditions and over a broad electrochemical window, and spectroelectrochemistry studies of the Ru₂(*ap*)-bridge-Ru₂(*ap*) type compounds have provided clear evidence for facile charge delocalization across oligoynyl (bridge = C_{2n})^{22,24,25,110} and aryl (bridge = C₆H₄) bridges.¹¹¹ The chemical robustness of Ru₂(*ap*)₄ based compounds also allows for iterative on-complex *Cadiot-Chodkiewicz* coupling, yielding extended oligo-yne compounds Ru₂(*ap*)₄(C_{2k}SiR₃) with *k* up to 5.¹¹² The ability to mediate charge transfer has been exploited in the construct of prototypical molecular wires²⁶ and devices.^{27,28,113} Recent work by the laboratory of Akita further illustrates the unique conductivity characteristics afforded by the tunable valence orbital distribution of Ru₂ alkynyls near the Fermi level of nano-junction.³⁴ In addition to Ru₂(*ap*)₄ based organometallics, assemblies based on Ru₂(*ap*)₄(CN) have been utilized for studying spin-coupling and metal-metal charge transfer transitions by the laboratory of Sheng in recent years.^{70,114,115} Kadish and Van Caemelbecke investigated the formation of water soluble Ru₂(OAc)₃(L)Cl with L as a variety of fluorinated *ap* ligands.¹¹⁶

In addition to *ap* and its fluorinated analogues, two other types of bridging ligands, DArF (DArF = *N,N'*-diarylformamidinate, Figure 3.1) and DMBA (DMBA = *N,N'*-dimethylbenzamidinate), have been frequently employed to support Ru₂(III,III) organometallic compounds.^{18,117–120} While bis-alkynyls Ru₂(III,III) are attainable with all three types of ligands, the steric requirements enforced by the bridging ligands' flanking phenyls^{35,121} has resulted in bis-aryls Ru₂(III,III) only being achieved with DMBA thus far.³⁶ Hence, the arrangement of dissymmetric *N,N'*-bidentate ligands around the Ru₂ core, Figure 3.1, is significant in dictating the number of aryl ligands at the axial positions.

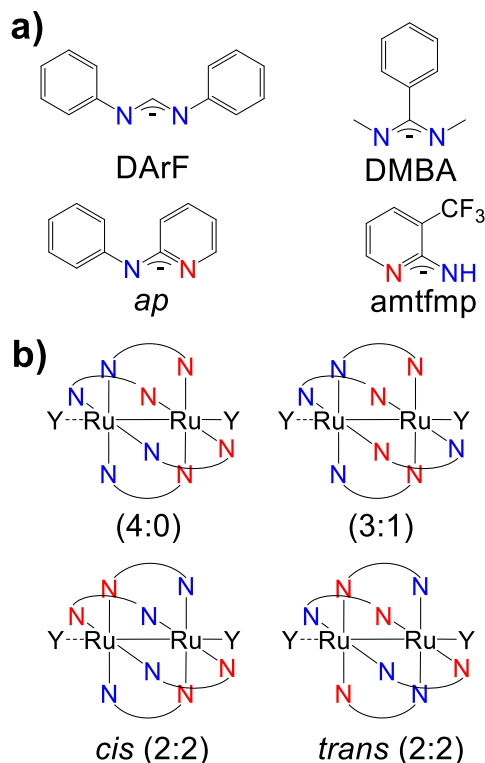


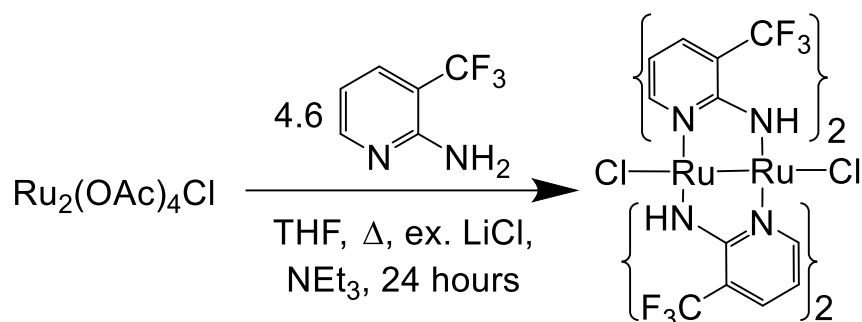
Figure 3.1. a) symmetric and asymmetric N,N' bridging ligands and b) possible configurations of Ru_2 compounds ($Y = -Cl, -C\equiv C$ and $-Ar$)

In recent years, Kataoka *et al.* have developed several $Ru_2(III,III)$ dichloro compounds based on less bulky bridging ligands including benzamidine,¹²² 2-aminopyridinate (amp) and 2-amino-4-methylpyridinate,¹²³ and 2-amino-3-(trifluoromethyl)pyridinate (amtfmp).¹²⁴ All $Ru_2(III,III)$ dichloro compounds based on 2-aminopyridinate type ligands adopted a *cis* (2:2) arrangement, despite the multiple possible configurations shown in Figure 3.1.^{123,124} Among the many interesting attributes reported for $Ru_2(amtfmp)_4Cl_2$ are its drastic electrochromism in the NIR window and a high degree of electron deficiency evidenced by a very anodic $Ru_2^{+6/+5}$ couple (0.36 V *vs* SCE).¹²⁴ Intrigued by the impact of organometallic derivatization on such an electron poor Ru_2 building block, we have explored both the alkynylation and arylation at the axial positions of $Ru_2(amtfmp)_4Cl_2$, and the details of synthesis and structural and voltammetric characterizations are reported here.

3.3 Results and Discussion

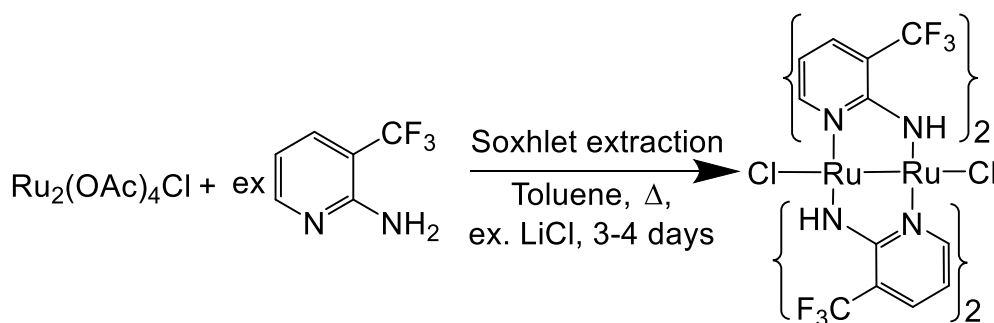
3.3.1 Synthesis

In the original report by Kataoka, $\text{Ru}_2(\text{amtfmp})_4\text{Cl}_2$ was prepared from refluxing $\text{Ru}_2(\text{OAc})_4\text{Cl}$ with Hamtfmp in THF / Et_3N , in a yield of 54% shown in Scheme 3.1 below.¹²⁴



Scheme 3.1. Synthesis of $\text{Ru}_2(\text{amtfmp})_4\text{Cl}_2$ following literature procedures¹²⁴

Aiming to increase the yield, we prepared $\text{Ru}_2(\text{amtfmp})_4\text{Cl}_2$ using a protocol developed for $\text{Ru}_2(\text{ap})_4\text{Cl}$, akin to Scheme 1.2 in section 1.3.1 above and as outlined in Scheme 3.2 below: refluxing $\text{Ru}_2(\text{OAc})_4\text{Cl}$ with 8 equiv. of Hamtfmp and LiCl in excess, while the condenser was outfit with a micro Soxhlet extractor containing K_2CO_3 to drive the reaction.^{75,125,126}



Scheme 3.2. Synthesis of $\text{Ru}_2(\text{amtfmp})_4\text{Cl}_2$ used in this work

$\text{Ru}_2(\text{amtfmp})_4\text{Cl}_2$ was obtained as a deep blue solid in a yield (55%) comparable to the original report¹²⁴ after purification. Thin-layer chromatography (TLC) with 1:2 THF/hexanes with 3% MeOH (v/v) revealed the presence of two isomers with very similar R_f values ($R_f = 0.30, 0.33$) in the purified material (Figure 3.2, 'Sox' column).

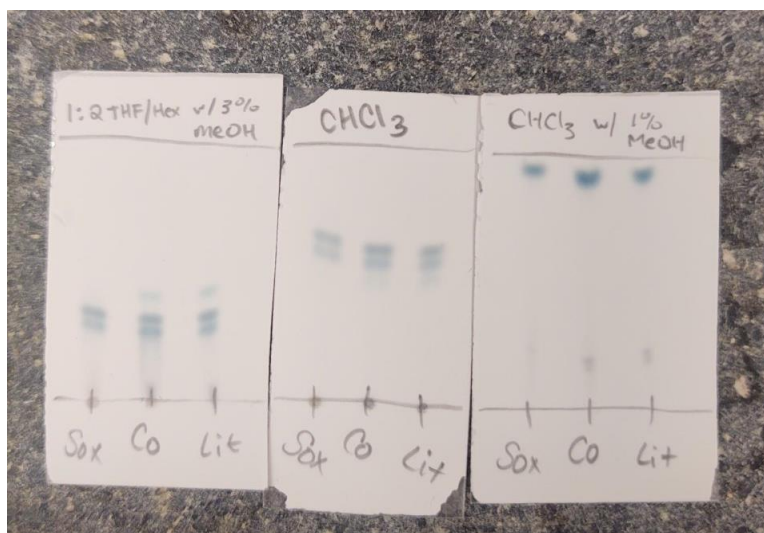
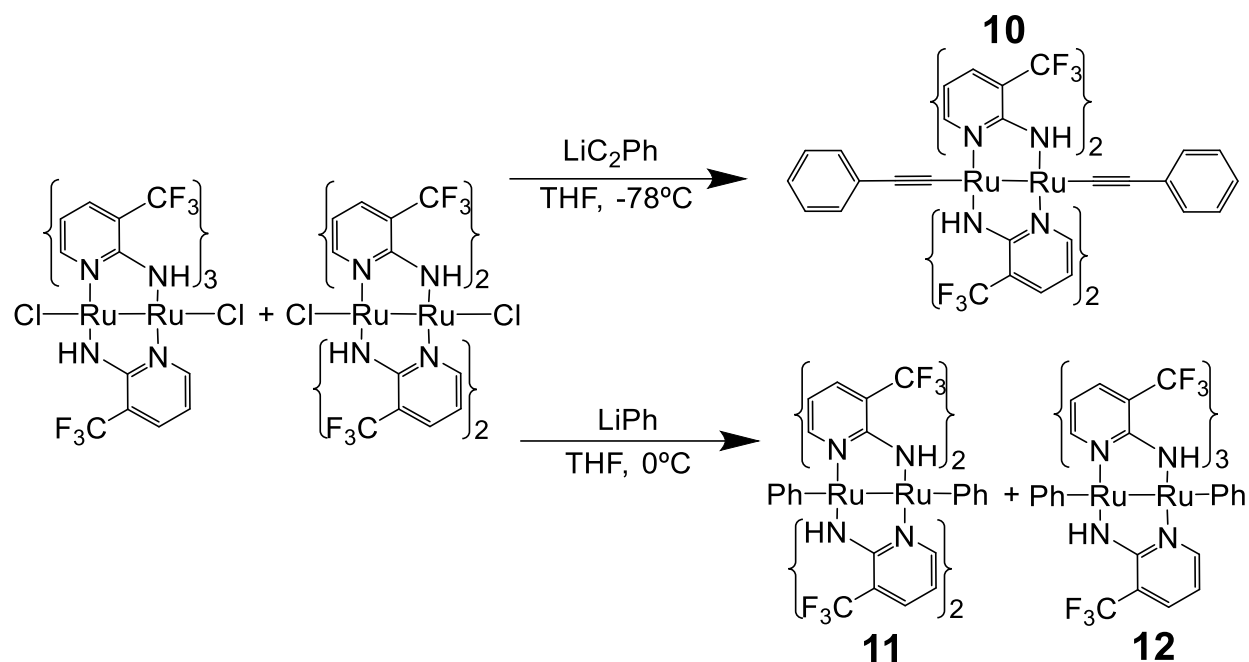


Figure 3.2. TLC plates of the Soxhlet product (left lane in all plates, abbreviated as ‘Sox’), a co-spot of the Soxhlet and literature products (center lane, abbreviated as ‘Co’), and the literature product (right lane in all plates, abbreviated as ‘Lit’)

It is likely that the higher reaction temperature achieved in refluxing toluene enabled the formation of the two different isomers instead of just the *cis* (2:2) isomer reported by Kataoka.^{123,124} Furthermore, $\text{Ru}_2(\text{amtfmp})_4\text{Cl}_2$ prepared using Kataoka protocol *in our laboratory* comprised two isomers as well (see Experimental Section 3.5.4, also Figure 3.2, ‘Lit’ column). Previously, Bear and Kadish’s molten syntheses ($>120^\circ\text{C}$) of $\text{Ru}_2(\text{F}_x\text{ap})_4\text{Cl}$ ($x = 2, 3$) produced a mixture of the (4,0) and (3,1) isomers regardless of reaction length.^{127,128} The lability of both fluorinated and unfluorinated anilinopyridinate ligands has also been observed upon reaction with CN^- , Cl^- or $\text{C}\equiv\text{CC}_5\text{H}_4\text{N}$.^{129,130} In the case of CN^- , the coordination mode could be controlled via reaction temperature, resulting in rearrangement of two F_5ap ligands to facilitate a CN^- ligand that is σ -bonded to one Ru atom and π -bonded to the other Ru over axial coordination.¹³⁰ While attempts to crystallize the (3:1) isomer of $\text{Ru}_2(\text{amtfmp})_4\text{Cl}_2$ have failed thus far, ^{19}F NMR confirmed the presence of a small amount of the (3:1) isomer in the purified material (Figure C.4 in Appendix C below).



Scheme 3.3. Synthetic approach to produce Ru₂(amtfmp)₄(Y)₂ (Y = C₂Ph, Ph) compounds **10–12**

As shown in Scheme 3.3, the bis-alkynyl Ru₂(amtfmp)₄(C≡CPh)₂ (**10**) and bis-aryl Ru₂(amtfmp)₄(Ph)₂ were prepared from the reaction of Ru₂(amtfmp)₄Cl₂ with excess LiC₂Ph or LiPh.^{118,121} The *cis* (2:2) Ru₂(amtfmp)₄(C≡CPh)₂ isomer (**10**) was isolated as a blue-green solid (36% based on Ru₂) and structurally identified (see below in section 3.3.2), while the corresponding (3:1) bis-alkynyl isomer was not isolated in spite of the presence of (3:1) isomer in the starting material. From the analogous LiPh reaction, a crude bis-aryl product was isolated in 33% yield (based on Ru₂) after a silica plug purification, which is a mixture of a deep red species (*R_f* = 0.73, 1:2 THF/hexanes w/ 3% MeOH (v/v)) and a purple species (*R_f* = 0.70, 1:2 THF/hexanes w/ 3% MeOH (v/v)). Careful silica column purification (1:2 THF/hexanes w/ 3% MeOH) yielded clean red fraction (**11**, 12%) and purple fraction (**12**, 7%), which were unambiguously identified respectively as the *cis* (2:2) and (3:1) isomers using crystallography (see below). The low (combined) yields of compounds **10–12** is likely attributed to the *in situ* reduction of Ru₂(amtfmp)₄Cl₂ by organo-lithium species. A large quantity of red baseline species is always present in all of the above-mentioned reactions (Figure C.13 in Appendix C), and its absorption spectrum (Figure 3.3) matches that reported for [Ru₂(amtfmp)₄Cl₂]⁻¹.¹²⁴ The red solid can be converted to the starting materials Ru₂(amtfmp)₄Cl₂ via re-oxidation upon exposure to air as a suspension in CH₂Cl₂ in *ca.* 40% yield.

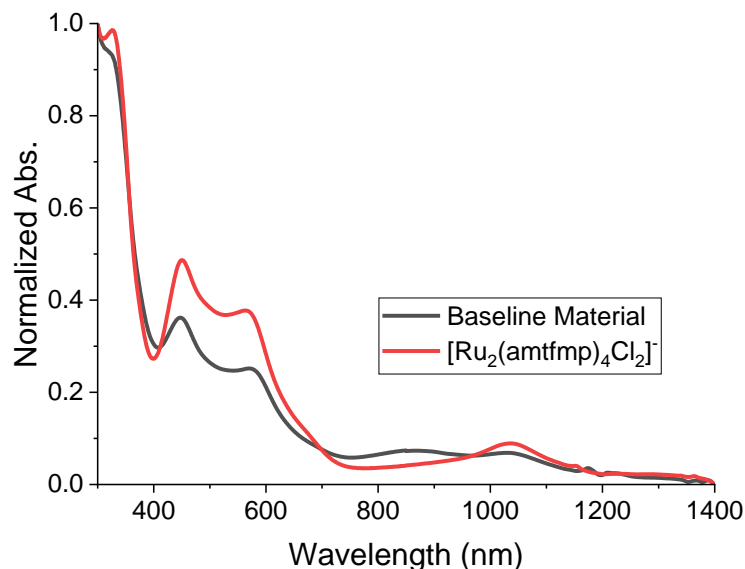


Figure 3.3. Normalized vis-NIR absorption spectra in MeOH of $[\text{Ru}_2(\text{amtftp})_4\text{Cl}_2]^-$ (red line) and the baseline material from arylations (black line)

A later test reaction with LiC_2TIPS was attempted to probe if the steric bulkiness of ligands could limit reactivity to only the *cis* (2:2) $\text{Ru}_2(\text{amtftp})_4\text{Cl}_2$. Following the reaction conditions outlined in Scheme 3.3 and as detailed in section 3.5.6 below, it was found that despite the use of a large, bulky alkynyl substituent, both isomers reacted as shown in the TLC plates in Figure C.14 in Appendix C below.

Upon isolation, compounds **10–12** are relatively stable both as solids and in solution in ambient conditions, with **10** degrading to intractable products within a week, and **11** and **12** stable for over a month. Like the related $\text{Ru}_2(\text{III,III})$ bis-alkynyl / bis-aryl compounds based on $\text{Ru}_2(\text{DMBA})_4$,^{118,121} compounds **10–12** are diamagnetic, enabling characterization via ^1H and ^{19}F NMR spectroscopy. With an effective C_{2h} symmetry, the four amtftp ligands in both **10** and **11** are equivalent and hence there is only one fluorine peak (Figures C.5 and C.6). The (3:1) arrangement of amtftp in **12** resulted in three fluorine peaks, one double the intensity of the other two (Figure C.7), confirming that one set of *trans* amtftp ligands experience similar environments while the other set of *trans* ligands are in different environments. Further characterization was achieved using electrospray mass spectroscopy (ESI-MS), vis-NIR and FT-IR (in the case of **10**, Figure 3.4) spectroscopies, cyclic (CV) and differential pulse voltammetry (DPV), single-crystal X-ray diffraction studies and combustion analysis.

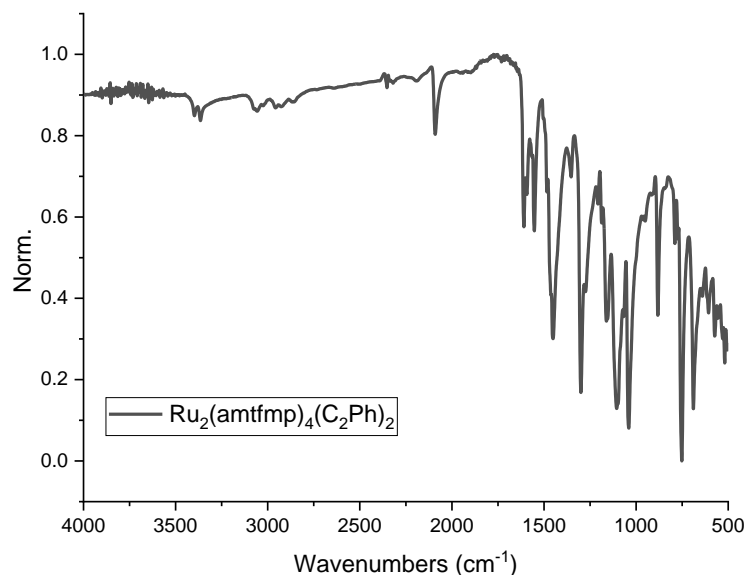


Figure 3.4. FTIR spectra of **10**

3.3.2 Molecular Structures

Molecular structures of compounds **10**, **11** and **12** have been determined using single-crystal X-ray diffraction, as shown in Figures 3.5–3.7, respectively, and selected bond lengths are given in Table 3.1. In **10** and **11**, the bridging amtftp ligands adopt a *cis* (2:2) arrangement around the Ru₂ unit and both structures contain a crystallographic inversion center in the midpoint of the Ru–Ru bond. Compound **12** contains three bridging amtftp ligands in the same orientation with the fourth ligand opposite, resulting in a *C*₁ symmetry. The Ru–Ru bond lengths for **10** (2.4656(4) Å), **11** (2.5144[4] Å) and **12** (2.5035(4) Å) are all significantly lengthened when compared to Ru₂(amtftp)₄Cl₂ (2.330[2] Å),¹²⁴ highlighting the weakening of the σ(Ru–Ru) bond by the strong electron-donation from the alkynyl and aryl ligands. The Ru–Ru bond length for **10** is a close match to Ru₂(DMBA)₄(C≡CR)₂ (avg. 2.45 Å),^{118,131} but the Ru–Ru bond lengths are slightly lengthened for **11** and **12** when compared to other Ru₂(III,III) σ-aryl compounds (Ru₂(DMBA)₄(Ar)₂: avg. 2.4989 Å).³⁶

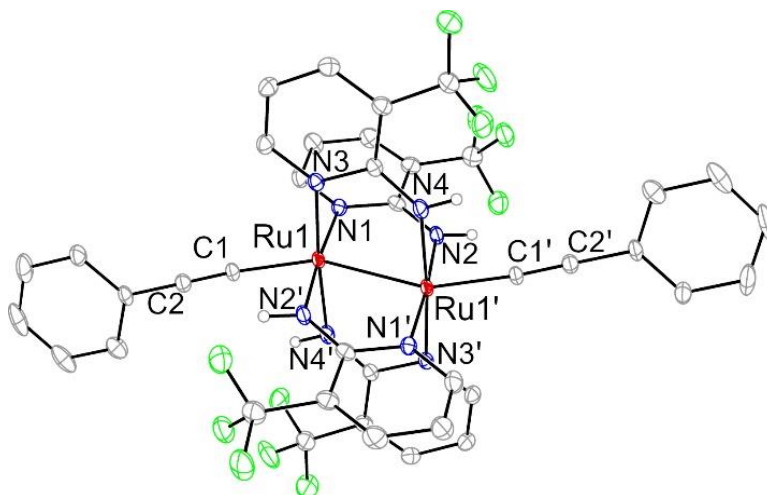


Figure 3.5. ORTEP plot of **10** at 30% probability level. Most H atoms omitted for clarity

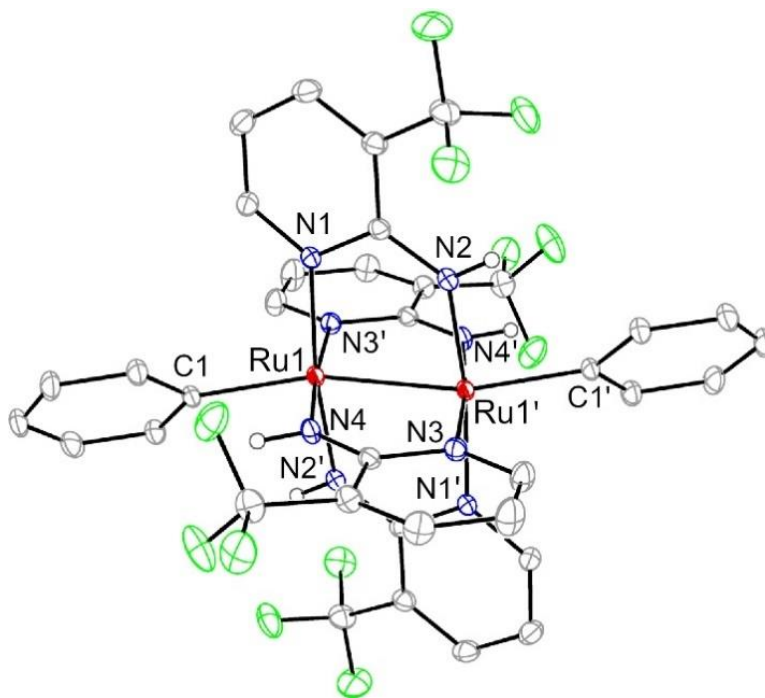


Figure 3.6. ORTEP plot of **11** at 30% probability level. Most H atoms omitted for clarity

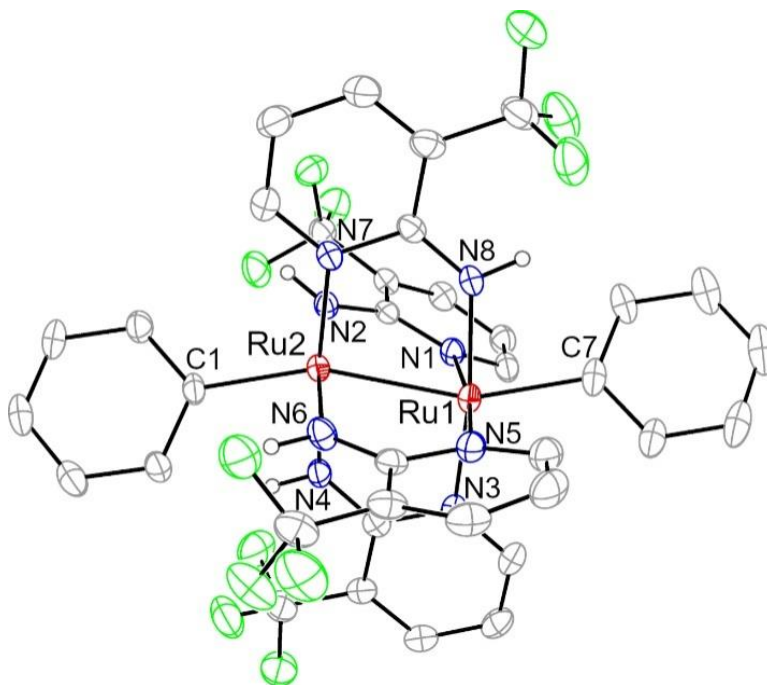


Figure 3.7. ORTEP plot of **12** at 30% probability level. Most H atoms omitted for clarity

The averaged Ru–C bond lengths for **11** (2.047[3] Å) and **12** (2.055[5] Å) are significantly longer than that of **10** (1.979(3) Å), matching the trend from previous comparisons between either aryl Ru₂(II,III)³⁵ or bis-aryl Ru₂(III,III)³⁶ compounds and their alkynyl or bis-alkynyl counterparts. Again, the Ru–C bond length of **10** is a good match when compared to Ru₂(DMBA)₄(C≡CR)₂ compounds (avg. 1.97 Å)^{118,131} while **11** and **12** are slightly shortened when compared to Ru₂(DMBA)₄(Ar)₂ compounds (avg. 2.071 Å),³⁶ complimenting the increased Ru–Ru bond lengths discussed above. This suggests a more robust engagement of the Ru d_z² orbitals by the stronger σ donating Ar[−] ligands, forming slightly stronger Ru–C σ bonds.³⁶

Compounds **10–12** exhibit significant distortions from an idealized paddlewheel geometry as highlighted by the large deviation of Ru–Ru–C from linearity (avg. 158°, Table 3.1). This whole molecule distortion observed in compounds **10–12** is attributed to a second-order Jahn-Teller (SOJT) effect. Thorough documentation and analysis of this effect has been described elsewhere for related Ru₂(III,III)L₄X₂ type compounds,²⁰ including the Ru₂(DMBA)₄(C≡CR)₂^{118,131,132} and Ru₂(DMBA)₄(Ar)₂ compounds.³⁶ Of note is the analogous Ru₂(III,III) σ-alkynyl compounds, such as Ru₂(DMBA)₄(C≡CR)₂^{118,132} (Ru–Ru–C ranges between 161–175°), do not present as significant distortions as observed in **10**. The partially repressed SOJT effect in Ru₂(DMBA)₄(C≡CR)₂ has been attributed to steric repulsion between the alkynyl substituents and the *N*-Me groups,²⁰ a

repulsion not achievable with the amino protons in amtfmp. The related Ru₂(DMBA)₄(Ar)₂ complexes, however, also present significant structural distortions (Ru–Ru–C: avg. 152°).³⁶ The relatively narrow range of Ru–Ru–C angle among **10–12** is plausibility related to the electronic structure instead of sterics: the angle is optimized to rotate the Ru *dπ* orbitals in the formally π^* (Ru–Ru) (HOMO-2, see DFT discussion in section 3.3.5 below) for a strong σ -bonding interaction.³⁶

Table 3.1. Selected bond lengths (Å) and angles (deg) for **10–12**

	10	11	12
Ru1–Ru2	2.4656(4)	2.5144[4]	2.5036(4)
Ru–C	1.979(3)	2.047[3]	2.040(4) / 2.070(4)
C1–C2	1.203(4)	----	----
Ru1'–Ru1–C1	157.23(8)	158.60[8]	159.3[1]
Ru1–N1	2.026(2)	2.032(2)	2.148(5)
Ru1–N3	2.058(2)	2.060(2)	2.072(4)
Ru1–N4	----	2.008(2)	----
Ru1–N5	----	----	2.071(4)
Ru1–N8	----	----	2.035(5)
Ru2(Ru1')–N2	2.051(3)	2.063(2)	1.981(6)
Ru2(Ru1')–N4	2.021(2)	----	2.046(3)
Ru2(Ru1')–N5	----	2.041(2)	----
Ru2(Ru1')–N6	----	2.045(2)	2.040(3)
Ru2(Ru1')–N7	----	2.062(2)	2.069(5)
Ru2(Ru1')–N8	----	2.012(2)	----

3.3.3 Electronic Absorption Spectra

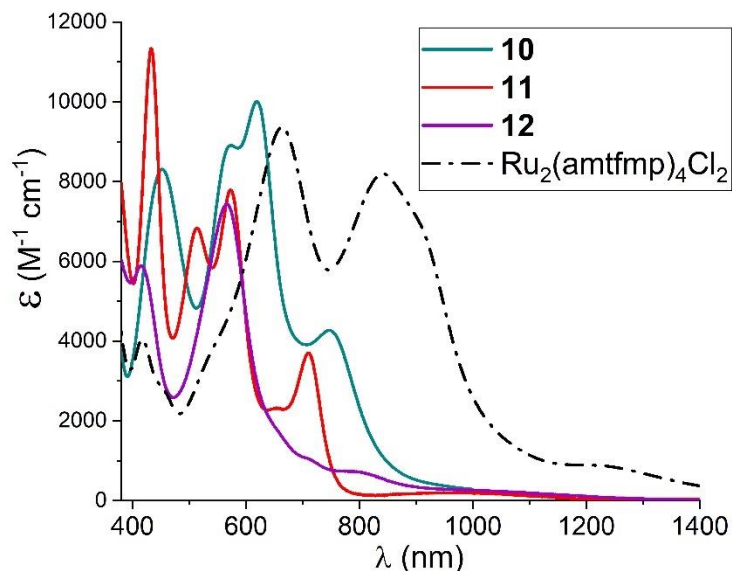


Figure 3.8. Vis-NIR absorption spectra of **10–12** and $\text{Ru}_2(\text{amtftp})_4\text{Cl}_2$ in THF

The Vis-NIR absorption spectra of compounds **10–12** and $\text{Ru}_2(\text{amtftp})_4\text{Cl}_2$ recorded in THF are shown in Figure 3.8. $\text{Ru}_2(\text{amtftp})_4\text{Cl}_2$ is deeply colored and its absorption spectrum is dominated by intense metal charge transfer transition (LMCT,¹²⁴ see DFT discussion below) bands at 660 and 845 nm. Upon alkynylation, the LMCT bands of **10** were blue shifted from that of $\text{Ru}_2(\text{amtftp})_4\text{Cl}_2$ and split into four bands. Arylation of diruthenium further blue shifts the LMCT bands in **11** and **12**, and a satellite band appears next to the lowest energy LMCT band in **11** (656 nm) as well. In the case of **12**, only two intense visible transitions are observed (415 and 566 nm), aligning reasonably with two of the transitions in **11** (433 and 573 nm). Less intense transitions ($\leq 1000 \text{ M}^{-1}\text{cm}^{-1}$) at lower energies (710 and 800 nm) in **12** can also be observed, presumably of reduced intensities due to the lower symmetry of **12** compared to **11**. Compounds **11** and **12** also exhibit a weak and broad band between 800 – 1100 nm, while such a band is not obvious in **10**, likely obscured by the LMCT band. The low intensity ($< 300 \text{ M}^{-1}\text{cm}^{-1}$) suggests that the transition is primarily localized on the Ru_2 core, similar to the case of $\text{Ru}_2(\text{DMBA})_4(\text{Ar})_2$.³⁶

3.3.4 Electrochemical Studies

The redox properties of **10–12** were examined using cyclic (CV) and differential pulse voltammetry (DPV). An isomeric mix of $\text{Ru}_2(\text{amtfmp})_4\text{Cl}_2$ and pure *cis* (2:2) $\text{Ru}_2(\text{amtfmp})_4\text{Cl}_2$ are plotted in Figure 3.9, while the voltammograms of **10–12** are displayed in Figure 3.10. The respective redox potentials for **10–12** are listed in Table 3.2.

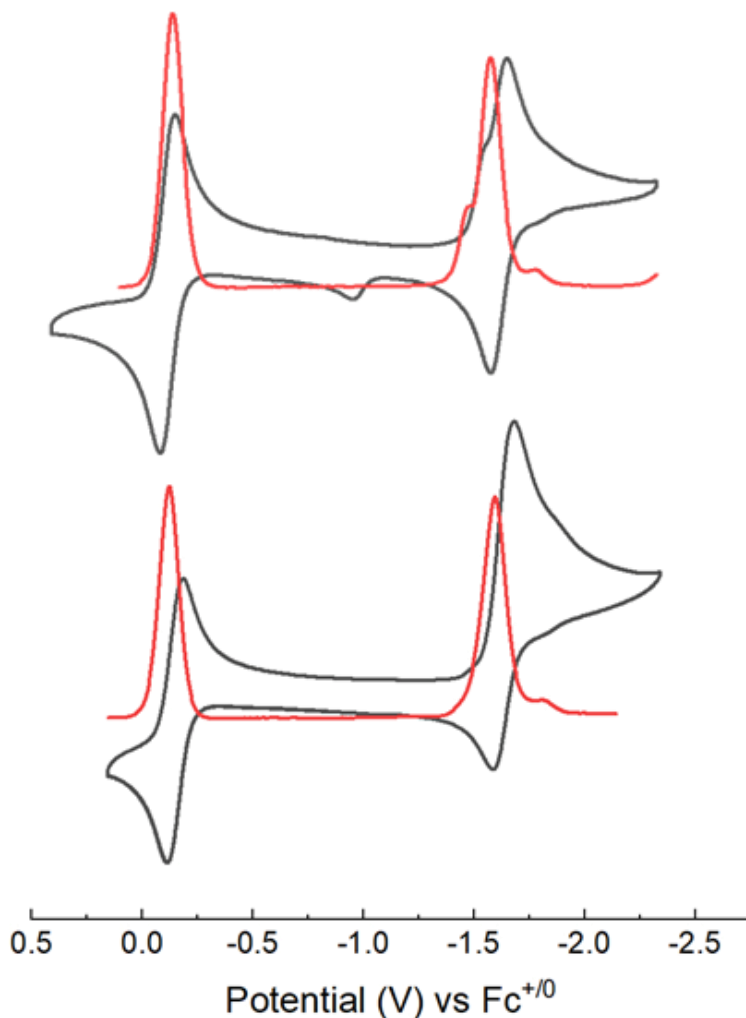


Figure 3.9. Cyclic (black) and differential pulse (red) voltammograms of a mixture of *cis* (2:2) and (3:1) $\text{Ru}_2(\text{amtfmp})_4\text{Cl}_2$ (top) and *cis* (2:2) $\text{Ru}_2(\text{amtfmp})_4\text{Cl}_2$ (bottom) (1.0 mM) recorded in 0.10 M THF solutions of $[\text{Bu}_4\text{N}][\text{PF}_6]$ at a scan rate of 0.1 V/s

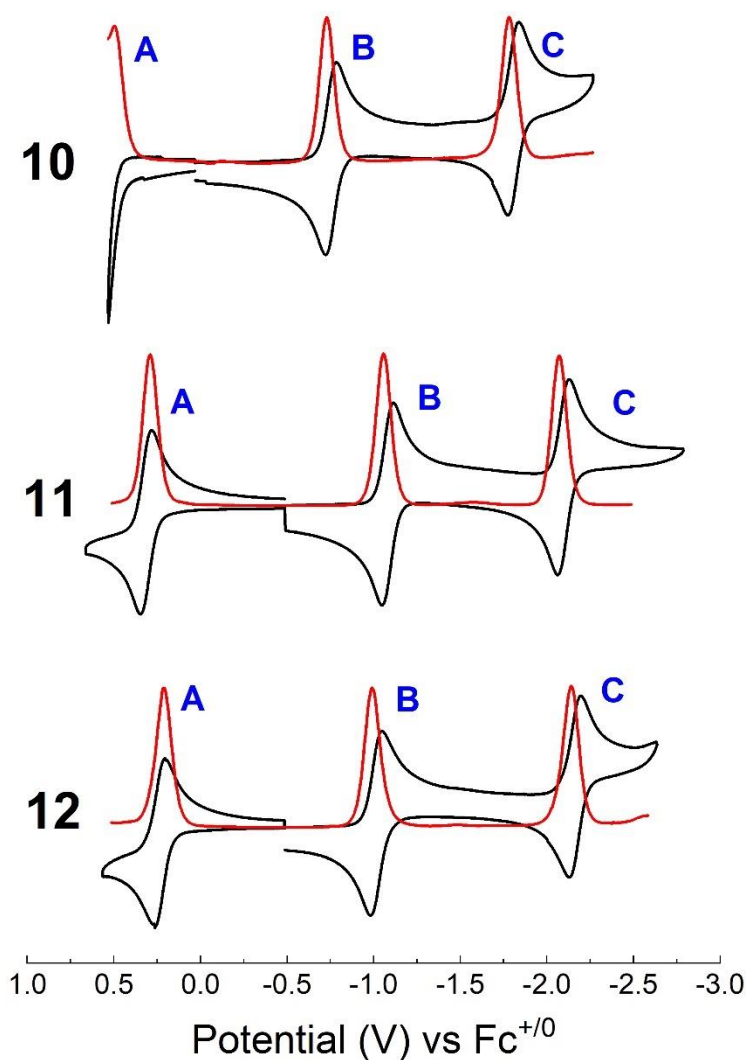


Figure 3.10. Cyclic (black) and differential pulse (red) voltammograms of compounds **10–12** (1.0 mM) recorded in 0.10 M THF solutions of [Bu₄N][PF₆] at a scan rate of 0.10 V/s

All compounds exhibit two reversible reductions, **B** (Ru₂^{6+/5+}) at -0.75 (**10**), -1.08 (**11**) and -1.01 V (**12**) (*versus* Fc^{+/0}) respectively, and **C** (Ru₂^{5+/4+}) at -1.81 V (**10**), -2.10 (**11**) and -2.16 V (**12**). Compounds **11** and **12** both exhibit one reversible oxidation **A** (Ru₂^{7+/6+}) at 0.31 (**11**) and 0.24 V (**12**), however a peak potentially corresponding to an analogous, irreversible peak **A** is visible at ca. 0.60 V (at the edge of the potential window allowed in THF) in the DPV of **10** shown in Figure 3.11 below. The cathodically shifted oxidation and reduction potentials in **11** and **12** highlight the aryl ligand being a stronger electron-donor than both chloro and alkynyl ligands (see discussion above). Both reductions **B** and **C** for compounds **10–12** are cathodically shifted from

the dichloro starting material (Figure 3.9 and Table 3.3).¹²⁴ The couple **B** is shifted by ca. -0.88 V for the bisaryl compounds **11** and **12**, but only shifted by -0.57 V for **10**. The couple **C** is only shifted by ca. -0.43 V for **10–12** when compared to $\text{Ru}_2(\text{amttmp})_4\text{Cl}_2$.

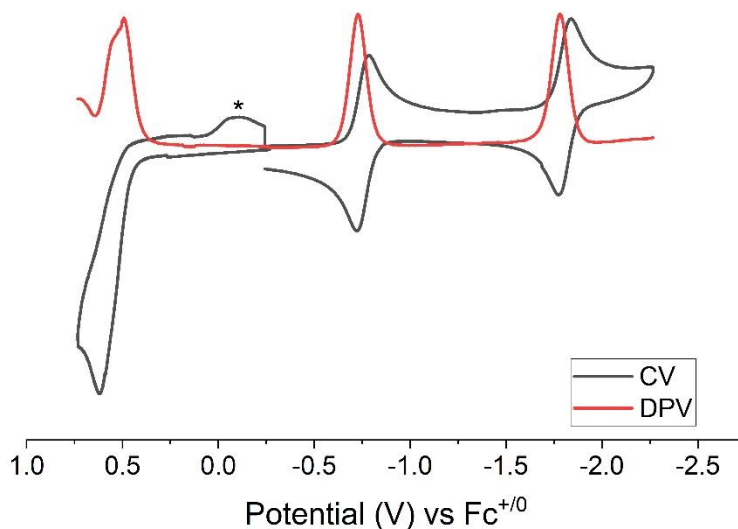


Figure 3.11. Cyclic (black) and differential pulse (red) voltammograms of **10** recorded in 0.10 M THF solutions of $[\text{Bu}_4\text{N}][\text{PF}_6]$ at a scan rate of 0.10 V/s. Possible degradation product peak denoted as * in the scan

Table 3.2. Electrode Potentials (in V vs $\text{Fc}^{+/0}$) for $\text{Ru}_2(\text{amttmp})_4(\text{Y})_2$ in THF

Y	A	B	C
$-\text{C}_2\text{Ph}$ (10)	0.62*	-0.75	-1.81
$-\text{Ph}$ (11)	0.31	-1.08	-2.10
$-\text{Ph}$ (12)	0.24	-1.01	-2.16
$-\text{Cl}$	----	-0.17	-1.59

The contrast in electrode potentials between **11** and **12** is different from that reported for (4,0), (3,1) and (2,2)-*trans* geometric isomers of $\text{Ru}_2(\text{F}_5\text{ap})_4\text{Cl}$ (F_5ap = pentafluoroanilinopyridinate). All geometric isomers of $\text{Ru}_2(\text{F}_5\text{ap})_4\text{Cl}$ exhibited reversible

$\text{Ru}_2^{5+/4+}$, $\text{Ru}_2^{6+/5+}$ and $\text{Ru}_2^{7+/6+}$ redox processes, all of which were sensitive to the type of regioisomer that was being studied. All processes cathodically shifted by at least 0.10 V when comparing the (4,0) processes to either the (3,1) or the (2,2)-*trans* isomers.¹²⁸ When comparing the redox events of **11** and **12**, a similar cathodic shift of at least 0.06 V is observed in the oxidation **A** ($\text{Ru}_2^{7+/6+}$) and the second reduction **C** ($\text{Ru}_2^{5+/4+}$). However, the first reduction **B** ($\text{Ru}_2^{6+/5+}$), which is proposed to occur on the LUMO of the two compounds, for **12** is anodically shifted by 0.07 V from that of **11**. Presumably the LUMO of the two compounds is comprised of differing δ^* / π^* orbitals, generated through the differing bond requirements of the isomers. This contrasts with previous studies on the (4,0) and (3,1) $\text{Ru}_2(\text{F}_x\text{ap})_4\text{Cl}$ ($x = 1-3$)¹²⁷ and $\text{Ru}_2(\text{F}_x\text{ap})_4(\text{C}_2\text{Ph})_2$ ($x = 1, 2, 5$)¹⁹ isomers: these demonstrated that the highest filled orbital (first oxidation event), either δ^* (-Cl) or π^* ((-C₂Ph)₂), is more sensitive to isomer type than the lowest unoccupied orbitals (first reduction event).

When the electrode potentials of **10** are compared to $\text{Ru}_2(\text{DMBA})_4(\text{C}_2\text{Ph})_2$,¹¹⁸ there is an approximate 0.85 V anodic shift of both reduction events **B** and **C** (Table 3.3), highlighting the strong electron-withdrawing nature of amtfmp. With respect to $\text{Ru}_2(\text{DMBA})_4(\text{Ph})_2$, compounds **11** and **12** also exhibit anodic shifts of events **A** and **B**: 0.74 V for **A** and 0.94 V for **B** (Table 3.3). The second reduction event is irreversible in $\text{Ru}_2(\text{DMBA})_4(\text{Ph})_2$ due to the dissociation of a Ph,³⁶ but is perfectly reversible in **11** and **12**, which indicates the remarkable stability of $[\text{Ru}_2(\text{amtfmp})_4(\text{Ph})_2]^{2-}$.

Table 3.3. Electrochemical data from CV (V vs Ag/AgCl)

Compound	A ($\text{Ru}_2^{7+/6+}$)	B ($\text{Ru}_2^{6+/5+}$)	C ($\text{Ru}_2^{5+/4+}$)	Solvent
<i>cis</i> 2:2 $\text{Ru}_2(\text{amtfmp})_4\text{Cl}_2$	----	0.15	-1.32	THF
10	----	-0.29	-1.34	THF
$\text{Ru}_2(\text{DMBA})_4(\text{C}_2\text{Ph})_2$ ¹¹⁸	0.52	-1.10	-2.20 ^a	THF
11	0.80	-0.59	-1.61	THF
12	0.72	-0.53	-1.68	THF
$\text{Ru}_2(\text{DMBA})_4(\text{Ph})_2$ ³⁶	0.04	-1.50	----	CH ₂ Cl ₂

3.3.5 Density Functional Theory Analysis

Density functional theory (DFT) calculations were also performed to better understand the electronic structures of **10** and **11**. Representations of the frontier molecular orbitals and their corresponding energies for **10'** and **11'** are shown in Figure 3.12 and Table 3.4, and the comparison between experimental (crystallographic) and DFT-optimized parameters is given in Table C.3 (Appendix C below). Computational details can be found in section 3.5.3.

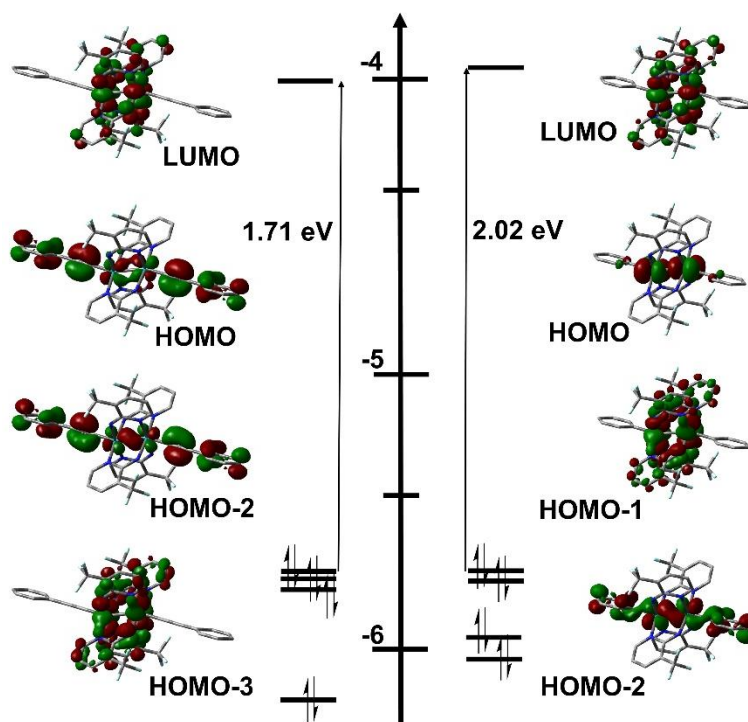


Figure 3.12. Molecular orbital diagrams of **10'** (left) and **11'** (right) obtained from DFT calculations, represented at $|\text{isovalue}| = 0.03$. The HOMO-1 for **10'** was omitted as it consists of the $d\pi - \pi$ interactions akin to the HOMO of **10'** but in the orthogonal orientation (plotted in Table 3.4)

Table 3.4. Molecular orbital diagram of **10'** and **11'** with corresponding energies (eV)

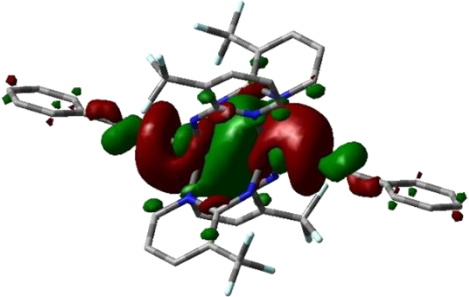
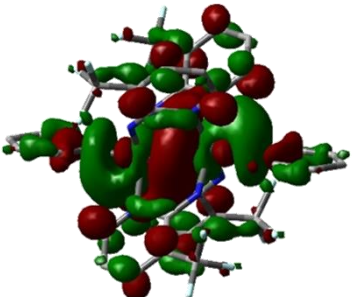
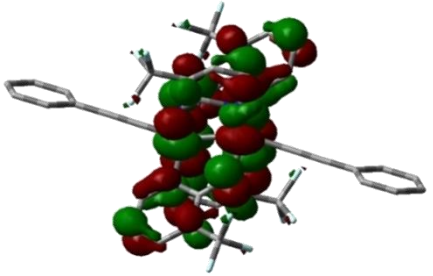
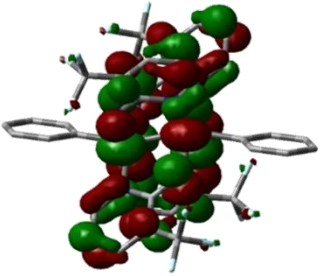
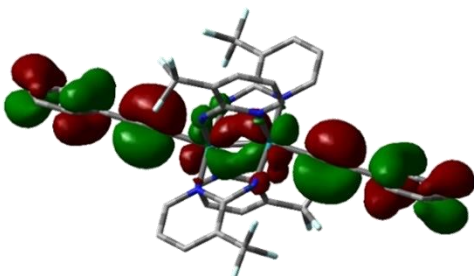
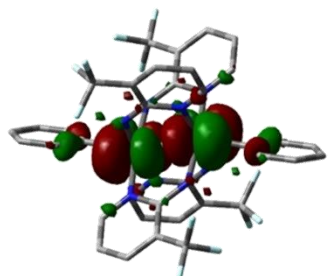
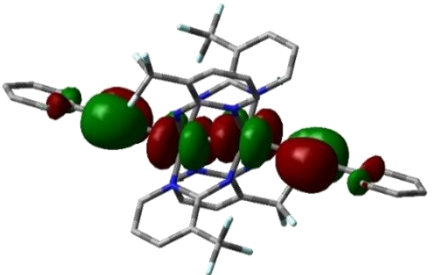
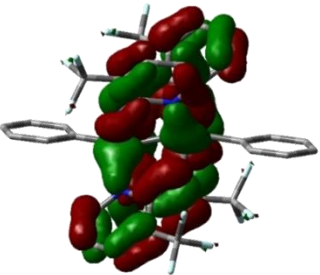
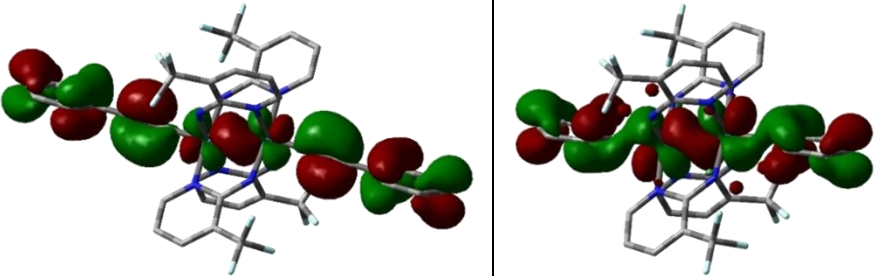
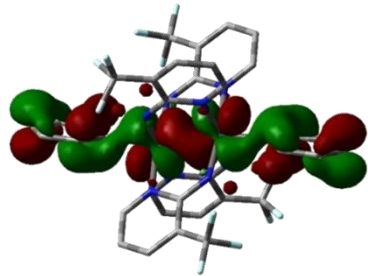
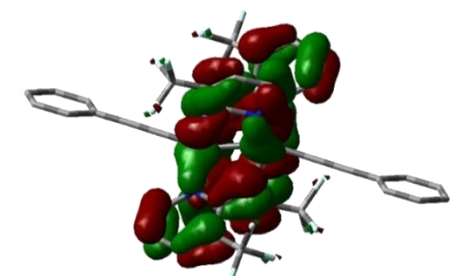
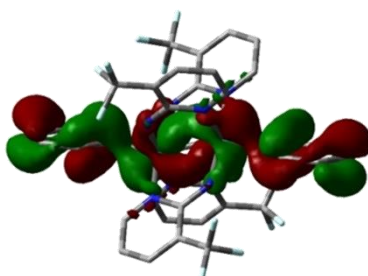
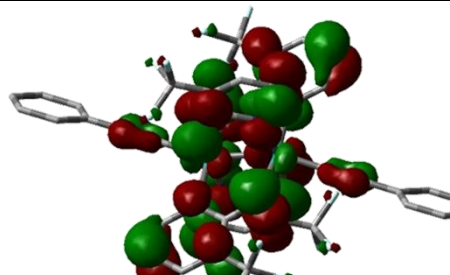
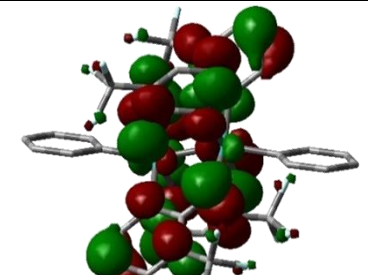
	10'	11'
LUMO +1	 -2.800 eV	 -2.247 eV
LUMO	 -4.082 eV	 -3.716 eV
HOMO	 -5.791 eV	 -5.731 eV
HOMO-1	 -5.801 eV	 -5.763 eV

Table 3.4 Continued

HOMO-2	 -5.843 eV	 -5.946 eV
HOMO-3	 -6.123 eV	 -6.034 eV
HOMO-4	 -6.239 eV	 -6.078 eV

It is clear from Figure 3.12 and Table 3.4 that the frontier molecular orbitals of both **10'** and **11'** are heavily mixed between the Ru₂ core and the bis-alkynyl (**10'**) and bis-aryl (**11'**) ligands. As postulated in the voltametric studies above, the HOMO of **11'** is mainly based on $d\pi^*$ interactions within the Ru₂ core with some limited ligand interaction, analogous to the previously characterized Ru₂(DMBA)₄(Ar)₂.³⁶ In contrast, the HOMO of **10'** is mainly the antibonding $d\pi$ (Ru₂) - π (C \equiv C-Ph) combination, consistent with the acetylide ligand being a π -base.¹³³ For both **10'** and **11'**, the HOMO-2 orbital has gained some σ (Ru-Ru) character via the SOJT distortion, i.e. caused by large deviations from linearity in the Ru-Ru-C bond angles. Around this orbital, both a δ (Ru₂) / π (Ru-N) orbital (HOMO-1) and a π (Ru-Ru) / π (Ru-Ar) orbital (HOMO-3) can also be

found. While **10'** does contain the analogous orbitals, they are found in a slightly different order, with only the HOMO-2 and LUMO matching the order for **11'**. The LUMO and higher-energy orbitals in both **10'** and **11'** are localized on the $\delta^*(\text{Ru}_2)$ orbitals (Table 3.4) with some nonbonding $\pi(\text{N}-\text{C}-\text{N})$ amtfmp ligand contributions, suggesting that the reductions observed in voltametric studies (see discussion above) are also primarily based on the Ru_2 core. Thus, the overall ground state configurations of **10'** and **11'** (and presumably **12**, based on diamagnetic ^1H NMR) can be represented as $\pi^4\delta^2(\pi^*)^4$ ($S = 0$), matching the previously characterized $\text{Ru}_2(\text{DMBA})_4(\text{Ar})_2$ and $\text{Ru}_2(\text{DMBA})_4(\text{C}_2\text{R})_2$ compounds.^{36,118,119}

3.4 Conclusions

Preparation of organometallic derivatives of $\text{Ru}_2(\text{amtfmp})_4\text{Cl}_2$ has been successfully demonstrated in this study. Both the bis-alkynyl (**10**) and bis-aryl (**11** and **12**) derivatives exhibit multiple reversible one electron couples and are rich in colors, revealing their potential for applications as charge storage and electrochromic materials. In spite of the contrast in electron donicity between DMBA and amtfmp, $\text{Ru}_2(\text{amtfmp})_4(\text{Y})_2$ compounds are *iso*-electronic to the corresponding $\text{Ru}_2(\text{DMBA})_4(\text{Y})_2$ ($\text{Y} = \text{Cl}$, C_2Ph or Ph). A severe setback from synthesis perspective is that all $\text{Ru}_2(\text{amtfmp})_4(\text{Y})_2$ materials obtained by us are mixtures of *cis* (2:2) and (3:1) isomers, a reflection of the substitution lability of amtfmp ligand. Preparing $\text{Ru}_2(\text{amtfmp})_4(\text{Y})_2$ of both good isomeric purity and respectable yield is a bottleneck towards material applications, and an ongoing effort in our laboratory.

3.5 Experimental Section

General Methods. $\text{Ru}_2(\text{OAc})_4\text{Cl}$ was prepared according to a previously reported method.¹ $n\text{BuLi}$ (2.5 M in hexanes) was purchased from Sigma-Aldrich. 2-amino-3-(trifluoromethyl)pyridine, phenylacetylene, and bromobenzene were purchased from Oakwood Chemicals and used without further purification. Tetrahydrofuran (THF) was freshly distilled over sodium/benzophenone. All reactions were performed under a dry nitrogen atmosphere implementing standard Schlenk procedures unless otherwise noted, with workups occurring in ambient conditions.

Physical methods. UV-vis-NIR spectra were obtained with a JASCO V-780 spectrophotometer in THF solutions. FT-IR spectrum of **10** was measured as a neat sample using a JASCO FT/IR-6300 spectrometer equipped with a diamond ATR attachment. ESI-MS were analyzed on an Advion Mass Spectrometer. ^1H and ^{19}F NMR spectra were recorded on a Varian Inova 300 spectrometer operating at 300 MHz (^1H) and 282 MHz (^{19}F). Cyclic and differential pulse voltammograms were recorded in 0.1 M $[\text{Bu}_4\text{N}][\text{PF}_6]$ solution (4 mL THF, Ar-degassed) on a CHI620A voltammetric analyzer with a glassy-carbon working electrode (diameter 2 mm), a Pt-wire auxiliary electrode, and a Ag/AgCl reference electrode. The concentration of Ru_2 species was always *ca.* 1.0 mM. The $\text{Fc}^{+/0}$ couple was observed at *ca.* 0.480 ± 0.011 V (vs Ag/AgCl) under the noted experimental conditions. Elemental analyses were performed by Atlantic Microlab, Inc. Magnetic susceptibility of $\text{Ru}_2(\text{amtftp})_4\text{Cl}_2$ was measured with a Johnson Matthey MarkII magnetic susceptibility balance at 294 ± 2 K.

3.5.1 Synthesis Details

$\text{Ru}_2(\text{amtftp})_4\text{Cl}_2$. To a 100 mL round bottom flask was added $\text{Ru}_2(\text{OAc})_4\text{Cl}$ (240 mg, 0.50 mmol), 2-amino-3-(trifluoromethyl)pyridine (650 mg, 4.0 mmol), excess LiCl (300 mg, 7.0 mmol) and 60 mL toluene, and a micro Soxhlet extraction apparatus with a K_2CO_3 -filled glass thimble mounted atop the flask. The reaction was then refluxed at *ca.* 130°C for a week, with the K_2CO_3 changed daily for the first three days, and then once after. After cooling to room temperature, the deep blue crude mixture was filtered over Celite and the remaining solid was washed with methanol. All fractions were combined and after solvent removal, the residue was dissolved in CH_2Cl_2 , exposed to air to re-oxidize after reduction from methanol exposure, and filtered once TLC confirmed product presence (usually 2–3 days). This was repeated over the course of two weeks until no more product was identified via TLC. The deep blue filtrate was dried to a dark solid, while any remaining residue was washed with methanol, condensed, and redissolved in CH_2Cl_2 . Final purification of the deep blue filtrate was achieved by running a CH_2Cl_2 (0 – 5% methanol) silica plug. Yield: 255 mg $\text{Ru}_2(\text{amtftp})_4\text{Cl}_2$ (55% yield based on Ru). $\text{Ru}_2(\text{amtftp})_4\text{Cl}_2$ was recrystallized in a 1:25 THF/hexanes (v/v) before EA. TLC with 1:2 THF / hexanes with 3% methanol (v/v) revealed presence of two blue spots, $R_f = 0.33$; 0.30. Elem. Anal. Found (Calcd) for $\text{C}_{28}\text{H}_{24}\text{N}_8\text{O}_1\text{F}_{12}\text{Cl}_2\text{Ru}_2$ ($\text{Ru}_2(\text{amtftp})_4\text{Cl}_2 \cdot 1\text{THF}$) : C, 33.88 (33.98); H, 2.17 (2.44); N, 11.75 (11.32). ESI-MS (m/z , based on ^{101}Ru): $[\text{M}]^- = 918.3$. UV-Vis (in THF) λ / nm

($\epsilon / \text{M}^{-1} \text{cm}^{-1}$): 662 (9400), 843 (8200), 1200 (900). Electrochemistry (THF, vs $\text{Fc}^{+/0}$) $E_{1/2} / \text{V}$, $\Delta E_p / \text{mV}$, $i_{\text{backward}}/i_{\text{forward}}$: -0.168 (66, 0.98), -1.591 (71, 0.83). μ_{eff} : 2.71 μ_B . ^{19}F NMR (CDCl_3 , 293 K) δ , ppm = -45.72 (major); -46.01, -46.84, -47.92 (minor).

cis (2:2) $\text{Ru}_2(\text{amtfmp})_4(\text{C}_2\text{Ph})_2$ (10). Phenylacetylene (0.15 mL, 1.4 mmol) was dissolved in 4.0 mL THF and the solution degassed three times. This solution was then treated with 0.70 mL (1.8 mmol) of $n\text{BuLi}$ at -78°C and then allowed to reach room temperature. All the alkynyllithium solution was added to a 50 mL solution of $\text{Ru}_2(\text{amtfmp})_4\text{Cl}_2$ in THF (190 mg, 0.21 mmol), after which an immediate color change from blue to deep red was observed. The reaction mixture was stirred for 1 hour under N_2 and after exposure to air turned a deep blue-green. After filtering over Celite and removing the solvent, the crude reaction mixture was purified with a silica plug run with 1:2 THF/hexanes with ca. 3% MeOH (v/v), to isolate **10** as a deep blue solid. Compound **10** was recrystallized in a 1:1:25 THF/ethyl acetate (EtOAc)/hexanes (v/v) before EA. Column chromatography (1:3 EtOAc/hexanes) was required to purify before electrochemical experiments. Single crystals suitable for X-ray diffraction were grown by layering hexanes over a concentrated solution of **10** in THF. Yield: 80 mg (36% based on Ru). TLC with 1:2 THF/hexanes with 3% methanol (v/v), $R_f = 0.64$. Elem. Anal. Found (Calcd) for $\text{C}_{44}\text{H}_{34}\text{N}_8\text{O}_2\text{F}_{12}\text{Ru}_2$ (**10**·1EtOAc): C, 46.16 (46.48); H, 3.33 (3.01); N, 9.66 (9.86). ESI-MS (m/z , based on ^{101}Ru): $[\text{M}]^+ = 1050$. IR $\bar{\nu} / \text{cm}^{-1}$: 2090 $\bar{\nu}(\text{C}\equiv\text{C})$. UV-Vis (in THF) λ / nm ($\epsilon / \text{M}^{-1} \text{cm}^{-1}$): 452 (8300), 573 (8900), 619 (10000), 748 (4300). Electrochemistry (THF, vs $\text{Fc}^{+/0}$) $E_{1/2} / \text{V}$, $\Delta E_p / \text{mV}$, $i_{\text{backward}}/i_{\text{forward}}$: 0.619, irrev., -0.75 (62, 1.00), -1.81 (66, 0.96). ^1H NMR (CDCl_3 , 293 K) δ , ppm = 9.64 (d, $J = 6.0$ Hz, 4H, H_A (amtfmp)), 9.43 (s, 4H, H_B (-NH)), 7.61 – 7.53 (m, 4H, H_C (amtfmp)), 7.33 (d, $J = 4.4$ Hz, 8H, H_D (amtfmp/aryl)), 7.00 – 6.96 (m, 2H, H_E (aryl)), 6.68 (t, $J = 6.9$ Hz, 4H, H_F (aryl)). ^{19}F NMR (CDCl_3 , 293 K) δ , ppm = -65.38.

cis (2:2) $\text{Ru}_2(\text{amtfmp})_4(\text{C}_6\text{H}_5)_2$ (11) and (3:1) $\text{Ru}_2(\text{amtfmp})_4(\text{C}_6\text{H}_5)_2$ (12). Bromobenzene (0.50 mL, 4.8 mmol) was dissolved in 4.0 mL THF and treated with 2.4 mL $n\text{BuLi}$ (6.0 mmol) at 0°C . The aryllithium solution was then cannula transferred to a 70 mL solution of $\text{Ru}_2(\text{amtfmp})_4\text{Cl}_2$ in THF (550 mg, 0.60 mmol). A color change from deep blue to red was observed. The reaction mixture stirred for 1 h at room temperature, and after exposure to air changed to purple. After filtering over Celite and removing the solvent, the crude product was purified via a silica plug run with 1:2 THF/hexanes with ca. 3% MeOH (v/v), to isolate 260 mg (33% combined yield based on Ru) of **11** and **12**. From this plug, 220 mg of the starting material, $\text{Ru}_2(\text{amtfmp})_4\text{Cl}_2$,

was re-collected (40% of the original starting material). The isomers were further purified by column chromatography. Two different product bands were eluted with 1:2 THF/hexanes with ca. 3% MeOH (v/v), the front band red (**11**) and the back band purple (**12**). Compound **11** was recrystallized in a 1:1:25 THF/EtOAc/hexanes (v/v) before EA. Single crystals suitable for X-ray diffraction were grown by layering hexanes over a concentrated solution of **11** in THF. Yield of **11**: 95 mg (12% based on Ru). TLC with 1:2 THF/hexanes with 3% methanol (v/v), R_f = 0.73. Elem. Anal. Found (Calcd) for $C_{44}H_{42}N_8O_3F_{12}Ru_2$ (**11**·1THF·1EtOAc): C, 45.50 (45.52); H, 3.45 (3.65); N, 9.35 (9.65). ESI-MS (m/z , based on ^{101}Ru): $[M+H]^+$ = 1001.8. UV-Vis (in THF) λ / nm (ϵ / $M^{-1} cm^{-1}$): 433 (11300), 514 (6800), 573, (7800), 656 (2300), 710 (3700), 989 (190). Electrochemistry (THF, vs $Fc^{+/0}$) $E_{1/2}$ / V, ΔE_p / mV, $i_{backward}/i_{forward}$: 0.31 (65, 0.97), -1.08 (66, 1.01), -2.10 (70, 1.13). 1H NMR ($CDCl_3$, 293K) δ , ppm = 9.17 (s, 4H, H_D (-NH)), 8.68 (d, J = 6.1 Hz, 4H, H_C (amtfmp)), 7.48 (d, J = 7.0 Hz, 4H, H_A (amtfmp)), 7.28 (t, J = 6.0 Hz, 2H, H_B (amtfmp)), 7.24 (t, 2H, H_B (amtfmp)), 7.09 (t, J = 7.6 Hz, 4H, H_E (aryl)), 7.02 – 6.96 (m, 2H, H_G (aryl)), 6.43 (t, J = 6.7 Hz, 4H, H_F (aryl)). ^{19}F NMR ($CDCl_3$, 293 K) δ , ppm = -65.30.

(3:1) $Ru_2(amtfmp)_4(C_6H_5)_2$ (12**).** Compound **12** was recrystallized in a 1:1:25 THF/EtOAc/hexanes (v/v) before EA. Single crystals suitable for X-ray diffraction were grown by layering hexanes over a concentrated solution of **12** in ethyl acetate. Yield of **12**: 45 mg (7% based on Ru). TLC with 1:2 THF/hexanes with 3% methanol (v/v), R_f = 0.70. Elem. Anal. Found (Calcd) for $C_{44}H_{44}N_8O_5F_{12}Ru_2$ (**12**·2EtOAc·1H₂O): C, 44.11 (44.22); H, 3.91 (3.71); N, 9.04 (9.38). ESI-MS (m/z , based on ^{101}Ru): $[M+H]^+$ = 1001.8. UV-Vis (in THF) λ / nm (ϵ / $M^{-1} cm^{-1}$): 415 (5900), 566 (7400), 710 (1000), 800 (700), 988 (270). Electrochemistry (THF, vs $Fc^{+/0}$) $E_{1/2}$ / V, ΔE_p / mV, $i_{backward}/i_{forward}$: 0.236 (59, 0.89), -1.01 (68, 1.00), -2.16 (66, 0.96). 1H NMR ($CDCl_3$, 293 K) δ , ppm = 10.50 (s, 1H, H_A (-NH)), 9.62 (d, J = 6.6 Hz, 1H, H_B , (amtfmp)), 8.92 (d, J = 6.1 Hz, 1H, H_C , (amtfmp)), 8.59 – 8.41 (m, 2H, H_D , (amtfmp)), 7.84 (t, J = 3.4 Hz, 1H, H_E , (-NH)), 7.54 (d, J = 7.4 Hz, 1H, H_F , (amtfmp)), 7.46 (t, J = 8.2 Hz, 2H, H_G , (amtfmp)), 7.36–7.29 (m, 4H, H_H , (aryl/amtfmp)), 7.14 (t, J = 7.5 Hz, 2H, H_I , (amtfmp)), 6.99 (s, 2H, H_J , (-NH)), 6.84 (t, J = 6.9 Hz, 2H, H_K , (aryl)), 6.77 (t, J = 8.0 Hz, 1H, H_L , (amtfmp)), 6.61 (d, J = 7.8 Hz, 2H, H_M , (aryl)), 6.44 (t, J = 6.6 Hz, 1H, H_N , (aryl)), 6.37 (t, J = 6.6 Hz, 1H, H_O , (aryl)), 6.00 (t, J = 6.9 Hz, 2H, H_P , (aryl)). ^{19}F NMR ($CDCl_3$, 293 K) δ , ppm = -64.55, -65.21, -65.62.

3.5.2 X-ray Crystallographic Details

Crystals suitable for X-ray diffraction analysis were grown by layering hexanes over a concentrated solution of either **10** or **11** in THF and **12** in ethyl acetate. Single crystals of **11** were coated with paraffin oil and quickly transferred to the goniometer head of a Bruker Quest diffractometer with a fixed chi angle, a sealed tube fine focus X-ray tube, single crystal curved graphite incident beam monochromator, a Photon II area detector and an Oxford Cryosystems low temperature device. Examination and data collection were performed with Mo K α radiation ($\lambda = 0.71073$ Å) at 150 K. Single crystals of **10** and **12** were coated with paraffin oil and quickly transferred to the goniometer head of a Bruker Quest diffractometer with kappa geometry, an I- μ -S microsource X-ray tube, laterally graded multilayer (Goebel) mirror single crystal for monochromatization, a Photon-III C14 area detector and an Oxford Cryosystems low temperature device. Examination and data collection were performed with Cu K α radiation ($\lambda = 1.54178$ Å) at 150 K. Full crystallographic details can be found in Table C.1 in Appendix C below.

Data were collected, reflections were indexed and processed, and the files scaled and corrected for absorption using APEX3⁸¹ and SADABS.⁵¹ The space groups were assigned using XPREP within the SHELXTL suite of programs^{52,53} and solved by direct methods using ShelXS⁵³ or dual methods using ShelXT⁵⁴ and refined by full matrix least squares against F² with all reflections using Shelxl2018⁵⁵ using the graphical interface Shelxle.⁵⁷ Complete crystallographic data, in CIF format, have been deposited with the Cambridge Crystallographic Data Centre. CCDC 2182912-2182914 contains the supplementary crystallographic data for this paper. These data can be obtained free of charge from The Cambridge Crystallographic Data Centre via www.ccdc.cam.ac.uk/data_request/cif.

3.5.3 Computational Methods

Geometry optimizations of structures **10** and **11** based on the respective crystal structures were done using restricted open-shell density functional theory (DFT); the B3LYP functional and lanl2dz basis set were used for all atoms¹³⁴ in tetrahydrofuran. Frequency analyses were carried out for both the optimized structures **10'** and **11'**, shown in Figures C.8 and C.9 in Appendix C, and stationary points were confirmed. All calculations were carried out with the Gaussian 16, Rev. A.03.⁸⁴

3.5.4 Synthesis of $\text{Ru}_2(\text{amtfmp})_4\text{Cl}_2$ following literature procedure

$\text{Ru}_2(\text{amtfmp})_4\text{Cl}_2$.¹²⁴ To a 200 mL round bottom flask was added $\text{Ru}_2(\text{OAc})_4\text{Cl}_2$ (144 mg, 0.3 mmol), 2-amino-3-(trifluoromethyl)pyridine (225 mg, 1.39 mmol), excess LiCl, (130 mg, 3.06 mmol), 1.00 mL NEt_3 and 60 mL THF. A condenser was attached, and the reaction refluxed for 24 hours, the reaction mixture darkening to a deep red-purple during this time (Figure C.10 in Appendix C below). After cooling to room temperature, the reaction mixture was filtered through Celite to remove excess LiCl (Figure C.11), condensed to a dark solid, and dried. This solid was then dissolved in ca. 10 mL CHCl_3 and sat for ~2 hours to turn blue. Column chromatography ($\text{CHCl}_3 \rightarrow 5\% \text{ MeOH}$ in CHCl_3 (v/v)) first removed the excess ligand and then a large blue band eluted with the CHCl_3 w/ 5% MeOH (v/v). Multiple fractions were collected (Figure C.12), combined, and dried. Weight: 181 mg (65% yield based on Ru). TLC analysis using 1:2 THF/hexanes w/ 3% MeOH, CHCl_3 , and CHCl_3 w/ 5% MeOH revealed the presence of isomers in purified product obtained from literature procedure (Figure 3.2 above in section 3.3.1).

3.5.5 Synthesis of $\text{Ru}_2(\text{amtfmp})_4(\text{Ph})_2$ using material from 3.5.4

$\text{Ru}_2(\text{amtfmp})_4(\text{Ph})_2$. Bromobenzene (0.10 mL, 0.95 mmol) was dissolved in 4.0 mL THF and treated with 0.5 mL $n\text{BuLi}$ (1.25 mmol) at 0°C . The aryllithium solution was then cannula transferred to a 30 mL solution of $\text{Ru}_2(\text{amtfmp})_4\text{Cl}_2$ (from the literature synthesis in section 3.5.4 above) in THF (126 mg, 0.14 mmol). A color change from deep blue to red was observed. The reaction mixture stirred for 1 h at room temperature, and after exposure to air changed to purple. After filtering over Celite and removing the solvent, the crude material was dried. TLC analysis of this crude material with 1:2 THF/hexanes w/ 3% MeOH confirmed presence of both **11** and **12** as red and purple spots respectively (Figure C.13). Baseline spot matches the reduced material, $[\text{Ru}_2(\text{amtfmp})_4\text{Cl}_2]^-$, as discussed in Figure 3.3 in section 3.3.1 above.

3.5.6 Synthesis of $\text{Ru}_2(\text{amtfmp})_4(\text{C}_2\text{TIPS})_2$

$\text{Ru}_2(\text{amtfmp})_4(\text{C}_2\text{TIPS})_2$. (Triisopropylsilyl)acetylene (0.20 mL, 0.87 mmol) was dissolved in 4.0 mL THF and treated with 0.5 mL $n\text{BuLi}$ (1.25 mmol) at -78°C . This solution was then cannula transferred to a 30 mL solution of $\text{Ru}_2(\text{amtfmp})_4\text{Cl}_2$ (from the literature synthesis in section 3.5.4 above) in THF (133 mg, 0.14 mmol). A color change from deep blue to red was

observed. The reaction mixture stirred for 1 h at room temperature, turning a brown color during this time, and after exposure to air changed to deep green. After filtering over Celite and removing the solvent, the crude material was dried. TLC analysis of this crude material with hexanes (right plate) confirmed presence of two isomers (Figure C.14) and no unreacted starting material, 1:3 EtOAc / hexanes (left plate), confirming that the bulkiness of the ligand does not influence the reactivity of the two isomers in $\text{Ru}_2(\text{amtftp})_4\text{Cl}_2$. MS analysis displayed desired product m/z ratio at 1209 $[\text{M-H}]^+$, however a large number of peaks with the same Ru_2 isotope pattern were also observed (Figure C.15).

CHAPTER 4. SYNTHESES AND MATERIAL APPLICATIONS OF RU(II)(BISPHOSPHINE)₂ ALKYNYL

Reproduced (adapted) with permission from L. A. Miller-Clark and T. Ren, *Journal of Organometallic Chemistry*, 2021, **951**, 122003. Copyright 2021, Elsevier B.V.. DOI: 10.1016/j.jorganchem.2021.122003

4.1 Abstract

Described in this review are the synthetic methods to produce both mono- and bis-alkynyl Ru(II)(L-L)₂ type complexes, where L-L is dppe, dppm, or dmpe. This synthetic tool kit encompasses reactions utilizing trimethylstannyl capped reagents, Ru-alkyl starting materials, or the 16 e⁻ [RuCl(dppe)₂]⁺ intermediate to produce the desired Ru(II)(L-L)₂ alkynyl complexes. Advantages and drawbacks of each synthetic approach are touched upon. A brief overview of material applications of these complexes is also provided, highlighting their promises as efficient non-linear optical materials, wire-like molecules, molecular wires and switches, and active molecules in dye-sensitized solar cells.

4.2 Introduction

Chemistry of transition metal alkynyl compounds is a rich and dynamic research area.^{64,135–137} These complexes, ranging from monomeric complexes with a single alkynyl ligand to polymeric complexes, can trace their origins of interest back to the homoleptic hexakis-alkynyl [M(C≡C-R)₆]ⁿ⁻ (M = Cr, Mn, Fe, and Co), tetrakis-alkynyl [M(C≡C-R)₄]ⁿ⁻ (M = Mn, Ni, Pd, Pt, Zn, Cd, and Hg), and bis-alkynyl [M(C≡C-R)₂]ⁿ⁻ (M = Cu, Ag, and Au) complexes by Nast and co-workers¹³⁸ as well to the dehydro-halogenation reactions that generated polymeric alkynyl complexes containing Ni, Pd, and Pt, reported by Hagihara and co-workers in the 1970s and 1980s.^{139–141} Transition metal-alkynyl complexes are promising candidates for a variety of material applications, such as NLO materials,¹⁴¹ photovoltaics,^{61,62} OLED,¹⁴² molecular wires,^{20,143,144} and active species for nanoscale devices.^{28,145}

Given the abundance of sweeping surveys of transition metal alkynyl compounds^{64,133,135–137,146,147} since the original review by Nast,¹³⁸ the primary focus of this review will be the synthetic strategy for preparing *trans*- mono- and bis-alkynyl complexes based on Ru(II)(L-L)₂ units with

L-L as dppe(1,2-bis(diphenylphosphino)ethane) or dppm (1,2-bis(diphenylphosphino)methane)), an area with only one other recent review, dedicated to the unconventional reactions with Ru(II)/Os(II) dppm frameworks.¹⁴⁸ Generic structures of each framework's mono- and bis-alkynyl complexes with expanded ligand frameworks are provided in Figure 4.1. This review also provides a brief overview of the material applications of these Ru(II) complexes.

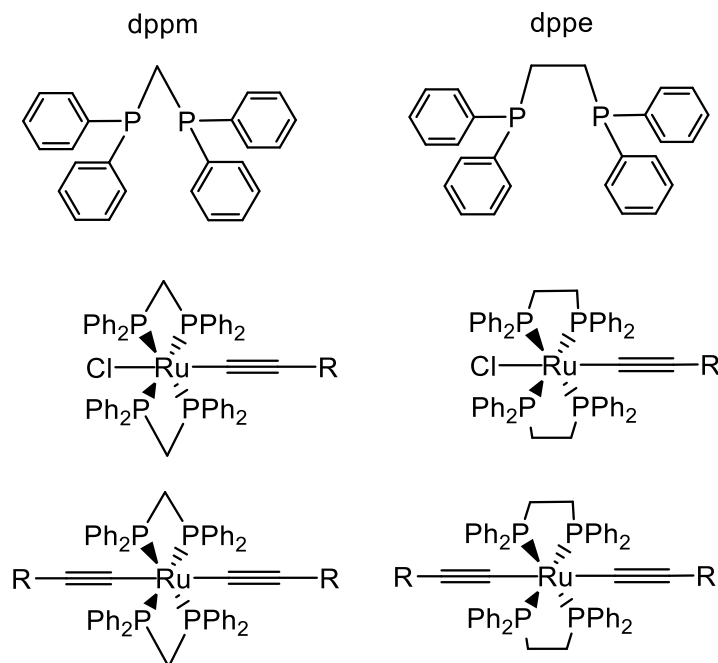


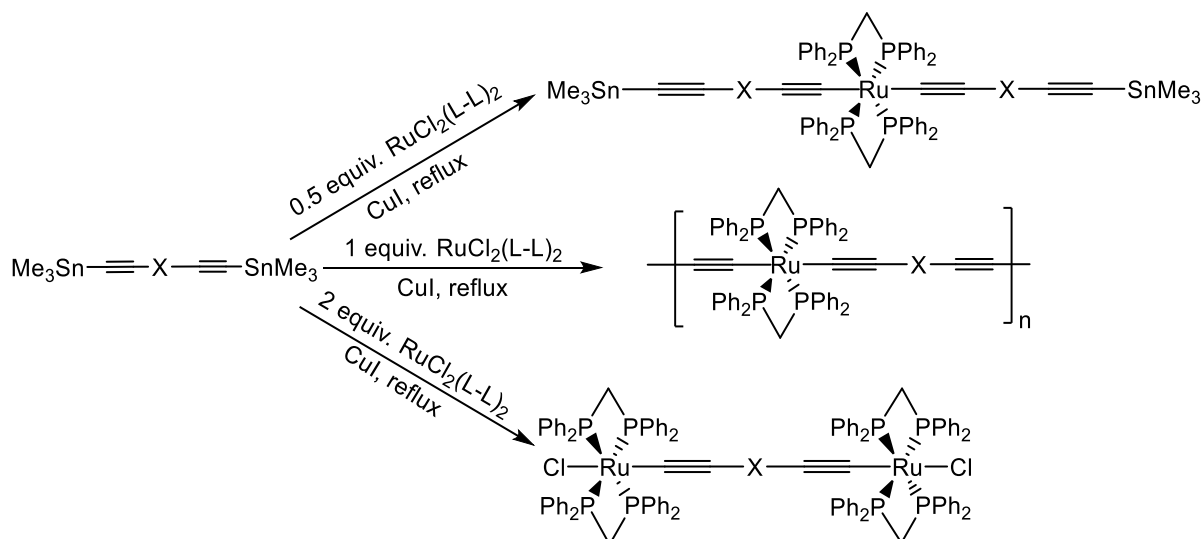
Figure 4.1. Representative structures of *trans* mono- and bis-alkynyl compounds based on dppm (left) and dppe (right)

4.3 Synthetic methods for Ru bis-alkynyl complexes

4.3.1 Synthesis from trimethylstannyl alkynyl

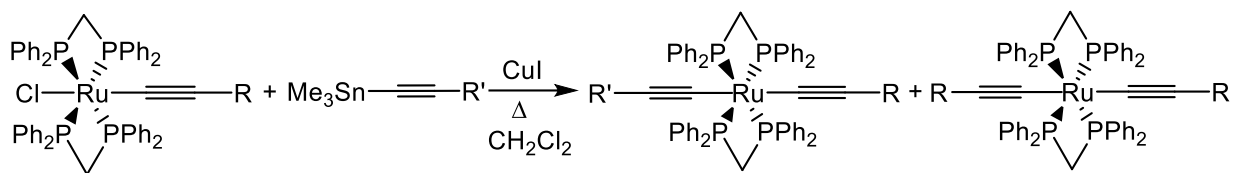
Prior to 1990s, synthetic methods based on a Cu(I) assisted dehydro-halogenation reaction (Hagihara coupling)^{140,149} successfully produced a large number of group 10 metal alkynyl complexes. However, Hagihara coupling cannot be extended to other metal alkynyls as the use of amines as solvents rendered most phosphine-containing starting materials (besides those in Group 10) unstable and prone to ligand substitution.⁶⁴ In the mid-1990s, Lewis and co-workers took inspiration from a metathesis reaction first reported by Lappert *et al.*¹⁵⁰ that utilized the trimethylstannyl alkynyl reagents and metal chlorides, and reported the first copper-catalyzed syntheses of Ru-based alkynyl dimers¹⁵¹ and polymers,¹⁵² while avoiding the use of harsh amine

solvents. The approach developed by Lewis and co-workers (Scheme 4.1) was found to reliably synthesize *trans*-Ru alkynyl structures of bi- and polymeric complexes with phosphine backbones (L-L)₂ (L-L = dppe or dppm), but was not applicable for the preparation of mono-alkynyl complexes.¹⁵²



Scheme 4.1. Synthesis based on trimethylstannyl alkynyls; X = bridge groups

The only products obtained from the reaction between *trans*- $\text{RuCl}_2(\text{L-L})_2$ and *one equiv* of $\text{Me}_3\text{Sn}(\text{C}\equiv\text{C}-\text{R})$ were the dichloro starting material and the symmetrical bis-alkynyl complex, implying the second chloride substitution was the faster step of the two. In order to successfully generate mono-alkynyl Ru complexes, Lewis and co-workers utilized Dixneuf's alternative synthetic route that generates a vinylidene (see section 4.3.2 below), followed by deprotonation with a short alumina column or DBU (1,8-Diazabicyclo[5.4.0]undec-7-ene) to generate the desired mono-alkynyl complexes as starting materials for further additions onto the Ru center (Scheme 4.2). In most ligand combinations, the second alkynyl addition generated both the desired unsymmetrical bis-alkynyl complex and one of the two possible symmetrical bis-alkynyl complexes,¹⁵¹ presumably through a disproportionation mechanism which has been observed in other synthetic methods.¹⁵³



Scheme 4.2. Synthesis of Ru bis-alkynyls utilizing trimethylstannyl reagents

In order to generate soluble polymeric complexes, high purity *trans*-RuCl₂(dppm)₂ starting material and an exact Ru to ligand stoichiometry (1:1) were deemed essential to obtain a high degree of polymerization.¹⁵² Polymers of higher molecular weight ($M_w > 55000$) were achieved with Ru(dppm)₂ unit¹⁵² than those with Ru(depe)₂ unit ($M_w < 30000$; depe = 1,2-bis(diethylphosphino)ethane)¹⁵⁴ using the CuI-catalyzed method. While these polymers were characterized by gel permeation chromatography and ¹H and ³¹P NMR techniques, there was NO structure-oriented study such as powder X-ray diffraction or electron microscopy.

In the late 1990s, Wolf and co-workers successfully expanded upon Lewis' synthetic method. Through the reaction of tributylstannyl reagents, R-C≡C-Sn(*n*-Bu)₃ (R = Fc, 2-thienyl, 5-(2,2'-bithienyl), and 5-(2,2':5',2''-terthienyl)) with *cis*-RuCl₂(dppm)₂, both the symmetric, bis-alkynyl *trans*- and *cis*-Ru(C≡C-R)₂(dppm)₂ complexes were generated.^{155–157} The reactions with R = Fc yielded products in either the *cis* or *trans* configuration, depending on both the amount of CuI and the reaction temperature. When a catalytic amount of CuI was utilized (5-25%) and the reaction was heated to reflux in 1,2-dichloroethane, the *trans*-Ru(C≡C-Fc)₂(dppm)₂ was obtained in high yield. However, when a stoichiometric amount of CuI was utilized under reflux conditions, two new products with similar ¹H NMR spectra were obtained, and elemental analysis suggested the presence of both [Ru(C≡C-Fc)₂(dppm)₂]CuI and [Ru(C≡C-Fc)₂(dppm)₂]CuCl. After performing metathesis on [Ru(C≡C-Fc)₂(dppm)₂]CuCl with NaI, the [*cis*-Ru(C≡C-Fc)₂(dppm)₂]CuI complex was isolated (see Figure 4.2); this complex was also generated through the room temperature reaction of *cis*-RuCl₂(dppm)₂ with Fc-C≡C-Sn(*n*-Bu)₃ in CH₂Cl₂. The CuI unit is bonded in a η² fashion to both acetylide bonds, presumably what holds the complex in the *cis* configuration. Removal of the CuI yielded *trans*-Ru(C≡C-Fc)₂(dppm)₂, and reaction of the *trans* bis-alkynyl with a stoichiometric amount of CuI successfully regenerated the *cis* product, demonstrating the stabilization of the *cis* isomer by CuI η² bonds.¹⁵⁶ These Fc-modified complexes exhibit strong orbital interactions (more detail in section 4.4.2 below) between the Ru center and

the ancillary ferrocene ligands. Similar to the work of Lewis, the vinylidene method had to be utilized to generate mono-acetylide complexes (see section 4.3.2 below).¹⁵⁷

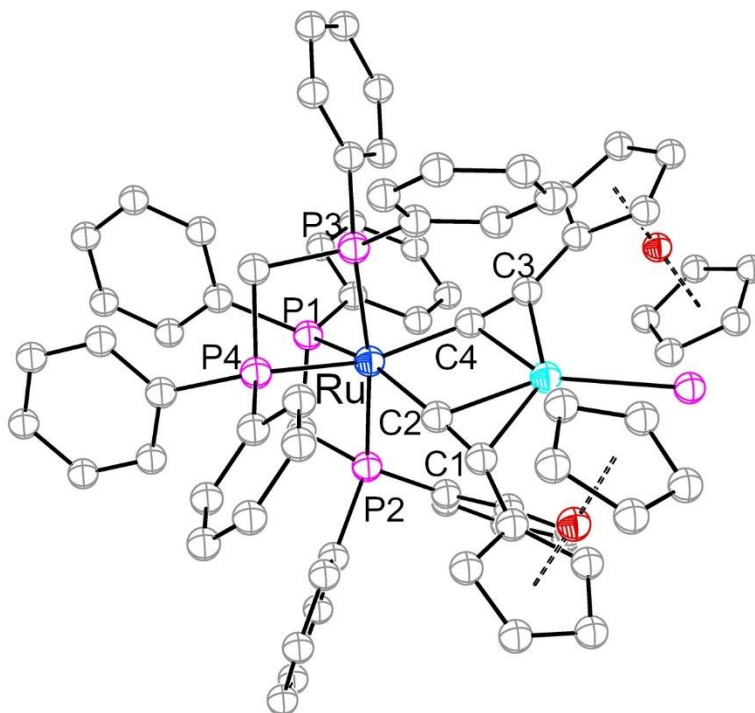


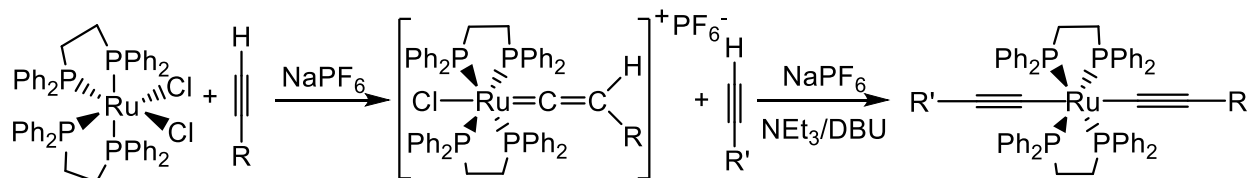
Figure 4.2. Molecular structure of $[cis\text{-Ru}(\text{C}\equiv\text{C-Fc})_2(\text{dppm})_2]\text{CuI}$ generated from CCDC 1238773

Although the use of tin-modified alkynyl ligands requires an extra step to prepare tin reagents and raises the concern of toxicity,^{158,159} Lewis's innovative synthetic method avoids the use of amine solvents, and hence broadens the scope of Ru alkynylation reactions. Lewis *et al.* utilized this method to generate Ni(II), Pd(II), Pt(II), and Rh(I) alkynyl complexes.¹⁶⁰ Lo Sterzo *et al.* have adapted this method to generate both mono-alkynyl and bridged alkynyl cyclopentadienyl Ru complexes via a palladium-catalyzed trimethylstannyl synthetic route.¹⁶¹ Cotton demonstrated the preferential alkynylation of the trimethylstannyl complexes at the Ru-Ru-Cl position, while avoiding alkynylation of the modified anilinoipyridinate backbones.¹⁶²

4.3.2 Synthesis through vinylidene formation

Starting with cis-RuCl₂(L-L)₂ (L-L = dppe/dppe)

Pioneered by Dixneuf and co-workers, an efficient and stepwise synthetic approach to the synthesis of both mono- and unsymmetric bis-alkynyl Ru species is to use the starting material *cis*-RuCl₂(dppe)₂ to generate a reactive vinylidene intermediate. These vinylidene intermediates are air-stable and insensitive to attack by methanol as has been observed with other RuCl₂(PR₃)(arene) derivatives.¹⁵³ Their detailed studies demonstrated that the *cis*-RuCl₂(dppe)₂ isomer readily activated terminal alkynes in the presence of a non-coordinating salt, typically NaPF₆, to form stable vinylidene complexes as shown in Scheme 4.3. In contrast, the *trans* isomer undergoes a much slower reaction that requires 5-7 days to generate vinylidenes.^{151,163} Generally, synthesis of mono-alkynyl complexes through vinylidene intermediates solely requires deprotonation of the vinylidene after removal of excess alkynyl ligand. Depending on the nature of second alkynyl ligand, further alkynylation of the vinylidene intermediate in the presence of NaPF₆ leads to either symmetric or unsymmetric Ru bis-alkynyl complexes.



Scheme 4.3. Unsymmetric Ru alkynyl synthesis through formation of vinylidene intermediate

As demonstrated above by Lewis *et al.*, use of either a suitable base like NEt₃ or DBU or a short alumina column deprotonated the vinylidene intermediates to yield the desired mono- or bis-alkynyl complexes.¹⁶⁴ The NaPF₆ salt is essential for this process because it promotes the formation of a 5-coordinate, 16 e- Ru species after chloride abstraction (generating NaCl), which is extremely reactive towards alkynyl rearrangement and vinylidene formation. Choice of solvent is also important: dichloromethane was the only solvent that gave desired bis-alkynyl products rather than tetrahydrofuran or methanol when starting from *cis/trans*-RuCl₂(L-L)₂.^{153,164} Dixneuf *et al.* also explored the use of *cis*-RuCl₂(dppm)₂ as a starting material for both mono- and bis-alkynyl complexes. While the conditions to generate an unsymmetric bis-alkynyl Ru complex are

similar to those utilized with *cis*-RuCl₂(dppe)₂, the attempts to generate desired *trans*-Ru(dppm)₂(C≡CR)(C≡CR') species were plagued by low yields.¹⁶⁴

While investigating *cis*-RuCl₂(dppm)₂ as a starting material, Low *et al.* have utilized more powerful halide extracting agents, such as thallium tetrafluoroborate (TlBF₄), and bases, 1,8-bis-dimethylaminonaphthalene (Proton Sponge), to prepare both *trans*- mono- and symmetrical bis-alkynyl complexes. These reactions follow the expected mechanistic pathway: formation of a vinylidene in moderate to high yields (63-80%) after reacting with terminal alkynes HC≡C-C₆H₄-R (R = NO₂, CO₂Me, C≡CSiMe₃, Me, OMe and H) for 1-2 hours,¹⁶⁵ followed by deprotonation with the Proton Sponge to yield the desired products. The authors emphasized that the stoichiometry of the reaction needs to be 1:1:1 (*cis*-RuCl₂(dppm)₂: ligand: TlBF₄) to prevent the generation of the symmetrical bis-alkynyl complexes during formation of the *trans*- mono-alkynyl complexes, for which the separation is challenging.

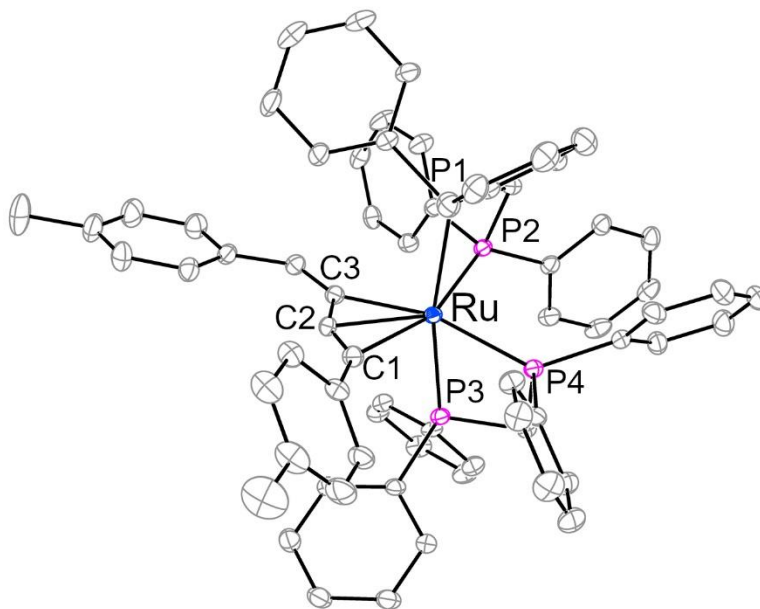


Figure 4.3. Molecular structure of [Ru(η³-{HC(C₆H₄-4-Me)=C-C≡C-C₆H₄-4-Me})-(dppm)₂]⁺ generated from CCDC 1426051

Use of electron-withdrawing or neutral R groups (R = NO₂, CO₂Me and C≡CSiMe₃) and an altered stoichiometric ratio of 1:2.1:2 (*cis*-RuCl₂(dppm)₂: ligand: TlBF₄) resulted in the desired symmetrical bis-alkynyl complexes *trans*-Ru(dppm)₂(C≡C-C₆H₄-R)₂.¹⁶⁶ However, use of electron-donating groups (R = Me and OMe) with an identical stoichiometric ratio generated

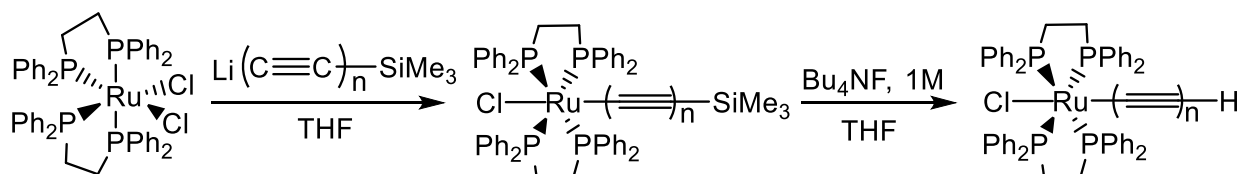
cationic η^3 -butenyne complexes $[\text{Ru}(\eta^3\text{-}\{\text{HC}(\text{C}_6\text{H}_4\text{-4-R})=\text{C}-\text{C}\equiv\text{C}-\text{C}_6\text{H}_4\text{-4-R}\})\text{-(dppm)}_2][\text{BF}_4]$ (Figure 4.3, R = -Me) instead. While ^1H NMR recorded during the reaction showed evidence of the formation of a symmetrical bis-alkynyl complex, all attempts to intercept the bis-alkynyl complexes resulted in the isolation of the η^3 -butenyne complexes only, indicating that the bis-alkynyl species underwent further conversion to the η^3 -butenyne species during work-up. The authors proposed a plausible mechanism based on DFT calculations that suggested a higher proportion of protonated alkyne-vinylidene species in solution is achievable with electron-donating alkyne ligands, resulting in favorable transitions to the η^3 -butenyne species. This pathway would not be favorable for the *cis*- $\text{RuCl}_2(\text{dppe})_2$ starting material, as the increased bite angle of the phosphines favors *trans*-arrangement of the alkyne ligands rather than the *cis* needed for the η^3 -butenyne species synthesis.¹⁶⁶

Alternative non-coordinating salts have also been employed during the syntheses of unsymmetric Ru-alkynyl complexes. Akita and co-workers utilized $\text{KB}(\text{C}_6\text{F}_5)_4$ ¹⁶⁷ to prevent desilylation of the trimethylsilylbutadiynyl ligand, which was observed during the attachment of the second acetylide in the presence of PF_6^- counteranion.

Synthesis through a vinylidene intermediate is invaluable for generating unsymmetric Ru bis-alkynyl complexes based on both $\text{Ru}(\text{dppe})_2$ and $\text{Ru}(\text{dppm})_2$ frameworks. The generation of unsymmetric bis-alkynyl complexes from *cis*- $\text{RuCl}_2(\text{dppm})_2$ is difficult, with reactions resulting in symmetric bis-alkynyl products, low yields of the desired products, and difficulty in separation. The vinylidene synthetic method is more beneficial with *cis*- $\text{RuCl}_2(\text{dppe})_2$ as the starting material, and many research groups have taken advantage of this method in generating unsymmetric Ru bis-alkynyl complexes due to the ease of alkyne addition, fast reaction at ambient temperature, and use of inexpensive materials (NEt_3 , NaPF_6). The most notable drawback is the issue with the order of ligand addition: successful generation of unsymmetric complex was only achieved through the first addition of the electron-withdrawing alkyne then addition of the electron-donating group.¹⁶⁸ The intermediate vinylidene complex was deprotonated before the introduction of the second alkyne in this study,¹⁶⁸ potentially impacting the *trans* influence experienced by the second alkyne during coordination.

Use of lithiated poly-ynyls

To generate an array of possible building blocks for larger bimetallic complexes bridged by poly-ynyl, Dixneuf *et al.* focused on the synthesis of mono- and bis-complexes with oligoynyls of varying length, namely *trans*-Ru(dppe)₂Cl(C_{2n}R) (*n* = 1 - 4) (R = SiMe₃, H) and *trans*-Ru(dppe)₂(C₄R)₂ (R = SiMe₃, H),¹⁶⁹ while the dppm framework has not been explored. The mono-complexes, *trans*-Ru(dppe)₂Cl(C_{2n}R), were produced in high yields through the reaction of *cis*-RuCl₂(dppe)₂ with LiC_{2n}SiMe₃, typically occurring overnight with purification achieved through a neutral alumina plug (Scheme 4.4). Desilylation of these mono-alkynyls utilizing Bu₄NF (TBAF) was successful for *n* = 2, 3 but the other two lengths either had too low a yield to generate enough useful product (*n* = 4) or could not be desilylated (*n* = 1) with any common desilylating agents (Bu₄NF in THF, KOH in CH₃OH, or K₂CO₃ in CH₃OH). This is in contrast to the successful production of *trans*-Ru(dppe)₂Cl(C₂H) from the reaction of *cis*-RuCl₂(dppe)₂ with HC₂SiMe₃ in the presence of DBU/NaPF₆, indicating that desilylation likely occurs before deprotonation to generate the alkyne.¹⁵³ Unsuccessful deprotonation of *n* = 1 was postulated to be due to increased steric hinderance of the [Ru(dppe)₂] fragment, or increased vinylidene-character of the alkyne in this complex.¹⁶⁹



Scheme 4.4. Synthesis of mono-alkynyl compounds using lithiated poly-ynyl

It is noteworthy that bis-complexes were not generated in Scheme 4.4 even with a large excess of lithiated poly-ynyl. To generate the symmetric complexes, *trans*-Ru(dppe)₂(C_{2n}R)₂, the vinylidenes obtained from the reaction of a terminal alkyne and *cis*-RuCl₂(dppe)₂ were deprotonated in the presence of NaPF₆.¹⁵³ As with the mono-alkynyl complexes, this approach was successful for producing the bis-complex with *n* = 2, but not in the case of *n* = 1. To generate the bimetallic complex *trans*-[Cl(dppe)₂-Ru-(C≡C)₆-Ru(dppe)₂Cl], Dixneuf and co-workers attempted the Glaser coupling reaction under both Eglinton (Cu(OAc)₂/py) and Hay (TMEDA/Cu) conditions using either the protected (*trans*-Ru(dppe)₂Cl(C≡C)₃SiMe₃) or deprotected (*trans*-

$\text{Ru}(\text{dppe})_2\text{Cl}(\text{C}\equiv\text{C})_3\text{-H}$) complexes. Successful coupling of the alkynes was achieved with the deprotected complex under Eglinton conditions to generate the C_{12} -bridged complex. Though less soluble and difficult to characterize, electronic communication between two Ru centers was observed in the C_{12} -bridged complex (see expanded discussion in section 4.4.2 below). Echoing issues encountered in the copper-catalyzed trimethylstannyl synthesis,¹⁵² the lithiation method was unsuccessful in replacing both chlorides on the starting material to generate the bis-complex. However, this method is a moderate to high yielding and facile synthetic approach for mono-complexes with minimal by-products.

Starting with $[\text{RuCl}(\text{dppe})_2]^+$

In the early 2000s, interest grew in the use of the isolated 5-coordinate 16 e^- $[\text{RuCl}(\text{dppe})_2]^+$ salt as a starting point to generate either mono- or bis-acetylide Ru complexes.^{170–175} From *cis*- $\text{RuCl}_2(\text{dppe})_2$, the reactive $[\text{RuCl}(\text{dppe})_2]\text{PF}_6$ species can be generated *in situ* through the ready abstraction of a chloride ligand with either NaPF_6 or NH_4PF_6 . However, *trans*- $\text{RuCl}_2(\text{dppe})_2$ requires the use of Ag(I) salts (commonly AgOTf or AgBF_4) to generate the desired $[\text{RuCl}(\text{dppe})_2]\text{OTf}$ or $[\text{RuCl}(\text{dppe})_2]\text{BF}_4$ complexes in a reasonable time scale (<1 hour at room temperature). This reaction can be monitored with an almost instantaneous color change from yellow to red. Advantageous as a starting material, $[\text{RuCl}(\text{dppe})_2]^+$ is easily isolated in high yield after the removal of AgCl , and stable at room temperature under ambient conditions. Although previously reported with a variety of counterions and phosphines,^{176–178} the structure of the triflate salt, shown in Figure 4.4 below, displays a “Y” distortion around the ruthenium center in the equatorial plane and deviates from the optimal trigonal bipyramidal structure.¹⁶³

The major advantage in utilizing the $[\text{RuCl}(\text{dppe})_2]\text{X}$ ($\text{X} = \text{PF}_6^-$, OTf^-) salt is the avoidance of the unreactive *trans* isomer commonly present in *cis*- $\text{RuCl}_2(\text{dppe})_2$ starting material. While it is possible to separate the two isomers, it requires careful, fractional crystallization in the dark.¹⁶³ Treatment of a mixture of isomers will therefore always give pure $[\text{RuCl}(\text{dppe})_2]^+$ as the product, removing the need to separate out the two isomers before alkyne additions, or purification from the unreacted *trans* isomer after alkyne addition. $[\text{RuCl}(\text{dppe})_2]^+$ has been frequently used in the synthesis of a wide variety of mono-alkynyl complexes, due to its expedient reactions with terminal alkynyl ligands (typically under 8 hours at room temperature). Purification simply

requires the removal of excess ligand and salts generated, with column chromatography only needed to separate out the symmetrical bis-alkynyl byproducts (if present).^{163,165,179}

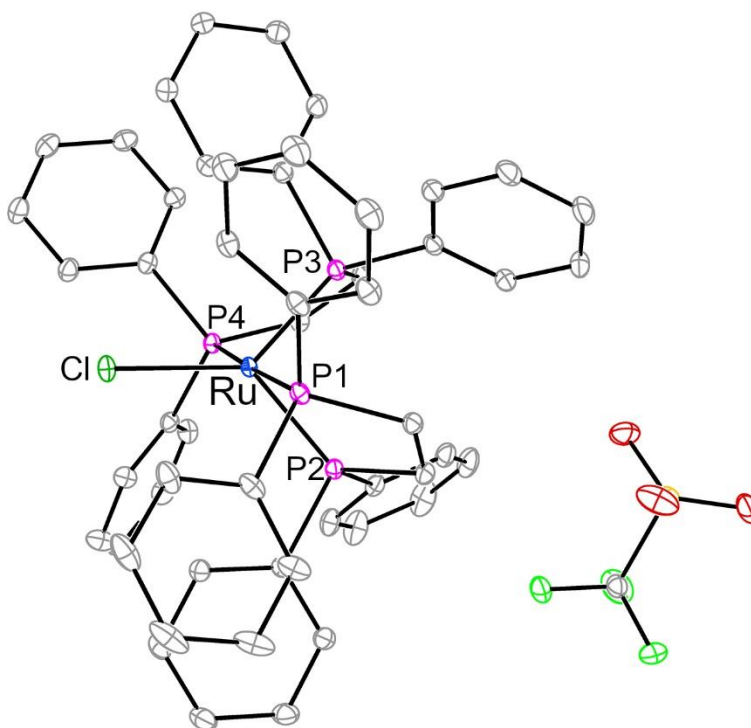
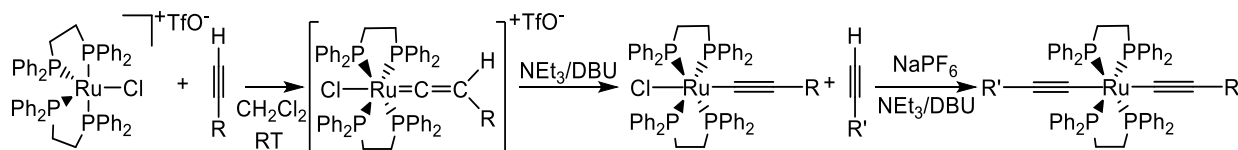


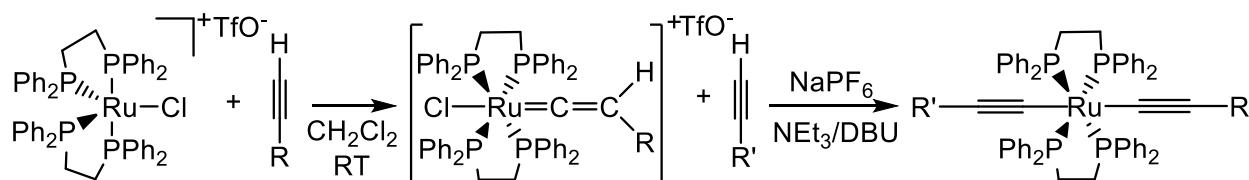
Figure 4.4. Molecular structure of $[\text{RuCl}(\text{dppe})_2]\text{OTf}$, generated from CCDC 719111

To add the second terminal alkynyl ligand, literature reports commonly follow a mechanistic pathway where the vinylidenes formed from the first addition are deprotonated to give the desired mono-alkynyl complexes (see Scheme 4.5). Removal of the excess alkyne ligand must be achieved before this deprotonation to prevent the formation of the symmetrical bis-alkynyl complex. The addition of the second ligand is accomplished upon the reaction of the mono-alkynyl and the desired alkynyl ligand in the presence of both NaPF_6 and NEt_3 .^{180,181}



Scheme 4.5. Pathway to generate unsymmetric Ru bis-alkynyls from $[\text{RuCl}(\text{dppe})_2]\text{OTf}$

A slightly different approach for *trans*-bis-alkynyls was advocated by the groups of Rigaut and Olivier (Scheme 4.6). Rather than adding a step to deprotonate the isolated vinylidene, the second ligand, a base (NEt₃ or DBU) and NaPF₆ were added to a one-pot reaction mixture with the vinylidene, which leads to the desired unsymmetric complexes in high yield.^{171,182–185} This mechanism is reminiscent of Scheme 4.3 and is rationalized based on the vinylidene being a better electron-donor to the metal center, which eases chloride abstraction prior to the addition of the second alkynyl ligand.¹⁵³ It is interesting to note in such an approach that the first alkynyl addition does not require the presence of an alkali metal salt but does so when the second alkynyl ligand is added. Another feature of interest is that when synthesizing unsymmetric species, the electron-donating alkynyl ligand is added before the electron-withdrawing alkynyl ligand,^{183,186} but others have noted differently¹⁶⁸ (see discussion above in section 4.3.2).

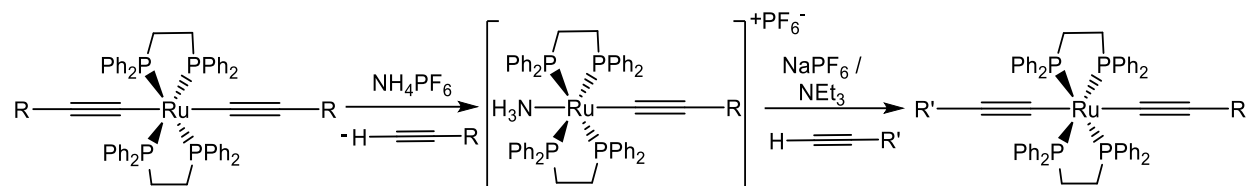


Scheme 4.6. Alternative pathway to unsymmetric Ru bis-alkynyls from [RuCl(dppe)₂]OTf

The use of [RuCl(dppe)₂]⁺ takes advantage of a previously under-utilized compound, *trans*-RuCl₂(dppe)₂, which provides ease of preparation as the [RuCl(dppe)₂]⁺ salt can be prepared from either isomer. The synthetic routes followed (Scheme 4.5 vs. Scheme 4.6) can also be varied, giving flexibility in the order of addition of the desired ligands. A potential drawback is that the triflate counteranion has been documented to produce triflate salt by-products which could react with the desired products. If the triflate interference occurs, the issue can be circumvented with the use of either a different Ag(I) salt or deprotonation with KO^tBu in methanol.¹⁶³

Use of mixed ligand complexes [Ru(C₂R)(X)(dppe)₂]⁺ (X = NH₃, H, CN, N≡C-R)

An alternative intermediate to [RuCl(dppe)₂]⁺ was first described by Touchard *et al.* in the seminal vinylidene paper.¹⁵³ As shown in Scheme 4.7, the reaction of *trans*-Ru(C₂R)₂(dppe)₂ (R = Ph, ⁿBu, SiMe₃) with NH₄PF₆ in dichloromethane resulted in the intermediate complexes *trans*-[Ru(C₂R)(NH₃)(dppe)₂]⁺, an example of which is shown in Figure 4.5 (R = Ph).



Scheme 4.7. Unsymmetric *trans*- bis-alkynyl Ru compounds via $[trans\text{-Ru}(\text{C}\equiv\text{C-R})(\text{NH}_3)(\text{dppe})_2]^+$

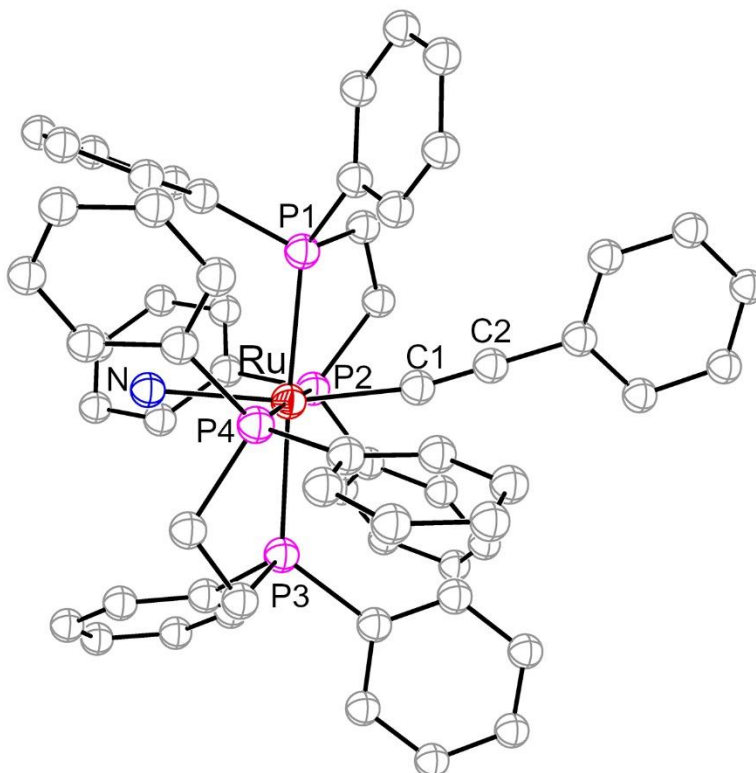


Figure 4.5. Molecular structure of $trans\text{-}[\text{Ru}(\text{C}_2\text{Ph})(\text{NH}_3)(\text{dppe})_2]^+$ generated from CCDC 1234388

Protonation of symmetrical bis-alkynyl complexes was also demonstrated using strong acids such as HCl, HBF₄, and CF₃CO₂H, but the intermediate complexes were observed to rapidly degrade, presumably due to the lack of a coordinating ligand for the open ruthenium coordination site.¹⁵³ The formation of these mixed ammonia-alkynyl ruthenium complexes proceeds with the protonation of one alkynyl ligand at the β carbon (C2 in Figure 4.5) with the ammonium ion, NH₄⁺. Protonation of the alkynyl ligand leads to the rearrangement to a vinylidene, promoting the release of the newly formed alkyne, and the rapid coordination of the NH₃ to the *in situ* generated 16 e⁻ Ru mono-alkynyl complex.

Subsequently, Dixneuf and co-workers expanded upon this type of reaction in order to synthesize the desired unsymmetric complexes using the mixed ligand complex $trans\text{-Ru}(\text{C}_2\text{R})(\text{NH}_3)(\text{dppe})_2^+$ as the starting material. Displacement of the labile NH_3 ligand with a different alkynyl ligand in methanol at 50°C resulted in the desired unsymmetric bis-alkynyl complexes in respectable yields ($>75\%$). The free ammonia ligand is displaced into the solvent and can deprotonate the intermediate vinylidene, regenerating the NH_4PF_6 salt and producing the desired bis-alkynyl complex, although NEt_3 can also be added to deprotonate the vinylidene if the use of NH_3 is unsuccessful (pK_b of $\text{NH}_3 = 4.75$; $\text{NEt}_3 = 3.75$). Expansion of this approach has also led to the generation of other mixed ligand systems such as hydrido-, carbonyl-, and isocyanide-alkynyl ruthenium complexes.¹⁸⁷

Complexes of mixed-ligands, $trans\text{-Ru}(\text{C}_2\text{R})(\text{NCR}')(\text{dppe})_2^+$ ($\text{NCR}' = \text{benzonitrile}$, cyanoferrocene, and 1,4-dicyanobenzene, and $\text{R} = \text{Ph}$ and Fc), were explored by Fillaut and co-workers.¹⁷² The reaction of $trans\text{-RuCl}(\text{C}_2\text{R})(\text{dppe})_2$ with nitriles in the presence of both NH_4PF_6 and NEt_3 in dichloromethane led to the rapid (< 1 hour at room temperature) formation of the mixed nitrile-alkynyl complexes, $trans\text{-[Ru}(\text{C}_2\text{R})(\text{NCR}')(\text{dppe})_2][\text{PF}_6]$. Bimetallic ruthenium complexes with either nitrile or alkynyl bridge were also generated in this study, albeit through differing synthetic methods. To generate the bridging nitrile complex (Figure 4.6), the reaction of $trans\text{-RuCl}(\text{C}\equiv\text{C-R})(\text{dppe})_2$ with varying equivalents of 1,4-dicyanobenzene led to the isolation of both the mono- (10 equivalents) and bimetallic (0.5 equivalents) complexes. Alternatively, the reaction of $[\text{RuCl}(\text{dppe})_2]^+$ with 1,4-diethynylbenzene afforded a bis-vinylidene complex, which was converted to a bimetallic complex with bridging alkynyl and terminal benzonitrile in the presence of NEt_3 , KPF_6 and 10 equivalents of benzonitrile.

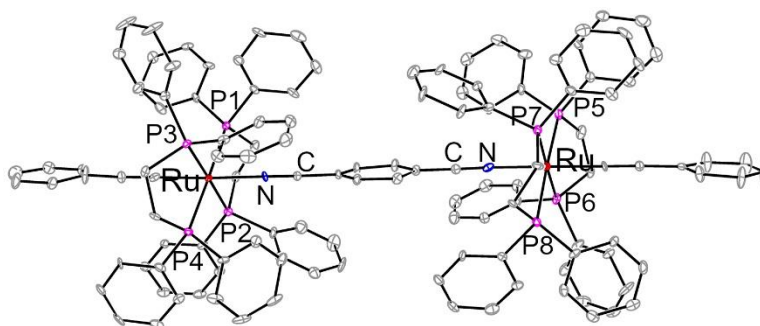
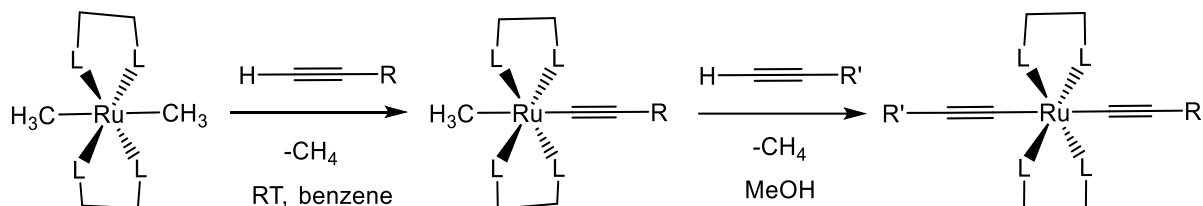


Figure 4.6. Molecular structure of $[(\text{dppe})_2(\text{Ph-C}\equiv\text{C})\text{Ru}(\text{N}\equiv\text{CC}_6\text{H}_4\text{C}\equiv\text{N})\text{Ru}(\text{C}\equiv\text{C-Ph})(\text{dppe})_2][\text{PF}_6]_2$ generated from CCDC 211235

4.3.3 Single bond metathesis synthesis of mono- and bis- Ru alkynyls



Scheme 4.8. Ru(II) bis-alkynyl synthesis from single-bond metathesis

Inspired by work on alkynyl complexes of Pt^{II} ,¹⁸⁸ Rh^{I} ,¹⁸⁹ and Co^{I} ,¹⁹⁰ Field *et al.* developed a single bond metathesis method to generate alkynyl complexes from alkyl complexes, initially based on a photochemical metathesis utilizing Fe^{II} methyl complexes.¹⁹¹ Both symmetric and unsymmetric Ru(II) bis-alkynyl complexes have been produced from a thermal metathesis reaction of *trans*- $\text{Ru}(\text{L-L})_2\text{Me}_2$ ($\text{L-L} = \text{dmpe}$ (di(methylphosphino)ethane)) (Scheme 4.8).¹⁹² *trans*- $\text{Ru}(\text{dmpe})_2\text{Me}_2$ (Figure 4.7) is the more reactive isomer that undergoes metathesis with an alkynyl ligand in less than 24 hours at room temperature, while the *cis*-isomer fails to react under the same conditions. As discussed below, the isomer dependence of reactivity $\text{Ru}(\text{dmpe})_2\text{Me}_2$ deviates from that of $\text{Ru}(\text{dppe})_2\text{Cl}_2$.

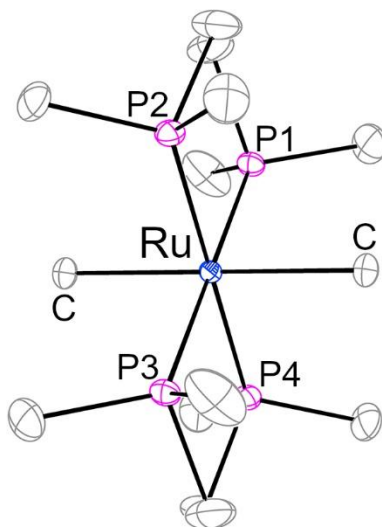


Figure 4.7. Molecular structure of *trans*- $\text{Ru}(\text{dmpe})_2\text{Me}_2$ generated from CCDC 665447

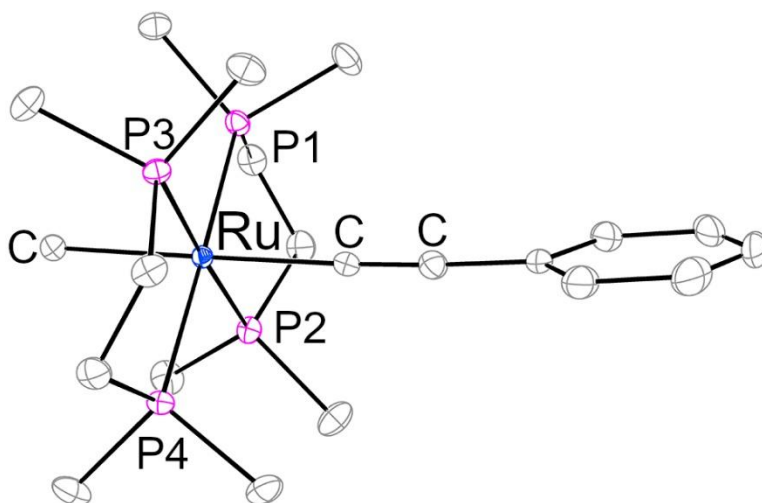


Figure 4.8. Molecular structure of *trans*-Ru(dmpe)₂Me(C≡C-Ph) generated from CCDC 665448

To generate symmetrical *trans*-bis-alkynyl complexes, only the presence of excess ligand and reflux are required to promote the metathesis reaction of *trans*-Ru(dmpe)₂Me₂ in benzene for solubility considerations. *trans*-Ru(dmpe)₂Me(C₂R) was identified as an intermediate through ³¹P NMR, and isolated after reaction with 1 equiv of alkynyl ligand at room temperature. *trans*-Ru(dmpe)₂Me(C₂R), an example shown in Figure 4.8, has proved to be a highly important starting point for the generation of symmetric, dissymmetric, and higher order di/tri-metallic alkynyl complexes. Later explorations into the synthesis of these symmetric *trans*- bis-alkynyl complexes with a wider range of ligands led to the discovery that *trans*-Ru(dmpe)₂Me₂ is actually capable of dimerizing terminal alkynes instead of undergoing single bond metathesis.¹⁹³ Under refluxing conditions, the di-alkyl starting material (5-8 mol%) was found to head-on dimerize terminal alkynes into either (*E*)- or (*Z*)-butenyne, dependent on the solvent and the alkynes utilized.

To prevent ligand scrambling and byproduct (symmetric bis-alkynyls) formation during the synthesis of unsymmetric complexes, replacement of the solvent with methanol (some benzene or toluene added to solubilize the starting materials) resulted in clean generation of the desired products under either thermo or photolytic conditions.¹⁹² Field and co-workers have utilized this synthetic method to generate numerous examples of both bi- and tri-metallic alkynyl bridged complexes,¹⁹⁴ and have begun studies to understand how both aromatic¹⁹⁴ and non-aromatic spacers¹⁹⁵ impact the electron transport pathways between the two end-capping Ru centers (see expanded discussion in section 4.4.2 below).

The advantage of this synthetic method is the limited effort required for work-up and purification after each metathesis reaction. The successful isolation of the mixed mono-alkynyl, mono-alkyl derivatives provides a useful stepping stone for the generation of a wide variety of bis- and polymeric Ru alkynyls. Methanol is noted to impact the solubility of the starting materials but is crucial to this synthetic method for generating products cleanly. As noted by Field *et al.*, this synthetic method provides another controlled route to highly polymerized products but does require the use of MeLi to generate the original starting material *trans*-Ru(dmpe)₂Me₂. As observed with the RuCl₂(dppe)₂ syntheses, *trans*-Ru(dmpe)₂Me₂ isomerizes into the kinetically inert *cis*-Ru(dmpe)₂Me₂ upon UV irradiation or sublimation, and conversion back to the *trans* orientation is deemed impossible.¹⁹² Avoiding exposure to UV light is critical to prevent the isomerization of both *cis*-RuCl₂(dppe)₂ and *trans*-Ru(dmpe)₂Me₂ into their respective kinetically inert isomers.

4.4 Electronic and opto-electronic materials

Beyond rich synthetic chemistry described above, *trans*-Ru(L-L)₂(C_{2n}R)₂ type compounds display intriguing electronic and optoelectronic properties owing to their electron-richness and extensively delocalized π -system. The Ru(II) center can be easily oxidized and reduced, and therefore serves as an effective ‘bridge’ for electron/hole to pass through, a highly desirable trait for materials design.⁶⁴

4.4.1 Non-linear optical materials

Non-linear optical (NLOs) materials possess inherent electronic properties that result in modification of the propagation characteristics of light they interact with, including changes to the phase, polarization, frequency, amplitude, or path of the light. The multitude of applications (optical storage, optical signal processing, frequency generation, optical signal switching, etc.) has garnered a long-standing interest in the pursuit of new NLO materials.¹⁹⁶ Studies of ruthenium-based alkynyl complexes have generally focused on the unsymmetric ‘donor-bridge-acceptor’ (D-B-A) construct. A more in-depth discussion on the theory of NLOs has recently been reviewed elsewhere.^{196,197}

The key metric for second-order NLO materials is a large hyperpolarizability value (β), classically achieved with 1) a polar charge distribution across the molecule (typically achieved with substituents with electron donating and accepting abilities opposite to each other), 2) a pathway for electron density to move through (π -conjugated electrons), and 3) an optimized conjugation length. Experimentally this is observed as metal-ligand charge transfer transitions, which are desirable at relatively low energies with high intensities. As such, Ru(II) alkynyl's NLOs properties are directly proportional to the amount and degree of effectiveness that electron density is able to be polarized throughout the molecule.

Humphrey^{179,181} and others¹⁹⁸ have successfully investigated the variation of bridge length, alkyne substituents, and use of the ligated metal unit as the 'donor' in dissymmetric systems to optimize the charge transfer and NLO properties of Ru(II)-based alkyne complexes. All Ru(II)-alkyne complexes have been prepared utilizing either a modification of the vinylidene synthesis or the use of $[\text{RuCl}(\text{dppe})_2]^+$ salts (see section 4.3.2 above), generating the desired products in moderate to high yields.

4.4.2 Molecular switches and wires

Molecular switches

The push towards molecular electronics necessitates molecules that possess inherent charge transfer properties to help realize the characteristics of operating as a 'wire' and as a 'switch'.¹⁴⁵ To be effective at either (or both), the designed molecules must undergo successful charge transport across the entire molecule.^{63,199} A good switch requires a component, typically a substituent of the alkyne ligand, that can be modulated with external stimuli such as light or electrical current to promote a change in the physical properties of the molecule (e.g., breaking or formation of bonds). These physical changes typically allow for modulation of the inherent electronic properties of the molecules, resulting in a molecule as a potential switch.²⁰⁰ Ideally these switches would be able to retain the 'information' in the form of electric current for long periods of time, but also be able to revert to the original state upon application of a different stimulus.

To realize a molecular switching system, Rigaut *et al.* utilized the vinylidene synthetic method (see section 4.3.2 above) to construct novel diarylethene-based organometallic complexes. The incorporation of oligo(phenyleneethynylene) (OPE) derivatives such as diethienylethene

(DTE) into a Ru(II)-alkynyl framework yielded functional switches: upon either UV/visible irradiation or electrochemical current application, the DTE unit can make or break a bond between the two thiophene rings. These Ru(II)-alkynyl molecules can then be derivatized to allow for immobilization on gold surfaces as SAMs (self-assembled monolayers) for switch testing, and devices realized includes a novel Au-molecule-Au transport junction that exhibits controllable switching of conductivity between two distinct states,^{68,201} as illustrated in Figure 4.9. Akita and co-workers have recently utilized a similar molecular framework to study the switching capability of the anthrahydroquinone(AHQ) / anthraquinone(AQ) system, as this substituent can achieve reversible switching between AHQ and AQ through both redox stimuli and pH stimuli when attached to the Ru(dppe)₂ framework.¹⁶⁷

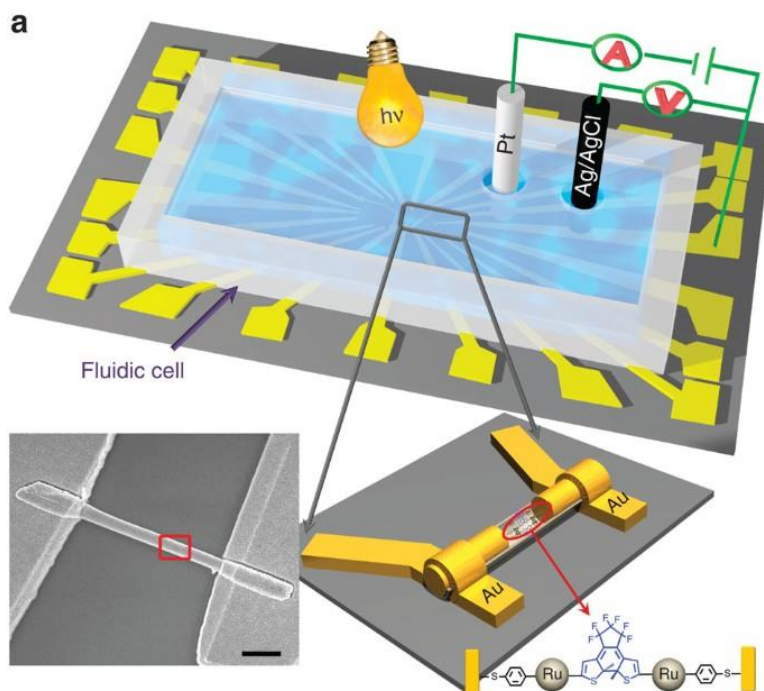


Figure 4.9. Schematics of the functionalized nanogap devices based on -Ru-(C₂-DTE-C₂)-Ru-complex. Inset: SEM image of a device fabricated by OWL-generated nanowire. Taken from Ref.⁶⁸

Wire-like molecules and molecular wires

Realization of molecular wires requires similar characteristics to those of molecular switches, although there is no need for components changing physical properties upon application of external stimuli. Here we draw distinction between the demonstration of “wire-like” features through bulk solution study and nano-junction measurement of conductance for authentic “molecular wires”.

The earliest comprehensive demonstration of the wire-like character of Ru(bisphosphine)₂alkynyls is the study of *trans*-Ru(dppe)₂(C₂Fc)₂ by Wolf and coworkers: the sequential Fc center oxidations were determined with a $\Delta E_{1/2}$ of 220 mV, and the [Fc---Fc]⁺¹ mixed valent ion was assigned as Robin-Day class II on the basis of spectroelectrochemical investigation of intervalence charge transfer (IVCT) bands.^{155,156} Rigaut *et al.* investigated wire-like molecules based on both the end-capped complex and complexes with multiple ruthenium fragments linked by the alkynyl chains. The end-capped *trans*-[Cl(dppe)₂Ru-(C≡C)₆-Ru(dppe)₂Cl] complex displayed sequential oxidations but no reductions within the solvent window.¹⁶⁹ When multiple Ru(dppe)₂ units were bridged with 1,4-diethynylbenzene, the resultant molecules exhibited Ru-Ru electronic interactions in different oxidation states.¹⁷¹ Use of other π -conjugated systems such as nitriles and thienyls have also been investigated for their abilities to modulate electron communication between ruthenium centers. Comparing electrochemical behaviors of bridged complexes, *trans*-[(dppe)₂(Ph-C≡C)Ru(1,4-N≡C-C₆H₄-C≡N)Ru(C≡C-Ph)(dppe)₂][PF₆]₂ and *trans*-[(dppe)₂(Ph-C≡N)Ru(1,4-C≡C-C₆H₄-C≡C)Ru(N≡C-Ph)(dppe)₂][PF₆]₂, the former displayed a single Ru(+3/+2) oxidation wave while the latter exhibited two Ru(+3/+2) oxidation waves, illustrating the importance of the nature of the bridges.¹⁷² The separation of the two oxidation potentials in *trans*-[(dppe)₂(Ph-C≡N)Ru(1,4-C≡C-C₆H₄-C≡C)Ru(N≡C-Ph)(dppe)₂]²⁺ was noted to be smaller than those of a similar compound, *trans*-[(dppe)₂Cl-Ru(1,4-C≡C-C₆H₄-C≡C)Ru-Cl(dppe)₂],²⁰² highlighting the effect of the capping ligands on the HOMO level.

A series of bimetallic Ru complexes [Cl(dppe)₂Ru-C≡C-(3R-C₄H₂S)-C≡C-Ru(dppe)₂Cl] (R = H, C₂H₅, C₃H₇, C₄H₉, C₆H₁₃, OMe, CN) were prepared using the vinylidene method by Patra *et al.*²⁰³ The Ru-Ru interaction is negatively attenuated by the introduction of 3-R substituent of the thienylethynyl group, which was attributed to the adverse substituent effect on thermodynamic stability of the resultant cations by the authors. The potential separations of the stepwise Ru(+3/+2) oxidation waves can be as large as 390 mV (R = H), indicating strong Ru-Ru interactions, while

that of $R = CN$ is negligible. Field *et. al.* have also probed electronic interactions through polycyclic saturated and pseudo-aromatic spacers.¹⁹⁵ The bridging complexes [*trans,trans*-{Ru(dmpe)₂(C≡C'Bu)}₂(μ-C≡C-C₈H₁₂-C≡C)], [*trans,trans*-{Ru(dmpe)₂(C≡C'Bu)}₂(μ-C≡C-*p*-C₂B₁₀H₁₀-C≡C)], and [*trans,trans*-{Ru(dmpe)₂(C≡C'Bu)}₂(μ-C≡C-*p*-C₆H₄-C≡C)] all displayed two Ru(+3/+2) waves, with separations ranging from the moderate 69 mV (-C₈H₁₂-) to significant 295 mV (-C₆H₄-). It should be noted that further comparison of the degree of electron delocalization in the last four examples^{172,195,202,203} is challenging due to both the absence of proper analysis of IVCT bands and moderate $\Delta E_{1/2}$ values.

The first study of authentic “molecular wires” was the conductance study of Ru(II) alkynyls from the cross-wire junction measurement of the SAMs formed by *trans*-Ru(dppe)₂(C₂Ar)₂ and its dimeric / trimeric analogues with nitrile capping groups by Rigaut, Frisbie and coworkers,²⁰⁴ and noteworthy among many interesting findings is a very weak distance dependence of the wire resistance. Similar conclusions were drawn from the subsequent CP-AFM (conducting probe atomic force microscopy) measurement of the same group of Ru(II) σ -acetylides with thiol-caps by Rigaut, Frisbie *et al.*²⁰⁵ In the more recent years, Rigaut, Lagrost and coworkers examined the dynamics of the electron transfers within the monolayers of the afore-mentioned Ru(II) acetylides with high-speed voltammetry, and speculated the relevance of the rates determined to the possibility of charge storage and redox switchable devices.^{206,207}

Akita and co-workers demonstrated that single-molecule conductance of mono-Ru-molecular wires with pyridine termini is better than their organic counterparts, despite the increased length.²⁰⁸ The enhancement of the single molecule conductance over the pure organic analogue is attributed the improved energy alignment between the high-lying HOMO that is distributed across the entire Ru-alkynyl molecule and the Fermi level of Au electrodes. Using the Au(I) capped *trans*-(C_{2n})Ru(dppe)₂(C_{2n}) complexes ($n = 2 - 4$), Akita and coworkers achieved the direct insertion of -(C_{2n})Ru(dppe)₂(C_{2n})- fragment between Au nanojunction, and remarkably high conductance ($10^{-3} - 10^{-2} G_0$; G_0 is the conductance quantum) was determined using the STM-break junction technique,⁶⁷ as shown in Figure 4.10. *trans*-Ru(C₂-3-C₄H₃S)₂(dppe)₂ was studied using scanning tunnelling microscope break-junction technique by Martin, Lambert, Low and coworkers, which yielded a modest conductance range of 1 to $3 \times 10^{-4} G_0$.²⁰⁹ Elegantly designed by Cea, Martin, Low and coworkers, the SAM of *trans*-Ru(C₂-3-C₄H₃S)(C₂-1,4-C₆H₄C₂-Au(PPh₃))(dppe)₂ was formed on an Au substrate, and the removal of PPh₃ via mild thermal treatment resulted in the

formation of Au nanoparticles atop the SAM.²¹⁰ The CP-AFM measurement of the said junction gave an estimated conductance of $1.6 \times 10^{-4} G_0$.²¹⁰

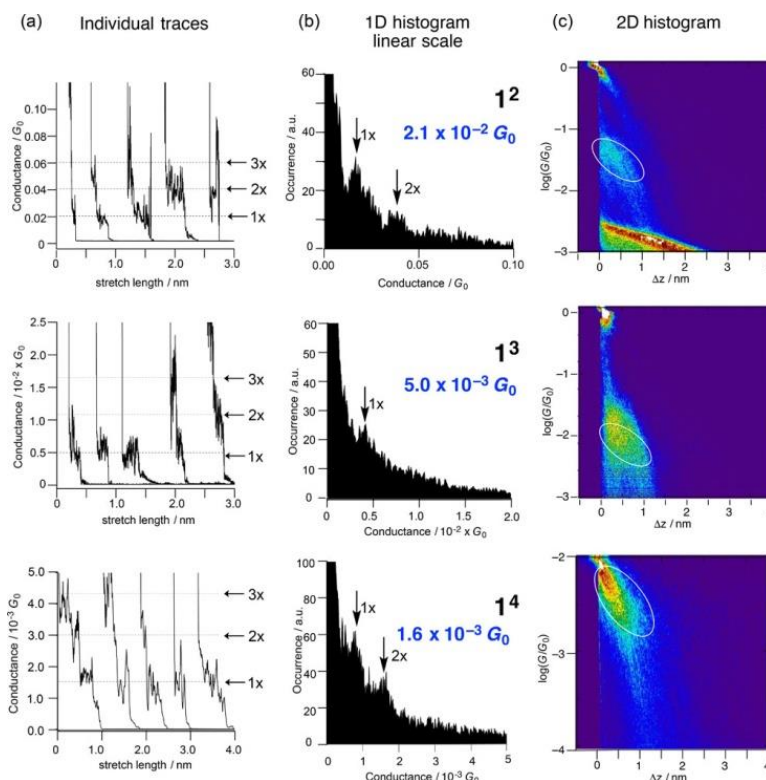


Figure 4.10. Molecular conductance of $-(C_{2n})Ru(dppe)_2(C_{2n})-$ measured with the STM-break junction technique; $n = 2$ (**1²**), 3 (**1³**) and 4 (**1⁴**). Taken from Ref.⁶⁷

Overall, many research groups have successfully modulated ligand design of Ru(II) alkynyl complexes and demonstrated their “wire-like” properties. However, device implementation of switches and wires remains a significant challenge.^{145,200}

4.4.3 Dye-sensitized solar cells

Over the past decade, dye-sensitized solar cells (DSSCs) have been viewed as a promising technology due to the high theoretical efficiencies and potential low cost.²¹¹ Again, Ru(II)-acetylide complexes are highly advantageous for this application due to their well-documented π -conjugation between the d orbitals with the π^* system of the alkynyl ligands that produces intense, low energy MLCT excitations. These excitations can be utilized to inject holes (p -type DSSC) or electrons (n -type DSSC) into the conduction band of the corresponding electrode (NiO or TiO_2)

upon photoexcitation of the dye. The other advantage of Ru(II)-acetylide complexes for models of dyes in DSSCs is their facile and high-yielding syntheses, as described above, easily producing a wide variety of model complexes for the study of charge transport through dissymmetric alkynyl complexes.

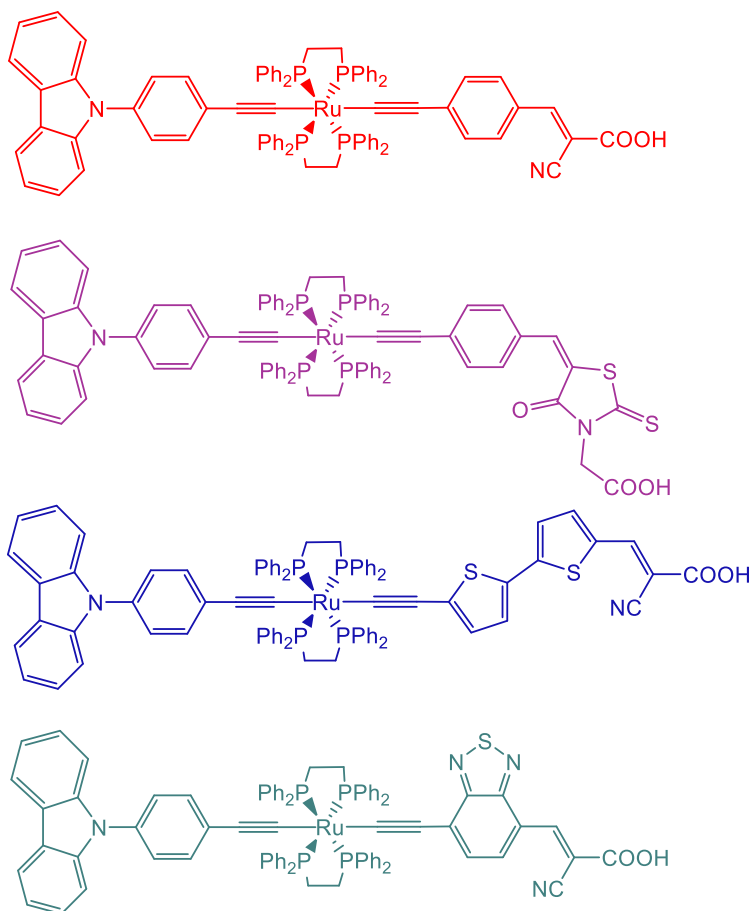


Figure 4.11. Representative ‘D-B-A’ molecules with varying anchors and ‘acceptor’ ligands for DSSCs from Ref.²¹², colored as they appear as CH₂Cl₂ solutions

The dye molecules, classically Ru-based organometallic molecules with high charge transport capabilities and the ability to efficiently absorb the solar spectrum, exhibit a ‘D-B-A’ framework that produces chromophores based on MLCT bands ranging from 520 – 660 nm (see Figure 4.11 above).²¹² These unsymmetrical Ru alkynyl complexes were some of the first examples of efficient blue dyes with overall power conversion efficiencies (PCEs) ranging from 6.10-7.08%. The device’s PCE was slightly improved (7.49%) when two dyes were co-deposited in a 4:1 ratio onto TiO₂, a result of panchromatic spectral absorption.²¹² Representative incident

photon-to-current conversion efficiency and current density–voltage profiles of a Ru based DSC¹⁸⁴ are provided in Figure 4.12. Green dyes, desirable for low-energy photon absorption in the 500 – 800 nm range, have also been generated using the Ru unsymmetrical framework with a PCE of 5.23%. Competitive back electron-transfer was attributed to the lower PCE in the green dye when compared to the related purple-blue dye (PCE of 6.45%).¹⁸²

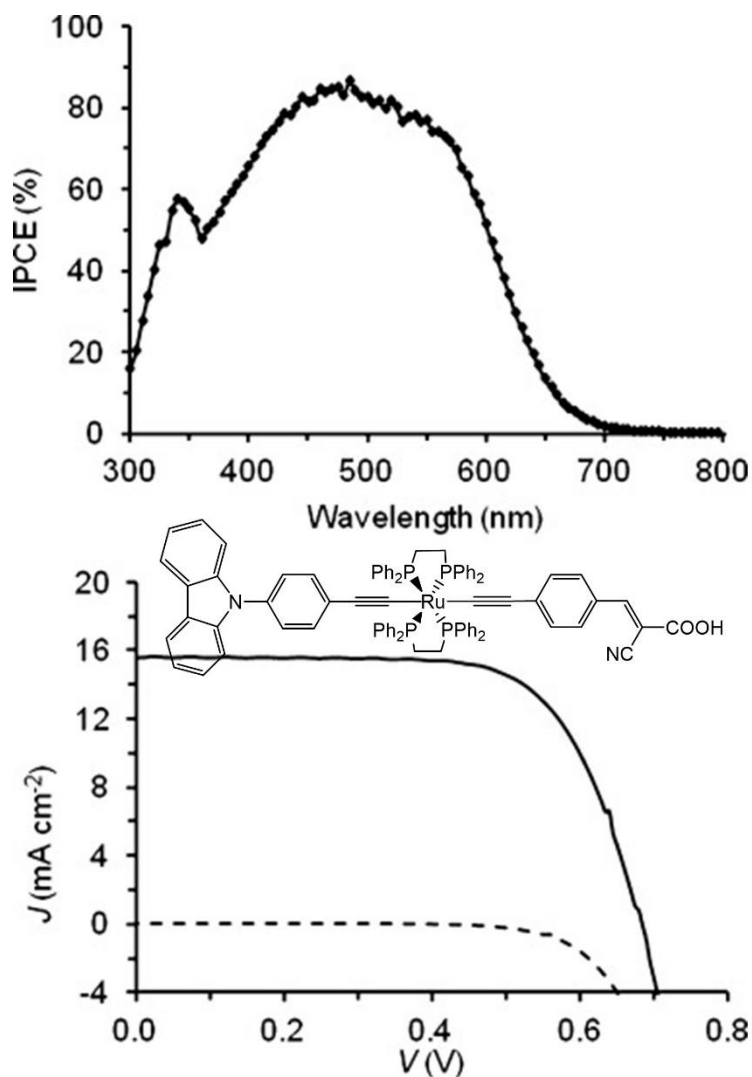


Figure 4.12. (top) Incident photon-to-current conversion efficiency (IPCE) and (bottom) current density–voltage profiles of a DSSC with a representative Ru dye (insert), under 100 mW cm^{-2} illumination (solid line) and in the dark (dashed line). Modified from Ref.¹⁸⁴

Modification of the dyes' anchoring groups also impact PCEs of DSSCs. Use of cyanoacrylic acid as the TiO₂ anchor resulted in both higher dye loading and increased dye

stability, generating higher PCEs (6.45% and 5.23%) when compared to dyes utilizing carboxylic acid anchors (PCE of 3.11%).¹⁸² For *n*-type DSSCs, these anchoring groups are typically located off the ‘acceptor’ substituent to facilitate injection of the electron into the TiO₂ support.^{182,184,212} For *p*-type DSSCs, these anchoring groups are located off the ‘donating’ substituent to facilitate injection of the hole into the NiO support. Olivier *et al.* have also investigated unsymmetrical Ru organometallic complexes as *p*-type DSSCs. Low overall PCEs were noted for their two complexes (0.079% and 0.038%) but are on par for dyes with the same anchoring group for this application.²¹³ The low PCEs were attributed to low dye-loading, and future optimization will be based on varying anchoring groups and alkynyl substituents.¹⁸³ Of note is how features that help improve DSSCs capabilities also improve NLO characteristics, a possibility investigated by Nisic and coworkers.¹⁸⁶

4.5 Conclusions and future outlooks

This review focuses on common synthetic schemes to generate mono- and bis-alkynyl complexes based on Ru(dppe)₂ and Ru(dppm)₂ units. These complexes exhibit rich spectroscopic and electronic features that lead to a wide variety of materials applications. These studies clearly demonstrate the importance of incorporating the Ru(L-L)₂ framework into a π -conjugated alkyne-based system to afford electronically / optically active molecules with tunable properties. A broad comparison between synthetic methods has been attempted to aid in the readers own synthetic design. The alkynylation of Ru(dppe/m)₂ often occurs at very mild conditions that are tolerant towards sensitive functional groups, which is highly desirable for the incorporation of chromophores and electron acceptors, as demonstrated in the above mentioned DSSC work. Additionally, facile preparation of Ru(dppe/m)₂ oligoynyl compounds allows for further exotic covalent transformation, such as the end capping with Au-carbene demonstrated by Akita and coworkers.⁶⁷ Other possible but unexplored transformations for Ru(dppe/m)₂ alkynyls include the *click* reaction to form 1,2,3-triazole derivatives,²¹⁴ the [2+2] cycloaddition reaction between two C \equiv C bonds (demonstrated for CpRu(dppe) alkynyls),²¹⁵ and the CA-RE ([2+2] cycloaddition and retroelectrocyclization) reaction with electrophilic olefins.^{215,216} Since a rich variety of chromophores and electrophores can be introduced using these transformations, the sky is the limit for Ru(dppe/m)₂ alkynyls as synthons for opto-electronic materials.

CHAPTER 5. SYNTHESIS, STRUCTURAL & SPECTROSCOPIC ANALYSIS OF MONO- AND UNSYMMETRIC BIS-ALKYNYL COMPOUNDS BASED ON RU(II)(C₂NAP^R)

5.1 Abstract

The synthesis and characterization of both mono- and bis-alkynyl Ru compounds utilizing the highly electron-withdrawing NAP^R moiety (NAP^R = *N*-R-1,8-naphthalimide) based on either a Ru(II)(dppe)₂ (dppe = 1,2-bis(diphenylphosphino)ethane) bridge or a Ru(II)(dppm)₂ (dppm = 1,2-bis(diphenylphosphino)methane) bridge are reported herein. The four mono-alkynyl compounds, *trans*-RuCl(C₂NAP^R)(dppe)₂ (**13** and **14**) and *trans*-RuCl(C₂NAP^R)(dppm)₂ (**16** and **17**) were prepared by reaction of *cis*-RuCl₂(dppe)₂ or *cis*-RuCl₂(dppm)₂ and HC₂NAP^R in the presence of a weak base, with R as isopropyl (iPr, **13**, **16**) and mesityl (mes, **14**, **17**). Preparation of an unsymmetric bis-alkynyl compound **15**, *trans*-Ru(C₂Ph)(C₂NAP^{mes})(dppe)₂, was achieved via reaction of a previously reported mixed-ligand intermediate, [(dppe)₂Ru(NH₃)(C₂Ph)]PF₆, with HC₂NAP^{mes} in the presence of a weak base. All new compounds were characterized via electronic absorption, fluorescence, IR, and ¹H NMR spectroscopies and cyclic voltammetry. The molecular structures of **13–17** were established using single-crystal X-ray diffraction analysis, and preliminary density functional theory analysis was performed to investigate the electronic structures of **14**, **15** and **17**.

5.2 Introduction

Organometallic compounds that incorporate metal atoms into the conjugated π network of alkynyl ligands have long been studied for use as photovoltaic materials,^{62,211,217} non-linear optical materials^{196,197,218} and molecular electronic devices.^{219,220} Metal-acetylide motifs have long been known to mediate charge transfer between two metal centers and have been used as building blocks for constructing prototypical molecular wires^{26,221} and devices.^{27,113,200,219,222} The attraction arises from the electron-rich nature of the d⁶(M)-C \equiv C fragments,²²³ the ease of modification with known synthetic methods^{64,135,224} and the rigid nature of these compounds that results in easily determined structure-property relationships. The use of ruthenium bis-alkynyl compounds as *bridging* units has been explored in dye-sensitized solar cells by Olivier,^{182–184,225} in non-linear optical systems

by Humphrey^{168,181,226} and others,¹⁹⁸ as ‘wire-like’ molecular compounds by Low,^{220,227–229} and as dual-responsive molecular switches by Akita¹⁶⁷ and Rigaut,^{68,171,185,200,230} who with X. Guo has recently demonstrated functional single-molecule electrical channels within a solid-state configuration.²³¹

Photo-induced electron-transfer (PET) is a field of intense study due to its relevance to both natural photosynthetic processes²³² and photovoltaic systems.²³³ The mechanism of intramolecular PET typically involves the formation of a charge separated excited state (CSS) after the absorption of solar energy, with the goal of generating a photocurrent.^{234,235} These CSSs are formed after electron density shifts from an electron donor (*D*) to an electron acceptor (*A*) via a bridging unit (*B*) and may be long lived. Molecular donor-bridge-acceptor (*D-B-A*) structures have arisen as model systems of PET processes in the past 20 years.^{236,237} Despite a shift towards modulation of these intramolecular PET processes using external stimuli such as pH changes²³⁸ or hydrogen bonding,²³⁹ modulation on the molecular scale remains a challenge. An alternative approach has been perturbation of the generated excited states via excitation of a bond along the PET pathway. Weinstein and co-workers have developed an elegant example utilizing *trans*-Pt(II)-bis-alkynyl *D-B-A* compounds and demonstrated that the decay pathways of the PET excited state could be significantly attenuated through IR excitation of the C≡C bonds.^{240,241}

Our laboratory has been exploring alkynyl chemistry based on the M(cyclam) unit where M = Cr, Fe, Co and Ni.^{242,243} Multiple *D-B-A* complexes based on Co(cyclam) have been prepared and investigated for PET processes therein. However, low-lying metal-centered states were found to quickly deactivate the desired CSS, resulting in a short CSS lifetime and no chance for IR modulation.²⁴⁴ With the reported ease of synthesis of unsymmetric bis-alkynyl ruthenium compounds,^{64,135,224} we became interested in the impact of attaching a highly electron-withdrawing (*A*) alkynyl ligand, HC₂NAP^R (R = isopropyl, mesityl), to a Ru(II)(dppe)₂ or Ru(II)(dppm)₂ *bridging* unit to generate both the *B-A* and *D-B-A* compounds (see Figure 5.1 below) to complement our previous Co(cyclam) studies. The details of synthesis and structural, spectroscopic and voltammetric characterizations are reported herein.

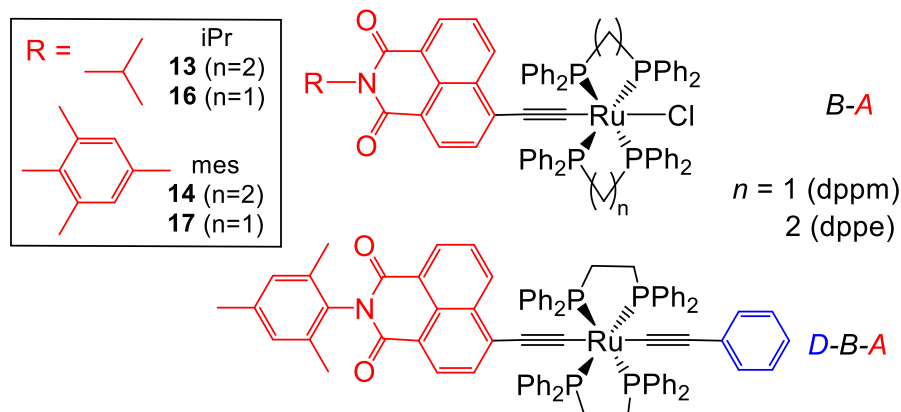
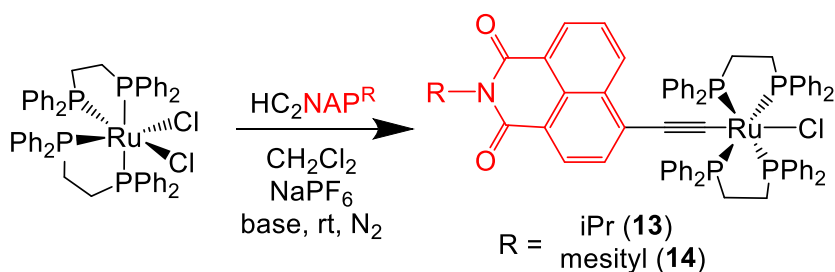


Figure 5.1. (top) *trans*-RuCl(C₂NAP^R) compounds (*B-A*) based on dppe (**13** and **14**) or dppm (**16** and **17**) units; (bottom) *trans*-Ru(C₂NAP^{mes})(C₂Ph)(dppe)₂ (**15**) (*D-B-A*) compound

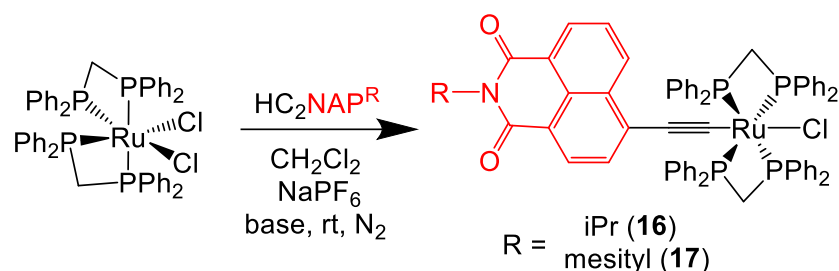
5.3 Results and Discussion

5.3.1 Synthesis

As shown in Schemes 5.1 and 5.2, the reaction between *cis*-RuCl₂(dppe)₂ (Scheme 5.1) or *cis*-RuCl₂(dppm)₂ (Scheme 5.2) and HC₂NAP^R (R = iPr, mesityl)^{245,246} under N₂ utilizing weak base conditions in the presence of a non-coordinating salt (a method pioneered by Touchard, see section 4.3.2 above),¹⁵³ generated the desired mono-alkynyl *B-A* (where *B* is the ‘bridge’ and *A* the ‘e⁻ acceptor’) compounds, *trans*-RuCl(C₂NAP^R)(dppe)₂ (**13** and **14**) and *trans*-RuCl(C₂NAP^R)(dppm)₂ (**16** and **17**).

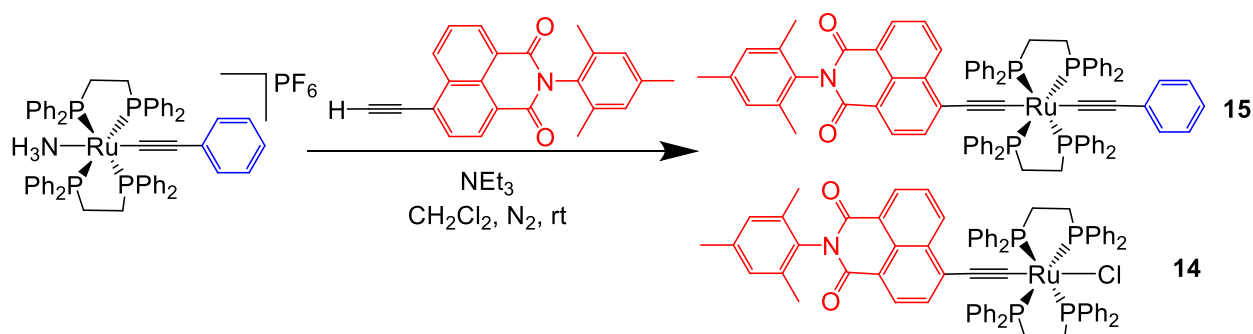


Scheme 5.1. Synthesis of **13** and **14** using *cis*-RuCl₂(dppe)₂, HC₂NAP^R (R = iPr, mesityl) and weak base conditions



Scheme 5.2. Synthesis of **16** and **17** using *cis*-RuCl₂(dppm)₂, HC₂NAP^R (R = iPr, mesityl) and weak base conditions

Although initial yields of the crude mono-alkynyl materials were high, significant losses of the product occurred during purification via column chromatography and during recrystallization attempts, particularly in chlorinated solvents but also in non-chlorinated solvents, resulting in low yields (9–30%). Degradation of **13–17** to a [Ru(dppe/m)₂]⁺ complex and free -C₂NAP^R materials was readily observed via TLC monitoring upon prolonged exposure to light for all compounds studied herein, so light was excluded as much as possible during synthesis, purifications, and characterization. This sensitivity to both light and chlorinated solvents was not reported for related Co(cyclam)(C₂NAP^{mes})²⁴⁶ or *trans*-Pt(PBu₃)₂(C₂NAP^{octyl}) complexes,²⁴⁰ but was observed for both the CpRu(dppe)(C₂NAP^{Me}) and Cp*Ru(dppe)(C₂NAP^{Me}) metal alkynyl compounds.²⁴⁷ Despite previous reports of tight control of equivalencies of alkynyl ligands needed to prevent formation of the symmetric bis-alkynyl products,¹⁶³ no evidence (TLC or MS) of the formation of the symmetrical *trans*-Ru(C₂NAP^R)₂(dppe/m)₂ has been found during these reactions. A 1:1 ratio of Ru to alkyne ligand was utilized to ease purification of the desired products.



Scheme 5.3. Synthesis of **15** (and by-product **14**) using [(dppe)₂Ru(NH₃)(C₂Ph)]PF₆, HC₂NAP^{mes} and weak base conditions

Synthesis of an unsymmetric bis-alkynyl *D-B-A* compound, *trans*-Ru(C₂Ph)(C₂NAP^{mes})(dppe)₂ (**15**), was achieved through use of an underutilized synthetic pathway previously reported by Touchard et al.,^{153,187} shown in Scheme 5.3. Reacting the previously reported mixed ligand complex, [(dppe)₂Ru(NH₃)(C₂Ph)]PF₆,¹⁸⁷ with HC₂NAP^{mes} in the presence of triethylamine (NEt₃) gave both **14** and **15** as products. Column chromatography (1:2 THF/hexanes w/ 3% MeOH, v/v) was required to purify **15** from **14** and -C₂NAP^{mes} impurities. Attempts to utilize the vinylidene pathway¹⁵³ to generate **15** produced both **15** and **14**, but the yields of **15** were so low that attempts to purify before degradation were unsuccessful. Lithiations of **14** with LiC₂Ph degraded the starting material to intractable products. The production of **14** during the synthesis of **15** is postulated to be caused by degradation of **15** via loss of the -C₂Ph ligand and coordination of a Cl⁻ from the CH₂Cl₂ solvent utilized for this reaction. Attempts to generate an unsymmetric *D-B-A* compound utilizing the dppm framework were unsuccessful, as reactions using vinylidene intermediates, like the dppe framework, only produced the mono-alkynyl *B-A* compounds **16** or **17**. An analogous [(dppm)₂Ru(NH₃)(C₂Ph)]PF₆ complex has not been synthesized but remains an intriguing possibility for future studies.

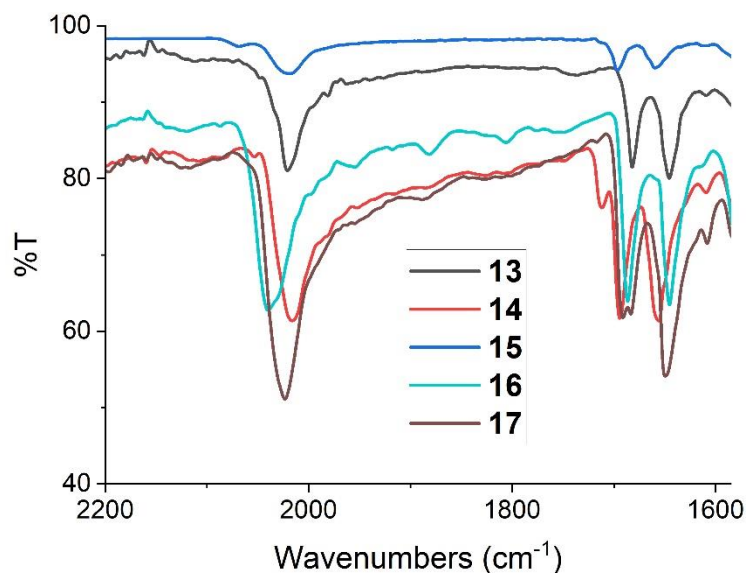


Figure 5.2. FTIR spectra of **13–17**

Compounds **13–17** are all deep red-purple solids, and – if sequestered from light and chlorinated solvents – are stable for over a month. The compounds are diamagnetic, enabling

characterization of some of these compounds with ^1H NMR (Figures D.1 and D.2 in Appendix D below). The characteristic $\nu(\text{C}\equiv\text{C})$ stretch observed in the FTIR spectra (shown in Figure 5.2) indicated the successful incorporation of the alkynyl ligands for compounds **13**–**17**, with **15** containing two stretches, one for each alkyne. The distinctive $\nu(\text{C}=\text{O})$ stretches are also visible in Figure 5.2, confirming incorporation of the -NAP^{R} ligand. Additionally, all compounds were analyzed with electronic absorption and fluorescence spectroscopies, cyclic and differential pulse voltammetry, and single crystal X-ray diffraction studies.

5.3.2 Molecular Structures

The compounds **13**–**17** have been characterized with single crystal X-ray diffraction. Their molecular structures are shown in Figures 5.3–5.7, with selected bond lengths and angles provided in Table 5.1. Full crystallographic details can be found in Table D.1 in Appendix D below.

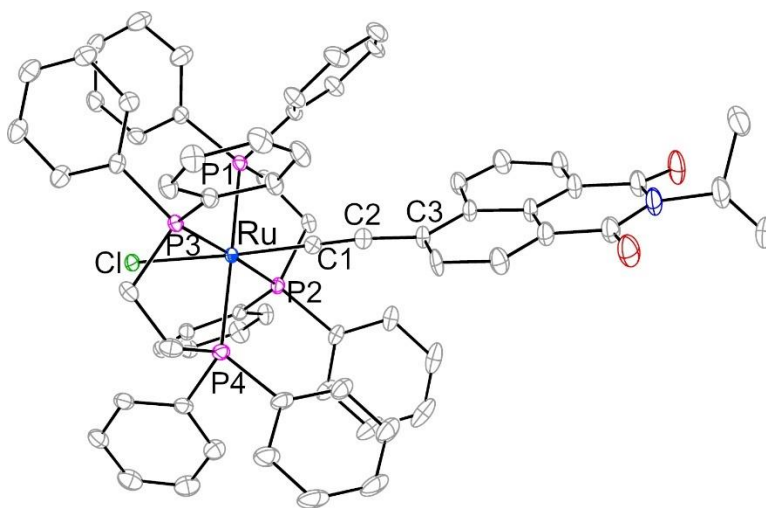


Figure 5.3. ORTEP plot of **13** at 30% probability level. H atoms, disorder and solvent molecules removed for clarity

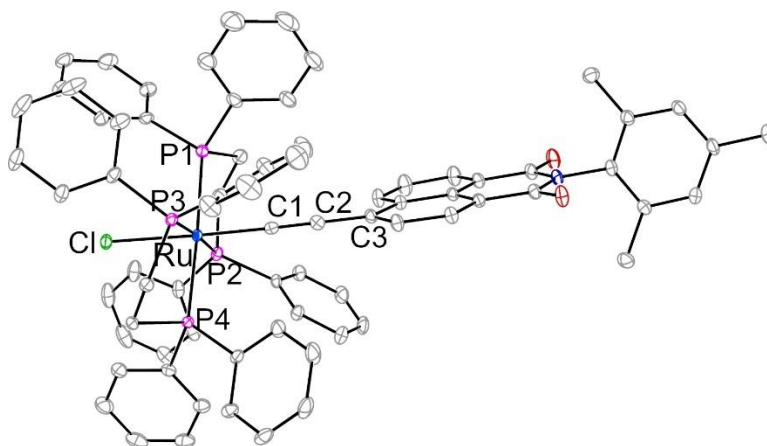


Figure 5.4. ORTEP plot of **14** at 30% probability level. H atoms, disorder and solvent molecules removed for clarity

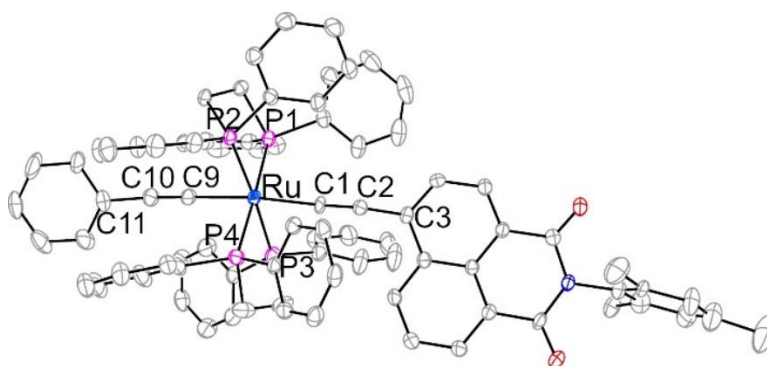


Figure 5.5. ORTEP plot of **15** at 30% probability level. H atoms and disorder removed for clarity

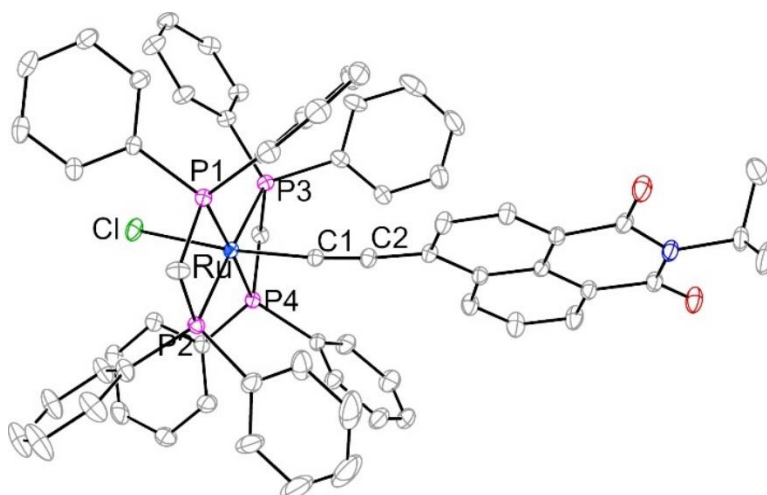


Figure 5.6. ORTEP plot of **16** at 30% probability level. H atoms, disorder and solvent molecules removed for clarity

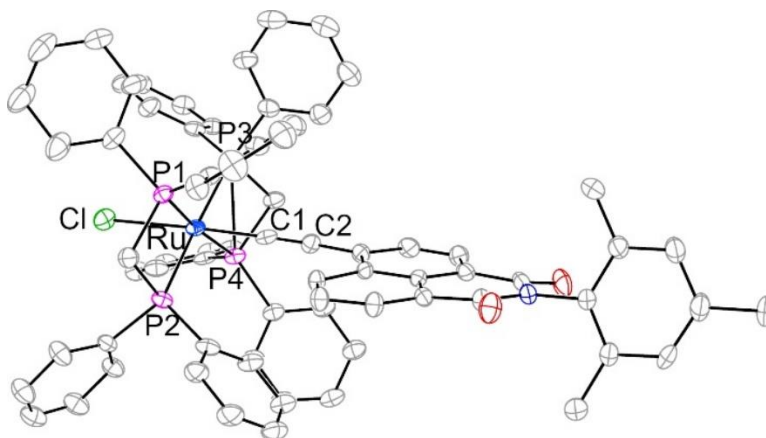


Figure 5.7. ORTEP plot of **17** at 30% probability level. H atoms and disorder removed for clarity

The Ru centers of compounds **13–17** all assume a pseudo-octahedral geometry with the alkynyl and Cl/alkynyl *trans*- to each other. Consistent with other unsymmetric bis-alkynyl compounds,^{152,165,181,248–250} the Ru–C bond lengths in **15** (2.060(2) and 2.079(2) Å) are significantly longer than the Ru–C bond lengths for the mono-alkynyl compounds, 1.988(5) Å (**13**), 1.988(6) Å (**14**), 1.988(4) Å (**16**), and 1.983(5) Å (**17**). This is consistent with the increased *trans*-influence of the alkynyl ligand, as alkynyl ligands are a stronger σ -donor than the chloride ion. This increased donor strength results in a weaker bond, increasing the Ru–C bond lengths in **15**.

When compared to previously reported *trans*-RuCl(C₂R)(dppe)₂ compounds,^{151,152,163,251,252} the Ru–C bond lengths for **13** and **14** are notably short (comparisons provided in Table D.2 and D.3), but the Ru–Cl bond lengths (2.4712(8) Å for **13** and 2.4781(5) Å for **14**) are about average. This suggests that the strong electron-withdrawing nature of -NAP^R does impact the Ru–C bond length, presumably due to the removal of electron density, but does not strongly impact the bonds *trans* to it. No large difference in either Ru–Cl or Ru–C bond lengths is noted when comparing the dpmm mono-alkynyl complexes (**16** and **17**) with the dppe analogues (**13** and **14**).

Table 5.1. Selected bond lengths (Å) and angles (deg.) for compounds **13–17**

	13	14	15	16	17
Ru–Cl	2.4712(8)	2.4781(5)	-	2.465(1)	2.4878(2)
Ru–C1	1.988(5)	1.988(6)	2.060(2)	1.988(4)	1.983(5)
Ru–C9	-	-	2.079(2)	-	-
C1–C2	1.200(6)	1.210(6)	1.222(1)	1.216(6)	1.223(7)
C9–C10	-	-	1.199(3)	-	-
Ru–P _{avg}	2.383[2]	2.368[1]	2.358[1]	2.347[2]	2.351[3]
Cl–Ru–C1	177.0(5)	176.7(2)	-	173.0(1)	173.18(2)
C1–Ru–C9	-	-	174.57(9)	-	-
C1–C2–C3	173.1(8)	178.3(5)	175.9(7)	173.5(4)	172.7(7)
C9–C10–C11	-	-	172.0(3)	-	-

5.3.3 UV/Vis Absorption and Emission Spectra

The UV-Vis absorption spectra of compounds **13–17** and HC₂NAP^{mes} as THF solutions are shown in Figures 5.8 and 5.9 and the λ_{max} and ν_{max} of the MLCT transitions are given in Table 5.2. These compounds are all colored a deep red-purple, a stark change from the bright yellow of the *cis*-RuCl₂(dppe)₂ starting material, matching other CpRu(C₂NAP^{Me}) and Cp^{*}Ru(C₂NAP^{Me}) compounds.²⁴⁷

The ground-state absorption spectra of compounds **13–17** are dominated in the visible region by an intense transition at *ca.* 525 nm (19000 cm⁻¹) in THF. This is a broad band, indicating that multiple transitions close in energy could be contributing to this peak. Compound **15** was soluble enough in non-polar solvents such as hexanes to record an absorption spectrum (Figure 5.11) to investigate if any further structuring could be observed in this band. While a slight new shoulder was observed at a slightly higher energy to the hypsochromatically shifted λ_{max} , no obvious new peaks arose. This contrasts with the CpRu(C₂NAP^{Me}) and Cp^{*}Ru(C₂NAP^{Me}) compounds, which displayed two high intensity bands between 300 – 350 nm which match the vibronic structuring of a naphthalimide π - π^* transition. A strong, lower energy band at *ca.* 520 nm is visible for both compounds in polar solvents (ethanol), but this band resolved into two distinct peaks and blueshifted (to *ca.* 460 – 518 nm) in less polar solvents (hexanes).²⁴⁷

The sensitivity of the λ_{max} of this peak to solvent polarity, along with its high extinction coefficient, confirms this is a charge transfer transition: presumably a metal to ligand charge transfer (MLCT) transition (see DFT discussion below in section 5.3.5). This assignment can be transferred to **13** and **14** based on the DFT calculations, despite the lack of confirmation of solvent polarity sensitivity due to their insolubility in non-polar solvents. The sole presence of a CT band in the visible spectrum does contrast with the related $\text{Co}(\text{cyclam})(\text{C}_2\text{NAP}^{\text{mes}})^{246}$ and *trans*- $\text{Pt}(\text{PBU}_3)_2(\text{C}_2\text{NAP}^{\text{octyl}})$ compounds,²⁴⁰ whose lowest energy transitions were both reported at *ca.* 430 nm (in CH_2Cl_2) and attributed to either a predominately NAP^{mes} based $\pi\text{-}\pi^*$ transition ($\text{Co}(\text{cyclam})$)^{244,246} or as mixed metal-ligand-to-ligand charge transfer (Pt).²⁴⁰

Table 5.2. Absorption and emission data for **13–17**

	λ_{max} (nm)	$\bar{\nu}_{\text{max}}$ (cm^{-1})	λ_{ex} (nm)	$\bar{\nu}_{\text{ex}}$ (cm^{-1})	λ_{em} (nm)	$\bar{\nu}_{\text{em}}$ (cm^{-1})
13^a	526	19000	505	19800	610, 710 (sh)	16400, 14100
14^a	530	18900	505	19800	610, 720 (sh)	16400, 13900
15^a	525	19000	515	19400	604	16600
15^b	480 (sh), 509	20800, 19600	470	21300	548	18300
16^a	518	19300	-	-	-	-
17^a	515	19400	500	20000	645	15500

^aTHF; ^bhexanes

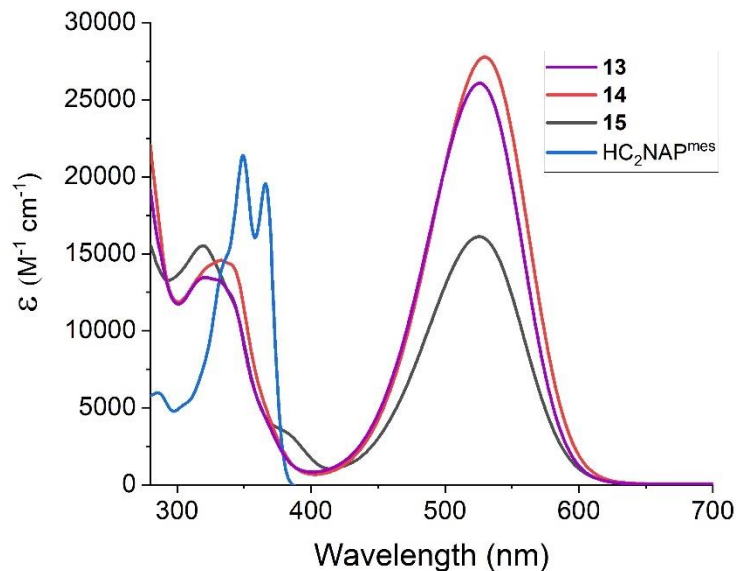


Figure 5.8. UV-vis absorption spectra of compounds **13**–**15** and HC₂NAP^{mes} in THF

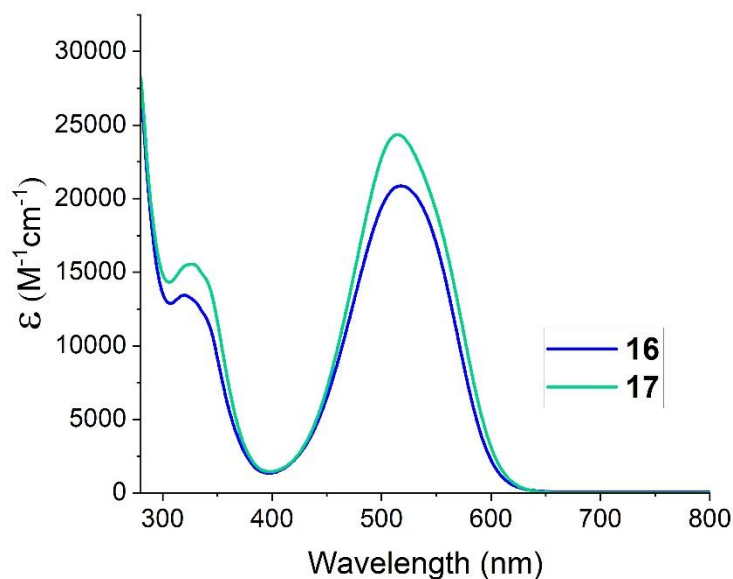


Figure 5.9. UV-vis absorption spectra of compounds **16** and **17** in THF

The use of a chromophore (NAP^R) as the acceptor ligand gives another handle on characterizing the impact of attaching the Ru(II)(dppe)₂ σ -alkynyl bond. Compounds **13**–**15** and **17** are all fluorescent as N₂-degassed solutions (as shown in Figures 5.10 and 5.11 below). Emission of **16** was not collected due to consistent contamination with HC₂NAP^{iPr}. The emission profiles of **13** and **14** somewhat resemble that of TMSC₂NAP^{mes}²⁴⁶ and HC₂NAP^{iPr}²⁴⁴ with all containing a two-humped emission profile. The two-humped profile is somewhat lost in the THF

spectra of **15** but is partially revealed in the hexanes emission spectra (Figure 5.11). The large Stokes shift for **13–15** and **17** in THF (79 – 130 nm; compare λ_{em} and λ_{max} in Table 5.2) and the shift of **15**'s λ_{em} maximum from 604 nm (THF) to 548 nm (hexanes) when the solvent polarity is changed suggests that the observed emission in **13–15** and **17** occurs from the MLCT transition's excited state. This blue-shift of ν_{em} and ν_{max} is equivalent when moving from THF to hexanes (*ca.* 1800 cm^{-1}), indicating emission is occurring from the same state in both solvents.

Moreover, the emission maximum of **13–15** and **17** is significantly red-shifted compared to $\text{HC}_2\text{NAP}^{\text{iPr}}$ and $\text{Co}(\text{cyclam})(\text{C}_2\text{NAP}^{\text{iPr}})$ species (399 – 441 nm in CH_2Cl_2).²⁴⁴ The related *trans*- $\text{Pt}(\text{PBU}_3)_2(\text{C}_2\text{NAP}^{\text{octyl}})$ compounds²⁴⁰ reported dual emission, based out of a charge transfer state and the ^3NAP state, while the $\text{Co}(\text{cyclam})(\text{C}_2\text{NAP}^{\text{R}})$ complexes only reported emission based off the NAP^{R} excited state transition.²⁴⁶ There is also little to no difference between the emission of **14** and **15**, suggesting that the $-\text{C}_2\text{Ph}$ 'donor' alkynyl ligand did not significantly impact the electronics of the $\text{Ru}(\text{II})$ -bound $-\text{C}_2\text{NAP}^{\text{mes}}$ ligand, similar to what was observed in the redox events discussed below.

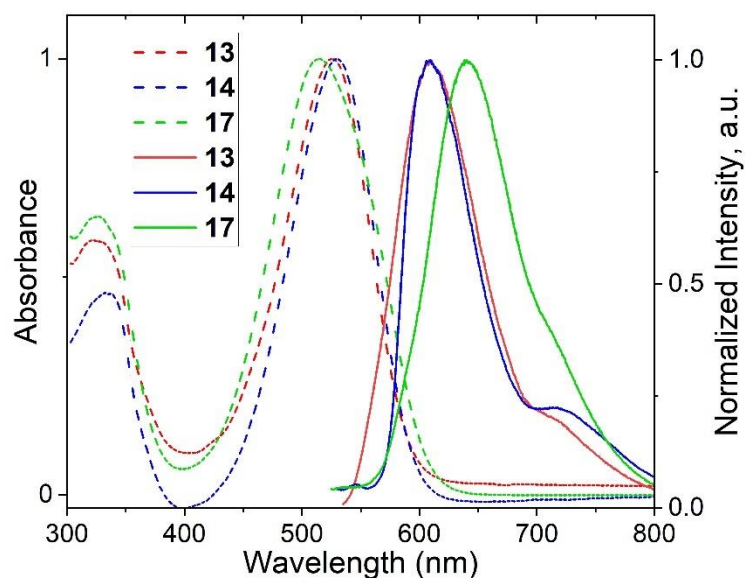


Figure 5.10. Normalized absorption (dashed lines) and emission spectra (solid lines) of **13**, **14**, and **17** in THF as N_2 -degassed solutions

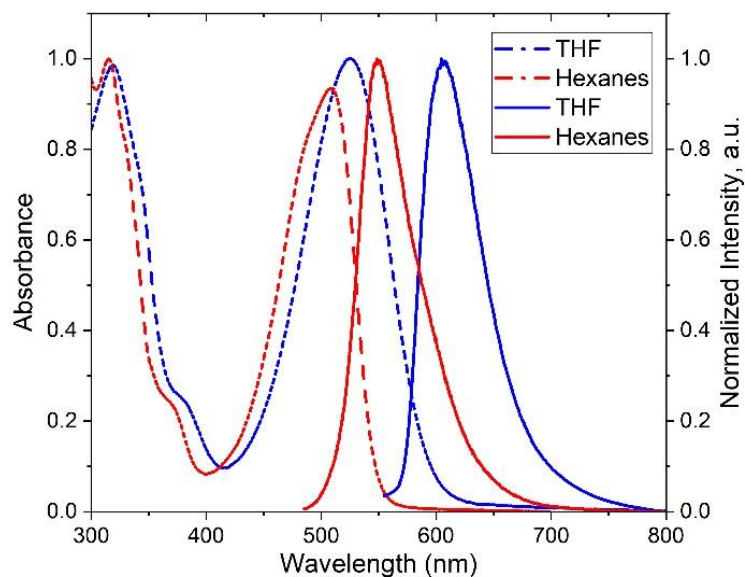


Figure 5.11. Normalized absorption (dashed lines) and emission spectra (solid lines) of **15** in hexanes (red lines) or THF (blue lines) as N₂-degassed solutions

5.3.4 Electrochemical Studies

The redox properties of **13–17** were examined using cyclic (CV) and differential pulse voltammetry (DPV). Their voltammograms are shown in Figures 5.12 and 5.13 below and the electrode potentials versus Fc⁺⁰ are given in Table 5.3. All compounds exhibit one reversible reduction **B** (NAP^{0/-1}) and one reversible oxidation **A** (Ru^{3+/2+}). Slight degradation of the compounds **14**, **15** and **17** can be observed in the CV / DPV scans in Figures 5.12 and 5.13 and it is attributed to light exposure during the experiments that degraded the material to free -C₂NAP^{mes} materials, attributed to new, irreversible peak growth at ca. -1.5 V ($E_{1/2}$ of HC₂NAP^{mes} at -1.52 V vs. Fc⁺⁰ in MeCN).²⁴⁶

Table 5.3. Electrode Potentials (in V vs Fc⁺⁰) for **13–17** in THF

	A	B
13	0.19	-2.06
14	0.21	-2.00
15	0.17	-1.99
16	0.12	-2.12
17	0.14	-2.04

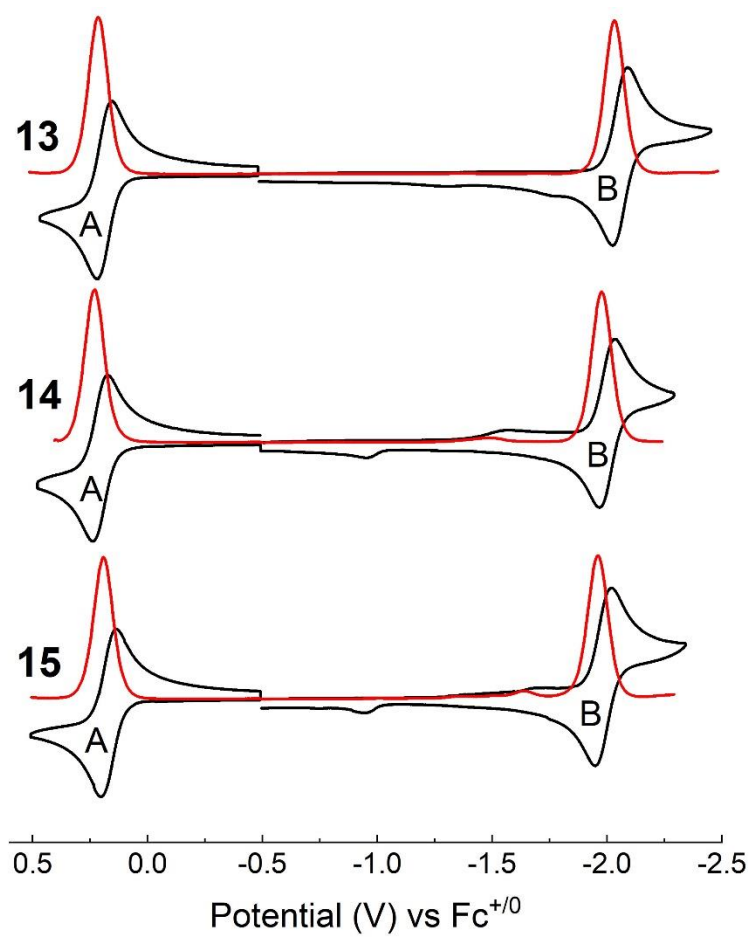


Figure 5.12. Cyclic (black) and differential pulse (red) voltammograms of compounds **13–15** (1.0 mM) recorded in 0.10 M THF solutions of $[\text{Bu}_4\text{N}][\text{PF}_6]$ at a scan rate of 0.10 V/s

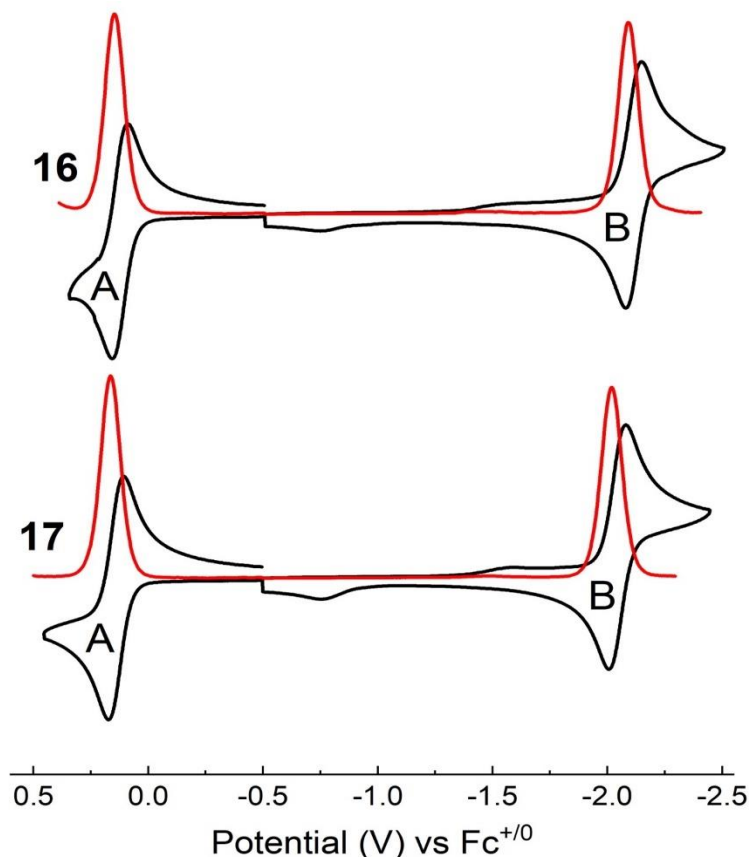


Figure 5.13. Cyclic (black) and differential pulse (red) voltammograms of compounds **16** and **17** (1.0 mM) recorded in 0.10 M THF solutions of $[\text{Bu}_4\text{N}][\text{PF}_6]$ at a scan rate of 0.10 V/s

Comparison of the redox potentials for **A** and **B** between the two *trans*- $\text{RuCl}(\text{C}_2\text{NAP}^{\text{R}})(\text{dppe})_2$ compounds, **13** ($-\text{C}_2\text{NAP}^{\text{iPr}}$) and **14** ($-\text{C}_2\text{NAP}^{\text{mes}}$), reveals a slight anodic shift (20 mV of **A**, 60 mV of **B**) of the oxidation and reduction potentials moving from **13** to **14**. The $-\text{NAP}^{\text{iPr}}$ substituent is expected to be more electron rich than the $-\text{NAP}^{\text{mes}}$ substituent, hence the electrochemical events for **13** are cathodically shifted from that of **14**. A similar anodic shift of the redox potentials of **16** to **17** can be observed (20 mV of **A**, 80 mV of **B**) when comparing the *trans*- $\text{RuCl}(\text{C}_2\text{NAP}^{\text{R}})(\text{dppm})_2$ compounds. When comparing the two *trans*- $\text{RuCl}(\text{C}_2\text{NAP}^{\text{R}})(\text{dppe})_2$ to the *trans*- $\text{RuCl}(\text{C}_2\text{NAP}^{\text{R}})(\text{dppm})_2$ compounds (**13** vs. **16**; **14** vs. **17**), a cathodic shift of both **A** and **B** is observed (ca. 70 mV shift of **A**, ca. 50 mV shift of **B**). This contrasts with previously reported comparisons between *trans*- $\text{RuCl}(\text{C}_2\text{R})(\text{dppe})_2$ and *trans*- $\text{RuCl}(\text{C}_2\text{R})(\text{dppm})_2$ compounds, which reported little to no shifts of either the $\text{Ru}^{3+/2+}$ oxidation or an alkynyl reduction potential.^{151,179}

Comparison of the mono-alkynyl **14** to the bis-alkynyl compound **15**, reveals a cathodic shift of the $\text{Ru}^{3+/2+}$ oxidation **A** (40 mV), however a corresponding cathodic shift of the $\text{NAP}^{0/-1}$ reduction **B** is not observed. The cathodic shift of **A** is consistent with previous studies and is attributed to the increased donor strength of the phenylacetylide versus the chloride ion at the *trans* position.^{151,181} The lack of a cathodic shift of **B** is also consistent with previous reports on both the $\text{Pt-NAP}^{\text{octyl}}$ compounds²⁴⁰ and $\text{Co}(\text{cyclam})(\text{C}_2\text{NAP}^{\text{R}})$ complexes²⁴⁶ where no change was observed in their $\text{NAP}^{0/-1}$ reduction potential despite changing the *trans* axial ligand. This lack of cathodic shift of **B** suggests little to no communication of the increased electron donor strength *trans* to the NAP^{mes} through the metal-acetylide center in the electronic ground state.

5.3.5 Density Functional Theory Analysis

Density functional theory (DFT) calculations were also performed to better understand the ground-state electronic structures of **14**, **15** and **17** using their respective crystal structures as starting geometries. Representations of selected frontier molecular orbitals and their corresponding energies for **14'**, **15'** and **17'** are shown in Figure 5.14 and Table 5.4, and the comparison between experimental (crystallographic) and DFT-optimized parameters is given in Table D.4 (Appendix D below). Computational details can be found in section 5.5.3 below.

As postulated above in the voltammetric studies, the theoretical calculations revealed that the closely spaced, highest fully occupied molecular orbital (HOMO) and the HOMO-1 for **14'** and **17'** are spread over the extended π -conjugated system, with a strong antibonding $\pi(\text{Ru}-\text{C}\equiv\text{C})$ character (ca. 38% Ru and 11% $\text{C}\equiv\text{C}$) and some chloride contribution (11% in HOMO-1). These MOs roughly correspond to the perpendicular, degenerate π -manifolds on the alkynyl ligands. For **15'**, the HOMO and HOMO-1 orbitals are also spread over the π -conjugated system, however more of this electron density is spread into the $-\text{C}\equiv\text{C}-\text{Ph}$ fragment (37% Ru, 15% $\text{C}\equiv\text{C}_{\text{Ph}}$, 11% $\text{C}\equiv\text{C}_{\text{NAP}}$). This suggests that the visible transitions observed in the UV-vis absorption spectra are actually (metal+ligand) to ligand charge transitions, similar to the $\text{Pt-NAP}^{\text{octyl}}$ compounds.²⁴⁰ For **14'**, **15'** and **17'**, the LUMOs are primarily localized on the electron-withdrawing $-\text{C}\equiv\text{C}-\text{NAP}^{\text{mes}}$ fragment with minimal Ru antibonding $d\pi$ character, confirming that the reduction observed in voltammetric studies (see discussion above) is based on the $-\text{NAP}^{\text{mes}}$ fragment. The limited contribution by the $\text{Ru}-\text{C}\equiv\text{C}$ fragment to the LUMO can also explain why there is limited to no shift of the $\text{NAP}^{0/-1}$ reduction when moving from **14** (Cl^- *trans*) to **15** ($\text{C}\equiv\text{CPh}$ *trans*).

Higher energy orbitals are mainly localized on $\delta^*(\text{Ru})$ orbitals ($\text{LUMO}+1 = 30\% \text{ Ru}$) with some antibonding Ru–P contributions. The localization of the LUMO on the electro-withdrawing unit tracks with previously reported calculations on *trans*- $\text{RuCl}(\text{C}\equiv\text{C-R})(\text{dppe})_2$ ²²³ and *trans*- $\text{Ru}(\text{C}\equiv\text{C-R})(\text{C}\equiv\text{C-R}')(\text{dppe})_2$ ^{182–184} compounds. Of note is that there is no obvious $\pi\text{-}\pi^*$ transition localized on NAP^{mes} as has been previously reported in the $\text{Co}(\text{cyclam})(\text{C}_2\text{NAP}^{\text{R}})$ complexes, even in lower-lying occupied orbitals.²⁴⁴

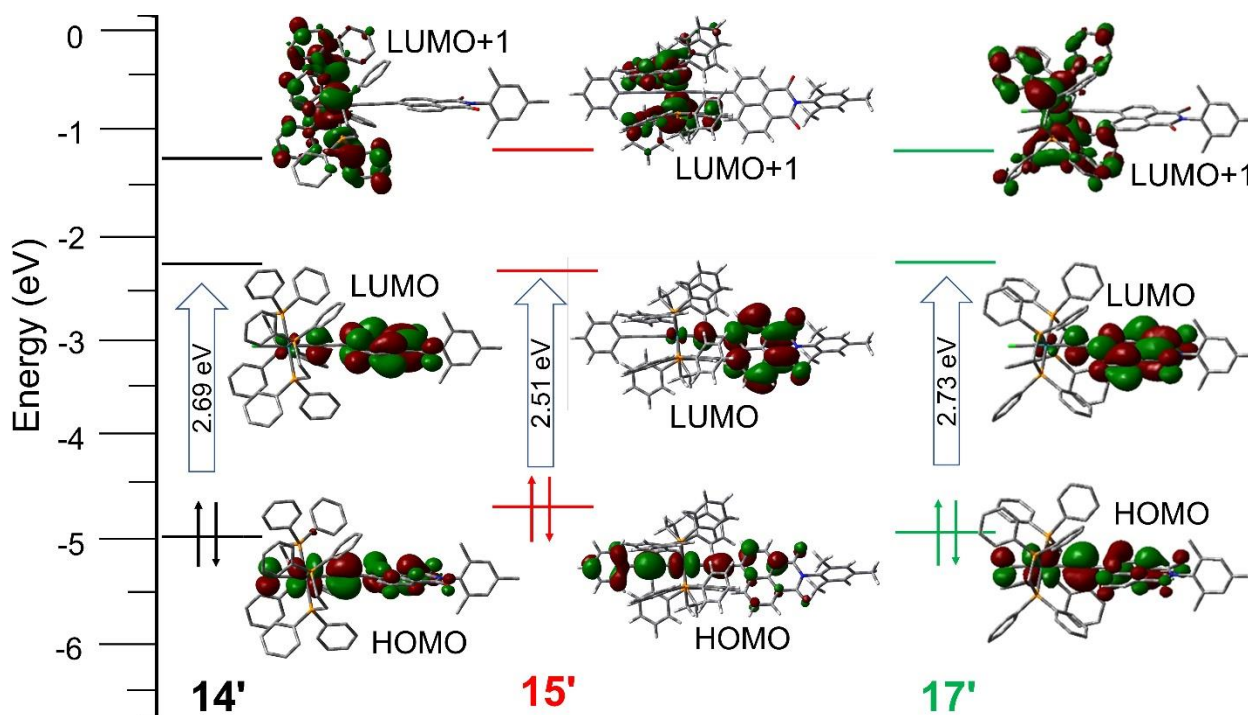
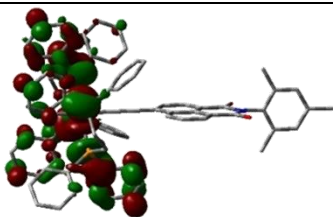
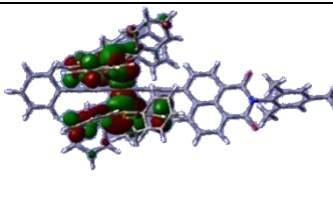
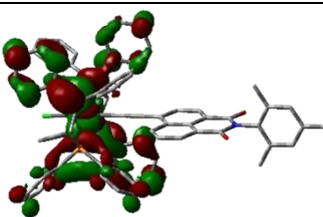
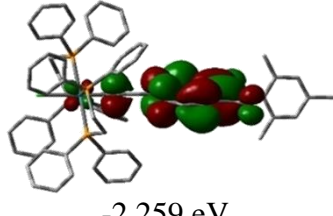
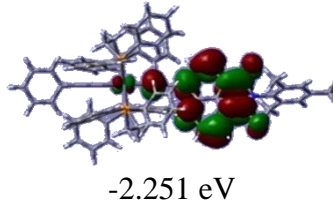
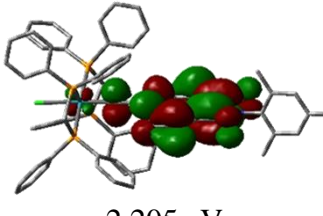
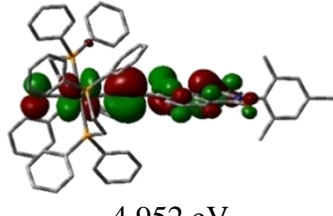
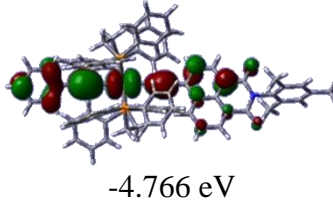
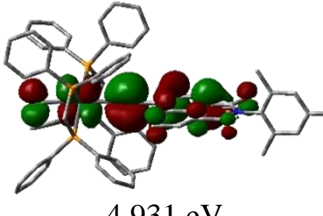
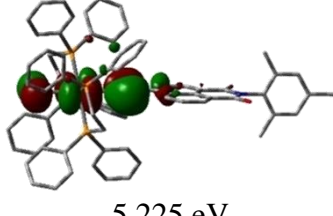
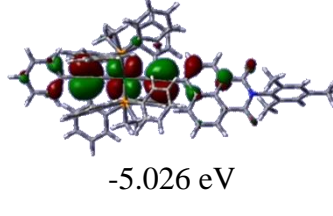
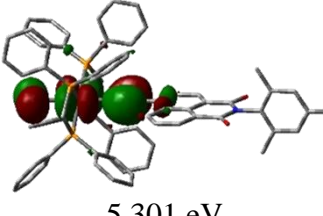
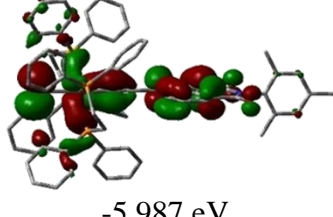
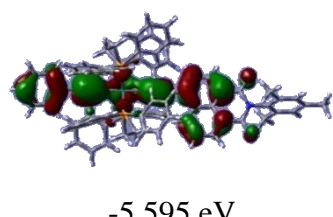
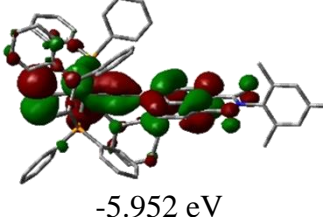
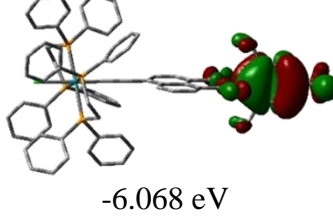
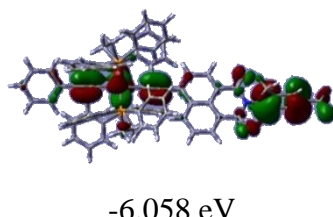
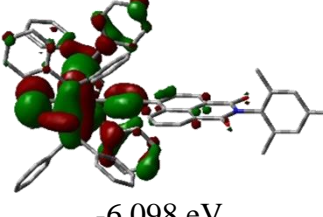


Figure 5.14. Frontier molecular orbitals of **14'** (left), **15'** (center), and **17'** (right) derived from DFT calculations. MOs are plotted at $|\text{isovalue}| = 0.025$

Table 5.4. Selected MO diagram of **14'**, **15'** and **17'** with corresponding energies (eV)

	14'	15'	17'
LUMO+1	 -1.225 eV	 -1.188 eV	 -1.370 eV
LUMO	 -2.259 eV	 -2.251 eV	 -2.205 eV
HOMO	 -4.952 eV	 -4.766 eV	 -4.931 eV
HOMO-1	 -5.225 eV	 -5.026 eV	 -5.301 eV
HOMO-2	 -5.987 eV	 -5.595 eV	 -5.952 eV
HOMO-3	 -6.068 eV	 -6.058 eV	 -6.098 eV

TD-DFT calculations using the same level of theory as the ground-state calculations were then performed on **15'** to investigate the different photoinduced electronic transitions in its spectra. The simulated absorption spectrum is presented in Figure 5.15 below, with energies and related oscillator strengths of these excited states provided in Table D.4 in Appendix D below. The simulated absorption spectrum is in reasonable agreement with the experimental, showing two absorption bands, one in the visible and one in the UV. The whole calculated spectrum exhibits a global blueshift of ca. 80 nm, which has previously been attributed to an inadequacy of the basis set (LANL2DZ) in describing the metal-based fragment;¹⁸⁴ however, calculations that attempted to utilize other basis sets did not converge.

These calculations confirm that the broad absorption band observed in the visible region (see Figure 5.8) has the major contribution of a HOMO \rightarrow LUMO transition, with a minor contribution of the HOMO-2 \rightarrow LUMO transition, explaining the broadness of the peak in THF and the additional transition observed when in non-polar solvents (Figure 5.11). Given the location of the HOMO, the HOMO-2 and the LUMO, the main absorption band of **15'** (and presumably **14'** and **17'** based on their orbital localizations) contains a strong MLCT character, with some possible interligand charge transfer contribution.

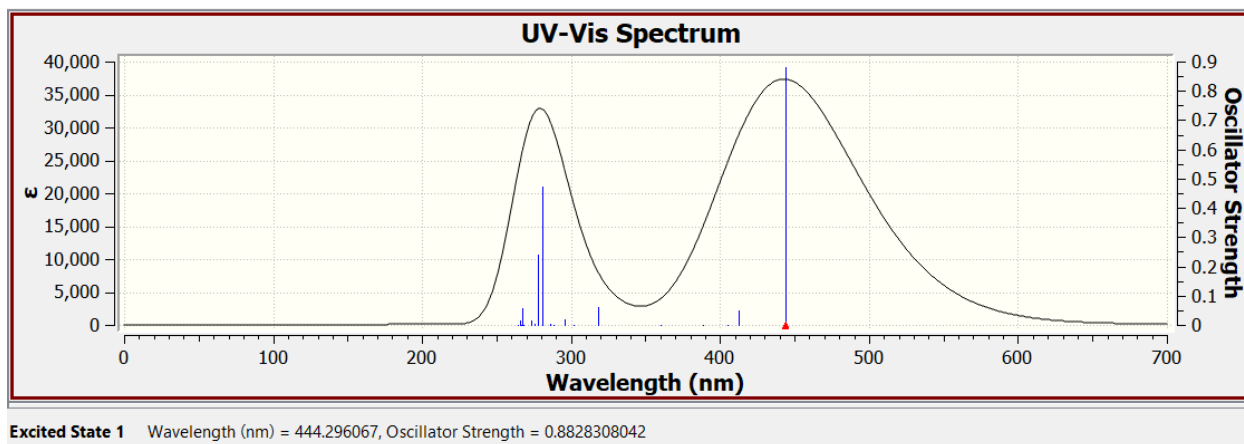


Figure 5.15. TD-DFT calculated UV-Vis spectrum of **15'** in THF (first 20 transitions)

5.4 Conclusions

Reported in this contribution are several new *trans*-RuCl(C₂NAP^R)(dppe)₂ compounds (R = iPr (**13**), mes (**14**)) and *trans*-RuCl(C₂NAP^R)(dppm)₂ (R = iPr (**16**), mes (**17**)) generated using traditional weak base conditions. Use of an underutilized synthetic pathway allowed for synthesis

of the *trans*-Ru(C₂Ph)(C₂NAP^{mes})(dppe)₂ (**15**) compound. All compounds display a reversible Ru^{3+/2+} oxidation and NAP^{0/-1} reduction, whose potentials depend on which -C₂NAP^R ligand was coordinated to the Ru(dppe/m)₂ fragment between **13/16** and **14/17**. Comparisons of **14** and **15** revealed the Ru^{3+/2+} oxidation was sensitive to Cl⁻ vs -C₂Ph coordination but the NAP^{0/-1} reduction was not. A severe setback to further synthetic manipulations to generate a true *D-B-A* compound with an electron-donating alkynyl ligand is the demonstrated sensitivity towards light and chlorinated solvents by all -C₂NAP^R based compounds and the easily lost ligand *trans* to the -C₂NAP^{mes} ligand in **15** during synthesis. Preparing a true *D-B-A* compound is highly desired for further charge-transfer characterizations and is an ongoing effort in our laboratory.

5.5 Experimental Section

General Methods. Literature procedures were followed in the preparations of *cis*-RuCl₂(dppe)₂,²⁵³ *cis*-RuCl₂(dppm)₂,²⁵⁴ 4-ethynyl-*N*-isopropyl-1,8-naphthalimide,²⁴⁴ 4-ethynyl-*N*-mesityl-1,8-naphthalimide,²⁴⁶ and [(dppe)₂Ru(NH₃)(C₂Ph)]PF₆.^{153,187} Triethylamine (NEt₃) was purchased from Fisher Chemical and distilled from potassium hydroxide before use. 1,8-Diazabicyclo[5.4.0]undec-7-ene (DBU) and all other reagents were obtained from commercially available sources and used without further purification. The reactions were carried out using Schlenk techniques under dry N₂ but no special care was taken to avoid air during work-up. Solvents were dried from appropriate agents (sodium for THF; calcium hydride for dichloromethane) and freshly distilled under nitrogen before use. All reactions, and whenever possible the purifications and characterizations, occurred in the dark.

Physical Methods. UV/Vis-NIR spectra were obtained with a JASCO V-670 UV/Vis-NIR spectrophotometer. Infrared spectra were obtained on a JASCO FT-IR 6300 spectrometer via ATR on a ZnSe crystal. ¹H NMR spectra for **13** and **16** were recorded on a Varian INOVA300 NMR operating at 300 MHz. Cyclic and differential pulse voltammograms were recorded in 0.1 M [Bu₄N][PF₆] and 1.0 mM ruthenium species solutions (4.0 mL THF, Ar degassed) using a CHI620A voltammetric analyzer with a glassy carbon working electrode (diameter = 2 mm), Pt-wire counter electrode, and an Ag/AgCl reference electrode, with ferrocene used as an external reference. Emission studies were measured as either THF or hexanes solutions with a Varian Cary Eclipse fluorescence spectrophotometer after degassing with dry N₂. Single crystal X-ray

diffraction data were collected on Nonius Kappa CCD and Bruker Quest Instruments as detailed in section 5.5.2 below.

5.5.1 Synthesis details

***trans*-RuCl(C≡C-NAP^{iPr})(dppe)₂ (13).** In a 50 mL Schlenk flask, *cis*-RuCl₂(dppe)₂ (101 mg, 0.10 mmol) and NaPF₆ (35.1 mg, 0.21 mmol) were dissolved in 3.0 mL of CH₂Cl₂, to which a 7.0 mL solution of CH₂Cl₂ containing 4-ethynyl-*N*-isopropyl-1,8-naphthalimide (HC₂NAP^{iPr}; 28.5 mg, 0.108 mmol) was added. After the addition of 4 drops of NEt₃, the solution was stirred at rt overnight. The crude reaction mix was then filtered over Celite and condensation of the filtrate gave a berry-purple solid. This crude solid was purified with a silica column with THF/hexanes (v/v, 1:4) which yielded 30.7 mg of pure **13** (25% yield based on Ru). UV-Vis (in THF) λ / nm (ε / M⁻¹ cm⁻¹): 321 (13500), 526 (26000). IR (cm⁻¹): C=O, 1682 (s), 1646 (s); C≡C, 2021 (s). Electrochemistry (THF, vs Fc⁺⁰) *E*_{1/2} / V, Δ*E*_p / mV, *i*_{backward}/*i*_{forward}: 0.188, 70, 0.94; -2.058, 70, 0.92. ¹H NMR (CDCl₃, 292 K) δ, ppm = 8.34 (d, *J* = 7.7 Hz, 2H), 7.52 (d, *J* = 7.4 Hz, 8H), 7.19 (t, *J* = 6.9 Hz, 12H), 7.08 (t, *J* = 7.4 Hz, 5H), 6.99 (t, *J* = 7.7 Hz, 9H), 6.86 (t, *J* = 7.6 Hz, 9H), 5.52 – 5.40 (m, 1H), 2.81 (d, *J* = 34.5 Hz, 8H), 1.60 (d, *J* = 6.9 Hz, 6H).

***trans*-RuCl(C≡C-NAP^{mes})(dppe)₂ (14).** In a 25 mL Schlenk flask, *cis*-RuCl₂(dppe)₂ (101 mg, 0.10 mmol) and NaPF₆ (36.3 mg, 0.22 mmol) were dissolved in 3.0 mL CH₂Cl₂, to which a 7.0 mL solution of CH₂Cl₂ containing 4-ethynyl-*N*-mesityl-1,8-naphthalimide (HC₂NAP^{mes}; 36.0 mg, 0.106 mmol) was added. To this, 1.0 mL of DBU/CH₂Cl₂ solution was added (1.4 equiv.) and the solution was stirred at rt overnight. Filtration over Celite and condensation of the filtrate gave a deep purple solid. The crude solid was purified with a THF and hexanes recrystallization which yielded 12.1 mg of **14** as a purple solid (9% yield based on Ru). UV-Vis (in THF) λ / nm (ε / M⁻¹ cm⁻¹): 333 (14600), 530 (27800). IR (cm⁻¹): C=O, 1694 (s), 1655 (s); C≡C, 2016 (s). Electrochemistry (THF, vs Fc⁺⁰) *E*_{1/2} / V, Δ*E*_p / mV, *i*_{backward}/*i*_{forward}: 0.205, 70, 0.96; -2.000, 70, 0.93.

***trans*-Ru(C≡C-Ph)(C≡C-NAP^{mes})(dppe)₂ (15).** The complex [(dppe)₂Ru(NH₃)(C₂Ph)]PF₆ (97 mg, 0.08 mmol) was dissolved in 10.0 mL CH₂Cl₂, to which a 10.0 mL solution of CH₂Cl₂ containing HC₂NAP^{mes} (60 mg, 0.18 mmol) was added. After the addition of 0.1 mL NEt₃ (0.72 mmol), the reaction was stirred for 1 h at room temperature. Pentane (20.0 mL) was added to crash out any unreacted starting material, and the crude mixture filtered

and condensed to a deep purple solid. TLC of the crude mixture (1:2 THF/hexanes w/ 3% MeOH, v/v) revealed the presence of both **14** and **15** in the solid. This crude mixture was purified with a silica column with THF/hexanes (v/v, 1:2 w/ 3% MeOH). UV-Vis (in THF) λ / nm (ϵ / M⁻¹ cm⁻¹): 320 (15500), 377 (3600), 525 (16100). IR (cm⁻¹): C=O, 1697 (s), 1660 (s); C \equiv C, 2068 (w), 2019 (s). Electrochemistry (THF, vs Fc^{+/0}) $E_{1/2}$ / V, ΔE_p / mV, $i_{\text{backward}}/i_{\text{forward}}$: 0.1685, 69, 0.93; -1.985, 69, 0.91.

trans-RuCl(C \equiv C-NAP^{iPr})(dppm)₂ (16). In a 25 mL Schlenk flask, *cis*-RuCl₂(dppm)₂ (236 mg, 0.25 mmol) and NaPF₆ (57.1 mg, 0.34 mmol) were dissolved in 20.0 mL of CH₂Cl₂, to which HC₂NAP^{iPr} (55 mg, 0.21 mmol) was added. The solution was stirred at ca. 30°C overnight. The crude reaction mix was then filtered over Celite and condensation of the filtrate gave a berry-purple solid. This crude solid was purified with a silica plug with CH₂Cl₂/hexanes (1:6 w/ 5% NEt₃ v/v) which yielded 72 mg of pure **16** (30% yield based on Ru). UV-Vis (in THF) λ / nm (ϵ / M⁻¹ cm⁻¹): 320 (13400), 518 (21000). IR (cm⁻¹): C=O, 1686 (s), 1645 (s); C \equiv C, 2040 (s). Electrochemistry (THF, vs Fc^{+/0}) $E_{1/2}$ / V, ΔE_p / mV, $i_{\text{backward}}/i_{\text{forward}}$: 0.124, 70, 0.82; -2.115, 70, 0.91. ¹H NMR (300 MHz, CDCl₃) δ , ppm = 8.31 (s, 2H), 8.04 (d, J = 8.1 Hz, 2H), 7.46 (s, 16H), 7.35 – 7.28 (m, 7H), 7.18 (t, J = 8.0 Hz, 12H), 7.01 (t, J = 7.3 Hz, 9H), 5.99 (s, 1H), 5.02 (d, J = 4.9 Hz, 4H), 1.58 (s, 6H).

trans-RuCl(C \equiv C-NAP^{mes})(dppm)₂ (17). In a 25 mL Schlenk flask, *cis*-RuCl₂(dppm)₂ (150 mg, 0.16 mmol) and NaPF₆ (54.7 mg, 0.33 mmol) were dissolved in 3.0 mL THF, to which a 12.0 mL solution of THF containing HC₂NAP^{mes} (59.8 mg, 0.18 mmol) was added. To this, 3 drops of NEt₃ was added and the solution was stirred at rt overnight. Filtration over Celite and condensation of the filtrate gave a deep purple solid. Initial purification with a THF/hexanes recrystallization gave a crude purple solid. The crude solid was purified with a silica plug (1:1 THF/hexanes w/ 3% MeOH, v/v) which yielded 29.4 mg of **17** as a purple solid (15% yield based on Ru). UV-Vis (in THF) λ / nm (ϵ / M⁻¹ cm⁻¹): 327 (15500), 515 (24000). IR (cm⁻¹): C=O, 1685 (s), 1650 (s); C \equiv C, 2023 (s). Electrochemistry (THF, vs Fc^{+/0}) $E_{1/2}$ / V, ΔE_p / mV, $i_{\text{backward}}/i_{\text{forward}}$: 0.141, 70, 0.95; -2.044, 70, 0.87.

5.5.2 X-ray Crystallographic Details

Crystals suitable for X-ray diffraction analysis were grown by layering hexanes over a concentrated solution of **13**, **14**, and **17** in THF. Crystals suitable for X-ray diffraction analysis were grown by layering 1,2-dichlorobenzene and hexanes (1:1 v/v) over a concentrated solution of **16** in EtOAc. Crystals suitable for X-ray diffraction analysis were grown by slow evaporation of **15** in THF/hexanes. Single crystals of **13**, **14**, **16** and **17** were coated with paraffin oil and quickly transferred to the goniometer head of a Bruker Quest diffractometer with a fixed chi angle, a sealed tube fine focus X-ray tube, single crystal curved graphite incident beam monochromator, a Photon II area detector and an Oxford Cryosystems low temperature device. Examination and data collection were performed with Mo K α radiation ($\lambda = 0.71073 \text{ \AA}$) at 150 K. Single crystals of **15** were coated with paraffin oil and quickly transferred to the goniometer head of a Bruker Quest diffractometer with kappa geometry, an I- μ -S microsource X-ray tube, laterally graded multilayer (Goebel) mirror single crystal for monochromatization, a Photon-III C14 area detector and an Oxford Cryosystems low temperature device. Examination and data collection were performed with Cu K α radiation ($\lambda = 1.54178 \text{ \AA}$) at 150 K. In three of the structures, **15–17**, only part of the solvent molecules were sufficiently resolved to model, and were included as partially occupied. Based on the XRD data it was not possible to determine whether the remaining volume remained unoccupied, or if additional highly disordered solvate molecules are present. A complete removal of the partially occupied solvent molecules via the Squeeze procedure did not substantially improve the overall quality of the structure, and we thus decided to include the resolved fraction of the void content as partially occupied solvate molecules.

Data were collected, reflections were indexed and processed, and the files scaled and corrected for absorption using APEX3⁸¹ and SADABS.⁵¹ The space groups were assigned using XPREP within the SHELXTL^{52,53} suite of programs and solved by direct methods using ShelXS⁵³ or dual methods using ShelXT⁵⁴ and refined by full matrix least squares against F^2 with all reflections using Shelxl2018⁵⁵ using the graphical interface Shelxle.⁵⁷ Full crystallographic details can be found in Table D.1 in Appendix D below.

5.5.3 Computational Methods

Geometry optimizations of structures **14**, **15** and **17** based on the respective crystal structures were done using restricted closed-shell density functional theory (DFT); the B3LYP functional and lanl2dz basis set were used for all atoms.¹³⁴ Solvent effects were included for the TD-DFT calculations using a polarizable continuum model (CPCM)²⁵⁵ with THF. Frequency analyses were carried out for the optimized structures **14'**, **15'** and **17'**, shown in Figures D.3–D.5 in Appendix D, and stationary points were confirmed. The major atomic contributions to molecular orbitals of interest on the optimized structures were assessed as needed using the Pop=Orbitals=n keywords. All calculations were carried out with the Gaussian 16, Rev. A.03.⁸⁴

APPENDIX A: ADDITIONAL MATERIALS FOR DIRUTHENIUM ARYL COMPOUNDS – TUNING OF ELECTROCHEMICAL RESPONSES AND SOLUBILITY

Table A.1. Crystal data for compounds **2b**, **3b**, and **4b**

	2b	3b	4b
Chemical formula	C ₆₆ H ₇₃ N ₈ O ₄ Ru ₂ ·0.815(C ₆ H ₁₄)	C ₆₃ H ₆₇ N ₈ O ₅ Ru ₂ ·C ₄ H ₁₀ O	C ₆₄ H ₆₉ N ₈ O ₆ Ru ₂ ·1.316(C ₅ H ₁₂)
Fw, g/mol	1314.73	1292.50	1343.20
Space group	<i>P</i> $\bar{1}$	<i>P</i> $\bar{1}$	<i>C</i> 2/ <i>c</i>
<i>a</i> , Å	10.6576(4)	13.5208(4)	10.5619(12)
<i>b</i> , Å	17.2858(6)	14.1761(5)	34.317(6)
<i>c</i> , Å	19.4972(7)	17.9369(6)	18.756(3)
α °	107.2809(15)	67.298(1)	90
β °	94.7543(16)	86.515(1)	104.369(6)
γ °	96.8966(15)	74.075(1)	90
<i>V</i> , Å ³	3378.2(2)	3045.98(18)	6585.6(16)
<i>Z</i>	2	2	4
<i>T</i> , K	150	150	150
λ , Å	1.54178	0.71073	0.71073
ρ_{calcd} , g/cm ³	1.293	1.409	1.355
<i>R</i>	0.046	0.035	0.050
<i>R</i> _w (<i>F</i> ²)	0.122	0.074	0.135

Table A.2. Crystal data for compounds **1a**, **2a**, **3a**, **4a**, and **5a**

	1a	2a	3a	4a	5a
Chemical formula	$\text{C}_{60}\text{H}_{61}\text{N}_9\text{O}_8\text{Ru}_2 \cdot 2(\text{C}_3\text{H}_6\text{O})$	$\text{C}_{62}\text{H}_{65}\text{N}_8\text{O}_8\text{Ru}_2$	$\text{C}_{59}\text{H}_{59}\text{N}_8\text{O}_9\text{Ru}_2$	$\text{C}_{60}\text{H}_{61}\text{N}_8\text{O}_{10}\text{Ru}_2 \cdot \text{C}_4\text{H}_8\text{O}_2$	$\text{C}_{59}\text{H}_{56}\text{F}_3\text{N}_8\text{O}_8\text{Ru}_2$
Fw, g/mol	1355.48	1252.36	1226.28	1344.41	1264.26
Space group	<i>Pbca</i>	<i>I4</i>	<i>P2₁/c</i>	<i>P$\bar{1}$</i>	<i>P2₁/n</i>
<i>a</i> , Å	17.2181(8)	12.4116(2)	20.7861(9)	12.3210(4)	12.7603(5)
<i>b</i> , Å	24.2357(12)	12.4116(2)	15.6582(6)	12.9177(5)	21.0504(8)
<i>c</i> , Å	29.5233(16)	18.2620(6)	17.0761(7)	19.6606(7)	19.8667(7)
α °	90	90	90	108.3490(19)	90
β °	90	90	100.676(2)	91.745(2)	91.8246(15)
γ °	90	90	90	92.703(2)	90
<i>V</i> , Å ³	12319.9(11)	2813.22(13)	5461.6(4)	2963.37(19)	5333.7(3)
<i>Z</i>	8	2	4	2	4
<i>T</i> , K	150	150	150	150	150
λ , Å	1.54178	0.71073	0.71073	0.71073	0.71073
ρ_{calcd} , g/cm ³	1.462	1.479	1.491	1.507	1.574
<i>R</i>	0.032	0.024	0.030	0.036	0.041
<i>R_w</i> (<i>F</i> ²)	0.077	0.055	0.073	0.086	0.082

Table A.3. Electrochemical data from CV (V vs. Ag/AgCl) in THF

Compound	C	B (Ru ₂ ^{6+/5+})	A (Ru ₂ ^{5+/4+})
Ru ₂ (<i>ap</i>) ₄ Cl ⁷⁵	–	0.46	-0.834
Ru ₂ (DiMeO <i>ap</i>) ₄ Cl ⁴³	–	0.56	-0.75
1a	0.58	0.23	-1.15
2a	–	0.29	-1.11
3a	–	0.28	-1.11
4a	–	0.31	-1.10
5a	–	0.36	-0.97
6a	–	0.30	-1.08
Ru ₂ (<i>m</i> - ^{<i>i</i>} PrO <i>ap</i>) ₄ Cl ⁴⁴	–	0.55	-0.77
1b	0.61	0.24	-1.11
2b	–	0.32	-1.09
3b	–	0.28	-1.13
4b	–	0.29	-1.09
5b	–	0.37	-0.98
Ru ₂ (<i>ap</i>) ₄ (C ₂ -C ₆ H ₅) ⁵	–	0.44	-0.88
Ru ₂ (3-O ^{<i>i</i>} Bu <i>ap</i>) ₄ (C ₂ -C ₆ H ₅) ⁵	–	0.43	-0.87

Table A.4. Room temperature magnetism data using Evans method.⁴⁵ Solvent: CDCl₃; reference: ferrocene

Compound	Δδ (Hz)	[Ru ₂] (mM)	χ _M (emu/mol)	μ _{eff} (B.M.)
1a	24	3.23	5.84x10 ⁻³	3.9
2a	21	2.90	5.76x10 ⁻³	3.9
3a	24	3.11	6.14x10 ⁻³	4.0
4a	21	3.62	4.62x10 ⁻³	3.5
5a	17	2.45	5.36x10 ⁻³	3.8
6a	27	3.04	7.07x10 ⁻³	4.3
1b	18	3.20	4.55x10 ⁻³	3.5
2b	29	3.51	6.60x10 ⁻³	4.1
3b	15	2.46	4.90x10 ⁻³	3.6
4b	14	2.67	4.11x10 ⁻³	3.4
5b	23	3.18	5.78x10 ⁻³	3.9

APPENDIX B: ADDITIONAL MATERIALS FOR PHENYLENE AS AN EFFICIENT MEDIATOR FOR INTERMETALLIC COUPLING

Table B.1. Crystal data for complexes **8** and **9**

	8	9
Chemical Formula	$\text{C}_{96}\text{H}_{76}\text{N}_{18}\text{Ru}_4 \cdot 2.337(\text{OC}_4\text{H}_{10}) \cdot 0.824(\text{OC}_4\text{H}_8)$	$2(\text{C}_{51}\text{H}_{41}\text{N}_9\text{Ru}_2) \cdot \text{C}_5\text{H}_{12} \cdot \text{C}_4\text{H}_8\text{O}_2$
Fw, g/mol	2118.64	2124.38
Crystal System	Monoclinic	Monoclinic
Space group	$P2_1/c$	$P2_1/c$
a , Å	22.2621(10)	11.8877(5)
b , Å	22.2426(9)	20.4352(9)
c , Å	20.7463(9)	19.6259(9)
α °	90	90
β °	109.053(2)	101.0991(18)
γ °	90	90
V , Å ³	9710.1(7)	4678.5(4)
Z	4	2
T , K	150	150
λ , Å	1.54178	0.71073
ρ_{calcd} , g/cm ³	1.449	1.508
μ (mm ⁻¹)	5.43	0.70
$F(000)$	4340	2172
Crystal size (mm ³)	0.29 x 0.20 x 0.17	0.62 x 0.22 x 0.18
Radiation	CuK α	MoK α
2θ range (°)	2.1 to 74.7	2.3 to 33.2
Index ranges	$-25 < h < 27$; $-27 < k < 27$; $-25 < l < 25$	$-18 < h < 18$; $-31 < k < 31$; $-30 < l < 30$
Reflections collected	132368	233241
Independent reflections	19838	17892
Data/restraints/parameters	19838/786/1427	17892/312/765
R	0.0397	0.0292
$R_w(F^2)$	0.1063	0.0744
Largest diff. peak/hole e Å ⁻³	0.71, -1.16	0.89, -0.82

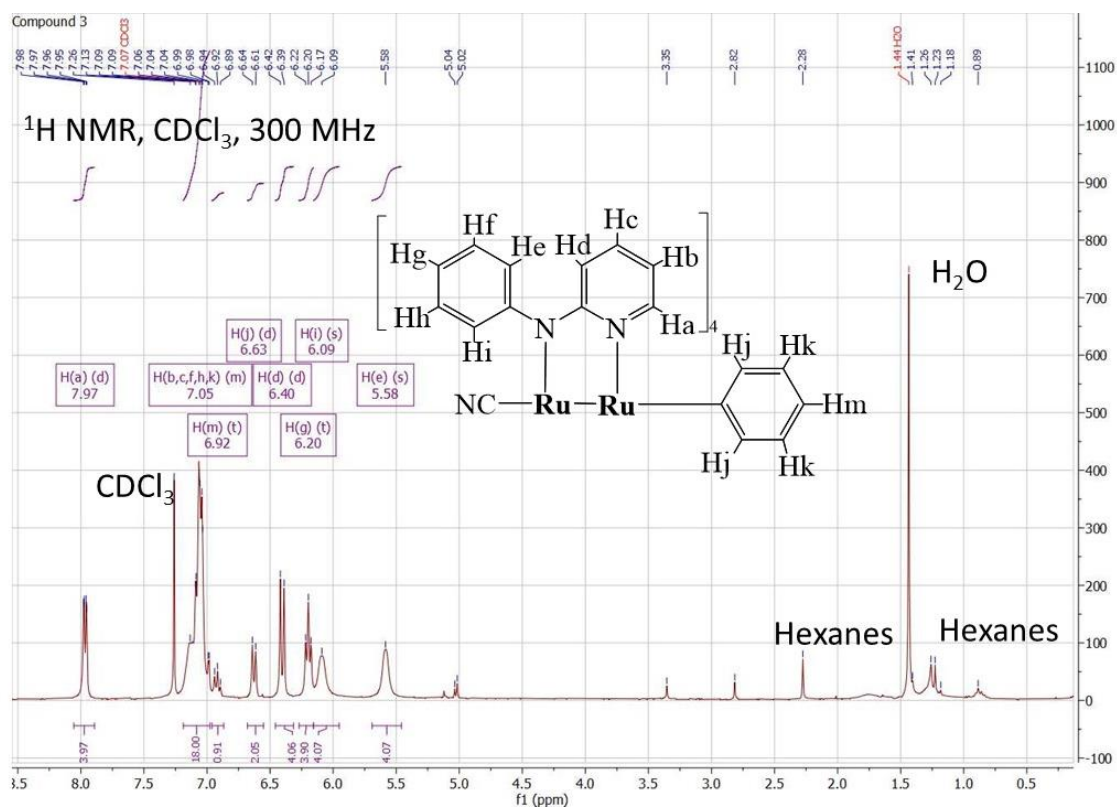


Figure B.2. ^1H NMR of **9** in CDCl_3 at 293 K. For the phenyl proton assignments, the peak Hm is almost overlapping with the multiplet, suggesting that Hk would be nearby. Hj would be shifted upfield due to closeness to the Ru_2 atoms. The remaining *ap*-based protons are assigned due to expected symmetry and comparisons to the base molecules, pyridine and aniline

Table B.2. Electrochemical data from CV (in V vs. Ag/AgCl)

Compound	+2/+1	+1/0	0/-1	-1/-2
7	-0.010	-0.131	-0.839	-1.068
8	0.838	0.547	-0.374	-0.551
9	----	0.741	-0.385	----
*Ru₂(ap)₄Cl⁷⁵	1.430	0.457	-0.834	----
*Ru₂(ap)₄(C₆H₅)³⁵	----	0.100	-1.160	----

*Measurements run in CH₂Cl₂. Compounds **7** – **9** run in THF

Table B.3. Electrochemical data for **7** and **8**

Compound	$\Delta E_{1/2}$ (+1) (mV)	K_c^a	$\Delta E_{1/2}$ (-1) (mV)	K_c^a
7	133	179	221	5568
8	291	85,546	174	889

$$^a K_c = 10^{\Delta E(\text{mV})/59}$$

Table B.4. Summary of optical & electrochemical data of **8** vs [Ru₂(ap)₄]₂(μ-(C≡C)_n) (n = 1, 2)

	8	[Ru ₂ (ap) ₄] ₂ (μ-C≡C) ²²	[Ru ₂ (ap) ₄] ₂ (μ-(C≡C) ₂) ²²
ΔE _{1/2} (+1) (mV)	291	280	170
ΔE _{1/2} (-1) (mV)	174	660	380
λ IVCT (cm ⁻¹) (ox.)	4,050	----	7,700
ε (M ⁻¹ cm ⁻¹) (ox.)	6,860	----	11,000
$\bar{\nu}_{1/2}$ (cm ⁻¹) (ox.)	1,716	----	1,820
Hab (cm ⁻¹) (ox.)	647	----	1,022
λ IVCT (cm ⁻¹) (red.)	----	----	8,450; 5,670
ε (M ⁻¹ cm ⁻¹) (red.)	----	----	27,000; 7,700
$\bar{\nu}_{1/2}$ (cm ⁻¹) (red.)	----	----	1,820; 1,630
Hab (cm ⁻¹) (red.)	----	----	1,678; 694
Ru–Ru (Å) Avg.	2.486[4]	----	2.332[2]

Peak Analysis

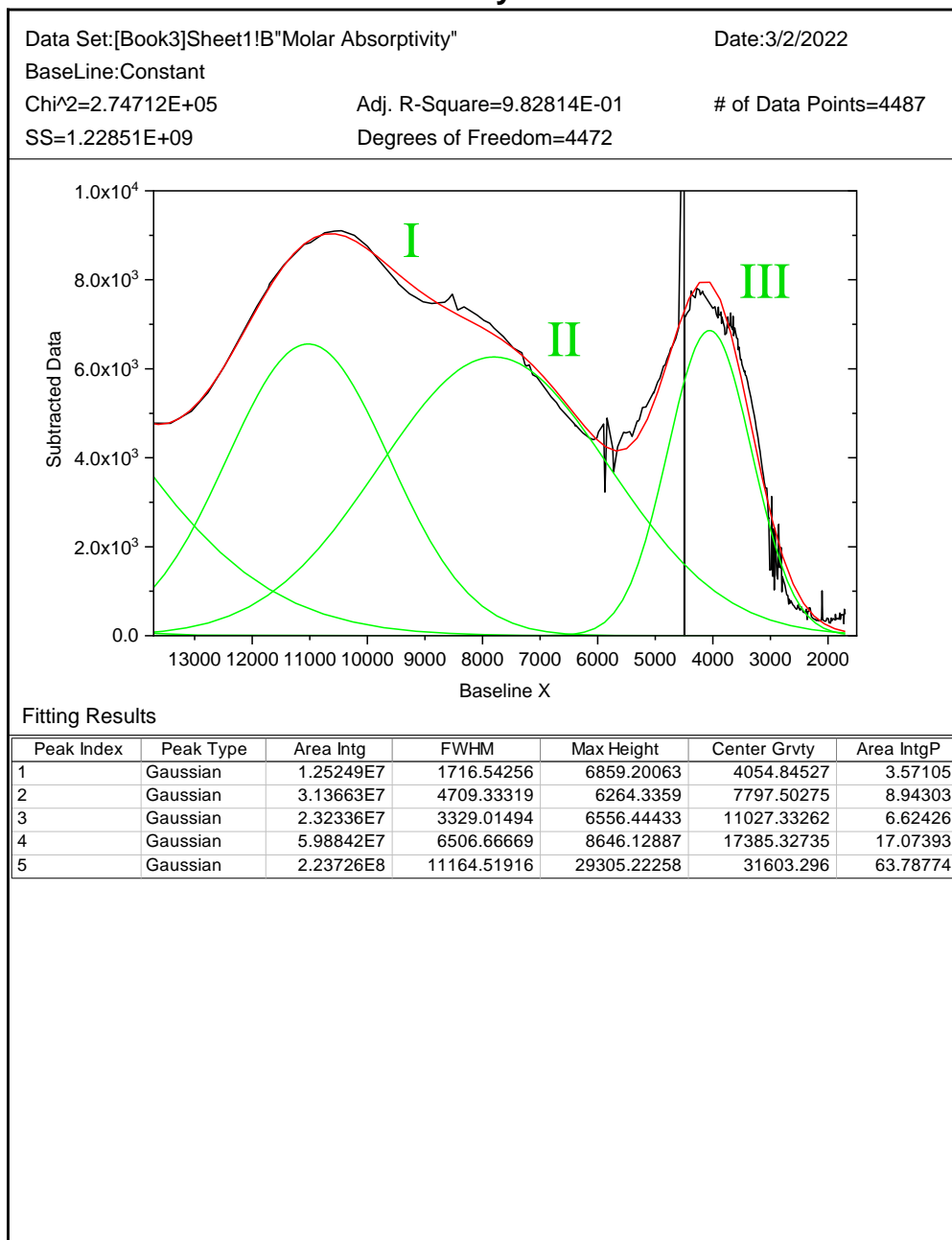


Figure B.3. Visible-NIR absorption spectrum (black line) of the mixed-valence complex $[\mathbf{8}]^+$ in 0.1 M $[\text{NBu}_4][\text{PF}_6]$ with additional IR data. Multiple Gaussian bands (green lines) and their sum (red line) to fit the absorption band of $[\mathbf{8}]^+$. IVCT peak of interest is III; labeled as #1 in peak index

Peak Analysis

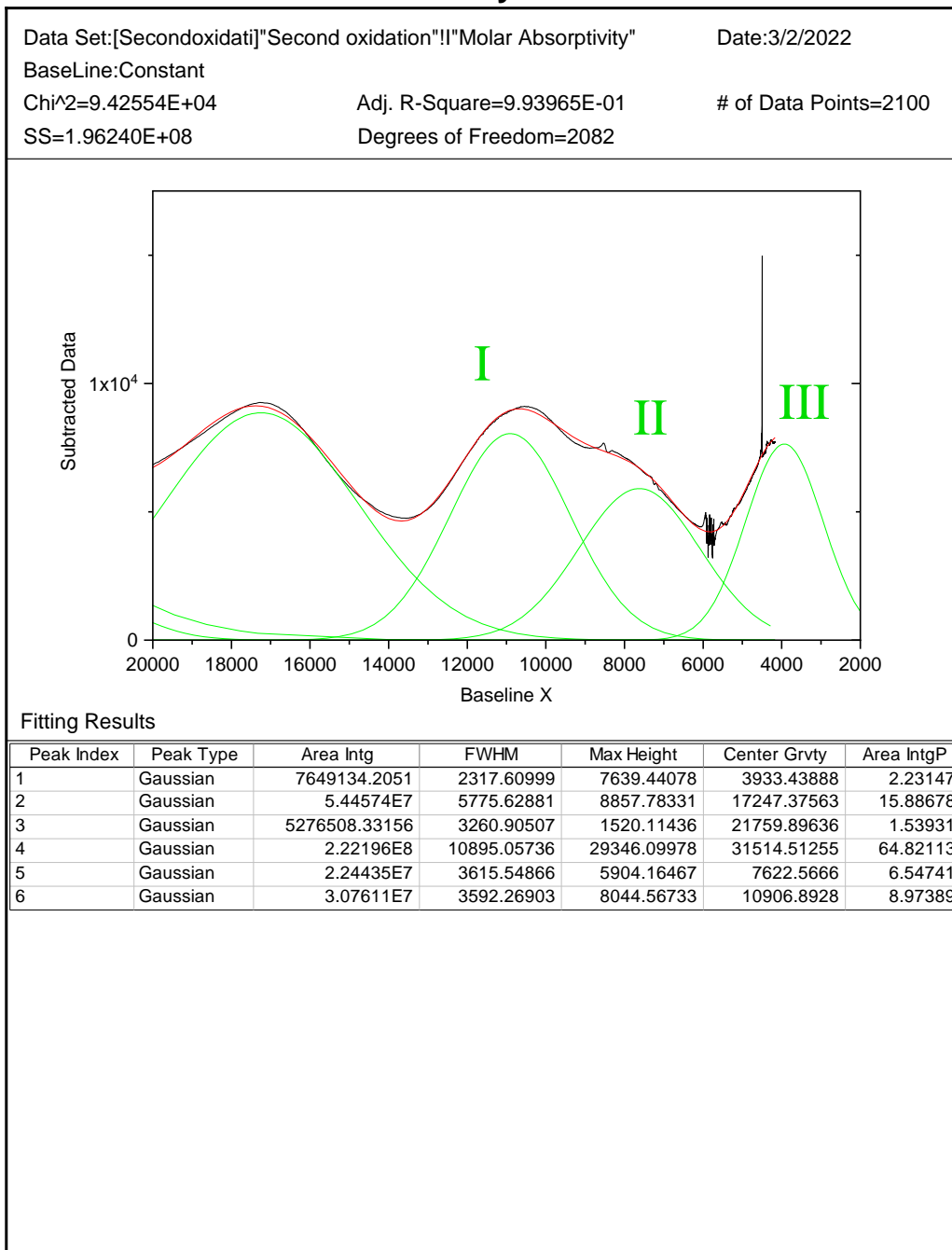


Figure B.4. Visible-NIR absorption spectrum (black line) of the mixed-valence complex $[8]^+$ in 0.1 M $[NBu_4][PF_6]$ without IR data. Multiple Gaussian bands (green lines) and their sum (red line) to fit the absorption band of $[8]^+$. IVCT peak of interest is peak III; labeled as #1 in peak index

Peak Analysis

Data Set:[Book1]Sheet1!C

Date:3/2/2022

BaseLine:Constant

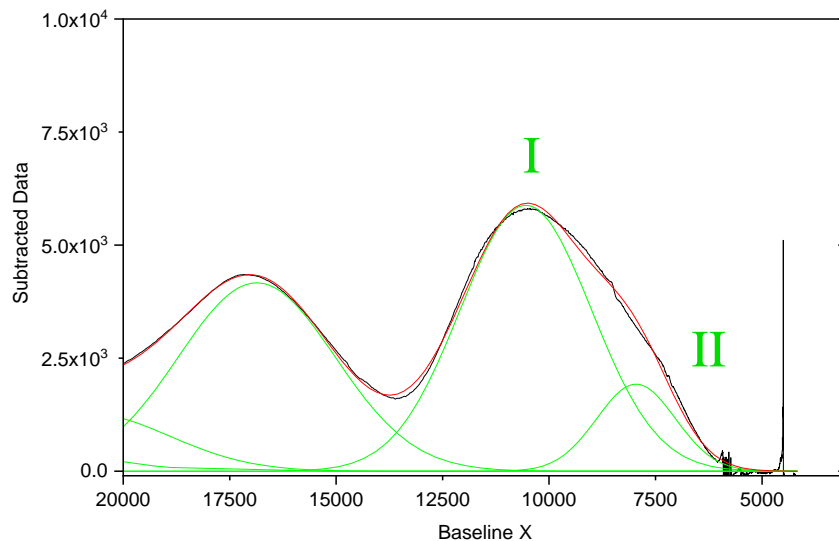
Chi^2=1.22173E+05

Adj. R-Square=9.89738E-01

of Data Points=2101

SS=2.54853E+08

Degrees of Freedom=2086



Fitting Results

Peak Index	Peak Type	Area Intg	FWHM	Max Height	Center Grvty	Area IntgP
1	Gaussian	2.27488E7	3634.95995	5879.42081	10546.35519	12.3543
2	Gaussian	1.92391E7	4339.28727	4165.1891	16865.42965	10.44828
3	Gaussian	1.31526E8	9016.53353	20258.84783	31580.36096	71.42849
4	Gaussian	6172690.21362	4549.64608	1274.57283	20832.26971	3.35223
5	Gaussian	4450037.63696	2172.38725	1924.43502	7957.32799	2.4167

Figure B.5. Visible-NIR absorption spectrum (black line) of the complex $[8]^{2+}$ in 0.1 M $[NBu_4][PF_6]$ in THF with IR data. Multiple Gaussian bands (green lines) and their sum (red line) to fit the absorption band of $[8]^{2+}$

Peak Analysis

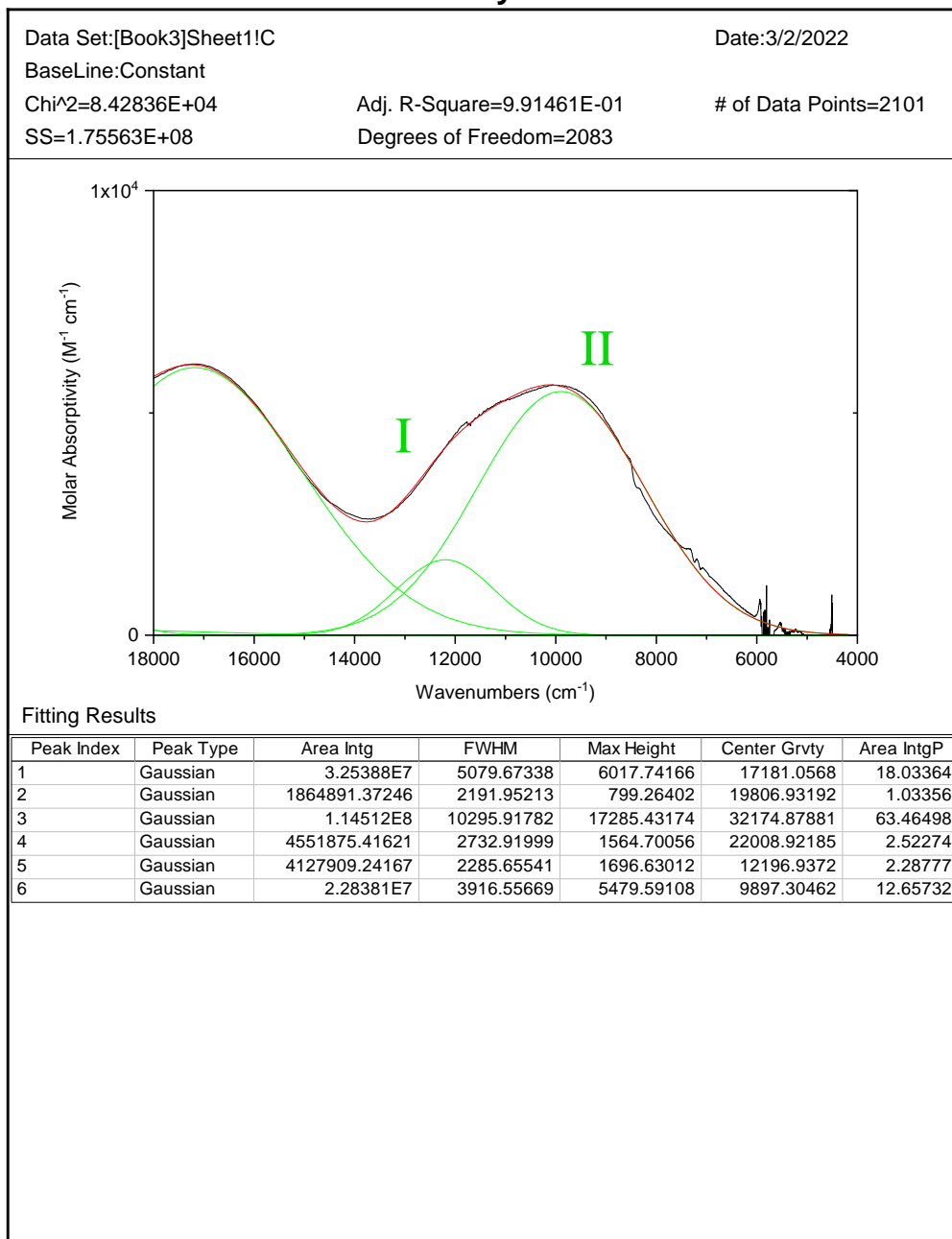


Figure B.6. Visible-NIR absorption spectrum (black line) of the complex $[9]^+$ in 0.1 M $[\text{NBu}_4][\text{PF}_6]$ in THF with IR data. Multiple Gaussian bands (green lines) and their sum (red line) to fit the absorption band of $[9]^+$

Hush Model Analysis (with IR data):

$$\Delta\bar{\nu}_{1/2\text{theor}} = (2310 * \bar{\nu}_{\text{IVCT}})^{0.5}$$

$$\Delta\bar{\nu}_{1/2\text{theor}} = (2310 * 4054)^{0.5} \rightarrow \Delta\bar{\nu}_{1/2\text{theor}} = 3,060 \text{ cm}^{-1} \text{ (experimental: } 1,716 \text{ cm}^{-1}\text{)}$$

$$H_{ab} = (0.0206 / r) * (\bar{\nu}_{\text{IVCT}} * \Delta\bar{\nu}_{1/2\text{exp}} * \epsilon)^{0.5} \text{ (} r = \text{geometric distance or number of bonds)}$$

$$H_{ab} = (0.0206 / 6.954) * (4054 * 1716 * 6859)^{0.5} \rightarrow H_{ab} = 647.1$$

Hush Model Analysis (w/o IR data):

$$\Delta\bar{\nu}_{1/2\text{theor}} = (2310 * \bar{\nu}_{\text{IVCT}})^{0.5}$$

$$\Delta\bar{\nu}_{1/2\text{theor}} = (2310 * 3933)^{0.5} \rightarrow \Delta\bar{\nu}_{1/2\text{theor}} = 3,014 \text{ cm}^{-1} \text{ (experimental: } 2,316 \text{ cm}^{-1}\text{)}$$

$$H_{ab} = (0.0206 / r) * (\bar{\nu}_{\text{IVCT}} * \Delta\bar{\nu}_{1/2\text{exp}} * \epsilon)^{0.5}$$

$$H_{ab} = (0.0206 / 6.954) * (3933 * 2316 * 7638)^{0.5} \rightarrow H_{ab} = 781.6$$

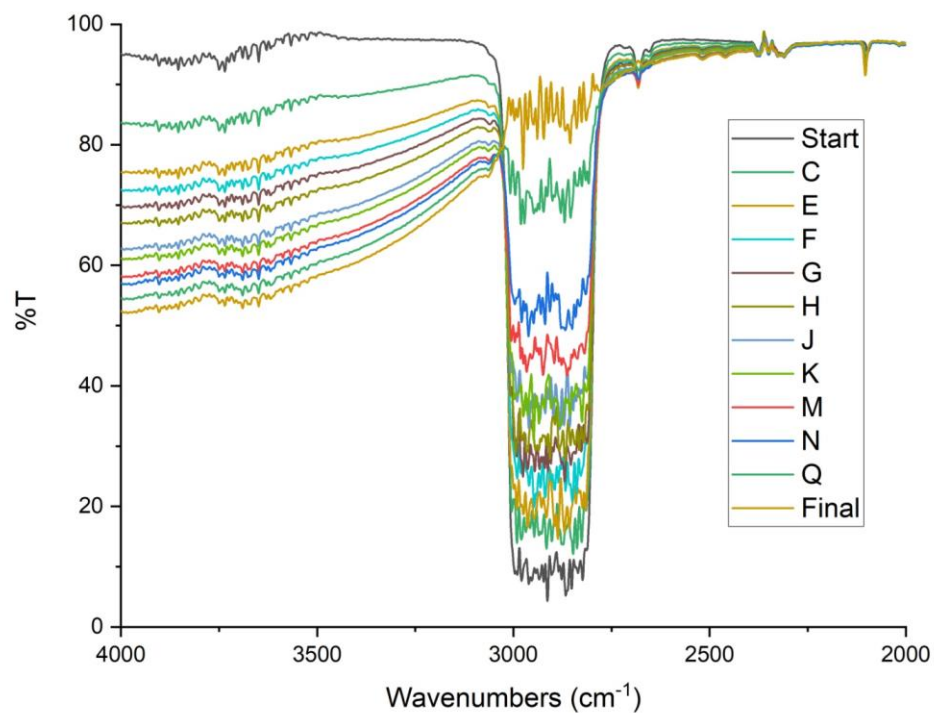


Figure B.7. Full FT-IR spectroelectrochemistry of **8** at 0.1 V vs Ag wire. 2 mM analyte with 0.1 M [Bu₄N][PF₆] in THF in all cases. Upon application of the potential, general absorption from 4,000 cm⁻¹ to *ca.* 2,500 cm⁻¹ is observed. This was determined not to be shifting of the baseline absorption as the area around $\bar{\nu}(\text{C}\equiv\text{N})$ does not experience the same large shifts (see Figure 2.13). Conversion from %T to absorbance then absorbance values to molar absorptivity values was done to generate the ‘missing’ half of the IVCT band in the spectra of [**8**]⁺

Table B.5. $\bar{\nu}(\text{C}\equiv\text{N})$ of [**8**]ⁿ⁻/[**8**]ⁿ⁺ (n = 1,2) and [**9**]^{+/-}

(cm ⁻¹)	[8] ²⁺	[8] ⁺	8	[8] ⁻	[8] ²⁻	[9] ⁺	9	[9] ⁻
$\bar{\nu}(\text{C}\equiv\text{N})$	2107	2103	2096	2092, 2069	2068	2119	2096	2070

Table B.6. Selected bond metrics for the DFT-optimized structure of **8**, vs experimental values*

Bond metrics, $\text{\AA}/^\circ$	Expt, 8	8 B97D3		8 B3LYP	
		S = 0	S = 1	S = 0	S = 1
Ru-Ru	2.4892(7), 2.4829(5)	2.49444	2.46186	2.52986	2.5306, 2.4362
Ru-C_{aryl}	2.052(3), 2.051(3)	2.020915	2.00454	2.06045	2.0488, 2.0639
Ru-C_{CN}	2.019(4), 2.013(3)	1.977115	1.97057	1.99883	2.0008
C\equivN	1.140(5), 1.143(4)	1.17343	1.17945	1.16177	1.16151
Ru-Ru-C_{aryl}	152.2(1), 147.1(1)	153.2346	154.4704	154.5895	154.249, 157.049
Ru-Ru-C_{CN}	168.0(1), 170.6(1)	167.2827	167.1395	166.7488	166.0565
$\nu(\text{C}\equiv\text{N})$	2096	2101.43	DNC	2204.34	2201.26, 2205.78

*All values are averages, unless there is a significant discrepancy in the two 'halves' of the molecule, in which case two values are reported. DNC = Calculation did not converge.

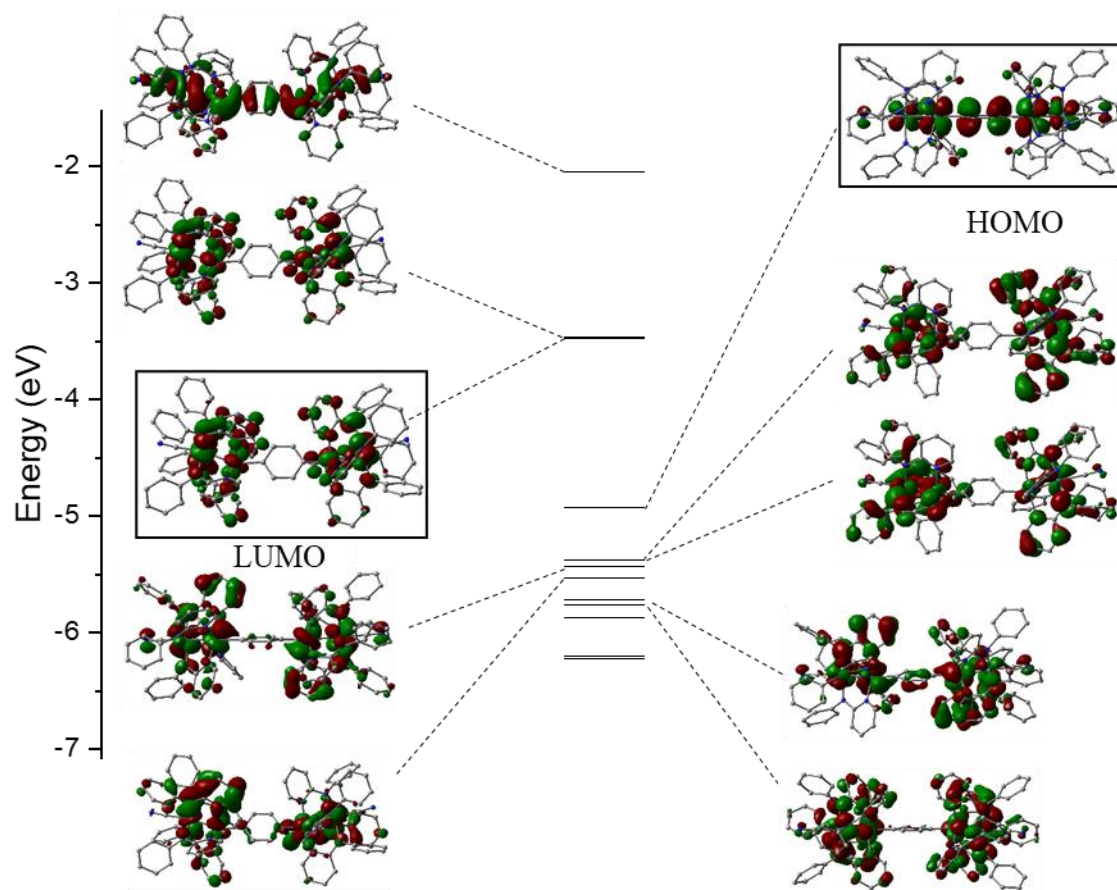


Figure B.8. Frontier α -spin molecular orbitals of **8**, $S = 0$, plotted at $|\text{Isovalue}| = 0.025$

Table B.7. Selected molecular orbitals of **8** ($S = 0$ state) (see Figure B.8. for orbital energies)

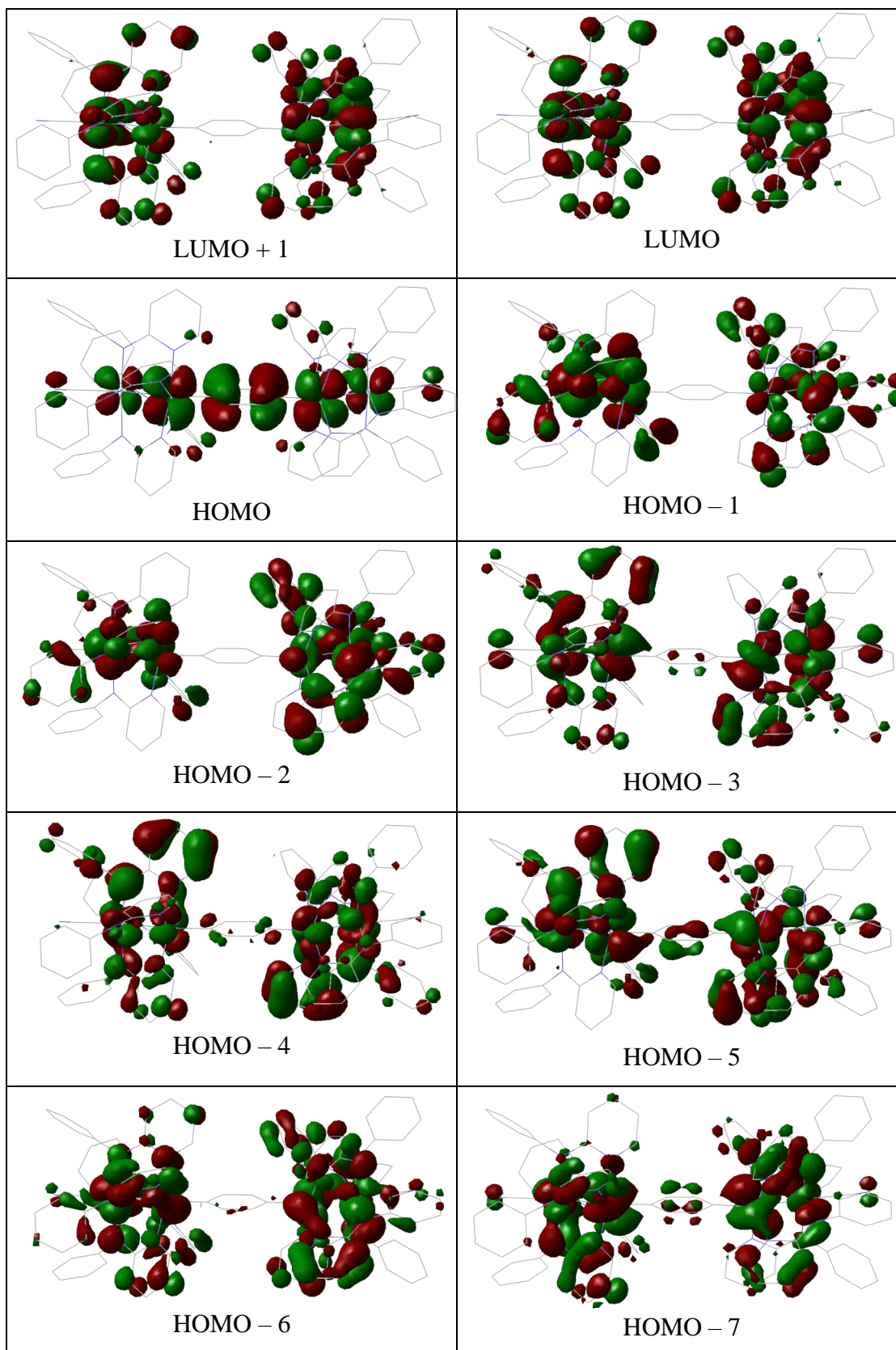


Table B.7 Continued

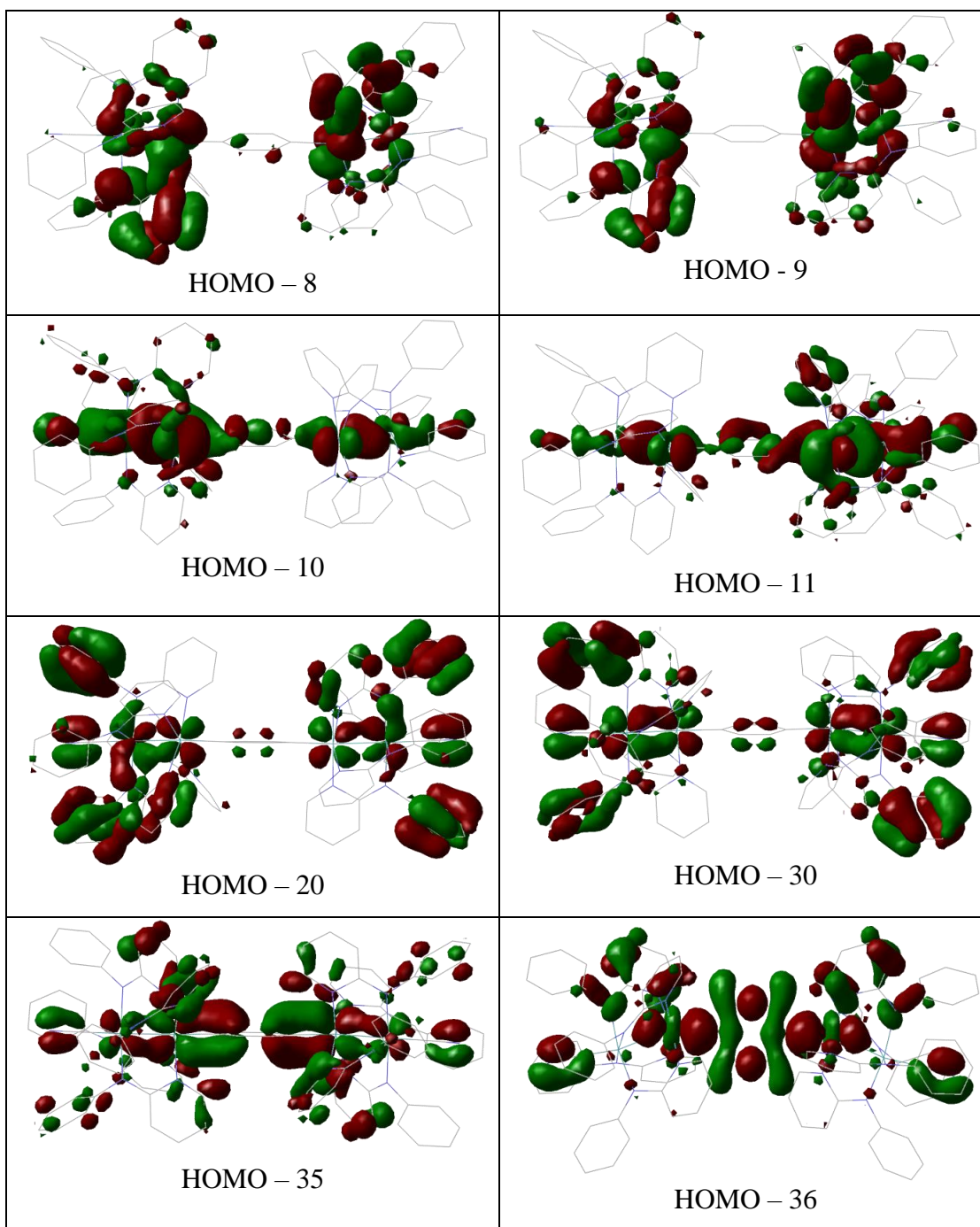


Table B.8. Some frontier molecular orbitals and % atomic/fragment orbital contributions

MO	% Ru contribution (Ru-Ru fragment orbitals) [†]	% phenylene contribution
LUMO + 1	49.64 ($\delta^*(\text{Ru}_2)$)	1.13
LUMO	48.75 ($\delta^*(\text{Ru}_2)$)	0.49
HOMO	62.10 ($\pi_{yz}^*(\text{Ru}_2)$)	25.86 (only 2p _y)
HOMO – 1	21.36 (mix, Ru1 and Ru3: $d_{yz}+d_{xz}$; Ru2 and Ru4: $d_{z2} + d_{xz}$)	0.74
HOMO – 2	23.27 (mix, Ru1 and Ru3: $d_{x2-y2}+d_{xz}$; Ru2 and Ru4: $d_{z2} + d_{xz}$)	0.95
HOMO – 3	53.06 ($\pi_{yz}^*(\text{Ru}_2)$)	1.54
HOMO – 4	24.27 (Mix; major d_{x2-y2})	2.43
HOMO – 5	29.98 (mix, Ru1 and Ru3: $d_{yz}+d_{xz}$; Ru2 and Ru4: $d_{z2} + d_{xy}$)	2.81
HOMO – 6	23.48 (mix, Ru1 and Ru3: $d_{x2-y2}+d_{z2}+d_{xz}$; Ru2 and Ru4: $d_{yz} + d_{xy}$)	0.93
HOMO – 7	50.54 ($\pi_{yz}^*(\text{Ru}_2)$)	2.64
HOMO – 8	41.91 ($\delta(\text{Ru}_2)$)	1.26
HOMO – 9	49.05 ($\delta(\text{Ru}_2)$)	0.82
HOMO – 10	56.94 ($\pi_{xz}^*(\text{Ru}_2)$)	4.29
HOMO – 11	55.37 ($\pi_{xz}^*(\text{Ru}_2)$)	5.98
HOMO – 20	18.89 ($\pi_{yz}(\text{Ru}_2) - \pi(\text{CN})$)	0.20
HOMO – 30	30.72 ($\pi_{yz}(\text{Ru}_2) - \pi(\text{CN})$)	2.4
HOMO – 35	29.10 ($\pi_{yz}(\text{Ru-C})$)	26.1
HOMO – 36	23.30 ($\sigma(\text{Ru-C})$)	26.2

[†]Where assignments of the Ru-Ru d-manifold could not be discerned due to extensive mixing, the component d-orbitals are listed.

Table B.9. Selected bond metrics for the DFT-optimized structure of **9**, vs experimental values

	Expt, 3	3 B97D3		3 B3LYP	
		S = 0	S = 1	S = 0	S = 1
Ru-Ru	2.5011(6)	2.50495	2.41004	2.52001	2.42176
Ru-C_{aryl}	2.052(2)	2.02367	2.04369	2.03573	2.04837
Ru-C_{CN}	2.008(2)	1.97202	2.00320	1.99359	2.00495
C≡N	1.156(2)	1.17310	1.17129	1.16908	1.16809
Ru-Ru-C_{aryl}	156.26(5)	152.36105	153.08416	153.23693	155.12857
Ru-Ru-C_{CN}	170.88(5)	168.01125	167.38325	167.99598	167.18985
ν(C≡N)	2089	2090.36	DNC	2224.79	2223.50

Table B.10. Selected bond metrics for the DFT-optimized structure of **[8]⁺**

	B97D3	B3LYP
Ru-Ru	2.46636	2.51132
Ru-C_{aryl}	2.00740	1.97618
Ru-C_{CN}	1.97741	1.99719
C≡N	1.17227	1.16171
Ru-Ru-C_{aryl}	153.85443	153.16124
Ru-Ru-C_{CN}	174.17953	167.9283

APPENDIX C: ADDITIONAL MATERIALS FOR BIS-ARYL AND BIS-ALKYNYL (III,III) COMPOUNDS BASED ON AN ELECTRON-DEFICIENT BUILDING BLOCK

Table C.1. Crystal data for compounds **10–12**

	10	11	12
Chemical formula	C ₄₀ H ₂₆ F ₁₂ N ₈ Ru ₂	C ₃₆ H ₂₆ F ₁₂ N ₈ Ru ₂	C ₃₆ H ₂₆ F ₁₂ N ₈ Ru ₂
Fw, g/mol	1048.83	1000.79	1000.79
Space group	<i>P</i> 2 ₁ / <i>c</i>	<i>P</i> $\bar{1}$	<i>P</i> 2 ₁ / <i>c</i>
<i>a</i> , Å	9.2793(7)	10.4699(7)	10.4004(9)
<i>b</i> , Å	10.2070(6)	13.0648(7)	16.8558(15)
<i>c</i> , Å	20.6261(12)	14.2903(9)	21.0170(17)
α °	90	82.929(3)	90
β °	94.009(2)	84.158(2)	100.805(4)
γ °	90	73.420(2)	90
<i>V</i> , Å ³	1948.8(2)	1854.6(2)	3619.1(5)
<i>Z</i>	2	2	4
<i>T</i> , K	150	150	150
λ , Å	1.54178	0.71073	1.54178
ρ_{calcd} , g/cm ³	1.787	1.792	1.837
<i>R</i>	0.033	0.035	0.044
<i>R_w</i> (<i>F</i> ²)	0.090	0.080	0.119

Table C.2. Solid state magnetism of Ru₂(amt₂mp)₄Cl₂ with diamagnetic corrections

Avg. χ_g (emu/mol)	Avg. χ_m (emu/mol)	Avg. μ_{eff} (B.M.)
3.83x10 ⁻⁶	3.52x10 ⁻³	2.71

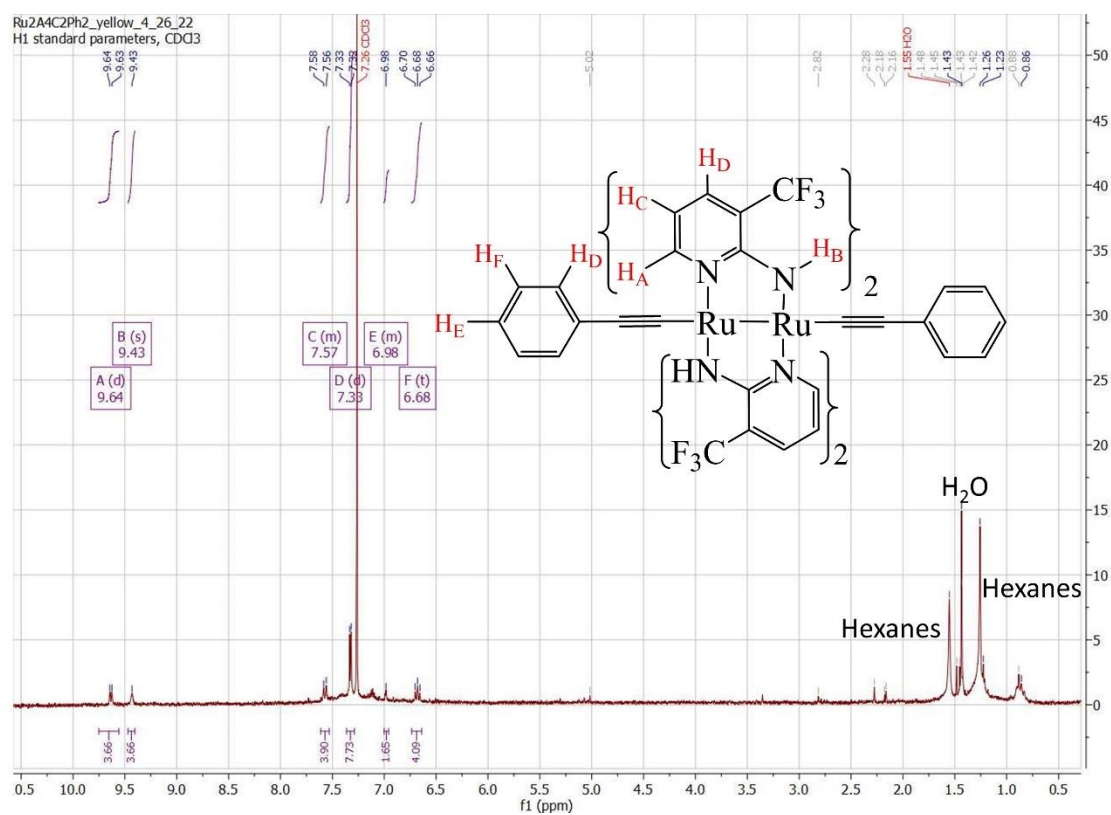


Figure C.1. 1H NMR of **10** in $CDCl_3$ at 293 K

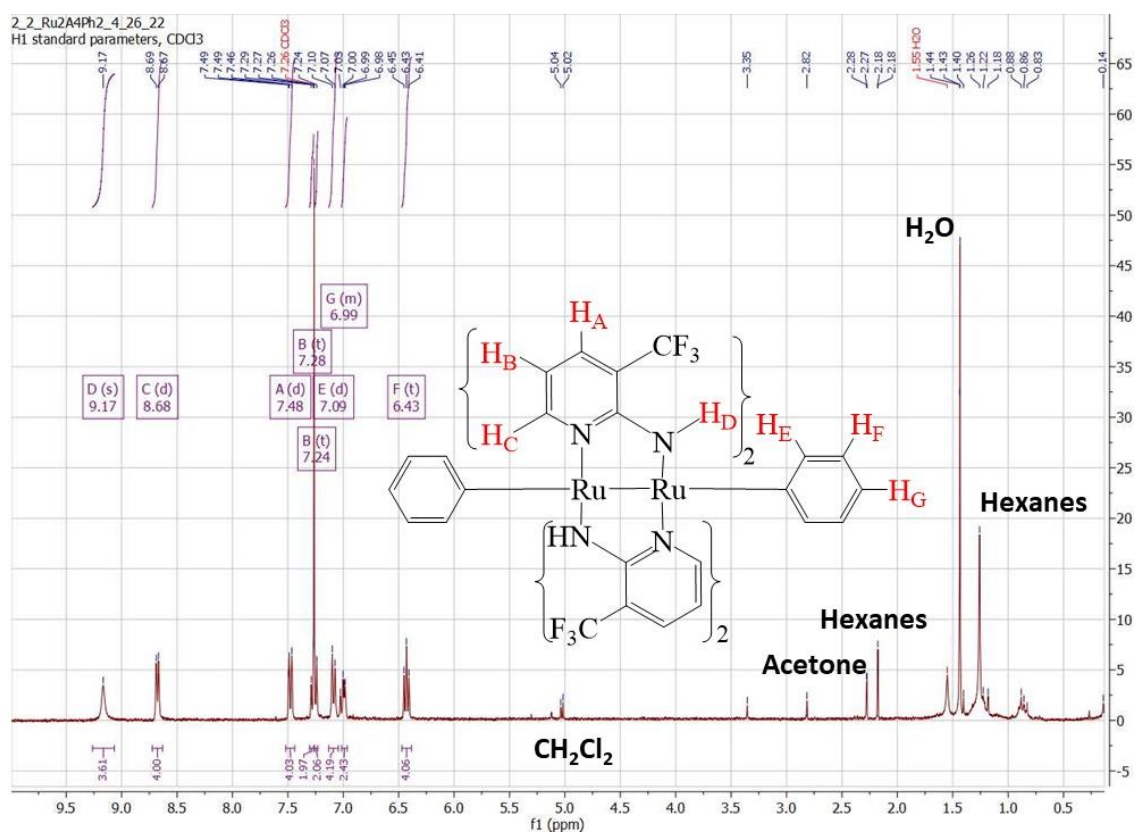


Figure C.2. ¹H NMR of **11** in CDCl₃ at 293 K. Proton H_B overlapped with the CDCl₃ solvent peak, however integration of the outlying portions gave a reasonably close integration of combined 4 H

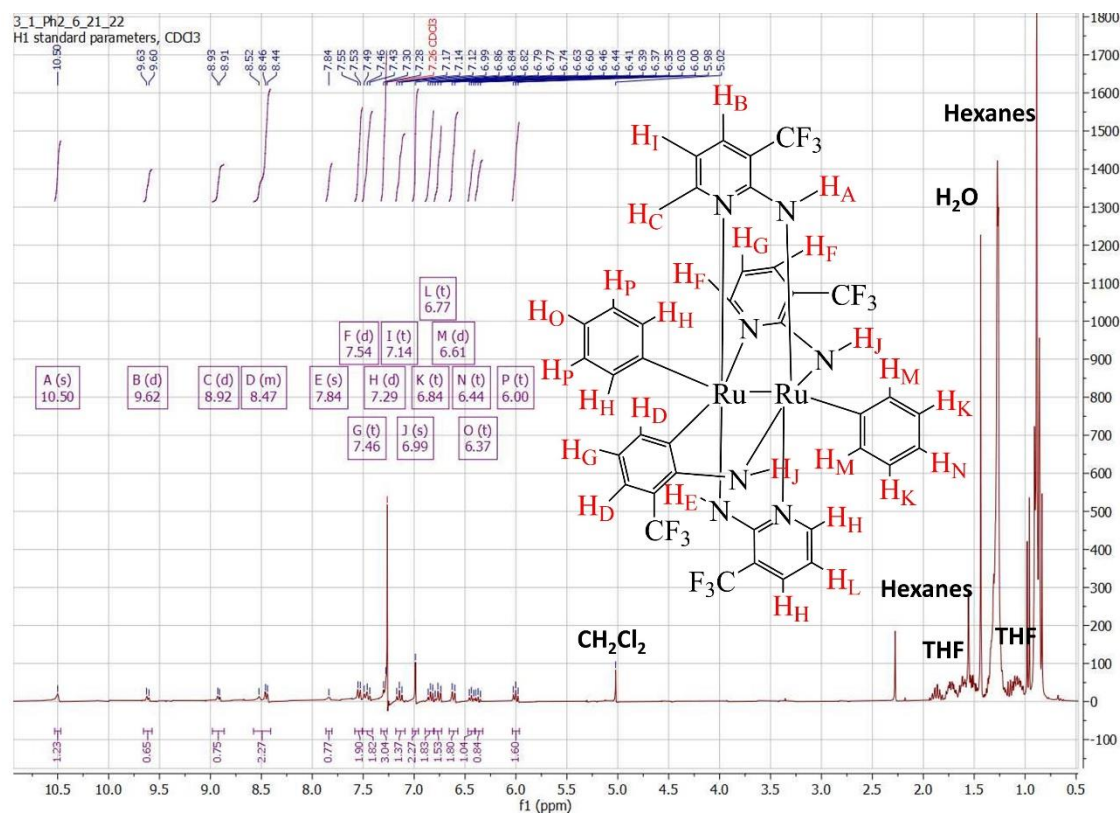


Figure C.3. ¹H NMR of **12** in CDCl₃ at 293 K

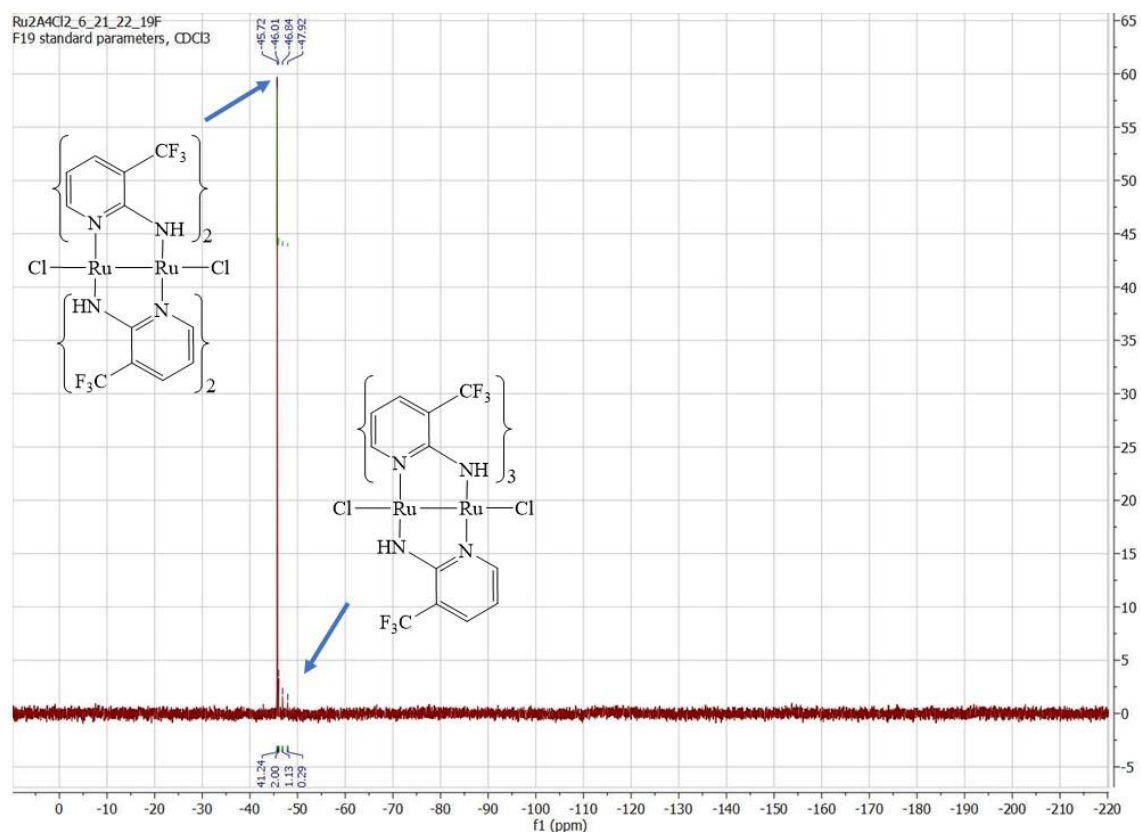


Figure C.4. ^{19}F NMR of $\text{Ru}_2(\text{amtftp})_4\text{Cl}_2$ in CDCl_3 at 293 K. The major fluorine peak (-45.72 ppm) indicates all $-\text{CF}_3$ groups are equivalent, supporting the *cis* (2:2) $\text{Ru}_2(\text{amtftp})_4$ arrangement of the bridging amtftp ligands. The minor fluorine peaks (-46.01, -46.82 and -47.92 ppm) are present in a rough 2:1:1 ratio, similar to **12**, supporting the (3:1) arrangement of the bridging amtftp ligands. A large shift from the free ligand, bis-alkynyl (**10**) and bis-aryl (**11** and **12**) ^{19}F peak positions is attributed to the paramagnetism of the material

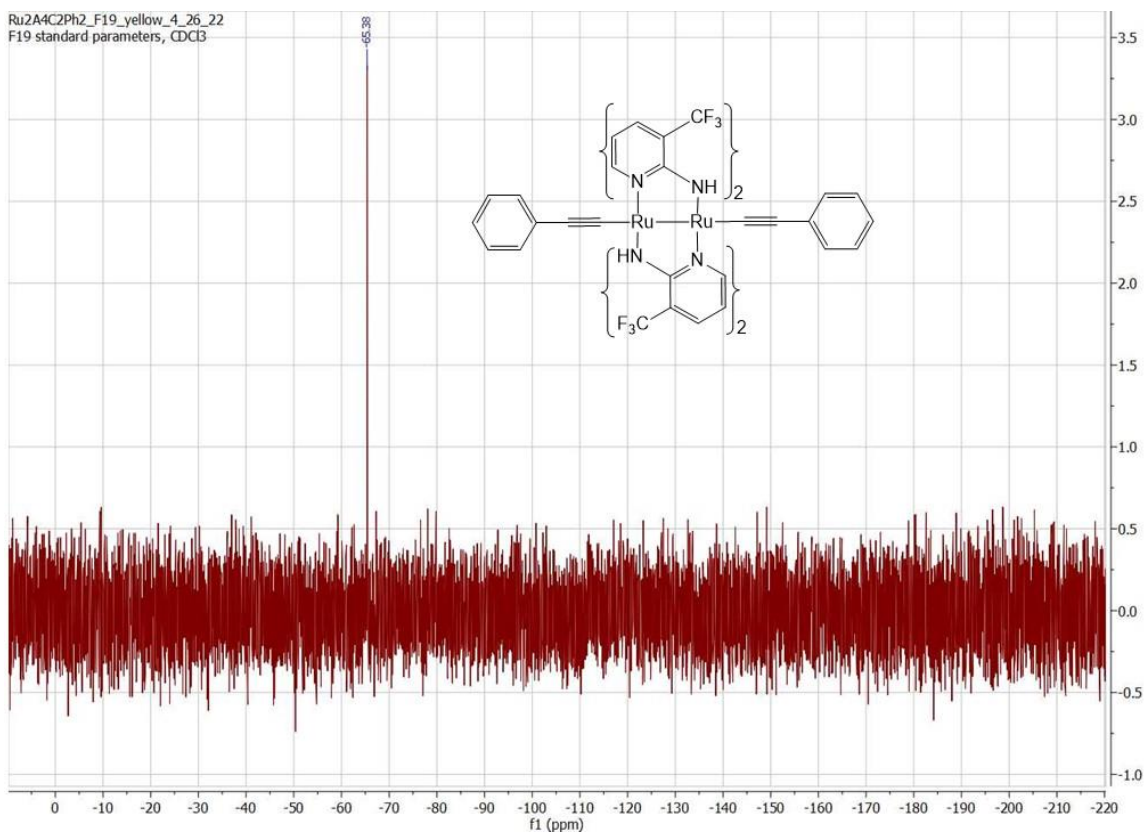


Figure C.5. ^{19}F NMR of **10** in CDCl_3 at 293 K. Only one fluorine peak indicates all $-\text{CF}_3$ groups are equivalent, supporting the *cis* (2:2) $\text{Ru}_2(\text{amtfmp})_4$ arrangement of the bridging amtfmp ligands

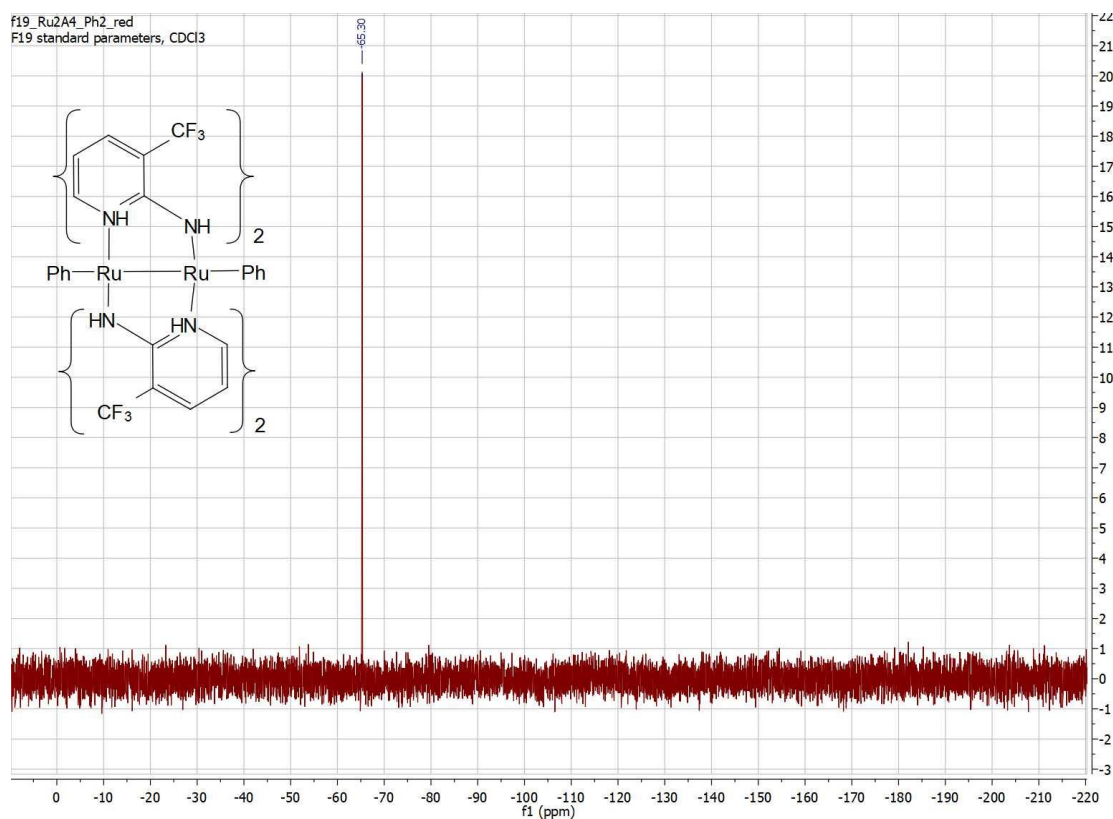


Figure C.6. ¹⁹F NMR of **11** in CDCl₃ at 293 K. Only one fluorine peak indicates all -CF₃ groups are equivalent, supporting the *cis* (2:2) Ru₂(amt₂fmp)₄ arrangement of the bridging amt₂fmp ligands

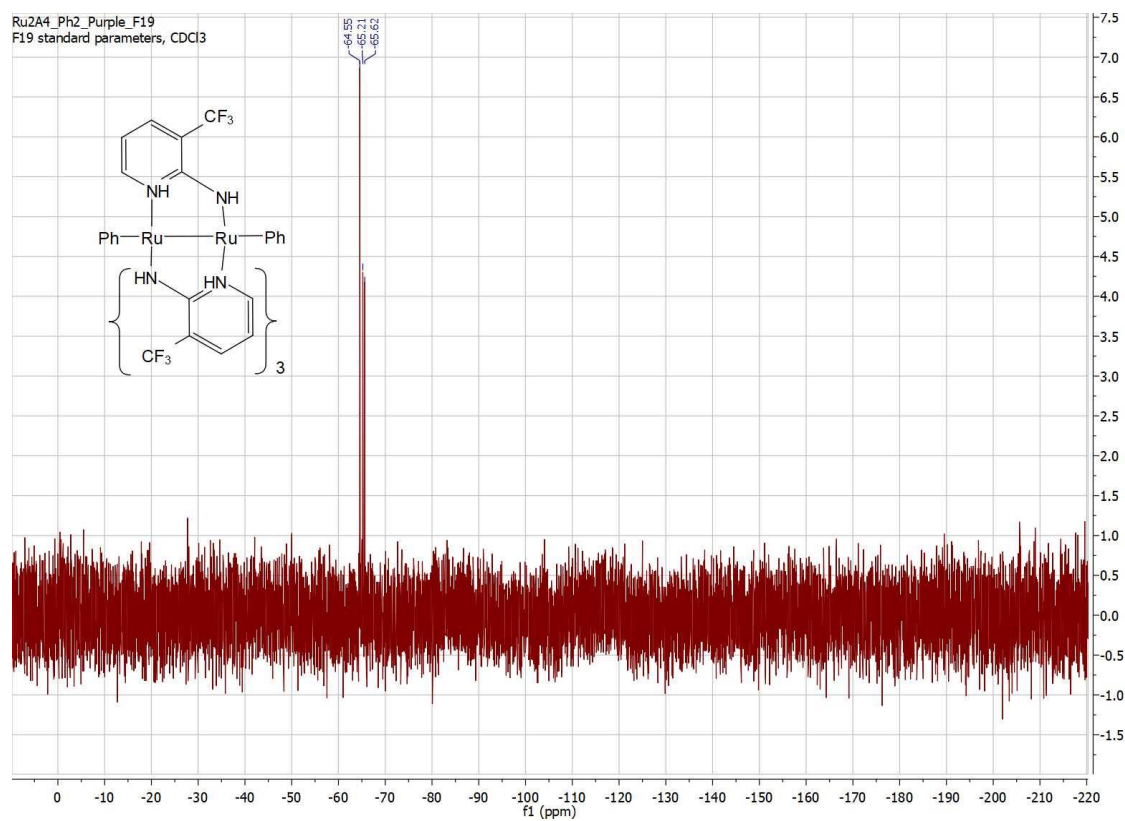


Figure C.7. ¹⁹F NMR of **12** in CDCl₃ at 293 K. Three fluorine peaks, with the largest being approximately double the size of the other two peaks supports the (3:1) arrangement of the bridging amtfmp ligands: two *trans* amtfmp ligands experience the same environment (large peak) while the other two *trans* amtfmp ligands experience different environments (two smaller peaks)

Table C.3. Selected geometric parameters from X-ray diffraction (**10** and **11**) and DFT calculations (**10'** and **11'**) for B3LYP / lanl2dz

Bond Length (Å) and Angle (deg.)	Experiment 10	10'	Experiment 11	11'
Ru–Ru	2.4656(4)	2.5299	2.5144[4]	2.56092
Ru–C	1.979(3)	1.9748	2.047[3]	2.04053
Ru–Ru–C	157.23(8)	158.8364	158.60[8]	160.48262
Ru–N1	2.026(2)	2.0557	2.032(2)	2.03698
Ru–N2	2.051(3)	2.0608	2.063(2)	2.05840
Ru–N3	2.058(2)	2.0572	2.060(2)	2.05839
Ru–N4	2.021(2)	2.0618	2.008(4)	2.03696

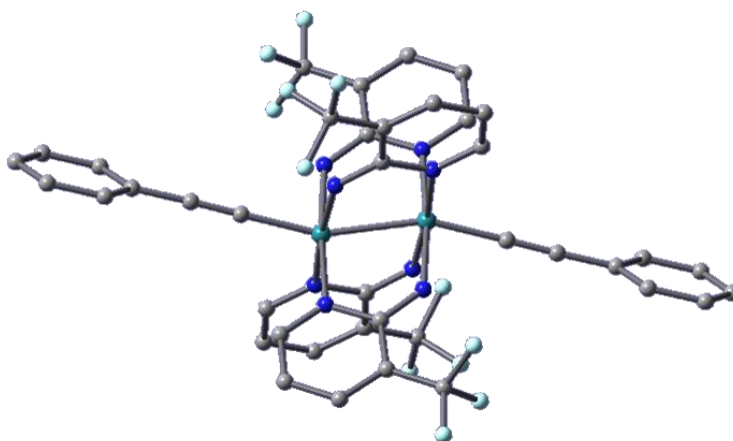


Figure C.8. DFT-optimized structure of **10'** using the B3LYP functional and lanl2dz basis set. Covalent radii of all atoms have been scaled by a factor of 0.35, and hydrogens have been omitted for clarity

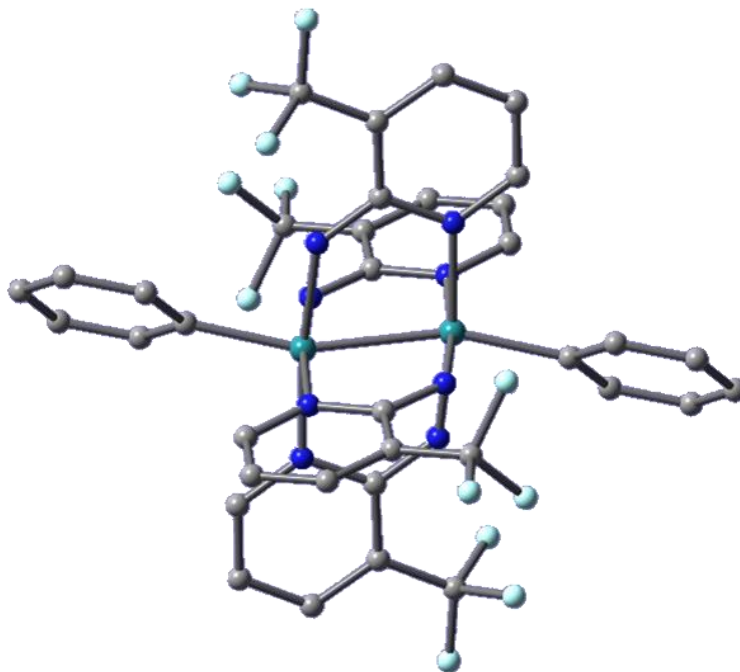


Figure C.9. DFT-optimized structure of **11'** using the B3LYP functional and lanl2dz basis set. Covalent radii of all atoms have been scaled by a factor of 0.35, and hydrogens have been omitted for clarity

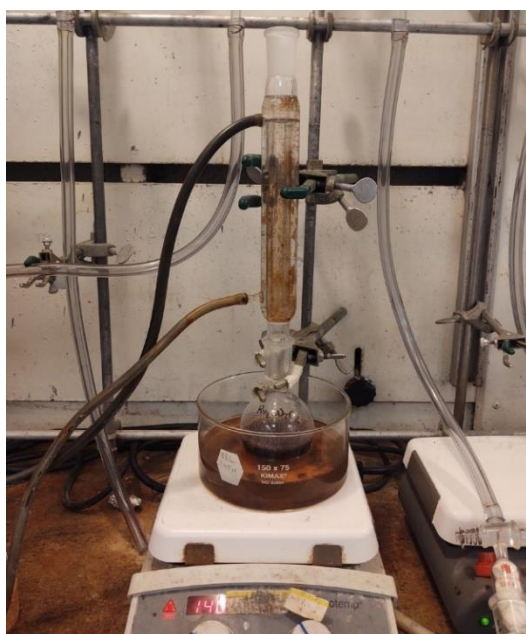


Figure C.10. Reflux apparatus used to synthesize $\text{Ru}_2(\text{amtfmp})_4\text{Cl}_2$



Figure C.11. Filtration of crude $\text{Ru}_4(\text{amtftp})_4\text{Cl}_2$ through Celite to remove excess LiCl . Solution was a dark red-purple



Figure C.12. Column purification of $\text{Ru}_2(\text{amtftp})_4\text{Cl}_2$. The excess ligand was removed by running CHCl_3 , the product ($\text{Ru}_2(\text{amtftp})_4\text{Cl}_2$) removed with CHCl_3 with 5% MeOH (v/v)



Figure C.13. TLC plate of the literature synthesis $\text{Ru}_2(\text{amtfmp})_4\text{Cl}_2$ material (left lane, abbreviated as 'SM'), a co-spot of the literature material and the crude lithiation product (center lane, abbreviated as 'Co'), and the crude aryl lithiation product (right lane, abbreviated as 'Lith')

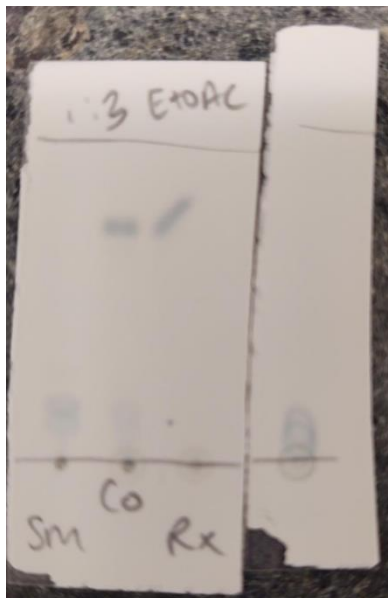


Figure C.14. Left plate: TLC plate analysis with 1:3 EtOAc / hexanes of the literature $\text{Ru}_2(\text{amtfmp})_4\text{Cl}_2$ material (left lane, abbreviated as 'SM'), a co-spot of the literature material and the crude lithiation product (center lane, abbreviated as 'Co'), and the crude alkynyl lithiation product (right lane, abbreviated as 'Rx'). Right plate: TLC plate analysis with hexanes of the crude alkynyl lithiation product.

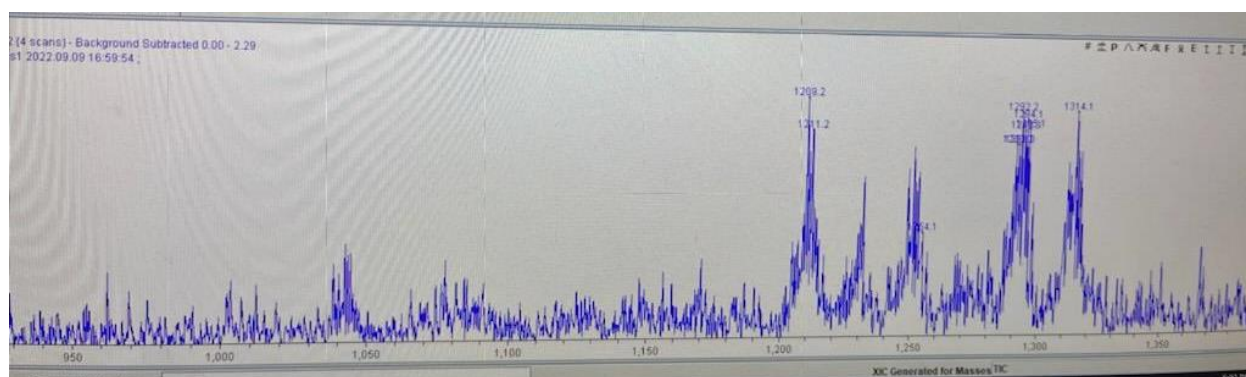


Figure C.15. Mass Spectrum of crude alkynyl lithiation product with desired product at 1209 ($[M-H]^+$) and other Ru_2 isotope peaks at higher m/z

**APPENDIX D: ADDITIONAL MATERIALS FOR SYNTHESIS, STRUCTURAL & SPECTROSCOPIC
ANALYSIS OF MONO- AND UNSYMMETRIC BIS-ALKYNYL COMPOUNDS BASED ON
RU(II)(C₂NAP^R)**

Table D.1. Crystal data for compounds **13–17**

	13	14	15	16	17
Chemical formula	(C ₆₇ H ₆₀ ClNO ₂ P ₄ Ru)· C ₆ H ₁₄	(C ₇₅ H ₆₄ ClNO ₂ P ₄ Ru)· 3(C ₄ H ₈ O)	C ₈₃ H ₆₉ NO ₂ P ₄ Ru	2(C ₆₇ H ₅₆ ClNO ₂ P ₄ Ru)· C ₅ H ₁₀ O ₂ ·C ₆ H ₁₄	C ₇₃ H ₆₀ ClNO ₂ P ₄ Ru
Fw, g/mol	1238.66	1487.98	1337.34	2523.35	1243.62
Space group	<i>P</i> 2 ₁ / <i>n</i>	<i>P</i> 1̄	<i>P</i> 1̄	<i>P</i> 2 ₁ / <i>n</i>	<i>I</i> 4̄
<i>a</i> , Å	11.4638 (6)	12.9797 (7)	12.6432 (6)	10.0568 (6)	26.0481 (9)
<i>b</i> , Å	32.8299 (17)	13.7053 (7)	13.8706 (7)	37.672 (2)	26.0481 (9)
<i>c</i> , Å	15.7008 (8)	21.1443 (12)	21.8919 (11)	17.9949 (9)	17.7955 (8)
<i>α</i> °	90	98.320 (3)	73.270 (2)	90	90
<i>β</i> °	92.077 (2)	92.086 (3)	75.428 (2)	96.4771 (19)	90
<i>γ</i> °	90	99.444 (3)	80.788 (2)	90	90
<i>V</i> , Å ³	5905.2 (5)	3664.4 (3)	3542.4 (3)	6774.0 (6)	12074.3 (10)
<i>Z</i>	4	2	2	2	8
<i>T</i> , K	150	150	150	150	150
<i>λ</i> , Å	0.71073	0.71073	1.54178	0.71073	0.71073
<i>ρ</i> _{calcd} , g/cm ³	1.393	1.349	1.254	1.237	1.368
<i>R</i>	0.044	0.060	0.058	0.032	0.067
<i>R</i> _w (<i>F</i> ²)	0.136	0.106	0.107	0.168	0.148

Table D.2. Comparisons of Ru–C and Ru–Cl bond lengths (Å) for **13** and **14** with other *trans*-RuCl(C≡C-R)(dppe)₂ compounds

R	Ru–C	Ru–Cl	Ref
NAP ^{iPr} (13)	1.988(5)	2.4712(8)	this work
NAP ^{mes} (14)	1.988(6)	2.4781(5)	this work
C ₆ H ₃ (Me-2)NO ₂ -4	2.013(11)	2.473(3)	151
C ₆ H ₄ NO ₂ -4	1.986(5)	2.500(1)	151
C ₆ H ₅	2.007(5)	2.4786(13)	152
C ₆ H ₄ NPh ₂	1.997(3)	2.5349(7)	251
C ₆ H ₄ F-4	2.013(4)	2.5149(10)	252
C ₆ H ₄ Me*2CH ₂ Cl ₂	2.007(4)	2.5096(8)	163
C ₆ H ₄ Me*0.5THF	2.009(5)	2.4907(12)	163

Table D.3. Comparisons of Ru–C bond lengths (Å) for **15** with other *trans*-Ru(C≡CR)(C≡CR')(dppe)₂ compounds

R	R'	Ru–C≡CR	Ru–C≡CR'	Ref
C ₆ H ₅	NAP ^{mes} (15)	2.060(2)	2.079(2)	this work
C ₆ H ₅	bpyCu(hfac) ₂	2.150(6)	2.074(4)	248
C ₆ H ₅	1,4-(C ₆ H ₄) ₂ -4-NO ₂	2.066(3)	2.066(3)	181
Fc	C ₆ H ₄ NPh ₂	2.082(3)	2.061(3)	249
C ₆ H ₅	C ₆ H ₅	2.061(5)	2.064(5)	152
C ₆ H ₅ C≡CBu ^t	C ₆ H ₅ C≡CBu ^t	2.057(2)	----	165
C≡CH	C≡CH	2.050(4)	----	250

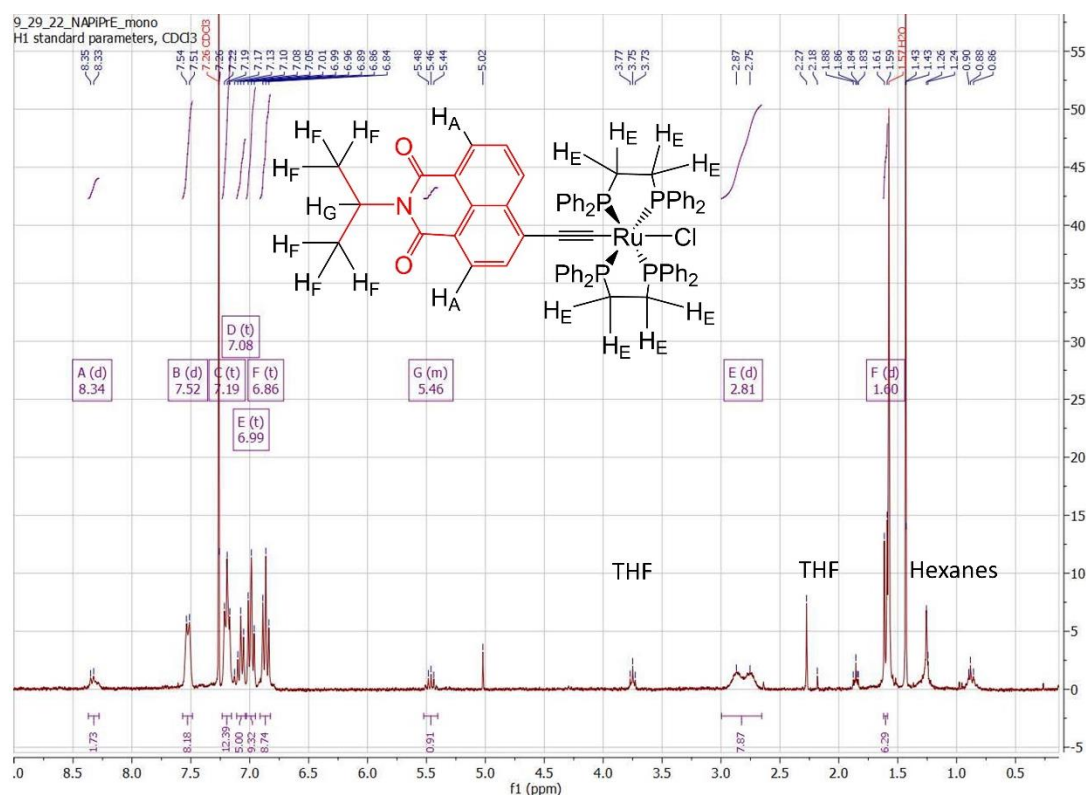


Figure D.1. ¹H NMR spectra of *trans*-RuCl(C₂NAP^{iPr})(dppe)₂ (**13**) in CDCl₃. Identifiable protons on structure noted, with the multiplets around 7.5 – 6.86 ppm assigned to remaining NAP and phenyl protons.

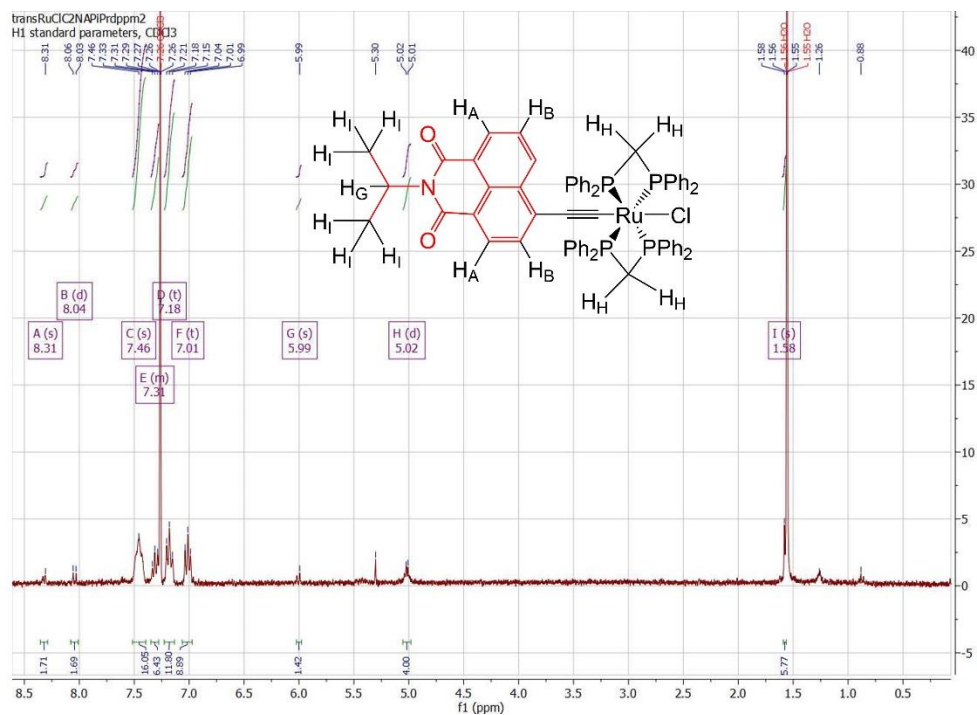


Figure D.1. ^1H NMR spectra of *trans*- $\text{RuCl}(\text{C}_2\text{NAP}^{\text{iPr}})(\text{dppm})_2$ (**16**) in CDCl_3 . Identifiable protons on structure noted, with the multiplets around 7.5 – 7.01 ppm assigned to remaining NAP and phenyl protons.

Table D.3. Selected geometric parameters from X-ray diffraction (**14**, **15**, and **17**) and DFT calculations (**14'**, **15'** and **17'**) for B3LYP / lanl2dz

Bond Length (Å) and Angle (deg.)	Exp. 14	14'	Exp. 15	15'	Exp. 17	17'
Ru–Cl	2.4781(5)	2.6101	----	----	2.4878(2)	2.6032
Ru–C1	1.988(6)	1.9855	2.060(2)	2.0581	1.983(5)	1.9894
Ru–C9	----	----	2.079(2)	2.0711	----	----
C1–C2 / C9–C10	1.210(6)	1.2512	1.222(1); 1.199(3)	1.2388; 1.2445	1.223(7)	1.2505
Ru–P _{avg}	2.368[1]	2.4931	2.358[1]	2.4604	2.351[3]	2.478
Cl–Ru–C1	176.7(2)	178.10	----	-	173.18(2)	173.32
C1–Ru–C9	----	-	174.57(9)	177.80	-	-
C1–C2–C3	178.3(5)	174.57	175.9(7)	176.09	172.7(7)	179.60
C9–C10–C11	----	----	172.0(3)	178.16	----	----

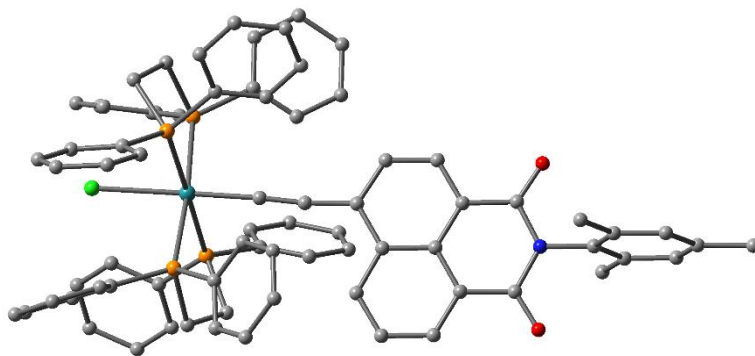


Figure D.3. DFT-optimized structure of **14'** using the B3LYP functional and lanl2dz basis set. Covalent radii of all atoms have been scaled by a factor of 0.35, and hydrogens have been omitted for clarity

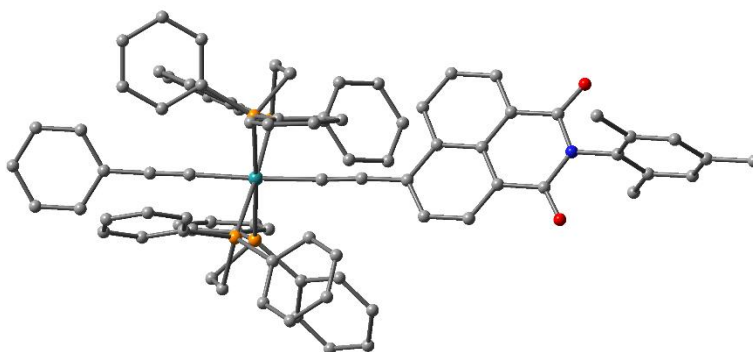


Figure D.4. DFT-optimized structure of **15'** using the B3LYP functional and lanl2dz basis set. Covalent radii of all atoms have been scaled by a factor of 0.35, and hydrogens have been omitted for clarity

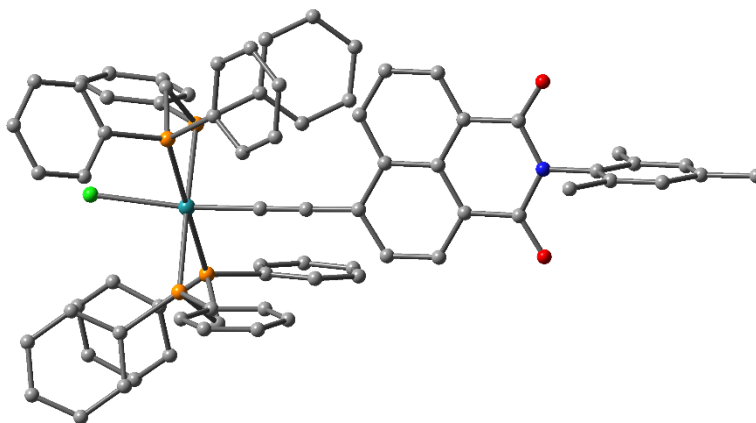


Figure D.5. DFT-optimized structure of **17'** using the B3LYP functional and lanl2dz basis set. Covalent radii of all atoms have been scaled by a factor of 0.35, and hydrogens have been omitted for clarity

Table D.4. Calculated UV-Vis transitions ($f \geq 0.01$) for **15'**, with significant transition contributions ($\geq 10\%$) listed

Excited State	Wavelength (nm)	Oscillator Strength	Significant Contributions
1	444.29	0.8828	HOMO-2 \rightarrow LUMO (16%) HOMO \rightarrow LUMO (78%)
2	412.60	0.0485	HOMO-3 \rightarrow LUMO (11%) HOMO-1 \rightarrow LUMO (84%)
6	318.39	0.0611	HOMO-2 \rightarrow LUMO (67%) HOMO \rightarrow LUMO (16%)
8	295.82	0.0200	HOMO-22 \rightarrow LUMO (21%) HOMO-20 \rightarrow LUMO (39%)
12	280.56	0.4716	HOMO-3 \rightarrow LUMO (23%) HOMO \rightarrow LUMO+2 (37%)
13	277.47	0.2384	HOMO-4 \rightarrow LUMO (41%) HOMO-3 \rightarrow LUMO (12%) HOMO \rightarrow LUMO+10 (12%) HOMO \rightarrow LUMO+11 (12%)
15	273.42	0.0165	HOMO-4 \rightarrow LUMO (36%) HOMO-1 \rightarrow LUMO+2 (12%)
17	267.46	0.0591	HOMO-5 \rightarrow LUMO (22%) HOMO \rightarrow LUMO+2 (22%) HOMO \rightarrow LUMO+3 (13%)
19	265.86	0.0136	HOMO \rightarrow LUMO+3 (93%)

REFERENCES

- (1) Stephenson, T. A.; Wilkinson, G. New Ruthenium Carboxylate Complexes. *J Inorg Nucl. Chem* **1966**, 28, 2285–2291.
- (2) Bennett, M. J.; Caulton, K. G.; Cotton, F. A. Structure of Tetra-N-Butyratodiruthenium Chloride a Compound With a Strong Metal-Metal Bond. *Inorg Chem* **1969**, 8 (1), 1–6.
- (3) Angaridis, P. Ruthenium Compounds. In *Multiple Bonds between Metal Atoms*; Cotton, F. A., Murillo, C. A., Walton, R. A., Eds.; Springer Science and Business Media, Inc.: New York, 2005.
- (4) Cortijo, M.; González-Prieto, R.; Herrero, S.; Priego, J. L.; Jiménez-Aparicio, R. The Use of Amidinate Ligands in Paddlewheel Diruthenium Chemistry. *Coord Chem Rev* **2019**, 400, Art. No. 213040.
- (5) Van Caemelbecke, E.; Phan, T.; Osterloh, W. R.; Kadish, K. M. Electrochemistry of Metal-Metal Bonded Diruthenium Complexes. *Coord Chem Rev* **2021**, 434, Article 213706.
- (6) Handa, M.; Sayama, Y.; Mikuriya, M.; Nukada, R.; Hiromitsu, I.; Kasuga, K. A Chain Complex of Ruthenium(II,III) Cation Dimer Linked by a Nitroxide Radical, [Ru₂(O₂CCMe₃)₄(NITPh)]_n(NITPh-2-Phenyl-4,4,5,5-Tetramethyl-4,5-Dihydro-1H-Imidazolyl-1-Oxy-3-Oxide). *Chem Lett* **1996**, 201–202.
- (7) Handa, M.; Sayama, Y.; Mikuriya, M.; Nukada, R.; Hiromitsu, I.; Kasuga, K. Structure and Magnetic Properties of a Chain Complex with Alternating Ru(II,III) Dimer and Nitroxide Radical Arrangement [Ru₂(O₂CCMe₃)₄(Nitph)]_n(BF₄)_n, Nitph = 2-Phenyl-4,4,5,5-Tetramethyl-4,5-Dihydro-1H-Imidazol-1-Oxyl 3-N-Oxide. *Bull Chem Soc Jpn* **1998**, 71 (1), 119–125.
- (8) Vos, T. E.; Liao, Y.; Shum, W. W.; Her, J.-H.; Stephens, P. W.; Reiff, W. M.; Miller, J. S. Diruthenium Tetraacetate Monocation, [Ru^{II/III}₂(O₂CMe)₄]⁺, Building Blocks for 3-D Molecule-Based Magnets. *J Am Chem Soc* **2004**, 126, 11630–11639.
- (9) Vos, T. E.; Miller, J. S. Building Blocks for 2D Molecule-Based Magnets: The Diruthenium Tetrapivalate Monocation Ru(II/III)₂(O(2)CtBu)₄ (+). *Angew Chem Int Ed* **2005**, 44 (16), 2416–2419.
- (10) Komiya, N.; Nakae, T.; Sato, H.; Naota, T. Water-Soluble Diruthenium Complexes Bearing Acetate and Carbonate Bridges: Highly Efficient Catalysts for Aerobic Oxidation of Alcohols in Water. *Chem Comm* **2006**, No. 46, 4829–4831.
- (11) Barker, J. E.; Ren, T. Diruthenium(II,III) Bis(Tetramethyl-1,3-Benzenedipropionate) As A Novel Catalyst for Tert-Butyl Hydroperoxide Oxygenation. *Inorg Chem* **2008**, 47, 2264–2266.

- (12) Lee, H. B.; Ren, T. Aerobic Oxygenation of Organic Sulfides Using Diruthenium Activators. *Inorg Chim Acta* **2009**, *362*, 1467–1470.
- (13) Harvey, M. E.; Musaev, D. G.; Du Bois, J. A. Diruthenium Catalyst for Selective, Intramolecular Allylic C-H Amination: Reaction Development and Mechanistic Insight Gained through Experiment and Theory. *J Am Chem Soc* **2011**, *133* (43), 17207–17216.
- (14) Villalobos, L.; Cao, Z.; Fanwick, P. E.; Ren, T. Diruthenium(II,III) Tetramidates as a New Class of Oxygenation Catalysts. *Dalton Trans* **2012**, *41*, 644–650.
- (15) Miyazawa, T.; Suzuki, T.; Kumagai, Y.; Takizawa, K.; Kikuchi, T.; Kato, S.; Onoda, A.; Hayashi, T.; Kamei, Y.; Kamiyama, F.; Anada, M.; Kojima, M.; Yoshino, T.; Matsunaga, S. Chiral Paddle-Wheel Diruthenium Complexes for Asymmetric Catalysis. *Nat. Cat* **2020**, *3* (10), 851–858.
- (16) Chakravarty, A. R.; Cotton, F. A. A New Diruthenium(II, III) Compound, Ru₂(CCPh)(PhNpy)₄·2CH₂Cl₂, with an Axial Acetylide Ligand. *Inorg Chim Acta* **1986**, *113*, 19–26.
- (17) Bear, J. L.; Han, B.; Huang, S. Molecular Structure and Electrochemistry of Ru₂(Dpf)₄(C≡C-C₆H₅)₂ (Dpf = N,N'-Diphenylformamidinate Ion): A Novel Ruthenium(III)-Ruthenium(III) Dimer. *J Am Chem Soc* **1993**, *115* (3), 1175–1177.
- (18) Bear, J. L.; Han, B.; Huang, S.; Kadish, K. M. Effect of Axial Ligands on the Oxidation State, Structure, and Electronic Configuration of Diruthenium Complexes. Synthesis and Characterization of Ru₂(Dpf)₄Cl, Ru₂(Dpf)₄(C≡CC₆H₅), Ru₂(Dpf)₄(C≡CC₆H₅)₂, and Ru₂(Dpf)₄(CN)₂. *Inorg. Chem.* **1996**, *35* (10), 3012–3021. <https://doi.org/10.1021/ic950864z>.
- (19) Kadish, K. M.; Phan, T. D.; Wang, L.-L.; Giribabu, L.; Thuriere, A.; Wellhoff, J.; Huang, S.; Van Caemelbecke, E.; Bear, J. L. Synthesis, Structural, Spectroscopic, and Electrochemical Characterization of High Oxidation State Diruthenium Complexes Containing Four Identical Unsymmetrical Bridging Ligands. *Inorg Chem* **2004**, *43*, 4825–4832.
- (20) Ren, T. Diruthenium σ -Alkynyl Compounds: A New Class of Conjugated Organometallics. *Organometallics* **2005**, *24* (21), 4854–4870. <https://doi.org/10.1021/om050452q>.
- (21) Ren, T.; Xu, G. L. Diruthenium Metallaynes: Versatile Chromophores and Electrophores. *Comm Inorg Chem* **2002**, *23* (5), 355–380.
- (22) Xu, G. L.; Zou, G.; Ni, Y. H.; DeRosa, M. C.; Crutchley, R. J.; Ren, T. Polyyne-Diyls Capped by Diruthenium Termini: A New Family of Carbon-Rich Organometallic Compounds and Distance-Dependent Electronic Coupling Therein. *J Am Chem Soc* **2003**, *125* (33), 10057–10065.
- (23) Xu, G.-L.; Crutchley, R. J.; DeRosa, M. C.; Pan, Q.-J.; Zhang, H.-X.; Wang, X.; Ren, T. Strong Electronic Couplings between Ferrocenyl Centers Mediated by Bis-Ethynyl/Butadiynyl Diruthenium Bridges. *J Am Chem Soc* **2005**, *127*, 13354–13363.

- (24) Xi, B.; Liu, I. P. C.; Xu, G. L.; Choudhuri, M. M. R.; Derosa, M. C.; Crutchley, R. J.; Ren, T. Modulation of Electronic Couplings within Ru₂-Polyyne Frameworks. *J. Am. Chem. Soc.* **2011**, *133* (38), 15094–15104. https://doi.org/10.1021/JA204813H/SUPPL_FILE/JA204813H_SI_003.PDF.
- (25) Cao, Z.; Xi, B.; Jodoin, D. S.; Zhang, L.; Cummings, S. P.; Gao, Y.; Tyler, S. F.; Fanwick, P. E.; Crutchley, R. J.; Ren, T. Diruthenium-Polyyne-Diyl-Diruthenium Wires: Electronic Coupling in the Long Distance Regime. *J. Am. Chem. Soc.* **2014**, *136* (34), 12174–12183. <https://doi.org/10.1021/ja507107t>.
- (26) Blum, A. S.; Ren, T.; Parish, D. A.; Trammell, S. A.; Moore, M. H.; Kushmerick, J. G.; Xu, G.-L.; Deschamps, J. R.; Pollack, S. K.; Shashidhar, R. Ru₂(Ap)₄(s-Oligo(Phenyleneethynyl)) Molecular Wires: Synthesis and Electronic Characterization. *J Am Chem Soc* **2005**, *127*, 10010–10011.
- (27) Mahapatro, A. K.; Ying, J.; Ren, T.; Janes, D. B. Electronic Transport through Ruthenium Based Redox-Active Molecules in Metal-Molecule-Metal Nanogap Junctions. *Nano Lett* **2008**, *8*, 2131–2136.
- (28) Zhu, H.; Pookpanratana, S. J.; Bonevich, J. E.; Natoli, S. N.; Hacker, C. A.; Ren, T.; Suehle, J. S.; Richter, C. A.; Li, Q. Redox-Active Molecular Nanowire Flash Memory for High-Endurance and High-Density Nonvolatile Memory Applications. *ACS Appl Mater Inter* **2015**, *7* (49), 27306–27313.
- (29) Jiang, K.; Pookpanratana, S. J.; Natoli, S. N.; Ren, T.; Sperling, B. A.; Robertson, J.; Richter, C. A.; Yu, S.; Li, Q. Nonvolatile Memory Based on Redox-Active Ruthenium Molecular Monolayers. *Appl Phys Lett* **2019**, *115*, Art. No. 162102.
- (30) Wong, K.-T.; Lehn, J.-M.; Peng, S.-M.; Lee, G.-H. Nanoscale Molecular Organometallo-Wires Containing Diruthenium Cores. *Chem Commun* **2000**, No. 22, 2259–2260.
- (31) Zuo, J.-L.; Herdtweck, E.; Kuhn, F. E. Diruthenium -Alkynyl Complexes as Potential Building Blocks for Heterometallic Molecular Rods. *J Chem Soc Dalton Trans* **2002**, No. 7, 1244–1246.
- (32) Kuo, C.; Chang, J.; Yeh, C.; Lee, G.; Wang, C.; Peng, S. Synthesis, Structures, Magnetism and Electrochemical Properties of Triruthenium-Acetylide Complexes. *Dalton Trans* **2005**, 3696–3701.
- (33) Zhang, X.-Y.; Zheng, Q. Q.; Chen-Xi, Q.; Zuo, J.-L. Some New Progress on Molecular Wires. *Chin. J Inorg Chem* **2011**, *27*, 1451–1464.
- (34) Ogawa, S.; Chattopadhyay, S.; Tanaka, Y.; Ohto, T.; Tada, T.; Tada, H.; Fujii, S.; Nishino, T.; Akita, M. Control of Dominant Conduction Orbitals by Peripheral Substituents in Paddle-Wheel Diruthenium Alkynyl Molecular Junctions. *Chem Sci* **2021**, *12*, 10871–10877.

- (35) Raghavan, A.; Mash, B. L.; Ren, T. Forging Ru-C Sp² Bonds in Paddlewheel Complexes Using the Lithium-Halogen Exchange Reaction. *Inorg. Chem.* **2019**, *58* (4), 2618–2626. <https://doi.org/10.1021/acs.inorgchem.8b03216>.
- (36) Raghavan, A.; Ren, T. Bisaryl Diruthenium(III) Paddlewheel Complexes: Synthesis and Characterization. *Organometallics* **2019**, *38* (19), 3888–3896. <https://doi.org/10.1021/acs.organomet.9b00555>.
- (37) Raghavan, A.; Yuan, F.; Ren, T. Drastic Tuning of the Electronic Structures of Ru₂-Aryl Complexes by Iso-Electronic Axial Ligands. *Inorg Chem* **2020**, *59* (13), 8663–8666.
- (38) Nichols, J. M.; Wolf, J.; Zavalij, P.; Varughese, B.; Doyle, M. P. Bis(Phenyl)Dirhodium(III) Caprolactamate: A Dinuclear Paddlewheel Complex with No Metal-Metal Bond. *J Am Chem Soc* **2007**, *129* (12), 3504–3505.
- (39) Xie, J.-H.; Zhou, L.; Lubek, C.; Doyle, M. P. Hetero-Bis(Sigma-Aryl)Dirhodium(III) Caprolactamates. Electronic Communication between Aryl Groups through Dirhodium(III). *Dalton Trans* **2009**, No. 15, 2871–2877.
- (40) Angelone, D.; Draksharapu, A.; Browne, W. R.; Choudhuri, M. M. R.; Crutchley, R. J.; Xu, X.; Xu, X.; Doyle, M. P. Dinuclear Compounds without a Metal-Metal Bond. Dirhodium(III,III) Carboxamidates. *Inorg Chim Acta* **2015**, *424*, 235–240.
- (41) Wolf, J.; Poli, R.; Xie, J.-H.; Nichols, J.; Xi, B.; Zavalij, P.; Doyle, M. P. Removal of Metal-Metal Bonding in a Dimetallic Paddlewheel Complex: Molecular and Electronic Structure of Bis(Phenyl) Dirhodium(III) Carboxamidate Compounds. *Organometallics* **2008**, *27*, 5836–5845.
- (42) Bear, J. L.; Han, B.; Li, Y.; Ngubane, S.; Caemelbecke, E. V.; Kadish, K. M. Synthesis , Spectroscopic Properties and Electrochemistry of Rh₂(Ap)₄(R) Where R = CH₃ or C₆H₅ and Ap = 2-Anilinopyridinate Anion. *Polyhedron* **2009**, *28* (8), 1551–1555. <https://doi.org/10.1016/j.poly.2009.03.012>.
- (43) Xi, B.; Xu, G. L.; Ying, J. W.; Han, H. L.; Cordova, A.; Ren, T. Further Molecular Engineering of Diruthenium-(2-Anilinopyridinate) Alkynyl Compounds through Ligand Design. *J. Organomet. Chem.* **2008**, *693* (8–9), 1656–1663. <https://doi.org/10.1016/J.JORGANCHEM.2007.11.050>.
- (44) Xu, G. L.; Cordova, A.; Ren, T. Molecular Engineering of Redox Rich Diruthenium Compounds: Further Investigation of Ru₂(Yap)₄X Type Compounds. *J Clust Sci* **2004**, *15*, 413–424.
- (45) Evans, D. F. The Determination of the Paramagnetic Susceptibility of Substances in Solution by Nuclear Magnetic Resonance. *J Chem Soc* **1959**, 2003–2005.
- (46) Corcos, A. R.; Roy, M. D.; Killian, M. M.; Dillon, S.; Brunold, T. C.; Berry, J. F. Electronic Structure of Anilinopyridinate-Supported (Ru²⁺)₅ Paddlewheel Compounds. *Inorg. Chem.* **2017**, *56* (23), 14662–14670. <https://doi.org/10.1021/acs.inorgchem.7b02557>.

- (47) Hansch, C.; Leo, A.; Taft, R. W. A Survey of Hammett Substituent Constants and Resonance and Field Parameters. *Chem Rev* **1991**, *91* (2), 165–195.
- (48) Dapperheld, S.; Steckhan, E.; Brinkhaus, K. H. G.; Esch, T. Organic Electron Transfer Systems, II. Substituted Triarylamine Cation-Radical Redox Systems - Synthesis, Electrochemical and Spectroscopic Properties, Hammet Behavior, and Suitability as Redox Catalysts. *Chem Ber* **1991**, *124* (11), 2557–2567.
- (49) Ren, T. Substituent Effects in Dinuclear Paddlewheel Compounds: Electrochemical and Spectroscopic Investigations. *Coord Chem Rev* **1998**, *175*, 43–58.
- (50) Bruker. Apex3 V2016.9-0, Saint V8.34A, Saint V8.37A; Bruker AXS Inc.: Madison, WI, 2016.
- (51) Krause, L.; Herbst-Irmer, R.; Sheldrick, G. M.; Stalke, D. Comparison of Silver and Molybdenum Microfocus X-Ray Sources for Single-Crystal Determination. *J Appl Cryst* **2015**, *48*, 3–10.
- (52) SHELXTL, Version 6.14; Bruker Advanced X-Ray Solutions, Bruker AXS Inc.: Madison, WI, 2000-2003.
- (53) Sheldrick, G. M. A Short History of SHELX. *Acta Cryst* **2008**, *64*, 112–122.
- (54) Sheldrick, G. M. SHELXT - Integrated Space-Group and Crystal-Structure Determination. *Acta Cryst A* **2015**, *A71*, 3–8.
- (55) Sheldrick, G. M. SHELXL 2018; University of Göttingen, Germany, 2018. **2018**.
- (56) Sheldrick, G. M. Crystal Structure Refinement with SHELXL. *Acta Cryst C* **2015**, *71*, 3–8.
- (57) Hubschle, C. B.; Sheldrick, G. M.; Dittrich, B. ShelXle: A Qt Graphical Interface for SHELXL. *J Appl Cryst* **2011**, *44* (6), 1281–1284.
- (58) Whittell, G. R.; Hager, M. D.; Schubert, U. S.; Manners, I. Functional Soft Materials from Metallopolymers and Metallosupramolecular Polymers. *Nat. Mater* **2011**, *10* (3), 176–188.
- (59) Winter, A.; Schubert, U. S. Synthesis and Characterization of Metallo-Supramolecular Polymers. *Chem Soc Rev* **2016**, *45*, 5311–5357.
- (60) Yam, V. W.-W.; Chan, A. K.-W.; Hong, E. Y.-H. Charge-Transfer Processes in Metal Complexes Enable Luminescence and Memory Functions. *Nat. Rev Chem* **2020**, *4* (10), 528–541.
- (61) Wong, W.-Y.; Ho, C.-L. Organometallic Photovoltaics: A New and Versatile Approach for Harvesting Solar Energy Using Conjugated Polymetallaynes. *Acc Chem Res* **2010**, *43*, 1246–1256.

- (62) Ho, C.-L.; Yu, Z.-Q.; Wong, W.-Y. Multifunctional Polymetallaynes: Properties, Functions and Applications. *Chem. Soc. Rev.* **2016**, *45* (19), 5264–5295. <https://doi.org/10.1039/C6CS00226A>.
- (63) Launay, J.-P. Long-Distance Intervalence Electron Transfer. *Chem Soc Rev* **2001**, *30* (6), 386–397.
- (64) Haque, A.; Al-Balushi, R. A.; Al-Busaidi, I. J.; Khan, M. S.; Raithby, P. R. Rise of Conjugated Poly-Ynes and Poly(Metalla-Ynes): From Design Through Synthesis to Structure-Property Relationships and Applications. *Chem Rev* **2018**, *118*, 8474–8597.
- (65) Bryce, M. R. A Review of Functional Linear Carbon Chains (Oligoynes, Polyyynes, Cumulenes) and Their Applications as Molecular Wires in Molecular Electronics and Optoelectronics. *J Mater Chem C* **2021**, *9*, 10524–10546.
- (66) Schull, T. L.; Kushmerick, J. G.; Patterson, C. H.; George, C.; Moore, M. H.; Pollack, S. K.; Shashidhar, R. Ligand Effects on Charge Transport in Platinum(II) Acetylides. *J Am Chem Soc* **2003**, *125* (11), 3202–3203.
- (67) Tanaka, Y.; Kato, Y.; Tada, T.; Fujii, S.; Kiguchi, M.; Akita, M. “Doping” of Polyyne with an Organometallic Fragment Leads to Highly Conductive Metallapolyne Molecular Wire. *J Am Chem Soc* **2018**, *140* (32), 10080–10084.
- (68) Meng, F.; Hervault, Y.-M.; Shao, Q.; Hu, B.; Norel, L.; Rigaut, S.; Chen, X. Orthogonally Modulated Molecular Transport Junctions for Resettable Electronic Logic Gates. *Nat. Commun.* **2014**, *5* (1), 3023. <https://doi.org/10.1038/ncomms4023>.
- (69) Alberico, D.; Scott, M. E.; Lautens, M. Aryl-Aryl Bond Formation by Transition-Metal-Catalyzed Direct Arylation. *Chem Rev* **2007**, *107* (1), 174–238.
- (70) Su, S. D.; Zhu, X. Q.; Wen, Y. H.; Zhang, L. T.; Yang, Y. Y.; Lin, C. S.; Wu, X. T.; Sheng, T. L. A Diruthenium-Based Mixed Spin Complex Ru-2(5+)(S=1/2)-CN-Ru-2(5+)(S=3/2). *Angew Chem Int Ed* **2019**, *58* (43), 15344–15348.
- (71) Trenerry, M. J.; Wallen, C. M.; Brown, T. R.; Park, S. V.; Berry, J. F. Spontaneous N₂ Formation by a Diruthenium Complex Enables Electrocatalytic and Aerobic Oxidation of Ammonia. *Nat. Chem* **2021**, *13* (12), 1221–1227.
- (72) Berry, J. F.; Lu, C. C. Metal-Metal Bonds: From Fundamentals to Applications. *Inorg Chem* **2017**, *56* (14), 7577–7581.
- (73) Demadis, K. D.; Hartshorn, C. M.; Meyer, T. J. The Localized-to-Delocalized Transition in Mixed-Valence Chemistry. *Chem Rev* **2001**, *101* (4), 2655–2686.
- (74) Brunschwig, B. S.; Creutz, C.; Sutin, N. Optical Transitions of Symmetrical Mixed-Valence Systems in the Class II-III Transition Regime. *Chem Soc Rev* **2002**, *31*, 168–184.

- (75) Zou, G.; Alvarez, J. C.; Ren, T. Ru- σ -Alkynyl Compounds of Tetraanilinopyridinato-Diruthenium(II,III) Core: Synthesis and Structural Characterization. *J. Organomet. Chem.* **2000**, 596 (1–2), 152–158. [https://doi.org/10.1016/S0022-328X\(99\)00642-7](https://doi.org/10.1016/S0022-328X(99)00642-7).
- (76) Chiarella, G. M.; Cotton, F. A.; Murillo, C. A.; Ventura, K.; Villagran, D.; Want, X. Manipulating Magnetism: Ru²⁺ Paddlewheels Devoid of Axial Ligands. *J Am Chem Soc* **2014**, 136 (27), 9580–9589.
- (77) Sutter, J.-P.; Grove, D. M.; Beley, M.; Collin, J.-P.; Veldman, N.; Spek, A. L.; Sauvage, J.-P.; van Koten, G. Copper(II)-Mediated Oxidative Coupling of Bis(Dimethylaminomethyl)Arylruthenium Complexes to Give [(Terpy)Ru(III)(Pincer-Pincer)-Ru(III)(Terpy)](CuCl₂)₄. *Angew Chem Int Ed* **1994**, 33 (12), 1282–1285.
- (78) Patoux, C.; Launay, J.-P.; Beley, M.; Chodorowski-Kimmes, S.; Collin, J.-P.; James, S.; Sauvage, J.-P. Long-Range Electronic Coupling in Bis(Cyclometalated) Ruthenium Complexes. *J Am Chem Soc* **1998**, 120, 3717–3725.
- (79) Pangborn, A. B.; Giardello, M. A.; Grubbs, R. H.; Rosen, R. K. Safe and Convenient Procedure for Solvent Purification. *Organometallics* **1996**, 15, 1518–1520.
- (80) Krekicik, J.; Danek, H.; Hartl, F. Simple Construction of an Infrared Optically Transparent Thin-Layer Electrochemical Cell: Applications to the Redox Reactions of Ferrocene, Mn₂(CO)₁₀ and Mn(CO)₃(3,5-Di-*t*-Butyl-Catecholate). *J Electroanal Chem* **1991**, 317, 179–187.
- (81) Bruker (2019). Apex3 V2019.1-0, Saint V8.40A, Bruker AXS Inc.: Madison (WI), USA.
- (82) Krause, L.; Sheldrick, G. M.; Stalke, D. *J Appl Cryst* **2015**, 48, 3–10.
- (83) Sheldrick, G. M. SHELXL 2016; University of Göttingen, Germany, 2016. **2016**.
- (84) Frisch, M. J.; Trucks, G. W.; Schlegel, H. B.; Scuseria, G. E.; Robb, M. A.; Cheeseman, J. R.; Scalmani, G.; Barone, V.; Petersson, G. A.; Nakatsuji, H.; Li, X.; Caricato, M.; Marenich, A. V.; Bloino, J.; Janesko, B. G.; Gomperts, R.; Mennucci, B.; Hratchian, H. P.; Ortiz, J. V.; Izmaylov, A. F.; Sonnenberg, J. L.; Williams-Young, D.; Ding, F.; Lipparini, F.; Egidi, F.; Goings, J.; Peng, B.; Petrone, A.; Henderson, T.; Ranasinghe, D.; Zakrzewski, V. G.; Gao, J.; Rega, N.; Zheng, G.; Liang, W.; Hada, M.; Ehara, M.; Toyota, K.; Fukuda, R.; Hasegawa, J.; Ishida, M.; Nakajima, T.; Honda, Y.; Kitao, O.; Nakai, H.; Vreven, T.; Throssell, K.; Montgomery, J. J. A.; Peralta, J. E.; Ogliaro, F.; Bearpark, M. J.; Heyd, J. J.; Brothers, E. N.; Kudin, K. N.; Staroverov, V. N.; Keith, T. A.; Kobayashi, R.; Normand, J.; Raghavachari, K.; Rendell, A. P.; Burant, J. C.; Iyengar, S. S.; Tomasi, J.; Cossi, M.; Millam, J. M.; Klene, M.; Adamo, C.; Cammi, R.; Ochterski, J. W.; Martin, R. L.; Morokuma, K.; Farkas, O.; Foresman, J. B.; Fox, D. J. Gaussian 16, Rev. A.03, 2016.
- (85) Grimme, S. Semiempirical GGA-Type Density Functional Constructed with a Long-Range Dispersion Correction. *J Comp Chem* **2006**, 27, 1787–1799.

- (86) Grimme, S.; Ehrlick, S.; Goerigk, L. Effect of the Damping Function in Dispersion Corrected Density Functional Theory. *J Comp Chem* **2011**, *32*, 1456–1465.
- (87) Becke, A. D. Density-Functional Thermochemistry. III. The Role of Exact Exchange. *J Chem Phys* **1993**, *98*, 5648–5652.
- (88) Lee, C.; Yang, W.; Parr, R. G. Development of the Colle-Salvetti Correlation-Energy Formula into a Functional of the Electron Density. *Phys Rev B* **1988**, *37*, 785–789.
- (89) Vosko, S. H.; Wilk, L.; Nusair, M. Accurate Spin-Dependent Electron Liquid Correlation Energies for Local Spin Density Calculations: A Critical Analysis. *Can J Phys* **1980**, *58*, 1200–1211.
- (90) Stephens, P. J.; Devlin, F. J.; Chabalowski, C. F.; Frisch, M. J. Ab Initio Calculation of Vibrational Absorption and Circular Dichroism Spectra Using Density Functional Force Fields. *J Phys Chem* **1994**, *98*, 11623–11627.
- (91) Weigend, F.; Ahlrichs, R. Balanced Basis Sets of Split Valence, Triple Zeta Valence and Quadruple Zeta Valence Quality for H to Rn: Design and Assessment of Accuracy. *Phys Chem Chem Phys* **2005**, *7*, 3297–3305.
- (92) Weigend, F. Accurate Coulomb-Fitting Basis Sets for H to Rn. *Phys Chem Chem Phys* **2006**, *8*, 1057–1065.
- (93) Casida, M. E.; Jamorski, C.; Casida, K. C.; Salahub, D. R. Molecular Excitation Energies to High-Lying Bound States from Time-Dependent Density-Functional Response Theory: Characterization and Correction of the Time-Dependent Local Density Approximation Ionization Threshold. *J Chem Phys* **1998**, *108*, 4439–4449.
- (94) Furche, F.; Ahlrichs, R. Adiabatic Time-Dependent Density Functional Methods for Excited State Properties. *J Chem Phys* **2002**, *117*, 7433–7447.
- (95) Liu, J.; Liang, W. Analytical Approach for the Excited-State Hessian in Time-Dependent Density Functional Theory: Formalism, Implementation and Performance. *J Chem Phys* **2001**, *115*, 184111.
- (96) Scalmani, G.; Frisch, M. J.; Mennucci, B.; Tomasi, J.; Cammi, R.; Barone, V. Geometries and Properties of Excited States in the Gas Phase and in Solution: Theory and Application of a Time-Dependent Density Functional Theory Polarizable Continuum Model. *J Chem Phys* **2006**, *124* (094107), 1–15.
- (97) Stratmann, R. E.; Scuseria, G. E.; Frisch, M. J. An Efficient Implementation of Time-Dependent Density-Functional Theory for the Calculation of Excitation Energies of Large Molecules. *J Chem Phys* **1998**, *109*, 8218–8224.
- (98) Caricato, M.; Ingrosso, F.; Mennucci, B.; Tomasi, J. Time-Dependent Polarizable Continuum Model: Theory and Application. *J Chem Phys* **2005**, *122* (154501), 1–10.

- (99) Yanai, T.; Tew, D.; Handy, N. A New Hybrid Exchange-Correlation Functional Using the Coulomb-Attenuating Method (CAM-B3LYP). *Chem Phys Lett* **2004**, *393*, 51–57.
- (100) Zhao, Y.; Truhlar, D. G. The M06 Suite of Density Functionals for Main Group Thermochemistry, Thermochemical Kinetics, Noncovalent Interactions, Excited States, and Transition Elements: Two New Functionals and Systematic Testing of Four M06-Class Functionals and 12 Other Functionals. *Theor Chem Acc* **2008**, *120*, 215–241.
- (101) Zhao, Y.; Truhlar, D. G. A New Local Density Functional for Main-Group Thermochemistry, Transition Metal Bonding, Thermochemical Kinetics, and Noncovalent Interactions. *J Chem Phys* **2006**, *125* (194101), 1–18.
- (102) Martin, R. L. Natural Transition Orbitals. *J Chem Phys* **2003**, *118*, 4775–4777.
- (103) *Multiple Bonds between Metal Atoms*, Third.; Cotton, F. A., Murillo, C. A., Walton, R. A., Eds.; Springer Science and Business Media, Inc.: New York, 2005.
- (104) Sayama, Y.; Handa, M.; Mikuriya, M.; Hiromitsu, I.; Kasuga, K. Ferromagnetic Chain Complex of Ruthenium(II,III) Pivalate with Pyridyl Nitronyl Nitroxide. *Chem Lett* **1998**, No. 8, 777–778.
- (105) Liao, Y.; Shum, W. W.; Miller, J. S. Synthesis and Magnetic Properties of 3-D [RuII/III₂(O₂CMe)₄]₃[MIII(CN)₆] (M = Cr, Fe, Co). *J Am Chem Soc* **2002**, *124* (32), 9336–9337.
- (106) Miyasaka, H.; Clérac, R.; Campos-Fernández, C. S.; Dunbar, K. R. Metal-Metal Bonded Diruthenium(II, III) Assemblies with the Polycyano Anionic Linkers N(CN)₂⁻, C(CN)₃⁻, and 1,4-Dicyanamido-2,5-Dimethylbenzene (DM-Dicyd₂⁻): Syntheses, Structures, and Magnetic Properties. *Inorg Chem* **2001**, *40* (7), 1663–1671.
- (107) Barral, M. C.; Gallo, T.; Herrero, S.; Jiménez-Aparicio, R.; Torres, M. R.; Urbanos, F. A. Equatorially Connected Diruthenium(II,III) Units toward Paramagnetic Supramolecular Structures with Singular Magnetic Properties. *Inorg Chem* **2006**, *45*, 3639–3647.
- (108) Barral, M. C.; Herrero, S.; Jiménez-Aparicio, R.; Torres, M. R.; Urbanos, F. A. A Spin-Admixed Ruthenium Complex. *Angew Chem Int Ed* **2005**, *44*, 305–307.
- (109) Corcos, A. R.; Pap, J. S.; Yang, T.; Berry, J. F. A Synthetic Oxygen Atom Transfer Photocycle from a Diruthenium Oxyanion Complex. *J Am Chem Soc* **2016**, *138*, 10032–10040.
- (110) Ying, J.-W.; Liu, I. P. C.; Xi, B.; Song, Y.; Campana, C.; Zuo, J.-L.; Ren, T. Linear Trimer of Diruthenium Linked by Butadiyn-Diyl Units; A Unique Electronic Wire. *Angew. Chem. - Int. Ed.* **2010**, *49*, 954–957.
- (111) Miller-Clark, L. A.; Raghavan, A.; Clendening, R. A.; Ren, T. Phenylene as an Efficient Mediator for Intermetallic Electronic Coupling. *Chem Commun* **2022**, *58*, 5478–5481.

- (112) Xu, G.-L.; Wang, C.-Y.; Ni, Y.-H.; Goodson, T. G.; Ren, T. Iterative Synthesis of Oligoynes Capped by A Ru₂(Ap)₄-Terminus and Their Voltammetric and Optoelectronic Properties. *Organometallics* **2005**, *24*, 3247–3254.
- (113) Pookpanratana, S.; Zhu, H.; Bittle, E. G.; Natoli, S. N.; Ren, T.; Richter, C. A.; Li, Q.; Hacker, C. A. Non-Volatile Memory Devices with Redox-Active Diruthenium Molecular Compound. *J. Phys. Condens. Matter* **2016**, *28* (9). <https://doi.org/10.1088/0953-8984/28/9/094009>.
- (114) Su, S.-D.; Zhu, X.-Q.; Wen, Y.-H.; Wu, X.-T.; Sheng, T.-L. Influence of Substitution Effect on MMCT in Mixed-Valence Cyanido-Bridged Fe(II)-CN-Ru₂(III,III)-NC-Fe(II) System. *Eur J Inorg Chem* **2021**, *2021* (34), 3474–3480.
- (115) Su, S.-D.; Wen, Y.-H.; Wu, X.-T.; Sheng, T.-L. Multiple MMCT Properties of the Diruthenium-Based Cyanido-Bridged Complex Ru^{VI}2-NC-Ru^{II}-CN-Ru^{VI}2. *Dalton Trans* **2022**, *51*, 10047–10054.
- (116) Osterloh, W. R.; Galindo, G.; Yates, M. J.; Caemelbecke, E. V.; Kadish, K. M. Synthesis, Structural and Physicochemical Properties of Water-Soluble Mixed-Ligand Diruthenium Complexes Containing Anilinopyridinate Bridging Ligands. *Inorg Chem* **2020**, *59*, 584–594.
- (117) Li, Y.; Han, B.; Kadish, K. M.; Bear, J. L. A Novel Diamagnetic Diruthenium(III) Complex Bridged by Four Unsymmetrical Carboxylate Type Ligands. Synthesis, Molecular Structure, Electrochemistry, and Spectroelectrochemistry of Ru₂(Pfap)₄(CCC₆H₅)₂, Where Pfap Is 2,3,4,5,6-Pentafluoro-2-Anilinopyridinate. *Inorg Chem* **1993**, *32*, 4175.
- (118) Xu, G.; Campana, C.; Ren, T. Tetrakis(N,N'-Dimethylbenzamidinato)Diruthenium(III) Compounds Bearing Axial Chloro and Alkynyl Ligands: A New Family of Redox Rich Diruthenium Compounds. *Inorg. Chem.* **2002**, *41* (13), 3521–3527. <https://doi.org/10.1021/IC0200794>.
- (119) Xu, G.; Ren, T. Synthesis and Characterization of Trans-Phenyethynylalkynyl Adducts on a Tetraanilinopyridinato-Diruthenium(III) Core. *J Organomet Chem* **2002**, *655*, 239–243.
- (120) Lin, C.; Ren, T.; Valente, E. J.; Zubkowski, J. D. Synthesis, Spectroscopy and Electrochemistry of Tetrakis(μ-N,N'-Diarylformamidinato)Di(Phenylethynyl)Diruthenium(III). *J. Chem. Soc. Dalton Trans.* **1998**, No. 4, 571–576. <https://doi.org/10.1039/A706190K>.
- (121) Miller-Clark, L. A.; Christ, P. E.; Ren, T. Diruthenium Aryl Compounds-Tuning of Electrochemical Responses and Solubility. *Dalton Trans.* **2022**, *51* (2), 580–586. <https://doi.org/10.1039/d1dt03957a>.
- (122) Kataoka, Y.; Mikami, S.; Sakiyama, H.; Mitsumi, M.; Kawamoto, T.; Handa, M. A Neutral Paddlewheel-Type Diruthenium(III) Complex with Benzamidinato Ligands: Synthesis, Crystal Structure, Magnetism, and Electrochemical and Absorption Properties. *Polyhedron* **2017**, *136*, 87–92.

- (123) Kataoka, Y.; Imasaki, N.; Arakawa, K.; Yano, N.; Sakiyama, H.; Sugimori, T.; Mitsumi, M.; Handa, M. Paddlewheel-Type Diruthenium(III, III) Tetrakis(2-Aminopyridinate) Complexes with NIR Absorption Features: Combined Experimental and Theoretical Study. *Dalton Trans* **2019**, 48 (33), 12421–12429.
- (124) Kataoka, Y.; Imasaki, N.; Yano, N.; Mitsumi, M.; Handa, M. Redox-Triggered Reversible Modulation of Intense near-Infrared and Visible Absorption Using a Paddlewheel-Type Diruthenium(III) Complex. *Dalton Trans* **2021**, 50 (27), 9547–9553.
- (125) Doyle, M. P.; Bagheri, V.; Wandless, T. J.; Harn, N. K.; Brinker, D. A.; Eagle, C. T.; Loh, K. L. Exceptionally High Trans (Anti) Stereoselectivity in Catalytic Cyclopropanation Reactions. *J Am Chem Soc* **1990**, 112 (5), 1906–1912.
- (126) Doyle, M. P.; Winchester, W. R.; Hoorn, J. A. A.; Lynch, V.; Simonsen, S. H.; Ghosh, R. Dirhodium(II) Tetrakis(Carboxamides) with Chiral Ligands. Structure and Selectivity in Catalytic Metal-Carbene Transformations. *J Am Chem Soc* **1993**, 115 (22), 9968–9978.
- (127) Kadish, K. M.; Wang, L.-L.; Thuriere, A.; Van Caemelbecke, E.; Bear, J. L. Factors Affecting the Electrochemical and Spectroelectrochemical Properties of Diruthenium(III,II) Complexes Containing Four Identical Unsymmetrical Bridging Ligands. *Inorg Chem* **2003**, 42, 834–843.
- (128) Bear, J. L.; Li, Y.; Han, B.; Caemelbecke, E. V.; Kadish, K. M. Isomer Effect on the Structure and Chemical Reactivity of Diruthenium Complexes. Synthesis and Characterization of the (4,0), (3,1), and (2,2) Trans Isomers of Ru₂(F5ap)₄Cl and Ru₂(F5ap)₄(CCPh)₂ Where F5ap Is the 2-(2,3,4,5,6-Pentafluoroanilino)Pyridinate Anion. *Inorg Chem* **1997**, 36 (24), 5449–5456.
- (129) Nguyen, M.; Phan, T.; Caemelbecke, E. V.; Kajonkijya, W.; Bear, J. L.; Kadish, K. M. Interconversion between (3,1) and (4,0) Isomers of Ru₂(L)₄X Complexes Where L Is 2-Anilinopyridinate or 2-(2,4,6-Trifluoroanilino)Pyridinate Anion and X = Cl⁻ or C≡CC₅H₄N. *Inorg Chem* **2008**, 47, 7775–7783.
- (130) Bear, J. L.; Chen, W.-Z.; Han, B.; Huang, S.; Wang, L.-L.; Thuriere, A.; Caemelbecke, E. V.; Kadish, K. M.; Ren, T. Cyanide Adducts on the Diruthenium Core of [Ru₂(L)₄]⁺ (L = Ap, CH₃ap, Fap or F3ap) as Potential Supramolecular Synthons. Electronic Properties and Binding Symmetry of the Bridging Ligand. *Inorg Chem* **2003**, 42, 6230–6240.
- (131) Hurst, S. K.; Xu, G. L.; Ren, T. Bis-Adducts of Substituted Phenylethynyl on a Ru₂(DMBA)₄ Core: Effect of Donor/Acceptor Modifications. *Organometallics* **2003**, 22 (20), 4118–4123. <https://doi.org/10.1021/om030401y>.
- (132) Ren, T. Dissymmetrical Trans-Ethynyl-Butadiynyl Adducts on a Diruthenium Core: Synthesis, Characterization, and Selective Deprotection. *Organometallics* **2002**, 21 (4), 732–738. <https://doi.org/10.1021/om0109004>.
- (133) Manna, J.; John, K. D.; Hopkins, M. D. The Bonding of Metal-Alkynyl Complexes. *Adv Organomet Chem* **1995**, 38, 79–154.

- (134) Parr, R. G.; Yang, W. *Density Functional Theory of Atoms and Molecules*; Oxford University Press: New York, 1989.
- (135) Long, N. J.; Williams, C. K. Metal Alkynyl Complexes: Synthesis and Materials. *Angew Chem Int Ed* **2003**, *42* (23), 2586–2617.
- (136) Bruce, M. I. Organometallic Chemistry of Vinylidene and Related Unsaturated Carbenes. *Chem Rev* **1991**, *91* (2), 197–257.
- (137) Bruce, M. I. Transition Metal Complexes Containing Allenylidene, Cumulenylidene, and Related Ligands. *Chem Rev* **1998**, *98* (8), 2797–2858.
- (138) Nast, R. Coordination Chemistry of Metal Alkynyl Compounds. *Coord Chem Rev* **1982**, *47*, 89–124.
- (139) Hagihara, N.; Sonogashira, K.; Takahashi, S. Linear Polymers Containing Transition Metals in the Main Chain. *Adv Polym Sci* **1981**, *40*, 149–179.
- (140) Sonogashira, K.; Fujikura, Y.; Yatake, T.; Toyoshima, N.; Takahashi, S.; Hagihara, N. Syntheses and Properties of Cis-Dialkynyl and Trans-Dialkynyl Complexes of Platinum(II). *J Organomet Chem* **1978**, *145* (1), 101–108.
- (141) Morrall, J. P.; Dalton, G. T.; Humphrey, M. G.; Samoc, M. Organotransition Metal Complexes for Nonlinear Optics. *Adv Organomet Chem* **2008**, *55*, 61–136.
- (142) Haque, A.; Xu, L. L.; Al-Balushi, R. A.; Al-Suti, M. K.; Ilmi, R.; Guo, Z. L.; Khan, M. S.; Wong, W. Y.; Raithby, P. R. Cyclometallated Tridentate Platinum(II) Arylacetylide Complexes: Old Wine in New Bottles. *Chem Soc Rev* **2019**, *48* (23), 5547–5563.
- (143) Low, P. J. Metal Complexes in Molecular Electronics: Progress and Possibilities. *Dalton Trans* **2005**, 2821–2824.
- (144) Gendron, F.; Groizard, T.; Le Guennic, B.; Halet, J. F. Electronic Properties of Poly-Yne Carbon Chains and Derivatives with Transition Metal End-Groups. *Eur J Inorg Chem* **2020**, *2020*, 667–681.
- (145) Xiang, D.; Wang, X.; Jia, C.; Lee, T.; Guo, X. Molecular-Scale Electronics: From Concept to Function. *Chem Rev* **2016**, *116* (7), 4318–4440.
- (146) Szafert, S.; Gladysz, J. A. Update 1 of: Carbon in One Dimension: Structural Analysis of the Higher Conjugated Polyynes. *Chem Rev* **2006**, *106*, PR1–PR33.
- (147) Szafert, S.; Gladysz, J. A. Carbon in One Dimension: Structural Analysis of the Higher Conjugated Polyynes. *Chem Rev* **2003**, *103*, 4175–4206.
- (148) Shek, H.-L.; Yeung, C.-F.; Chung, L.-H.; Wong, C.-Y. A Focused Review on the Unconventional Alkyne Activations by Ruthenium(II) and Osmium(II) Complexes Supported by 1,2-Bis(Diphenylphosphino)Methane (Dppm). *Polyhedron* **2021**, *197*, 115023.

- (149) Sonogashira, K.; Ohga, K.; Takahashi, S.; Hagihara, N. Studies of Poly-Yne Polymers Containing Transition Metals in the Main Chain; VI. *J Organomet Chem* **1980**, *188*, 237–243.
- (150) Cetinkaya, B.; Lappert, M. F.; McMeeking, J.; Palmer, D. E. Unsaturated π -Hydrocarbyl Transition Metal Complexes. Part 1. Trimethyltin Acetylides as Sources of Late Transition-Metal Derivatives: Metathesis, Oxidative Addition, and Oxidative Cleavage. *J Chem Soc Dalton Trans* **1973**, 1202–1208.
- (151) Younus, M.; Long, N. J.; Raithby, P. R.; Lewis, J.; Page, N. A.; White, A. J. P.; Williams, D. J.; Colbert, M. C. B.; Hodge, A. J.; Khan, M. S.; Parker, D. G. Synthesis and Characterisation of Mono-Acetylide and Unsymmetrical Bis-Acetylide Complexes of Ruthenium and Osmium: X-Ray Structure Determinations on [(Dppe)(2)Ru(Cl)(C \equiv C-C₆H₄-p-NO₂)], [(Dppe)(2)Ru(Cl)(C \equiv C-C₆H₃-o-CH₃-p-NO₂)] and [(Dppm)(2)Os(C \equiv C-C₆H₄-p-CH₃)(C \equiv C-C₆H₄-p-NO₂)]. *J Organomet Chem* **1999**, *578* (1–2), 198–209.
- (152) Faulkner, C. W.; Ingham, S. L.; Khan, M. S.; Lewis, J.; Long, N. J.; Raithby, P. R. Ruthenium(II) π -Acetylide Complexes Monomers, Dimers, and Polymers. *J Organomet Chem* **1994**, *482* (1–2), 139–145.
- (153) Touchard, D.; Haquette, P.; Guesmi, S.; Pichon, L. L.; Daridor, A.; Toupet, L.; Dixneuf, P. H. Vinylidene-, Alkynyl-, and Trans-Bis(Alkynyl)Ruthenium Complexes. Crystal Structure of Trans-[Ru(NH₃)(C \equiv CPh)(Ph₂PCH₂CH₂PPh₂)₂]PF₆. *Organometallics* **1997**, *16* (16), 3640–3648. <https://doi.org/10.1021/om970362o>.
- (154) Atherton, Z.; Faulkner, C. W.; Ingham, S. L.; Kakkar, A. K.; Khan, M. S.; Lewis, J.; Long, N. J.; Raithby, P. R. Rigid-Rod Sigma-Acetylide Complexes of Iron, Ruthenium and Osmium. *J Organomet Chem* **1993**, *462* (1–2), 265–270.
- (155) Jones, N. D.; Wolf, M. O.; Giaquinta, D. M. Synthesis of a Ferrocenyl-Capped Ruthenium(II) Bis(Acetylide) Complex: A Model for Organometallic Molecular Wires. *Organometallics* **1997**, *16*, 1352–1354.
- (156) Zhu, Y.; Clot, O.; Wolf, M. O.; Yap, G. P. A. Effect of Ancillary Ligands on Ru(II) on Electronic Delocalization in Ruthenium(II) Bisferrocenylacetylide Complexes. *J Am Chem Soc* **1998**, *120*, 1812–1821.
- (157) Zhu, Y.; Millet, D. B.; Wolf, M. O.; Rettig, S. J. Models for Conjugated Metal Acetylide Polymers: Ruthenium Oligothiénylacetylide Complexes. *Organometallics* **1999**, *18* (10), 1930–1938.
- (158) Wright, M. E. Synthesis of Conjugated Polymers Using an (N₆-Arene)Cr(CO)₃ Monomer. *Macromolecules* **1989**, *22*, 3256–3259.
- (159) Brown, A. W.; Verschoyle, R. D.; Street, B. W.; Aidridge, W. N.; Grindley, H. The Neurotoxicity of Trimethyltin Chloride in Hamsters, Gerbils and Marmosets. *J Appl Toxicol* **1984**, *4* (1), 12–21.

- (160) Davies, S. J.; Johnson, B. F. G.; Khan, M. S.; Lewis, J. Synthesis of Monomeric and Oligomeric Bis(Acetylide) Complexes of Platinum and Rhodium. *J Chem Soc Chem Commun* **1991**, 187–188.
- (161) Viola, E.; Lo Sterzo, C.; Crescenzi, R.; Frachey, G. Formation of Metal Sigma-Acetylides of Mo, W, and Ru via Palladium-Catalyzed Metal-Carbon Coupling. *J Organomet Chem* **1995**, 493, 55–59.
- (162) Cotton, F. A.; Stiriba, S. E.; Yokochi, A. Selectivity in Alkynylation: The Reaction between Ru-2(LL)(4)Cl and Me₃SnC≡CR (LL=2-Anilinopyridine, 2-Chloro- and 2-Bromo-Oxypyridine). *J Organomet Chem* **2000**, 595 (2), 300–302. [https://doi.org/10.1016/S0022-328X\(99\)00649-X](https://doi.org/10.1016/S0022-328X(99)00649-X).
- (163) Fox, M. A.; Harris, J. E.; Heider, S.; Perez-Gregorio, V.; Zakrzewska, M. E.; Farmer, J. D.; Yufit, D. S.; Howard, J. A. K.; Low, P. J. A Simple Synthesis of Trans-RuCl(C≡CR)(Dppe)(2) Complexes and Representative Molecular Structures. *J Organomet Chem* **2009**, 694 (15), 2350–2358.
- (164) Touchard, D.; Haquette, P.; Pirio, N.; Toupet, L.; Dixneuf, P. H. New Ruthenium Vinylidene Complexes as Intermediates for the Access to .Sigma.-Acetylide and Unsymmetrical Trans-Diynyl, Alkynyl Metal Complexes. Crystal Structures of [(Ph₂PCH₂PPh₂)₂(Cl)Ru=C=CH₂]PF₆ and [(Ph₂PCH₂PPh₂)₂(Cl)RuC.Tplbond.CH] Complexes. *Organometallics* **1993**, 12 (8), 3132–3139. <https://doi.org/10.1021/om00032a041>.
- (165) Marques-Gonzalez, S.; Parthey, M.; Yufit, D. S.; Howard, J. A. K.; Kaupp, M.; Low, P. J. Combined Spectroscopic and Quantum Chemical Study of Trans-Ru(C≡C-C₆H₄-R₁-4)(2)(Dppe)(2) (N⁺) and Trans-Ru(C≡C-C₆H₄-R₁-4)(C≡C-C₆H₄-R₂-4)(Dppe)(2) (N⁺) (N=0, 1) Complexes: Interpretations beyond the Lowest Energy Conformer Paradigm. *Organometallics* **2014**, 33 (18), 4947–4963.
- (166) Eaves, S. G.; Yufit, D. S.; Skelton, B. W.; Lynam, J. M.; Low, P. J. Reactions of Alkynes with Cis-RuCl₂(Dppm)₂: Exploring the Interplay of Vinylidene, Alkynyl and H₃-Butenynyl Complexes. *Dalton Trans.* **2015**, 44 (48), 21016–21024. <https://doi.org/10.1039/c5dt03844h>.
- (167) Oyama, Y.; Kawano, R.; Tanaka, Y.; Akita, M. Dinuclear Ruthenium Acetylide Complexes with Diethynylated Anthrahydroquinone and Anthraquinone Frameworks: A Multi-Stimuli-Responsive Organometallic Switch. *Dalton Trans* **2019**, 48 (21), 7432–7441.
- (168) Malvoti, F.; Rouxel, C.; Grelaud, G.; Toupet, L.; Roisnel, T.; Barlow, A.; Yang, X. W.; Wang, G. M.; Razak, F. I. A.; Stranger, R.; Cifuentes, M. P.; Humphrey, M. G.; Mongin, O.; Blanchard-Desce, M.; Paul-Roth, C. O.; Paul, F. Iron and Ruthenium Alkynyl Complexes with 2-Fluorenyl Groups: Some Linear and Nonlinear Optical Absorption Properties. *Eur J Inorg Chem* **2016**, No. 24, 3868–3882.
- (169) Rigaut, S.; Perruchon, J.; Pichon, L. L.; Touchard, D.; Dixneuf, P. H. Synthesis of Ruthenium Acetylides: New Building Blocks for Molecular Electronics. *J Organomet Chem* **2003**, 670, 37–44.

- (170) Rigaut, S.; Perruchon, J.; Guesmi, S.; Fave, C.; Touchard, D.; Dixneuf, P. H. Carbon-Rich Ruthenium Complexes Containing Bis(Allenylidene) and Mixed Alkynyl-Allenylidene Bridges. *Eur J Inorg Chem* **2005**, 447–460.
- (171) Olivier, C.; Kim, B.; Touchard, D.; Rigaut, S. Redox-Active Molecular Wires Incorporating Ruthenium(II) σ -Arylacetylide Complexes for Molecular Electronics. *Organometallics* **2008**, 27, 509–518. <https://doi.org/10.1021/om700779x>.
- (172) Fillaut, J.-L.; Dua, N. N.; Geneste, F.; Toupet, L.; Sinbandhit, S. Nitrile Ligands for Controlled Synthesis of Alkynyl-Ruthenium Based Homo and Hetero Bimetallic Systems. *J Organomet Chem* **2006**, 691, 5610–5618.
- (173) Fillaut, J.-L.; Andries, J.; Marwaha, R. D.; Lanoe, P.-H.; Lohio, O.; Toupet, L.; Williams, J. A. G. Flavonal Based Ruthenium Acetylides as Fluorescent Chemosensors for Lead Ions. *J Organomet Chem* **2008**, 693 (2), 228–234.
- (174) Gauthier, N.; Olivier, C.; Rigaut, S.; Touchard, D.; Roisnel, T.; Humphrey, M. G.; Paul, F. Intramolecular Optical Electron Transfer in Mixed-Valent Dinuclear Iron-Ruthenium Complexes Featuring a 1,4-Diethynylaryl Spacer. *Organometallics* **2008**, 27 (6), 1063–1072.
- (175) Weiss, D.; Dixneuf, P. H. Novel Polymetallic Vinylidene- and Allenylideneruthenium(II) Complexes. *Organometallics* **2003**, 22, 2209–2216.
- (176) Chin, B.; Lough, A. J.; Morris, R. H.; Schweitzer, C. T.; D'Agostino, C. Influence of Chloride versus Hydride on H-H Bonding and Acidity of the Trans Dihydrogen Ligand in the Complexes Trans-[Ru(H₂)X(PR₂CH₂CH₂PR₂)₂]⁺, X = Cl, H, R = Ph, Et. Crystal Structure Determinations of [RuCl(Dppe)₂]PF₆ and Trans-[Ru(H₂)Cl(Dppe)₂]PF₆. *Inorg Chem* **1994**, 33, 6278–6288.
- (177) Polam, J. R.; Porter, L. C. Ru(II) Complexes Containing Chelating Phosphine Ligands. Synthesis, Characterization, and X-Ray Crystal Structures of Dichlorobis(1,2-Bis(Diphenylphosphino)Ethane)Ru(II) and the Coordinatively Unsaturated Trigonal-Bipyramidal Cation, Chloro-Bis-(1,2-Bis(Diphenylphosphino)Ethane)Ru(II). *J Coord Chem* **1993**, 29, 109–119.
- (178) Cheredilin, D. N.; Dolgushin, F. M.; Balagurova, E. V.; Godovikov, I. A.; Chizhevsky, I. T. Synthesis of Cationic Ruthenium Diphosphine Complexes with Nido-Dicarbaundecaborate Anions. Molecular Structure of [RuCl(Dppe)₂]⁺[7,8-Nido-C₂B₉H₁₂]⁻. *Russ Chem Bull* **2004**, 53, 2086–2089. <https://doi.org/10.1007/s11172-005-0077-y>.
- (179) Du, J.; Kodikara, M. S.; Moxey, G. J.; Morshedi, M.; Barlow, A.; Quintana, C.; Wang, G. M.; Stranger, R.; Zhang, C.; Cifuentes, M. P.; Humphrey, M. G. Quadratic and Cubic Hyperpolarizabilities of Nitro-Phenyl/-Naphthalenyl/-Anthracenyl Alkynyl Complexes. *Dalton Trans* **2018**, 47 (13), 4560–4571.

- (180) Triadon, A.; Grelaud, G.; Richy, N.; Mongin, O.; Moxey, G. J.; Dixon, I. M.; Yang, X.; Wang, G.; Barlow, A.; Rault-Berthelot, J.; Cifuentes, M. P.; Humphrey, M. G.; Paul, F. Linear and Third-Order Nonlinear Optical Properties of Fe(H5-C5Me5)(K2-Dppe)- and Trans-Ru(K2-Dppe)2-Alkynyl Complexes Containing 2-Fluorenyl End Groups. *Organometallics* **2018**, 37 (14), 2245–2262. <https://doi.org/10.1021/acs.organomet.8b00229>.
- (181) Babgi, B. A.; Kodikara, M. S.; Morshedi, M.; Wang, H.; Quintana, C.; Schwich, T.; Moxey, G. J.; Steerteghem, N. V.; Clays, K.; Stranger, R.; Cifuentes, M. P.; Humphrey, M. G. Linear Optical, Quadratic and Cubic Nonlinear Optical, Electrochemical, and Theoretical Studies of “Rigid-Rod” Bis-Alkynyl Ruthenium Complexes. *ChemPlusChem* **2018**, 83 (7), 630–642. <https://doi.org/10.1002/cplu.201800093>.
- (182) Lyu, S.; Bertrand, C.; Hamamura, T.; Ducasse, L.; Toupance, T.; Olivier, C. Molecular Engineering of Ruthenium-Diacetylide Organometallic Complexes towards Efficient Green Dye for DSSC. *Dyes Pigments* **2018**, 158, 326–333. <https://doi.org/10.1016/j.dyepig.2018.05.060>.
- (183) Lyu, S.; Farre, Y.; Ducasse, L.; Pellegrin, Y.; Toupance, T.; Olivier, C.; Odobel, F. Push-Pull Ruthenium Diacetylide Complexes: New Dyes for p-Type Dye-Sensitized Solar Cells. *RSC Adv* **2016**, 6, 19928–19936.
- (184) De Sousa, S.; Ducasse, L.; Kauffmann, B.; Toupance, T.; Olivier, C. Functionalization of a Ruthenium-Diacetylide Organometallic Complex as a Next-Generation Push-Pull Chromophore. *Chem Eur J* **2014**, 20 (23), 7017–7024.
- (185) Liu, Y.; Ndiaye, C. M.; Lagrost, C.; Costuas, K.; Choua, S.; Turek, P.; Norel, L.; Rigaut, S. Diarylethene-Containing Carbon-Rich Ruthenium Organometallics: Tuning of Electrochromism. *Inorg Chem* **2014**, 53, 8172–8188.
- (186) Nisic, F.; Colombo, A.; Dragonetti, C.; Garoni, E.; Marinotto, D.; Righetto, S.; Angelis, F. D.; Lobello, M. G.; Salvatori, P.; Biagini, P.; Melchiorre, F. Functionalized Ruthenium Dialkynyl Complexes with High Second-Order Nonlinear Optical Properties and Good Potential as Dye Sensitizers for Solar Cells. *Organometallics* **2015**, 34 (1), 94–104. <https://doi.org/10.1021/om5009378>.
- (187) Touchard, D.; Guesmi, S.; Pichon, L. L.; Daridor, A.; Dixneuf, P. H. Ammonia Ruthenium Complexes for the Access to New Hydrido, Carbonyl and Isocyanide Ruthenium-Alkynyl Derivatives. *Inorg Chim Acta* **1998**, 280, 118–124.
- (188) Ozawa, F.; Mori, T. Preparation and C-Si Reductive Elimination Behavior of Cis-Alkynyl(Silyl)Platinum(II) Complexes. *Organometallics* **2003**, 22, 3593–3599.
- (189) Zargarian, D.; Chow, P.; Taylor, N. J.; Marder, T. B. Synthesis of RhI-s-Acetylide Complexes in Aqueous and Non-Aqueous Solutions: Molecular Structures of [(PMe3)4Rh(CC-Ph)] and [(PMe3)3Rh(CC-SiMe3)]. *J Chem Soc Chem Commun* **1989**, 540–544.

- (190) Klein, H.-F.; Karsch, H. H. Methyl Cobalt Compounds with Non-Chelating Ligands, I. Methyltetakis (Trimethylphosphine) Cobalt and Its Derivatives. *Chem Ber* **1975**, *108*, 944–955.
- (191) Field, L. D.; Turnbull, A. J.; Turner, P. Acetylide-Bridged Organometallic Oligomers via the Photochemical Metathesis of Methyl-Iron(II) Complexes. *J Am Chem Soc* **2002**, *124* (14), 3692–3702.
- (192) Field, L. D.; Magill, A. M.; Shearer, T. K.; Dalgarno, S. J.; Turner, P. Mono- and Bis-Acetylidoruthenium(II) Complexes by Controlled Metathesis of Methylruthenium Complexes with Acetylenes. *Organometallics* **2007**, *26*, 4776–4780.
- (193) Field, L. D.; Magill, A. M.; Shearer, T. K.; Dalgarno, S. J.; Bhadbhade, M. M. Symmetrical Bis(Acetylido)Ruthenium(II) Complexes. *Eur J Inorg Chem* **2011**, 3503–3510.
- (194) Field, L. D.; Magill, A. M.; Shearer, T. K.; Colbran, S. B.; Lee, S. T.; Dalgarno, S. J.; Bhadbhade, M. M. Controlled Synthesis of Dinuclear Acetylide-Bridged Ruthenium Complexes. *Organometallics* **2010**, *29*, 957–965.
- (195) Naik, S.; Scottwell, S. O.; Li, H. L.; Leong, C. F.; D'Alessandro, D. M.; Field, L. D. Dinuclear Acetylide-Bridged Ruthenium(Ii) Complexes with Rigid Non-Aromatic Spacers. *Dalton Trans* **2020**, *49* (8), 2687–2695.
- (196) Grelaud, G.; Cifuentes, M. P.; Paul, F.; Humphrey, M. G. Group 8 Metal Alkynyl Complexes for Nonlinear Optics. *J Organomet Chem* **2014**, *751*, 181–200.
- (197) Humphrey, M. G. Ruthenium Alkynyl Complexes in Non-Linear Optics. *Aust J Chem* **2018**, *71*, 731–742. <https://doi.org/10.1071/CH18325>.
- (198) Durand, R. J.; Gauthier, S.; Achelle, S.; Groizard, T.; Kahlal, S.; Saillard, J. Y.; Barsella, A.; Poul, N. L.; Guen, F. R. L. Push-Pull D- π -Ru- π -A Chromophores: Synthesis and Electrochemical, Photophysical and Second-Order Nonlinear Optical Properties. *Dalton Trans.* **2018**, *47* (11), 3965–3975. <https://doi.org/10.1039/c8dt00093j>.
- (199) Launay, J. P. Mixed-Valent Compounds and Their Properties - Recent Developments. *Eur J Inorg Chem* **2020**, *2020* (4), 329–341.
- (200) He, X.; Lagrost, C.; Norel, L.; Rigaut, S. Ruthenium(II) Sigma-Arylacetylide Complexes as Redox Active Units for (Multi-)Functional Molecular Devices. *Polyhedron* **2018**, *140*, 169–180.
- (201) Meng, F. B.; Hervault, Y. M.; Norel, L.; Costuas, K.; Van Dyck, C.; Geskin, V.; Cornil, J.; Hng, H. H.; Rigaut, S.; Chen, X. D. Photo-Modulable Molecular Transport Junctions Based on Organometallic Molecular Wires. *Chem Sci* **2012**, *3* (10), 3113–3118.

- (202) Lavastre, O.; Plass, J.; Bachmann, P.; Guesmi, S.; Moinet, C.; Dixneuf, P. H. Ruthenium or Ferrocenyl Homobimetallic and RuPdRu and FePdFe Heterotrimetallic Complexes Connected by Unsaturated, Carbon-Rich $\text{-C}\equiv\text{CC}_6\text{H}_4\text{C}\equiv\text{C-}$ Bridges. *Organometallics* **1997**, *16* (2), 184–189.
- (203) Roy, S. S.; Chowdhury, S. R.; Mishra, S.; Patra, S. K. Role of Substituents at the 3-Position of Thienylethynyl Spacer on Electronic Properties in Diruthenium(II) Organometallic Wire-Like Complexes. *Chem Asian J* **2020**, *15* (20), 3304–3313.
- (204) Kim, B.; Beebe, J. M.; Olivier, C.; Rigaut, S.; Touchard, D.; Kushmerick, J. G.; Zhu, X.-Y.; Frisbie, C. D. Temperature and Length Dependence of Charge Transport in Redox-Active Molecular Wires Incorporating Ruthenium(II) Bis(-Arylacetylide) Complexes. *J Phys Chem C* **2007**, *111* (20), 7521–7526.
- (205) Luo, L.; Benameur, A.; Brignou, P.; Choi, S. H.; Rigaut, S.; Frisbie, C. D. Length and Temperature Dependent Conduction of Ruthenium-Containing Redox-Active Molecular Wires. *J. Phys. Chem. C* **2011**, *115* (40), 19955–19961. <https://doi.org/10.1021/jp207336v>.
- (206) Mulas, A.; Hervault, Y. M.; Norel, L.; Rigaut, S.; Lagrost, C. Electron-Transfer Kinetics in Polymetallic Carbon-Rich Ruthenium(II) Bis(Sigma-Arylacetylides) Wires Connected to Gold. *ChemElectroChem* **2015**, *2* (11), 1799–1805.
- (207) Mulas, A.; Hervault, Y.-M.; He, X.; Di Piazza, E.; Norel, L.; Rigaut, S.; Lagrost, C. Fast Electron Transfer Exchange at Self-Assembled Monolayers of Organometallic Ruthenium(II) Sigma-Arylacetylide Complexes. *Langmuir* **2015**, *31* (25), 7138–7147.
- (208) Sugimoto, K.; Tanaka, Y.; Fujii, S.; Tada, T.; Kiguchi, M.; Akita, M. Organometallic Molecular Wires as Versatile Modules for Energy-Level Alignment of the Metal-Molecule-Metal Junction. *Chem Commun* **2016**, *52*, 5796–5799.
- (209) Bock, S.; Al-Owaedi, O. A.; Eaves, S. G.; Milan, D. C.; Lemmer, M.; Skelton, B. W.; Osorio, H. M.; Nichols, R. J.; Higgins, S. J.; Cea, P.; Long, N. J.; Albrecht, T.; Martin, S.; Lambert, C. J.; Low, P. J. Single-Molecule Conductance Studies of Organometallic Complexes Bearing 3-Thienyl Contacting Groups. *Chem Eur J* **2017**, *23* (9), 2133–2143.
- (210) Ezquerra, R.; Eaves, S. G.; Bock, S.; Skelton, B. W.; Pérez-Murano, F.; Cea, P.; Martín, S.; Low, P. J. New Routes to Organometallic Molecular Junctions via a Simple Thermal Processing Protocol. *J. Mater. Chem. C* **2019**, *7* (22), 6630–6640. <https://doi.org/10.1039/C9TC01305A>.

- (211) Almosni, S.; Delamarre, A.; Jehl, Z.; Suchet, D.; Cojocaru, L.; Giteau, M.; Behaghel, B.; Julian, A.; Ibrahim, C.; Tatry, L.; Wang, H.; Kubo, T.; Uchida, S.; Segawa, H.; Miyashita, N.; Tamaki, R.; Shoji, Y.; Yoshida, K.; Ahsan, N.; Watanabe, K.; Inoue, T.; Sugiyama, M.; Nakano, Y.; Hamamura, T.; Toupance, T.; Olivier, C.; Chambon, S.; Vignau, L.; Geffroy, C.; Cloutet, E.; Hadziioannou, G.; Cavassilas, N.; Rale, P.; Cattoni, A.; Collin, S.; Gibelli, F.; Paire, M.; Lombez, L.; Aureau, D.; Bouttemy, M.; Etcheberry, A.; Okada, Y.; Guillemoles, J.-F. Material Challenges for Solar Cells in the Twenty-First Century: Directions in Emerging Technologies. *Sci. Technol. Adv. Mater.* **2018**, *19* (1), 336–369. <https://doi.org/10.1080/14686996.2018.1433439>.
- (212) De Sousa, S.; Lyu, S.; Ducasse, L.; Toupance, T.; Olivier, C. Tuning Visible-Light Absorption Properties of Ru-Diacetylide Complexes: Simple Access to Colorful Efficient Dyes for DSSCs. *J Mater Chem A* **2015**, *3*, 18256–18264.
- (213) Liu, Z.; Li, W.; Topa, S.; Xu, X.; Zeng, X.; Zhao, Z.; Wang, M.; Chen, W.; Wang, F.; Cheng, Y.-B.; He, H. Fine-Tuning of Fluorene-Based Dye Structures for High Efficiency p-Type Dye-Sensitized Solar Cells. *ACS Appl Mater Interfaces* **2014**, *6* (13), 10614–10622.
- (214) Meldal, M.; Tornøe, C. W. Cu-Catalyzed Azide-Alkyne Cycloaddition. *Chem Rev* **2008**, *108*, 2952–3015.
- (215) Burgun, A.; Gendron, F.; Schauer, P. A.; Skelton, B. W.; Low, P. J.; Costuas, K.; Halet, J.-F.; Bruce, M. I.; Lapinte, C. Straightforward Access to Tetrametallic Complexes with a Square Array by Oxidative Dimerization of Organometallic Wires. *Organometallics* **2013**, *32*, 5015–5025. <https://doi.org/10.1021/om4003768>.
- (216) Bruce, M. I. Some Organometallic Chemistry of Tetracyanoethene: CN-Displacement and Cycloaddition Reactions with Alkynyl-Transition Metal Complexes and Related Chemistry. *Aust J Chem* **2011**, *64* (1), 77–103.
- (217) Xu, L.; Ho, C.-L.; Liu, L.; Wong, W.-Y. Molecular/Polymeric Metallaynes and Related Molecules: Solar Cell Materials and Devices. *Coord. Chem. Rev.* **2018**, *373*, 233–257. <https://doi.org/10.1016/j.ccr.2017.10.015>.
- (218) Zhang, L.; Humphrey, M. G. Multiphoton Absorption at Metal Alkynyl Complexes. *Coord. Chem. Rev.* **2022**, *473*, 214820. <https://doi.org/10.1016/j.ccr.2022.214820>.
- (219) Zhu, H.; Pookpanratana, S. J.; Bonevich, J. E.; Natoli, S. N.; Hacker, C. A.; Ren, T.; Suehle, J. S.; Richter, C. A.; Li, Q. Redox-Active Molecular Nanowire Flash Memory for High-Endurance and High-Density Non-Volatile Memory Applications. *ACS Appl Mater Interfaces* **2015**, *7*, 27306–27313.
- (220) Milan, D. C.; Vezzoli, A.; Planje, I. J.; Low, P. J. Metal Bis(Acetylide) Complex Molecular Wires: Concepts and Design Strategies. *Dalton Trans.* **2018**, *47* (40), 14125–14138. <https://doi.org/10.1039/C8DT02103A>.

- (221) Roy, S. S.; Sil, A.; Giri, D.; Chowdhury, S. R.; Mishra, S.; Patra, S. K. Diruthenium(II)-Capped Oligothiénylethynyl Bridged Highly Soluble Organometallic Wires Exhibiting Long-Range Electronic Coupling. *Dalton Trans.* **2018**, 47 (40), 14304–14317. <https://doi.org/10.1039/C8DT01818A>.
- (222) Lambert, C. J. Basic Concepts of Quantum Interference and Electron Transport in Single-Molecule Electronics. *Chem. Soc. Rev.* **2015**, 44 (4), 875–888. <https://doi.org/10.1039/C4CS00203B>.
- (223) Gauthier, N.; Tehouar, N.; Justaud, F.; Argouarch, G.; Cifuentes, M. P.; Toupet, L.; Touchard, D.; Halet, J. F.; Rigaut, S.; Humphrey, M. G.; Costuas, K.; Paul, F. Bonding and Electron Delocalization in Ruthenium(III) σ -Arylacetylide Radicals [TransCl(H₂-Dppe)₂RuC \equiv C(4-C₆H₄X)]⁺ (X = NO₂, C(O)H, C(O)Me, F, H, OMe, NMe₂): Misleading Aspects of the ESR Anisotropy. *Organometallics* **2009**, 28 (7), 2253–2266. <https://doi.org/10.1021/om801138q>.
- (224) Miller-Clark, L. A.; Ren, T. Syntheses and Material Applications of Ru(II)(Bisphosphine)₂ Alkynyls. *J. Organomet. Chem.* **2021**, 951, 122003. <https://doi.org/10.1016/j.jorganchem.2021.122003>.
- (225) Lyu, S.; Massin, J.; Pavone, M.; Muñoz-García, A. B.; Labrugère, C.; Toupance, T.; Chavarot-Kerlidou, M.; Artero, V.; Olivier, C. H₂-Evolving Dye-Sensitized Photocathode Based on a Ruthenium–Diacetylide/Cobaloxime Supramolecular Assembly. *ACS Appl. Energy Mater.* **2019**, 2 (7), 4971–4980. <https://doi.org/10.1021/acs.aem.9b00652>.
- (226) Quintana, C.; Morshedi, M.; Du, J.; Morrall, J. P. L.; Zaręba, J. K.; Samoc, M.; Cifuentes, M. P.; Humphrey, M. G. Hybrids of Gold Nanoparticles and Oligo(p-Phenyleneethynylene)s End-Functionalized with Alkynylruthenium Groups: Outstanding Two-Photon Absorption in the Second Biological Window. *Nano Res.* **2020**, 13 (10), 2755–2762. <https://doi.org/10.1007/s12274-020-2924-4>.
- (227) Naher, M.; Milan, D. C.; Al-Owaedi, O. A.; Planje, I. J.; Bock, S.; Hurtado-Gallego, J.; Bastante, P.; Abd Dawood, Z. M.; Rincón-García, L.; Rubio-Bollinger, G.; Higgins, S. J.; Agraït, N.; Lambert, C. J.; Nichols, R. J.; Low, P. J. Molecular Structure–(Thermo)Electric Property Relationships in Single-Molecule Junctions and Comparisons with Single- and Multiple-Parameter Models. *J. Am. Chem. Soc.* **2021**, 143 (10), 3817–3829. <https://doi.org/10.1021/jacs.0c11605>.
- (228) Naher, M.; Bock, S.; Langtry, Z. M.; O'Malley, K. M.; Sobolev, A. N.; Skelton, B. W.; Korb, M.; Low, P. J. Synthesis, Structure and Physical Properties of “Wire-like” Metal Complexes. *Organometallics* **2020**, 39 (24), 4667–4687. <https://doi.org/10.1021/acs.organomet.0c00685>.
- (229) Al-Owaedi, O. A.; Milan, D. C.; Oerthel, M.-C.; Bock, S.; Yufit, D. S.; Howard, J. A. K.; Higgins, S. J.; Nichols, R. J.; Lambert, C. J.; Bryce, M. R.; Low, P. J. Experimental and Computational Studies of the Single-Molecule Conductance of Ru(II) and Pt(II) Trans-Bis(Acetylide) Complexes. *Organometallics* **2016**, 35 (17), 2944–2954. <https://doi.org/10.1021/acs.organomet.6b00472>.

- (230) Mulas, A.; He, X.; Hervault, Y. M.; Norel, L.; Rigaut, S.; Lagrost, C. Dual-Responsive Molecular Switches Based on Dithienylethene–RuII Organometallics in Self-Assembled Monolayers Operating at Low Voltage. *Chem. - Eur. J.* **2017**, *23* (42), 10205–10214. <https://doi.org/10.1002/chem.201701903>.
- (231) Meng, L.; Xin, N.; Hu, C.; Sabea, H. A.; Zhang, M.; Jiang, H.; Ji, Y.; Jia, C.; Yan, Z.; Zhang, Q.; Gu, L.; He, X.; Selvanathan, P.; Norel, L.; Rigaut, S.; Guo, H.; Meng, S.; Guo, X. Dual-Gated Single-Molecule Field-Effect Transistors beyond Moore's Law. *Nat. Commun.* **2022**, *13* (1), 1410. <https://doi.org/10.1038/s41467-022-28999-x>.
- (232) Wasielewski, M. R. Photoinduced Electron Transfer in Supramolecular Systems for Artificial Photosynthesis. *Chem. Rev.* **1992**, *92* (3), 435–461. <https://doi.org/10.1021/cr00011a005>.
- (233) Hagfeldt, A.; Grätzel, M. Molecular Photovoltaics. *Acc. Chem. Res.* **2000**, *33* (5), 269–277. <https://doi.org/10.1021/ar980112j>.
- (234) Alstrum-Acevedo, J. H.; Brennaman, M. K.; Meyer, T. J. Chemical Approaches to Artificial Photosynthesis. 2. *Inorg. Chem.* **2005**, *44* (20), 6802–6827. <https://doi.org/10.1021/ic050904r>.
- (235) Eisenberg, R. Rethinking Water Splitting. *Science* **2009**, *324* (5923), 44–45. <https://doi.org/10.1126/science.1172247>.
- (236) Albinsson, B.; Mårtensson, J. Long-Range Electron and Excitation Energy Transfer in Donor–Bridge–Acceptor Systems. *J. Photochem. Photobiol. C Photochem. Rev.* **2008**, *9* (3), 138–155. <https://doi.org/10.1016/j.jphotochemrev.2008.01.002>.
- (237) Barbara, P. F.; Meyer, T. J.; Ratner, M. A. Contemporary Issues in Electron Transfer Research. *J. Phys. Chem.* **1996**, *100* (31), 13148–13168. <https://doi.org/10.1021/jp9605663>.
- (238) Gabe, Y.; Urano, Y.; Kikuchi, K.; Kojima, H.; Nagano, T. Highly Sensitive Fluorescence Probes for Nitric Oxide Based on Boron Dipyrromethene Chromophore Rational Design of Potentially Useful Bioimaging Fluorescence Probe. *J. Am. Chem. Soc.* **2004**, *126* (10), 3357–3367. <https://doi.org/10.1021/ja037944j>.
- (239) Sessler, J. L.; Wang, B.; Harriman, A. Photoinduced Energy Transfer in Associated, but Noncovalently-Linked Photosynthetic Model Systems. *J. Am. Chem. Soc.* **1995**, *117* (2), 704–714. <https://doi.org/10.1021/ja00107a014>.
- (240) Scattergood, P. A.; Delor, M.; Sazanovich, I. V.; Bouganov, O. V.; Tikhomirov, S. A.; Stasheuski, A. S.; Parker, A. W.; Greetham, G. M.; Towrie, M.; Davies, E. S.; Meijer, A. J. H. M.; Weinstein, J. A. Electron Transfer Dynamics and Excited State Branching in a Charge-Transfer Platinum(II) Donor-Bridge-Acceptor Assembly. *Dalton Trans.* **2014**, *43* (47), 17677–17693. <https://doi.org/10.1039/c4dt01682c>.

- (241) Delor, M.; Keane, T.; Scattergood, P. A.; Sazanovich, I. V.; Greetham, G. M.; Towrie, M.; Meijer, A. J. H. M.; Weinstein, J. A. On the Mechanism of Vibrational Control of Light-Induced Charge Transfer in Donor-Bridge-Acceptor Assemblies. *Nat. Chem.* **2015**, 7 (9), 689–695. <https://doi.org/10.1038/nchem.2327>.
- (242) Ren, T. Sustainable Metal Alkynyl Chemistry: 3d Metals and Polyaza Macrocyclic Ligands. *Chem. Commun.* **2016**, 52 (16), 3271–3279. <https://doi.org/10.1039/C5CC09365A>.
- (243) Banziger, S. D.; Ren, T. Syntheses, Structures and Bonding of 3d Metal Alkynyl Complexes of Cyclam and Its Derivatives. *J Organomet Chem* **2019**, 885, 39–48.
- (244) Banziger, S. D.; Li, X.; Valdiviezo, J.; Zeller, M.; Zhang, P.; Beratan, D. N.; Rubtsov, I. V.; Ren, T. Unsymmetrical Bis-Alkynyl Complexes Based on Co(III)(Cyclam): Synthesis, Ultrafast Charge Separation, and Analysis. *Inorg. Chem.* **2019**, 58 (22), 15487–15497. <https://doi.org/10.1021/acs.inorgchem.9b02557>.
- (245) Banziger, S. D.; Judkins, E. C.; Zeller, M. Diruthenium-DMBA Bis-Alkynyl Compounds with Hetero- and Extended-Aryl Appendant: Preparation and Electrochemical Property. *Chin. J. Inorg. Chem.* **2017**, 33 (11), 2103–2109. <https://doi.org/10.11862/CJIC.2017.238>.
- (246) Banziger, S. D.; Zeller, M.; Ren, T. New Synthetic Route for Cobalt(III) Dissymmetric Bisalkynyl Complexes Based on Cobalt(III)(Cyclam)(C₂NAP Mes). *Eur. J. Inorg. Chem.* **2019**, 2019 (44), 4766–4772. <https://doi.org/10.1002/ejic.201901070>.
- (247) McAdam, C. J.; Manning, A. R.; Robinson, B. H.; Simpson, J. Group 8 and 10 Metal Acetylide Naphthalimide Dyads. *Inorganica Chim. Acta* **2005**, 358 (5), 1673–1682. <https://doi.org/10.1016/j.ica.2004.12.013>.
- (248) Piazza, E. D.; Boilleau, C.; Vacher, A.; Merahi, K.; Norel, L.; Costuas, K.; Roisnel, T.; Choua, S.; Turek, P.; Rigaut, S. Ruthenium Carbon-Rich Group as a Redox-Switchable Metal Coupling Unit in Linear Trinuclear Complexes. *Inorg. Chem.* **2017**, 56 (23), 14540–14555. <https://doi.org/10.1021/acs.inorgchem.7b02288>.
- (249) Powell, C. E.; Hurst, S. K.; Morrall, J. P.; Cifuentes, M. P.; Roberts, R. L.; Samoc, M.; Humphrey, M. G. Organometallic Complexes for Nonlinear Optics. 39.1 Syntheses and Third-Order Nonlinear Optical Properties of First-Generation Peripherally Metalated Arylalkynyl Dendrimers. *Organometallics* **2007**, 26 (18), 4456–4463. <https://doi.org/10.1021/om700398n>.
- (250) Hurst, S. K.; Cifuentes, M. P.; McDonagh, A. M.; Humphrey, M. G.; Samoc, M.; Luther-Davies, B.; Asselberghs, I.; Persoons, A. Organometallic Complexes for Nonlinear Optics: Part 25. Quadratic and Cubic Hyperpolarizabilities of Some Dipolar and Quadrupolar Gold and Ruthenium Complexes. *J. Organomet. Chem.* **2002**, 642 (1), 259–267. [https://doi.org/10.1016/S0022-328X\(01\)01281-5](https://doi.org/10.1016/S0022-328X(01)01281-5).
- (251) Grelaud, G.; Cifuentes, M. P.; Schwich, T.; Argouarch, G.; Petrie, S.; Stranger, R.; Paul, F.; Humphrey, M. G. Multistate Redox-Active Metalated Triarylamines. *Eur. J. Inorg. Chem.* **2012**, 2012 (1), 65–75. <https://doi.org/10.1002/ejic.201100747>.

- (252) Morrall, J. P. L.; Cifuentes, M. P.; Humphrey, M. G.; Kellens, R.; Robijns, E.; Asselberghs, I.; Clays, K.; Persoons, A.; Samoc, M.; Willis, A. C. Organometallic Complexes for Nonlinear Optics. Part 36. Quadratic and Cubic Optical Nonlinearities of 4-Fluorophenylethynyl- and 4-Nitro-(E)-Stilbenylethynylruthenium Complexes. *Inorganica Chim. Acta* **2006**, 359 (3), 998–1005. <https://doi.org/10.1016/j.ica.2005.09.012>.
- (253) Bautista, M. T.; Cappellani, E. P.; Drouin, S. D.; Morris, R. H.; Schweitzer, C. T.; Sella, A.; Zubkowski, J. Preparation and Spectroscopic Properties of the η^2 -Dihydrogen Complexes $[MH(\eta^2-H_2)PR_2CH_2CH_2PR_2]_2$ + (M = Iron, Ruthenium; R = Ph, Et) and Trends in Properties down the Iron Group Triad. *J. Am. Chem. Soc.* **1991**, 113 (13), 4876–4887. <https://doi.org/10.1021/ja00013a025>.
- (254) Chaudret, B.; Commenges, G.; Poilblanc, R. Bis(Diphenylphosphino)Methane Complexes of Ruthenium(0) and Ruthenium(II). *J. Chem. Soc. Dalton Trans.* **1984**, No. 8, 1635. <https://doi.org/10.1039/dt9840001635>.
- (255) Tomasi, J.; Mennucci, B.; Cammi, R. Quantum Mechanical Continuum Solvation Models. *Chem. Rev.* **2005**, 105 (8), 2999–3094. <https://doi.org/10.1021/cr9904009>.

VITA

Lyndsy received her ACS Certified B.S. in Chemistry in May 2017 from Hope College. While at Hope College, Lyndsy worked in the laboratory of Prof. Amanda Eckermann. Her undergraduate research focused on the synthesis and characterization of both mono- and diruthenium piano-stool compounds for increased water solubility and anti-cancer properties.

After graduating from Hope College and spending the summer completing her work in the Eckermann group, Lyndsy moved to Purdue University in the fall of 2017. She began her graduate education at Purdue under the supervision of Prof. Tong Ren in December 2017. During this time, Lyndsy began working on attempting to synthesize dissymmetric bis-alkynyl compounds based on $\text{Ru(II)(biphosphine)}_2$ to investigate the electronic structures of ‘donor-bridge-acceptor’ molecules. This initial work has led to Lyndsy working on multiple diruthenium chemistry projects: the first focused on improving the solubility of diruthenium aryl compounds, the second on characterizing electronic communication via a phenylene bridging ligand, and the third on investigating the organometallic derivatization on an electron-poor bridging ligand. Between July 2021 and November 2022, she has published four papers on these projects above detailing her graduate work, with a fifth manuscript in preparation on the Ru(II)(dppe)_2 mono- and bis-alkynyl compounds.

LIST OF PUBLICATIONS

- (1) L. A. Miller-Clark and T. Ren, *Journal of Organometallic Chemistry*, **2021**, 951, 122003
- (2) A. J. Schuman; M. M. Mills; L. R. Segura; L. A. Miller-Clark; T. Ren, *Journal of Organometallic Chemistry*, **2021**, 954-955, 122110
- (3) L. A. Miller-Clark; P. E. Christ; T. Ren, *Dalton Transactions*, **2022**, 51, 580-586
- (4) L. A. Miller-Clark; A. Raghavan; R. A. Clendening; T. Ren, *Chemical Communications*, **2022**, 58, 5478-5481
- (5) L. A. Miller-Clark; P. E. Christ; B. T. Barbarini; T. Ren, *Inorganic Chemistry*, **2022**, 61, 14871-14879
- (6) L. A. Miller-Clark and T. Ren, *manuscript in preparation to Organometallics*